Synthesis of reaction-diffusion patterns with DNA : towards Turing patterns

Adrian Zambrano Ramirez

NNT : 2016SACLS214

THÈSE DE DOCTORAT
DE
L'UNIVERSITÉ PARIS-SACLAY
PRÉPARÉE À
L'UNIVERSITÉ PARIS-SUD

AU
LABORATOIRE DE PHOTONIQUE ET DE NANOSTRUCTURES - CNRS
ET AU
LABORATOIRE JEAN PERRIN – CNRS/UPMC

ÉCOLE DOCTORALE N°575
Electrical, optical, bio-physics and engineering (EOBE)

Spécialité : Physique

Par

Adrian Zambrano Ramirez

Synthesis of reaction-diffusion patterns with DNA: towards Turing patterns

Thèse présentée et soutenue à Paris, le 26 septembre 2016 :

Composition du Jury :

M. Mergny, Jean-Louis	Directeur de recherche, INSERM Bordeaux	Président
Mme. Taylor, Annette	Senior Lecturer, University of Sheffield	Rapporteur
M. Gasparutto, Didier	Directeur de recherche, CEA Grenoble	Rapporteur
M. Mergny, Jean-Louis	Directeur de recherche, INSERM Bordeaux	Examinateur
M. Michelin, Sébastien	Associate Professor, École Polytechnique	Examinateur
M. Estévez-Torres, André	Chargé de recherche, CNRS	Directeur de thèse
M. Galas, Jean-Christophe	Chargé de recherche, CNRS	Co-encadrant

Université Paris-Saclay
Espace Technologique / Immeuble Discovery
Route de l'Orme aux Merisiers RD 128 / 91190 Saint-Aubin, France

Acknowledgements

This work was started in the Laboratoire de photonique et nanostructures-CNRS (LPN), which is now part of the Centre for Nanoscience and Nanotechnology (C2N), and continued in the Laboratoire of Jean Perrin (LJP) at the Pierre-and-Marie-Curie University (UPMC).

I owe my deepest gratitude to André Estévez-Torres for supervising my PhD work with great enthusiasm and determination. This thesis would not have been possible without the constant motivation and support given to me by Jean-Christophe Galas (J.C.). I cannot find words to express my gratitude to my loyal friend and colleague Jonathan Lee Tin Wah for his countless personal and scientific advices. I consider it an honor to have worked with Anton Zadorin, whose exceptional intelligence and sense of humor enriched my research experience. I am very grateful for all the group meetings and fruitful discussions since they often led to a vast number of scientific ideas.

I would like to show my gratitude to close collaborators who largely contributed to my education: Alexandre Baccouche, Gines Guillaume, Nathanaël Aubert and Yannick Rondelez. I would like to acknowledge Olivier Languin and Vadim Dilhas for their contribution to the work presented in Chapter 2 and 3 during their internships. I am very much indebted to my many of my colleagues for supporting me: from the LPN (i) Antoine Barbot, Avishek Chowdhury, Hugo Salmon and Sébastien Sconly Alvo, and from the LJP (ii) Alexandre Deloupy, Anis Senoussi, Aurélien Bour and Florence Bansept. I am immensely grateful to all the researchers and secretaries of both host institutions for welcoming and allowing me to carry out my PhD project.

Acknowledgements

I would like to express my gratitude to the Ziegler-Boeckman family: Cornelia, Sven, Julian Erasmus and Louis Adrian. I also want to thank my dear friends who made my 3 years in France very pleasant and joyful: Dany Salado, Luis Hernandez and Uriel Esparza. I am sincerely and heartily grateful to my parents Rafael and Guadalupe and siblings Oscar and Alejandra for their unconditional love and support. I would like to thank Kitita Laura Luna for her immense encouragement and love during the past few years. I would like to express my gratitude to my dear friends Alan and Bobbi Metzger for their kindness and support. I am sure I have left out unintentionally many names, so I would like to thank all those who made this thesis possible.

Paris, 26 September 2016 Adrian

Résumé

Comment les systèmes vivants acquièrent leur forme et fonctions est une question fondamentale en biologie du développement. L'ordre spatial et spatiotemporel dans les systèmes biologiques résulte de réseaux de réaction biochimiques complexes qui interagissent au sein de la cellule. Les deux idées les plus influentes dans la biologie du développement utilisés pour expliquer la formation de motifs sont : (1) l'information positionnelle par Lewis Wolpert et (2) les systèmes de réaction-diffusion par Alan Turing. Dans l'information positionnelle, aussi connu comme le modèle du drapeau français, un gradient de morphogène préexistant à travers l'espace fournit des valeurs de position comme dans un système de coordonnées, ce qui est interprété en plusieurs zones chimiquement distinctes avec des frontières nettes. Pour expliquer l'apparition de motifs le célèbre mathématicien Alan Turing a proposé un processus physicochimique dans lequel l'espèce chimique réagit et se diffuse. Deux espèces chimiques principales sont impliquées dans cette diffusion de réaction (RD). L'une des espèces agit comme un activateur et l'autre comme un inhibiteur. Ces deux espèces sont interdépendantes et assemblées dans un réseau de réaction. L'activateur est capable de s'autoreproduire, mais produit en même temps un inhibiteur qui réprime la croissance de l'activateur. En outre, comme noté par Turing, le coefficient de diffusion de l'inhibiteur est plus grand que celui de l'activateur ; l'inhibiteur se propage donc plus rapidement d'une région spatiale riche en activateur. Les motifs apparaissent alors de cette différence entre activation à courte portée et inhibition à longue portée. Les mécanismes de diffusion de réaction, comme le modèle de Turing, sont essentiels pour comprendre comment la forme apparaît dans le monde du vivant ; cependant, ils restent en grande partie inexplorés en chimie.

Acknowledgements

Bien que des simulations numériques et l'analyse mathématique corroborent le potentiel incroyable de mécanismes de RD pour produire des motifs, la mise en œuvre de leurs contreparties expérimentales n'est pas facile. La raison principale à la difficulté de synthétiser des modèles chimiques arbitraires à partir de zéro est l'absence de système de RD entièrement programmable. La résolution de ce problème nécessite des approches ascendantes dans lesquel la cinétique et la diffusion peuvent être mises au point individuellement. De plus, ces systèmes dissipatifs hors-équilibre chimiques doivent être capables de s'auto-organiser dans des structures spatiotemporelles, comme des ondes qui se propagent ou des structures de Turing. Trois exigences principales sont nécessaires pour créer un motif chimique via le modèle de Turing : (i) contrôle de la topologie du réseau de réaction, (ii) contrôle de la diffusion de l'espèce activatrice et (iii) définition des conditions initiales et aux frontières dans lesquelles les réactions ont lieu. Afin d'obtenir une meilleure compréhension de la formation de motifs via la diffusion de réaction nous avons examiné chacune de ces trois exigences.

Dans le cas de la topologie de réseau nous utilisons l'acide désoxyribonucléique (l'ADN) comme espèce réactive chimique. L'ADN est une molécule fondamentale qui porte des informations génétiques pour des systèmes vivants, mais nous utilisons de l'ADN court oligos comme des blocs de construction pour assembler des réseaux de réaction de façon ascendante. La réactivité prévisible de l'ADN en raison des règles de paires de Watson-Crick (c'est-à-dire les paires A / T et C / G via le lien d'hydrogène) font de l'ADN un substrat chimique de choix pour des réseaux de réaction d'ingénierie. Autre avantage à l'utilisation de l'ADN : cette molécule peut être chimiquement modifiée pour interagir avec des billes ou des surfaces fonctionnalisées. En l'utilisant, nous proposons dans ce travail plusieurs stratégies qui offrent la possibilité de contrôler précisément et indépendamment le coefficient de diffusion de chaque espèce d'ADN individuelle aux nœuds de la réaction. Pour aborder la troisième exigence, nous avons exploité les avantages de la microfluidique (haute résolution spatiale et temporelle dans le traitement de liquide) pour précisément définir des conditions initiales et des frontières. Ainsi, ce travail est composé de trois chapitres expérimentaux, en plus des chapitres d'introduction.

Chapitre 1 – Dans ce chapitre, nous avons testé un réseau de réaction avec une topologie activateur-inhibiteur, comme requis par le mécanisme de Turing. D'abord, nous nous sommes concentrés sur le test d'un système de réaction à base d'ADN qui peut être assemblé dans des réseaux de réaction. Ces machines de reproduction d'ADN in-vitro sont surnommées : « PEN-DNA toolbox » pour : Polymérase/Exonucléase/Nickase, boîte à outils d'Assemblage de Réseau Dynamique. La boîte PEN-DNA toolbox emploie 3 enzymes : polymérase, exonucléase et nickase. Cette technologie permet de concevoir la topologie de réseau en utilisant des fonctionnalités analogues à celles trouvées dans des réseaux biologiques. Les nœuds de réaction sont connectés par une espèce d'ADN de reliure courte, simple brin, intercalée entre des motifs d'ADN plus longs. Donc, un réseau de réaction est réalisé en définissant un type de fonction de nœud, c'est-à-dire l'activateur ou l'inhibiteur, et en liant ce nœud à un autre. Dans ce chapitre nous avons utilisé un réseau avec une boucle de rétroaction négative capable de montrer un comportement oscillant. Nous nous sommes concentrés sur la recherche des conditions expérimentales qui assurent des oscillations temporelles. Pendant les expériences systématiques nous avons démontré que des fonctions d'opérateur logique de l'algèbre de Boole telle que la fonction NOT peuvent être implémentées en utilisant un nœud d'inhibition. Bien que, les conditions expérimentales pour des oscillations n'aient pas été trouvées, ce travail m'a permis de comprendre l'essentiel de notre système de réaction biochimique à base d'ADN.

Chapitre 2 – Les structures de Turing apparaissent à partir d'un réseau de réaction d'inhibiteur-activateur, dans lequel le coefficient de diffusion de l'activateur doit être beaucoup plus petit que celui de l'inhibiteur. Dans ce chapitre nous nous concentrons sur le défi de respecter la condition de diffusion de Turing en essayant de réduire le coefficient de diffusion effectif de l'activateur (α). Nous avons employé un réseau autocatalytique, dans lequel une espèce d'activateur d'ADN s'auto-reproduit sur un motif (de l'ADN matrice).

Un nœud autocatalytique est utilisé comme modèle de procuration de l'activateur. Ceci forme une partie du réseau de réaction inhibiteur/activateur pour des motifs de Turing. Le nœud autocatalytique est composé d'une espèce d'activateur d'ADN (α) qui

s'autoreproduit sur un modèle. L'objectif de ce travail est de réduire le coefficient de diffusion de l'espèce α. Pour cela nous travaillons sur la partie efficace du coefficient de diffusion α en immobilisant le motif dans des billes d'agarose réticulées. Nous avons étudié des ondes de propagation de l'espèce α dues à des processus de diffusion de réaction afin de démontrer notre stratégie. Nous avons divisé le coefficient de diffusion efficace par 4-4.7. Une deuxième stratégie a été testée : les motifs sont ici attachés à des billes magnétiques. La propagation du front d'onde et les expériences de cinétique ont montrés que nous avons divisé le coefficient de diffusion efficace par 2.4 par cette méthode.

Chapitre 3 – Cependant, nous avons trouvé une application pour les billes dans la morphogenèse de matériaux. Nous avons démontré que les réactions d'ADN peuvent être interfacées avec les billes magnétiques : un front de billes agrégées a été produit par un front de α. Nous avons aussi observé un motif stationnaire de α transféré en un motif de billes agrégées.

Chapitre 4– Après s'être intéressé au contrôle de la topologie de réseau et à la diffusion dans le Chapitre 1 et le Chapitre 2, ici nous abordons le problème des conditions aux frontières sur un système de réaction-diffusion à base d'ADN. Plus précisément, nous développons une technique microfluidique pour étudier la propagation d'ondes d'ADN dans des microréacteurs à la géométrie contrôlée. Nous examinons la dynamique de propagation d'un réseau de type proie-prédateur en guise d'application. Ce réseau consiste en la reproduction autocatalytique d'une espèce proie par la suite consommée par une espèce prédatrice autocatalytique. Dans un réacteur bien mélangé, le réseau génère une impulsion de concentration de proies suivies par une croissance sigmoïdale de prédateurs. Nous avons quantifié sa cinétique comme une fonction de la concentration en polymérase (pol), en enzyme de restriction (nick) et en prédateur. Ces réactions s'effectuant à 44°C, l'intégration dans des systèmes microfluidiques nécessite donc une technologie adaptée au risque d'évaporation.

Nous avons testé trois technologies : PDMS, autocollants et bas-coût. Les dispositifs PDMS sont compatibles avec notre réaction, cependant, l'évaporation demeure trop

importante malgré nos ajustements. Les dispositifs par autocollants constitués de colle photocurable sont, de manière analogue aux précédents, optiquement transparents et capables de reproduire des géométries de taille submicrométrique, mais présentent en plus l'avantage d'être moins poreux. L'évaporation est ainsi fortement réduite. Nous avons aussi exploré une méthode de fabrication bas-coût : des canaux prédécoupés dans du parafilm insérés entre deux lames de polystyrène ou de verre.

Finalement, nous avons étudié la propagation des ondes dans ces dispositifs. Dans des canaux rectilignes, nous avons observé que la vitesse relative de la vague poursuivante de prédateurs associée à la vague de proie dépendait de l'état de la propagation dynamique et des matériaux du canal. Pour caractériser les capacités de notre technique microfluidique à étudier l'impacte de la géométrie, nous avons étudié deux cas : la propagation du frond d'onde pour un canal coudé (avec un virage à 90°) et le calcul du chemin optimal dans un labyrinthe. De plus, pendant ce travail, une méthode microfluidique alternative pour étudier les conditions initiales de l'onde a été développé à l'aide de valves PDMS. En résumé, nous avons exploré des outils microfluidiques adaptés à l'étude de systèmes de réaction / diffusion à base d'ADN. Bien que l'évaporation demeure un défi, nous pensons que ce travail permet le contrôle de la géométrie de ces systèmes.

Conclusion – Cette thèse porte sur la mise en place et le développement d'une approche expérimentale pour l'étude de réseaux de réactions à base d'ADN. Nos résultats démontrent la capacité des réseaux d'ADN à se spatialiser sous la forme d'ondes progressives. Nous avons également pu obtenir des motifs stationnaires à base d'ADN et d'assemblages de billes. Ce travail contribue donc à la conception de motifs spatio-temporels de réactions chimiques et de matériaux par le biais de réseaux réactionnels biochimiques programmables. Nous apportons également de nouvelles données sur l'émergence d'ordre spatio-temporel à partir de processus de réaction-diffusion. De ce fait, cette étude contribue à une meilleure compréhension des principes fondamentaux qui régissent l'apparition d'une organisation moléculaire. De plus, la combinaison de réseaux synthétiques d'ADN, du contrôle du coefficient de diffusion de plusieurs espèces d'ADN et de la micro-fluidique peut donner lieu à des motifs

spatiaux stables, comme par exemple, les fameuses structures de Turing, ce qui tend à confirmer le rôle de celles-ci dans la morphogénèse.

Mots clefs : *Réaction-diffusion, réseaux de réaction de synthèse à base d'ADN, la formation de motif, microfluidique.*

Contents

Introduction

The emergence of order in living systems is a longstanding fundamental question that is perhaps comparable to the enigma of the origin of life. There are at least two ways to organize matter in living systems: a chemical and a mechanical [1]. A particularly fascinating problem in the emergence of form in living systems happens during embryo development, which starts with a fertilized embryo that is composed of identical cells. We distinguish three sequential phases driving the development of the embryo: pattern formation, cell differentiation and gastrulation. Pattern formation refers to the organization of the concentration of morphogenic molecules (e.g. gene regulators) in time and space, thus acting as a blueprint of the overall body plan so that well-ordered structures develop within the embryo [2]. This pattern of morphogens directs differentiation of cells. According to where the cells are located in the embryo they will become distinct cell types that are functionally and structurally different from each other [1, 2]. Finally during gastrulation dynamic cell movements lead to the formation of the three-layered body plan [3].

The two most influential ideas in developmental biology used to explain pattern formation are Wolpert's positional information (PI) [4–6] and Turing's reaction-diffusion self-organization[1] [7–9]. In the framework of positional information, also known as the French flag problem, a pre-existing morphogen gradient across space provides positional values as in a coordinate system, which is interpreted into several chemically-distinct zones with sharp borders (Fig. 1A). The Turing mechanism relies on self-organization by driving a system of an initially homogeneous distribution of

[1] In this context self-organization is defined as an out-of-equilibrium organization maintained by constantly consuming chemical energy.

chemicals into an inhomogeneous pattern of concentration by a process that involves solely reaction and diffusion (Fig. 1B). As opposed to the PI mechanism the Turing patterning does not rely on pre-existing heterogeneities to create more complex patterns downstream, but rather on self-organization which breaks the symmetry of the system by the intrinsic reaction-diffusion dynamics [10].

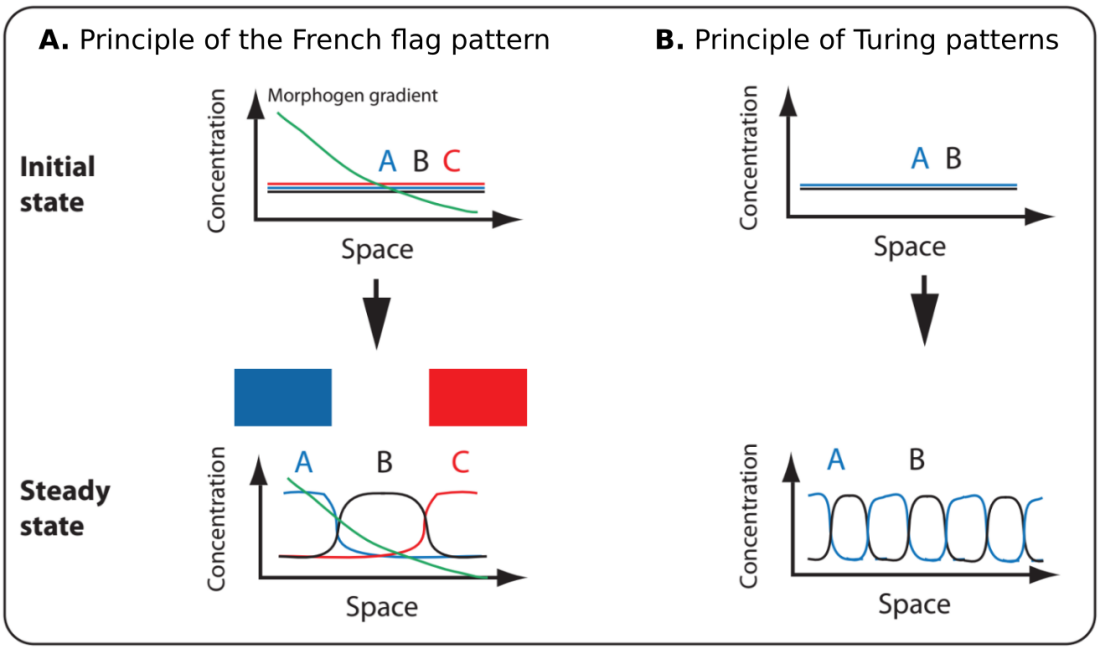

Figure 1 – **Principles of positional information (French flag) and Turing patterning.** **(A)** Chemical species A, B and C interpret a morphogen gradient as a positional coordinate system, thus generating three-chemically distinct zones with sharp borders. **(B)** A system containing a homogeneous distribution of chemical species A and B can break spontaneously the symmetry and self-organize into a periodic spatial pattern driven by an out-of-equilibrium, reaction-diffusion process.

Mechanical forces are key to structure the embryo during gastrulation [11]. On the contrary, diverse evidence indicate that pattern formation can be explained with reaction-diffusion mechanisms [12], where diffusion could be standard Brownian motion or result from a complicated process of cell-to-cell chemical communication. Although we do not ambition to explain the emergence of shape in biological systems, we exploit the valuable lessons learned from reaction-diffusion mechanisms in these systems to gain insights on how to control and generate chemical and material patterns. However, pattern formation in biological systems is highly complex and

difficult to characterize [13]. This PhD work is devoted to develop an experimental framework to investigate chemical spatiotemporal organization through mechanisms that could be at play during pattern formation in development. Our experimental framework is based on DNA hybridization and enzymatic reactions that can be maintained out of equilibrium in a closed system for long periods of time. These reactions self-organize through a reaction-diffusion mechanism. In this work we introduce new tools to increase the versatility of DNA-based networks as pattern-forming systems. We suggest that the good mechanistic description of this simpler system and a precise measurement of its kinetic rates and spatiotemporal dynamics allow to quantitatively investigate and characterize reaction-diffusion pattern formation mechanisms.

Reaction-diffusion Turing patterns

As a simplified model to explain how spatial symmetry could be broken in an initially homogeneous embryo the famous mathematician Alan Turing proposed in 1952 a physico-chemical mechanism in which chemical species react and diffuse [8]. In this reaction-diffusion (RD) model two main chemical species are involved. One of the species acts as an activator and the other as an inhibitor. These two species are interdependent and assembled into a reaction network with a negative feedback loop topology (Fig. 2). The activator is capable of autoreplication, but at the same time it produces an inhibitor, which then represses the growth of the activator (Fig. 2A-B). If the diffusion coefficient of the inhibitor is considerably larger than that of the activator (Fig. 2C) well-defined stationary concentration patterns emerge such as stripes and dots (Fig. 2D-E). For this reason, Gierer and Meinhardt [14] named independently this mechanism: *short-range activation and long-range inhibition*. The two requirements to generate chemical patterns via the Turing mechanism can be summarized as follows: (i) the topology of the reaction network must be composed of an inhibitor and an activator and (ii) the diffusivity of the activator species must be significantly smaller than that of the inhibitor.

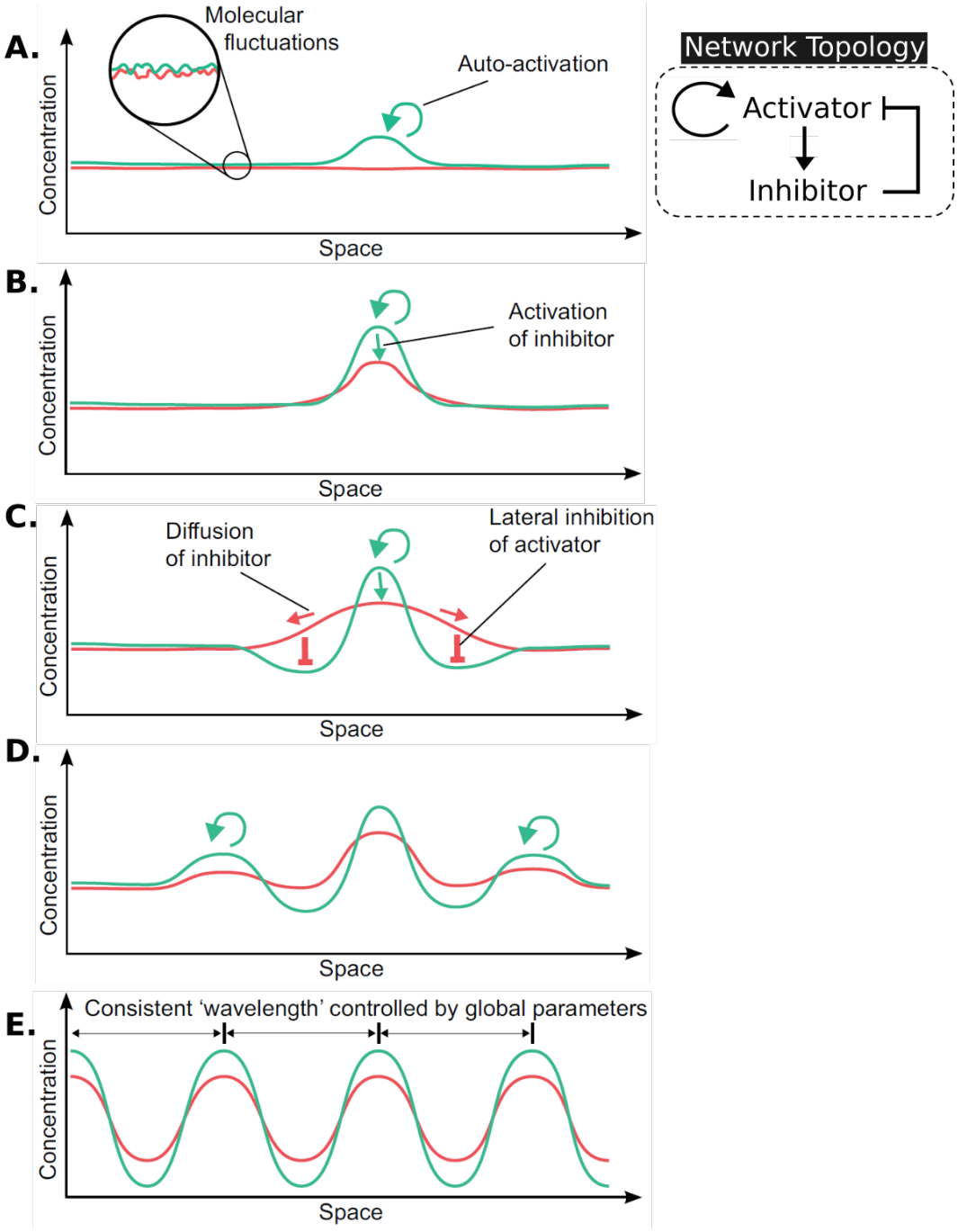

Figure 2 – **A periodic Turing pattern emerges from an activator-inhibitor model. (A)** Small fluctuations in an apparently homogeneous concentration of molecules across space are enhanced by a self-activator, which also **(B)** produces an inhibitor. **(C)** Then, the inhibitor moves out the activator rich zone due to its larger diffusivity, this results in the creation of inhibitor rich zones around the activator. **(D)** New activator and inhibitor peaks emerge until **(E)** a well-defined periodic pattern emerges across space. This figure was taken from [10].

Although numerical simulations and mathematical analysis corroborate the incredible potential of reaction-diffusion mechanisms to generate patterns, their experimental implementation is not trivial. This has motivated to search nonlinear chemical systems that may be capable of pattern formation. The most utilized chemical systems to investigate the emergence of spatiotemporal order are the Belousov-Zhabotinsky (BZ) reaction and its relatives [15]. The BZ systems involve mostly small inorganic molecules and sometimes organic [16] ones that undergo redox reactions. Unfortunately, most of these reactions occur at strongly acidic conditions and are thus not biocompatible [17].

The first experimental observation of chemical Turing patterns in 1990 [18, 19] and the experimental verification of Turing's predictions in 2014 [20] were made with BZ-related systems. Indeed, these chemical systems display rich nonlinear phenomena, both *temporal*, such as oscillations, multistability and chaos, as well as *spatiotemporal* such as stationary, i.e. Turing, spatial patterns and several types of traveling and standing waves [13].

Statement of the problem

Despite of the exceptional achievements in pattern formation with BZ-related systems, these are difficult to engineer, thus limiting their experimental implementation to few available mechanisms. Engineering reaction-diffusion systems that display spatiotemporal dynamics is done by controlling three key elements: (i) the topology of the network (how reactions are linked to each other, i.e. in a positive or negative feedback manner), (ii) the reaction rates and (iii) the diffusion coefficients.

In the early 2000s, bottom-up approaches in the emerging field of synthetic biology have demonstrated that it is possible to assemble reaction networks of gene regulators with controlled dynamical behaviors [21]. For example, the oscillatory behavior of the *repressilator* system emerged from three repressor–promoter pairs assembled into sequential negative-feedback loops [22].

This was possible because we knew from 30 years of biotechnology the engineering rules of activation and repression of genes by transcription factors. They are governed by the DNA sequence. The idea that DNA sequences could be used as an engineering building block was put together by Seeman in 1981 and founded the field of DNA nanotechnology. The versatility and the predictable reactivity of nucleic acids has demonstrated extraordinary capabilities to build nanostructures with arbitrary shapes [23, 24] and design computational elements [25]. More recently, using nucleic acids as a substrate to make programmable dynamic chemical systems with the lessons from synthetic biology and DNA nanotechnology has appeared as an attractive approach due to the simplicity to control reaction rates and network topology by the sequence. The two most notable systems involve oligonucleotides (short single strands of DNA or RNA) and enzymes: the PEN-DNA toolbox developed by Rondelez and collaborators in Tokyo [26] and the genelets developed by Winfree and collaborators in Caltech [27]. They were the first to engineer chemical oscillators from the bottom up in closed reactors. In 2013 our group, in collaboration with Rondelez's, reported the firs observation of chemical waves in a DNA-based system engineered from the bottom up [28] using the PEN-DNA toolbox. The programmability and biocompatibility of the PEN-DNA toolbox open new perspectives for the engineering of the reaction-diffusion chemical synthesis, in particular in two directions. Firstly to study biologically-inspired pattern-forming mechanisms in simplified, yet relevant, experimental conditions. Secondly to build new materials that would self-build by a process inspired from embryo morphogenesis. My PhD work makes part of this effort.

Thesis structure

We worked towards the goal of meeting the two requirements of Turing patterning, transferring chemical spatiotemporal behavior into material patterns, and imposing boundary conditions to spatiotemporal patterns. Therefore, the structure of this document is divided into four specific objectives resulting in four chapters. In chapter 1 we worked on testing a DNA-based reaction network with an inhibitor-activator topology. In chapter 2 we focused on developing a strategy to tune the diffusion

coefficient of activator DNA strands. In chapter 3 we explored how chemical patterns determine the shape of a material. Finally in chapter 4 we addressed the issue of controlling the geometry over a DNA-based reaction-diffusion system. Additionally, the appendix is composed of two articles obtained during this PhD work. The first article entitled "Synthesis and materialization of a reaction-diffusion French flag pattern" has been submitted and is related to Chapter 3 (Appendix B). The second article entitled "Pursuit-and-evasion reaction-diffusion waves in micro-reactors with tailored geometry" is published in *J. Phys. Chem. B* and is related to Chapter 4 (Appendix C). We have limited ourselves from referencing any text or figures to a minimum such that reading these two publications is not required to understand the four chapters of this manuscript. However, we encourage the reader to read them through if interested.

Chapter 1

In this chapter, we analyzed our in-vitro DNA-based reaction system by characterizing the temporal dynamics of a network with an inhibitor-activator topology. This reaction network, called the *Oligator*, operates in pseudo out-of-equilibrium conditions by consuming deoxynucleotides (dNTPs) as energy in a closed system. The Oligator was first engineered to display oscillatory dynamics by connecting three DNA species into a negative feedback loop by Montagne et al. [26]. The reactive core of the oligator is composed of an autocatalyst species that produces its own inhibitor and both species can be degraded by an exonuclease. We did an important modification to the Oligator system by replacing the original exonuclease that is not thermostable by a thermostable one. We tested the dynamics of each node of the Oligator's loop incrementally. Among these experiments we demonstrated that a logic function such as a NOT gate can be implemented using the inhibitor and inhibition node to deactivate the autocatalytic node. In these conditions we obtained forced oscillations by repeated injection of the inhibitor. Once the Oligator was fully connected, however, the oscillations were extremely damped and a correct range of parameters to produce sustained oscillations was not found. Our results suggest that the autocatalytic node

was too strong to produce oscillations. This chapter serves as an introduction to the DNA-enzyme reactions that appear in the rest of the chapters.

Chapter 2

In this chapter, we developed an approach to tune the diffusivity of single-stranded DNA in an autocatalytic reaction. Our strategy consisted of linking the template to microparticles, and since the activator binds to the template the diffusivity of the activator species should be reduced. The mobility of the activators depends on the time they are free and bound to the template, so we called this diffusivity the effective diffusion coefficient (D_{eff}). We tested our strategy by studying traveling fronts of activator species. We quantified how the diffusivity was tuned by relating the front velocity (v) to the effective diffusion coefficient and the rate growth kinetics (k): $v^2 = kD_{eff}$. Thereby, we studied the growth kinetics and the front propagation dynamics for three cases in which the templates were attached: to 30 µm diameter agarose beads that were closely packed (case 1) or diluted (case 2), and to 200 nm diameter magnetic beads that were diluted (case 3). Our preliminary results indicate that the reduction in diffusion of the activation species were: 1.5, 4.3 and 2.4 fold for the cases 1, 2 and 3 respectively. Importantly, the work in this chapter also allowed us to determine the compatibility of a variety of material supports with the PEN-DNA toolbox.

Chapter 3

Our work in Chapter 2 allowed us to master the coupling of DNA-enzyme reactors with microparticles. Here instead of using the particles to influence the properties of the DNA patterns we did the opposite. The work presented in this chapter was done in collaboration with Vadim Dilhas, a master student in our group. We utilized DNA-decorated microparticles that aggregate in the presence of a linker DNA strand. We transfered two types of DNA patterns into aggregation of microparticles in two situations: (i) a traveling front of activator species that directs a front of aggregating beads and (ii) a stationary front of activator species that induces the assembly of a

stationary pattern of aggregated beads. In this study chemical patterns determine the shape of a material, thus leading to what is to the best of our knowledge the first demonstration of a primitive morphogenic material.

Chapter 4

In this chapter, we explored the issue of setting boundary conditions to a DNA-based reaction-diffusion system. To do so, we developed a microfluidic technique to create micro-reactors with tailored geometry to study the propagation dynamics of a chemical Predator-Prey network. These reactions occurred at 44°C, thus causing evaporation problems in classical polydimethylsiloxane (PDMS) microfluidic devices. For such reason, we tested several microfabrication technologies using nonporous materials to reduce evaporation in these devices: (i) microfluidic stickers made of photocurable glue and (ii) a low-cost fabrication method that consisted in embedding pre-cut parafilm channels between two polystyrene (or glass) slides. We brought our reactions into straight microfluidic channels and characterized the prey and predator wavefront velocities. Then, to investigate geometry-related phenomena we analyzed two cases: front propagation along a 90° turn and computing the optimal path in a maze.

Contributions of this work

Due to the constraints inherent to a 3-year PhD program, chapters 1 and 2 introduce topics that are still work in progress. Although it was not possible to obtain sustained oscillations in the oligator network with a thermostable exonuclease (Chapter 1), I have thoroughly characterized the kinetics of this network. In particular, in the future the autocatalyst will need to be weakened to get a functional oscillator. Although the PEN-DNA toolbox is programmable is not plug and play and it calls for more efforts in developing computer-assisted design tools. I studied three novel strategies seeking to control the diffusion of single-stranded DNA (Chapter 2). Surprisingly the diluted dispersion of agarose beads containing templates worked best reaching a

4-fold decrease twice better than previous work [29]. Our inability to strongly reduce diffusion indicates however that many open questions remain. Instead, this work provided the foundation for controlling colloidal aggregation with DNA patterns resulting in entirely new type of materials: morphogenetic materials (Chapter 3). To the best of our knowledge this constitutes the first demonstration of a morphogenetic material. Finally I have developed microfluidic devices to study the effect of geometrical confinement and the computational capabilities of DNA-based traveling fronts (Chapter 4). Overall, we have expanded the number of available tools to study chemical and material pattern formation and advance towards Turing patterns with DNA.

1 Testing DNA-enzyme reaction networks

As we have discussed in the Introduction, a spatial Turing pattern emerges from an activator-inhibitor reaction network that operates out-of-equilibrium, however such type of network topologies are not naturally abundant in chemistry. This has led to research on synthetic systems to engineer reaction networks. In this chapter we will present one of such systems that is called the *PEN-DNA toolbox*. The Polymerase/Exonuclease/Nickase Dynamic Network Assembly toolbox (PEN-DNA toolbox) is a bottom-up approach to build reaction networks with programmable topology based on an in-vitro DNA replication machinery. It uses DNA as a chemical substrate due to its predictable reactivity and the possibility to interconnect short single strand species through longer strands. This, together with a DNA replication system based on three enzymatic reactions, can be used to link single nodes into dynamic reaction networks. Hence, engineering a reaction network (RN) topology is done by defining a type of node behavior, i.e. either as activator or inhibitor, and linking this node to another by sequence complementary.

In this chapter we focus on testing a network based on the PEN-DNA toolbox with an activator-inhibitor topology, which is a candidate reactive system for Turing patterning. This network, which we refer to as the *Oligator*, is designed to display an oscillatory behavior when set at the right experimental conditions. The Oligator is composed of three nodes connected in a negative feedback loop manner. The first node corresponds to the autocatalytic production of species α, which also activates

the linear growth of species β. This latter species triggers the production of species γ which inhibits the autocatalytic growth of α. We test systematically node by node till the network is fully connected. Subsequently, we search the experimental conditions at which the fully connected network displays an oscillatory behavior.

1.1 Introduction to the PEN-DNA toolbox

In this section we will cover the principles of the PEN-DNA toolbox. We will explain the basics of DNA as a chemical substrate for designing reaction networks. Subsequently, we will briefly describe the monitoring of DNA concentration by fluorescence.

1.1.1 The PEN-DNA toolbox for engineering reaction networks

The PEN-DNA toolbox is somewhat analogous to gene regulatory networks, which rely mostly on three basic actions: activation, inhibition and degradation [26]. In a gene regulatory network the transcription of a gene into RNA leads subsequently to the translation of RNA into a protein, which regulates the transcription of a second gene (Fig. 1.1A). The transcription and translation steps are activation steps, while the regulation can be either an activation or inhibition event. Furthermore, RNA and proteins can be degraded. In a similar manner, the PEN-DNA toolbox uses a DNA template (22-27 nucleotide long) for the replication of DNA strands (11-12 nucleotide long), which either activates or inhibits the production of a second DNA strand (Fig. 1.1B). Of course gene regulatory networks involve large molecules of 1000s of base pairs, whereas in the PEN-DNA toolbox the molecules are much smaller (10s base pairs). Thus, the PEN-DNA toolbox uses these three basic components (activation, inhibition and degradation), but without the complex gene expression machinery, to assemble dynamical reaction networks.

Before we describe how activation, inhibition and degradation work in the PEN-DNA toolbox it is important to note that this system uses DNA as a chemical substrate. DNA predictable reactivity due to Watson-Crick paring rules (i.e. A pairs to T, and C to G

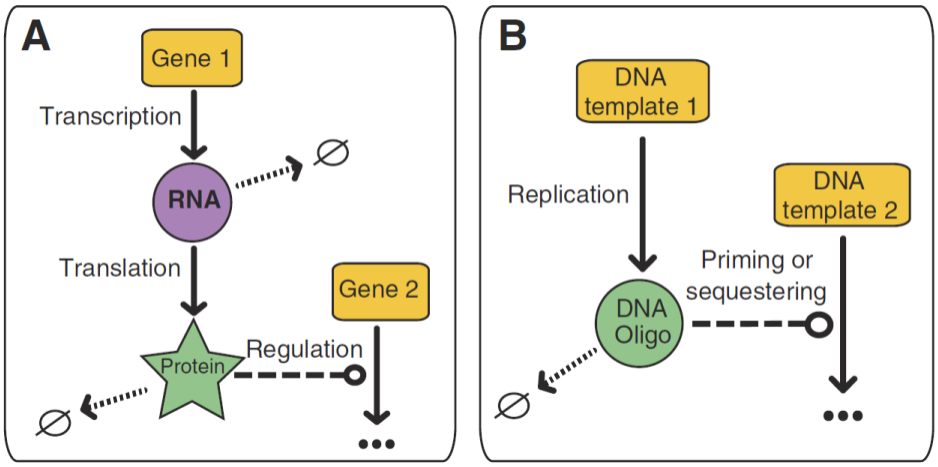

Figure 1.1 – **Schematic description of (A) a gene regulatory network and (B) the PEN-DNA toolbox.** The symbol (⊘ ←--) indicates degradation, the solid arrows represent an activation step, and the dashed lines are either regulatory events, whose nature may be either activating and inhibitory. This figure was taken from [26].

via hydrogen bonding) makes DNA a chemical substrate of choice for engineering reaction networks. In double-stranded DNA (dsDNA), two complementary sequences are hybridized anti-parallel to each other, one strand goes from 5' to 3' while the other is positioned 3' to 5' (Fig. 1.2). From now on we will be portraying DNA strands as arrows with a harpoon shape (⇀).

The PEN-DNA toolbox employs replication of encoded information through elongation, i.e. polymerization of nucleotides, of an input (11-12 nucleotide long) hybridized to a template (22-27-mer long) by *Bst* DNA polymerase, large fragment (pol) (Fig. 1.3). Subsequently, Nt.BstNBI, site specific endonuclease (nick), cleaves only the upper strand on the newly formed double-stranded DNA substrate at a precise location. Finally, the input and output species are released from the template. Templates are degradation resistant, but the rest of the species are destroyed by a single-stranded specific exonuclease such as ttRec$_J$ or RecJ$_f$ (exo), a thermophilic ortholog isolated from Thermus Thermophilus HB8 [30]. Double-stranded species (T_{in}, T_{ext}, T_{both} and T_{inhib}) are not degraded. Production inhibition of an output DNA species is achieved when an inhibitor strand partially hybridizes to the template, and since pol can only add nucleotides to the 3'-end on a fully hybridized dsDNA, the hanging end of the inhibitor prevents elongation.

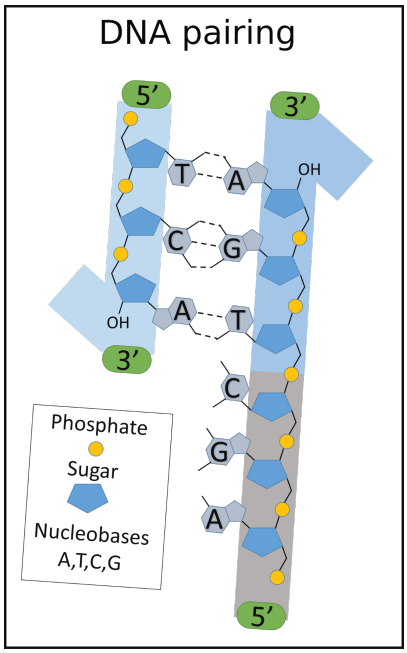

Figure 1.2 – **DNA composition.** DNA is composed of a phosphate group, a deoxyribose sugar moiety and four different nucleobases. DNA pairing is based on Watson and Crick rules. Complementary single-stranded sequences are hybridized anti-parallel into a double-stranded DNA.

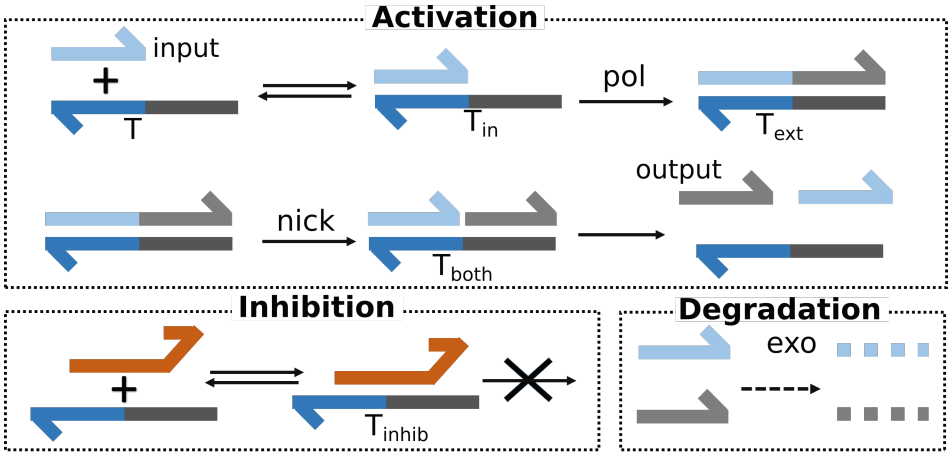

Figure 1.3 – **Basic reactions in the PEN-DNA toolbox.** The production of an output strand and its degradation involves three enzymatic reactions: (i) extension of input over a template by pol enzyme; (ii) cutting of the newly extended strand by nick enzyme; (iii) degradation of single strands by exo enzyme. Reaction (i) can be blocked by an inhibitor partially (3'-end hanging) hybridized to the temple.

In the PEN-DNA toolbox, the short strands are the dynamic species of interest while the template strands (which are longer) set the topology of the reaction network and their total concentration does not change. In other words, the nodes of the network are given by the short, degradable, strands (inputs and outputs) while the activation arrows are set by the longer, non-degradable, template strands. Bottom-up construction of reaction networks is achieved by designing the input and the output sequences and connecting them through activating or inhibitor species. The system is programmable because the connectivity (or topology) of the network is entirely defined by Watson-Crick pairing rules.

The robustness of the PEN-DNA toolbox and its variations has been demonstrated already by the engineering of several network topologies. An oscillator was designed with a positive feedback loop with a delay of a negative feedback loop [26]. Also a bistable switch was created by coupling two mutually inhibitory positive feeback loops [31]. The PEN-DNA toolbox has even allowed the designed of dynamical molecular behaviors that resemble collective relationships in animal populations such as Predator-Prey oscillations, competition-induced chaos, and symbiotic synchronization [32].

1.1.2 DNA hybridization reactions in the PEN-DNA toolbox

One can design a short DNA strand (ζ_{input}) to bind from the first base on the 3'-side to the middle of a template strand (T), as seen in Fig. 1.4. The template T has a second binding site, where an output species (ζ_{output}) can bind from the middle ending on the 5'-side. Both the input and output species may bind simultaneously to T at their respective positions forming complex T_{both}. An inhibitor species (inhib) is constructed to partially bind to T such that a hanging end is not bound. And when the inhibitor binds to T to form T_{inhib} it blocks the binding of the input species.

We can consider a two-state model for the hybridization of DNA strands that are less than 20 base-pair long. Thus, the equilibrium constant of dissociation, K_d, between a

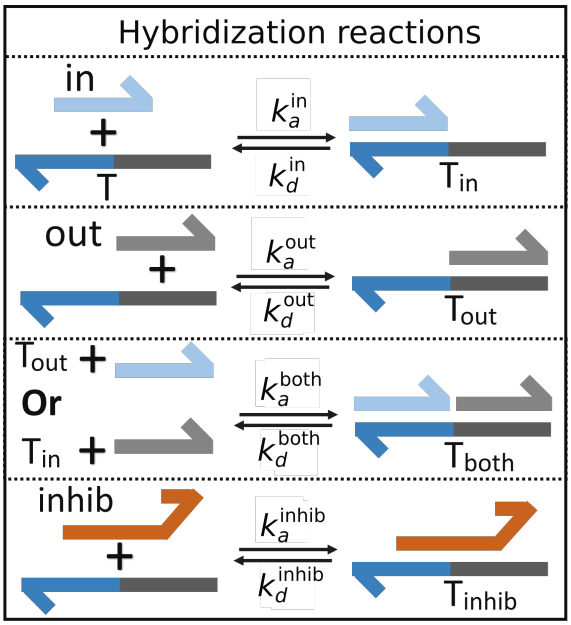

Figure 1.4 – **DNA hybridization reactions.** Short strands (in, out, inhib) bind reversely to template (T), consequently constructing complexes: T_{in},T_{out}, T_{both} and T_{inhib}.

template T and species ζ can be written as follows,

$$\zeta + \mathrm{T} \underset{k_d}{\overset{k_a}{\rightleftharpoons}} \mathrm{T}_\zeta \tag{1.1}$$

$$K_d = \frac{k_d}{k_a} = \frac{(\zeta_0 - T_\zeta)(T_0 - T_\zeta)}{T_\zeta}, \tag{1.2}$$

where ζ_0 and T_0 are the initial concentrations of the corresponding species, and T_ζ is the complex concentration reached at equilibrium. The association rate constant (k_a) can be considered fixed with a typical value around 0.06 nM^{-1} min^{-1}, since it depends mainly on the salt concentration but not on the sequence. While the dissociation rate constant (k_d) strongly depends on the sequence and can thus be tuned individually. Indeed, k_d determines the stability of dsDNA complexes (T_ζ = T_{in},T_{inhib}, etc.) and it is in function of the number of complementary bases and its type of base-pair, i.e. either TA or GC.

Hence, the main parameters to design active species and templates are: (i) determin-

ing their sequence and (ii) the number of pairing bases. This allows us to generate distinct chemicals species with predictable k_a and k_d.

1.1.3 Detection of DNA concentration

The concentration of DNA strands during reactions involving DNA-DNA hybridization can be probed conveniently through fluorescence. In the PEN-DNA toolbox, two methods to detect chemical species are generally used: (i) a non-specific using EvaGreen (EG), an intercalator dye with preferential binding to dsDNA and, (ii) a species specific one, called N-quenching, that uses a template labeled with a fluorophore modification on its 3' or 5' end.

The first technique consists in the increase of EvaGreen fluorescence as the concentration of dsDNA accumulates (Fig. 1.5A). Generally, the template concentration is fixed while the concentration of ζ species changes, so we monitor the formation of complexes T_ζ. The second one, N-quenching relies on the quenching of fluorescence when a base binds near the fluorophore due to the hybridization of a DNA strand (Fig. 1.5B).

EvaGreen allows us to monitor the overall dynamics with little influence on the kinetics of interest. And, N-quenching allows us to detect specific species. For example a dye on the 3'-side of a template will report the concentration of input species by quenching the fluorescence intensity as the concentration of input increases. In a similar manner, a dye on the 5' can monitor the output concentration.

For both techniques, using the two-state model in Eq.1.1 the relation between fluorescence signal and the concentration of dsDNA is given by

$$F = \phi_{\mathrm{T}}(T_0 - T_\zeta) + \phi_{\mathrm{T}_\zeta} T_\zeta + \Theta_b, \tag{1.3}$$

where ϕ_{T} and ϕ_{T_ζ} are proportional to the florescence quantum yields of species T and T_ζ respectively, and Θ_b is a background contribution. Assembling constant terms ($\phi_{\mathrm{T}} T_0 + \Theta_b = \Theta$) and ($\phi_{\mathrm{T}_\zeta} - \phi_{\mathrm{T}} = \phi$) returns a simple equation of fluorescence as a

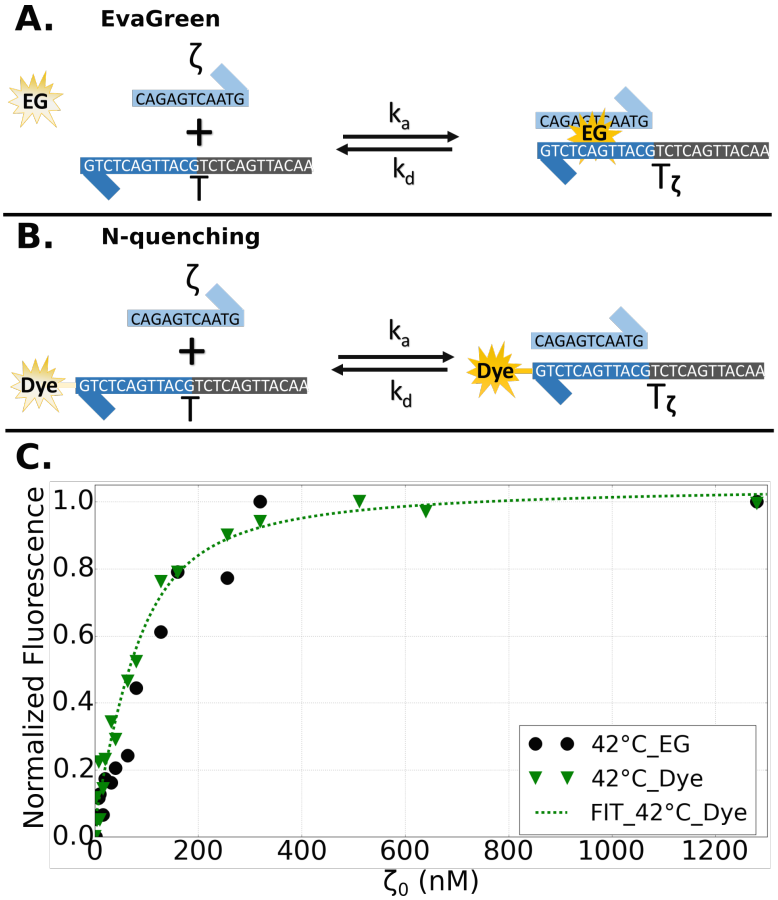

Figure 1.5 – **Detection of DNA species, ζ, upon hybridization to template, T, by intercalator EvaGreen and fluorophore modification, N-quenching, to the template.** **(A)** Fluorescence of EvaGreen increases in the presence of dsDNA during a hybridization reaction. **(B)** Hybridization of an input species to the template bases nearby a dye quenches its fluorescence. **(C)** DNA hybridization reactions at 42°C is monitored by EvaGreen and a dye on a template in buffer O. The template is titrated as function of the total concentration of ζ, ζ_0.

function of complex T_ζ,

$$F = \phi T_\zeta + \Theta. \tag{1.4}$$

Then, solving for T_ζ in Eq.1.2 and substituting this term into Eq.1.4 yields a relation of fluorescence and known concentrations of species T_0 and ζ_0,

$$F = \frac{\phi\left(K_d + T_0 + \zeta - \sqrt{\zeta^2 + (2K_d - 2T_0)\,\zeta_0 + {T_0}^2 + 2KdT_0 + {K_d}^2}\right)}{2} + \Theta. \tag{1.5}$$

K_d can be extracted experimentally by titrating a fixed template concentration with a range of ζ concentration. In Fig. 1.5 C, a hybridization reaction between species ζ and its complementary template is monitored using both techniques, then the data is fitted to Eq.1.5. The average K_d using EvaGreen (74 nM) was twice as large as the value obtained via N-quenching (36 nM), however, the values overlap within two standard deviations (Table 1.1). This is expected since we used the same template sequence. The parameter ϕ must be different since it is related to the quantum yield of the fluorophore. The absorption and emission wavelengths of EvaGreen and dye530 are different, $\lambda_{abs}/\lambda_{em}$ = 500/530 and 539/561 nm respectively. Therefore, the fluorescence can be measured in two separate channels in a real-time PCR with excitation detection wavelength, $\lambda_{ex}/\lambda_{de} = 470 \pm 10/510 \pm 5$ and $530 \pm 5/555 \pm 5$ nm.

Table 1.1 – **Dissociation constant and quantum yield parameters for EvaGreen and N-quenching.** The parameter values were obtained by fitting the data in Fig. 1.5 to Eq. (1.5). Average values are displayed within two standard deviations.

Parameter	EvaGreen	N-Quenching
K_d (nM), 42°C	73.8± 50.3	36.3±18.2
ϕ, 42°C	0.10± 0.02	0.37± 0.03

1.1.4 Analysis of the autocatalytic and linear growth

To give the reader an insight of the type of kinetics our reaction system posses we briefly analyze the basic reactions in the PEN-DNA toolbox with simple Michaelis-Menten equations. One can say that the single node is the simplest circuit in the PEN-DNA toolbox consisting of an input and its template along with the required enzymes. Two different functions are expected from such configuration: (i) a sigmoidal autoreplication, in which the product is identical to the input, and (ii) a linear production initiated by the input.

In Fig. 1.6A we have sketched these two networks with and without degradation. The template is represented with a solid arrow pointing to the direction of activation. In the case of autocatalysis the arrow is curved pointing back to α since the input and output species are identical. In linear production the template requires α to produce

β. The degradation of the species is indicated with the dashed arrow.

In Fig. 1.6B we use numerical simulations using DACCAD [33] to display how the temporal evolution of the output concentration is different from linear and nonlinear production. DACCAD solves for a PEN-DNA toolbox network a system of ordinary differential equations. It integrates all the DNA hybridization reactions as 2-state model (see Fig. 1.4) and the three enzymatic reactions as Michaelis-Menten processes. The rate constants are extracted from [31]. Autocatalysis displays its characteristic sigmoidal growth. The addition of degradation to autocatalysis allows the system to reach a steady state. In the absence of degradation we also see the initial sigmoidal growth, then the growth saturates. Linear production of β is stable without exo, whereas addition of degradation consumes the input α, thus, decreasing the production of β and eventually its complete elimination. We will discuss a simple model to understand the initial growth kinetics, i.e. when α or β are approximately to their initial values at time zero in Fig. 1.6B. We make clear that our analysis below does not capture the kinetics above the initial values of α or β.

The autocatalytic growth of α may be performed with or without degradation, but to simplify the analysis we will consider production without degradation only. The complex $T^{\alpha\alpha}_{in}$ first forms when α hybridizes on the input side of template $T^{\alpha\alpha}$ (Fig. 1.3). Then, the pol and nick step follow giving an overall reaction: $\alpha \longrightarrow 2\alpha$. The enzymatic reactions to replicate α can be described by Michaelis–Menten (MM) kinetics:

$$\mathrm{T}^{\alpha\alpha}_{in} + pol \underset{k^{pol}_{-1}}{\overset{k^{pol}_{1}}{\rightleftharpoons}} \mathrm{T}^{\alpha\alpha}_{in} pol \xrightarrow{k^{pol}_{2}} \mathrm{T}^{\alpha\alpha}_{ext} + pol \tag{1.6}$$

$$\mathrm{T}^{\alpha\alpha}_{ext} + nick \underset{k^{nick}_{-1}}{\overset{k^{nick}_{1}}{\rightleftharpoons}} \mathrm{T}^{\alpha\alpha}_{ext} nick \xrightarrow{k^{nick}_{2}} \mathrm{T}^{\alpha\alpha}_{both} + nick$$

In our conditions polymerization is the limiting reaction compared to nick. From Eq. (1.6) we have,

$$\frac{d\alpha}{dt} = \frac{k^{pol}_{2} pol T^{\alpha\alpha}_{in}}{T^{\alpha\alpha}_{in} + K_M} \tag{1.7}$$

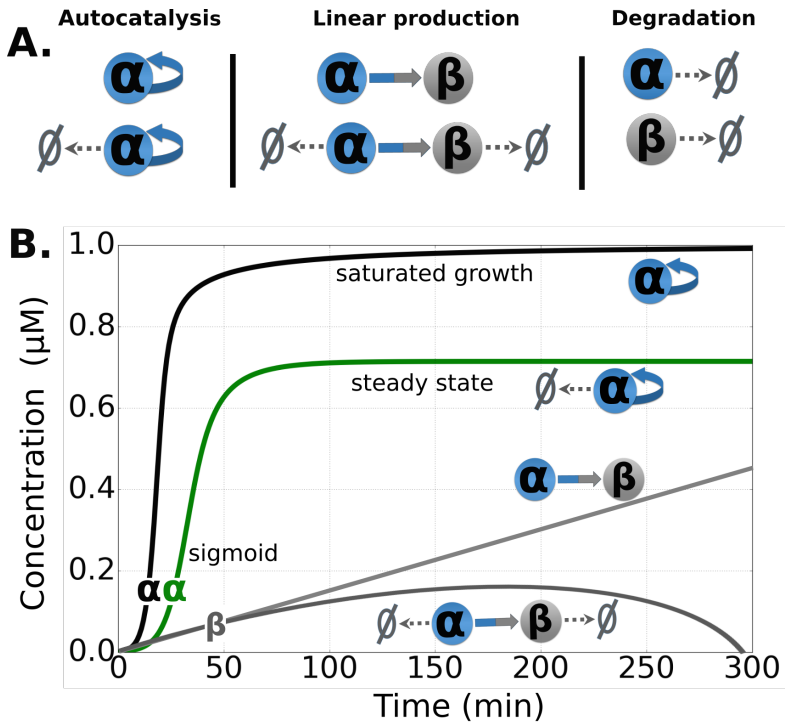

Figure 1.6 – **Autocatalytic and linear growth with and without degradation.** **(A)** *Autocatalysis:* A positive feedback loop is formed when α autoreplicates exponentially over a template (solid arrow) with or without degradation (dash arrow). *Linear production:* α initiates growth of β and species remain in solution, or they may be degraded. *Degradation:* Species α and β are degraded by enzyme exo. **(B)** Numerical simulations, using DACCAD [33], of: (i) autocatalytic growth of α with and without degradation, respectively, black and green line and (ii) linear production of β with and without degradation, respectively, dark gray and light lines.

where pol is the concentration of pol, k_2 is an enzymatic rate constant and K_M is the Michaelis–Menten constant. If $K_M \approx K_M + T_{in}^{\alpha\alpha}$, which is the case during initial growth when the concentration of α is low, then k_2, K_M and pol can be grouped into a constant, κ. Therefore, the solution to this simplified case is an exponential form that resembles first order non-reversible kinetics, $\alpha \xrightarrow{\kappa} 2\alpha$,

$$\frac{d\alpha}{dt} = \kappa\alpha \tag{1.8}$$

$$\alpha_t = \alpha_0 e^{\kappa t},$$

where α_0 is the initial concentration of α. In the case of a linear network, β requires template $T^{\alpha\beta}$ to initiate its production so in Eq. (1.6), β is the output instead of α, and a similar equation can be written:

$$\frac{d\beta}{dt} = \frac{k_2 pol T_{in}^{\alpha\beta}}{T_{in}^{\alpha\beta} + K_M} \tag{1.9}$$

Contrary to Eq. 1.7, $T_{in}^{\alpha\beta}$ is constant and thus grouped into κ, therefore a linear solution is displayed by this analogy of zero order kinetics, $\alpha \xrightarrow{\kappa} \alpha + \beta$:

$$\beta_t = \beta_0 + \kappa t. \tag{1.10}$$

Degradation of the species can be taken as a linear process $\alpha \xrightarrow{k} \oslash$, where $\oslash$ represents α chopped into nucleotide monophosphates (Fig. 1.6). For an autocatalytic network, a degradation term adds the ability to reach a steady state at full activation. This steady state is attained when the growth rate equals degradation,

$$\frac{d\alpha_{growth}}{dt} = \frac{d\alpha_{degradation}}{dt} \tag{1.11}$$

This steady state is distinguished as a horizontal line in the plot in Fig. 1.6B (green line). Linear and autocatalytic production have distinct functionalities in a network. A linear function will be used as a delay line in a network.

1.2 Three-node network with negative feedback design

In this section we present the *Oligator*, which is a three node network that was designed by Montagne et al. [26] to display an oscillatory behavior. We will first explain the network topology. Subsequently, the experimental conditions at which it was originally created are listed, as well as the modified conditions at which the work of this chapter will be carried out.

1.2.1 Reaction network topology of the Oligator system

The Oligator has a negative feedback topology, which consists of three DNA species, α, β and γ, with connected chemistry and constant degradation (Fig. 1.7 A). In this loop, α autoreplicates but also produces an intermediate species (β), serving as a delay step, that subsequently produces γ, an inhibitor of α. In this representation, a chemical activation (solid arrow) requires a three component machinery: a template (T), a polymerase (pol) and a nickase (nick). In order to keep the system responsive, linear degradation, represented by dashed arrows, of α, β and γ species, is accomplished by an exonuclease (exo). Inhibition, denoted by a blunt-end arrow, involves an inhibitor species that hybridizes reversibly to the template, thus blocking the hybridization of the input. In other words, inhibition results in the obstruction of the activation. As a simple demonstration of the possible oscillatory dynamics of all three chemical

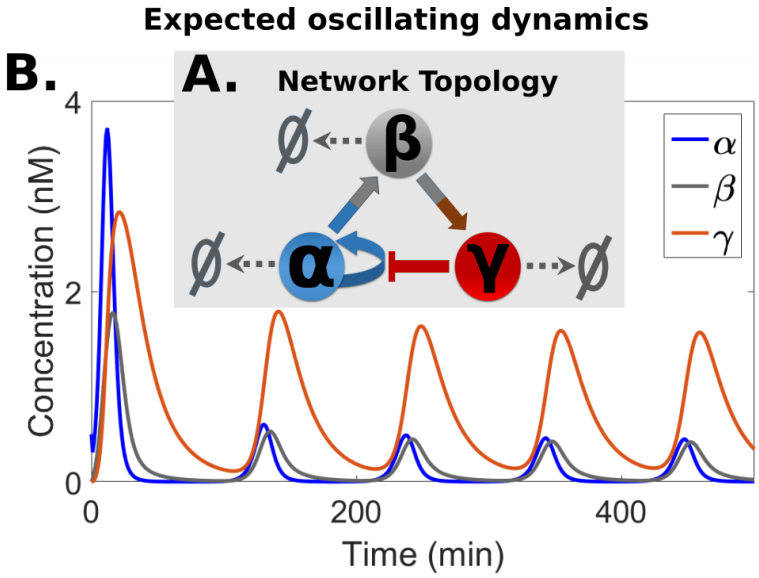

Figure 1.7 – **Network topology and expected oscillatory dynamics of the Oligator. (A)** The Oligator topology is a positive feedback loop coupled to a delayed negative feedback loop. Autoreplication of α uses a three component activation machinery: a template, pol and nick; this is represented by a solid arrow. α is also an activator to produce β which in turn activates the creation of inhibitor γ. This latter prevents enzymatic autoreplication of α, this step is represented by a blunt-end arrow. Dashed arrows denote degradation of chemical species by exo. **(B)** Numerical simulations under chosen conditions to generate sustained oscillations.

species of this network topology, a numerical simulation using DACCAD [33] was

plotted along side the network topology in Fig. 1.7 B. Chemical oscillations with a period of about 100 minutes are obtained if the autocatalyst grows up to an activated state, and it is subsequently turned off by an inhibitor. However, the autocatalytic node must be able to recover its ON-state and repeat the oscillatory ON-OFF cycle. From this statement, it can be recognized that the fundamental controlling aspects must be balanced to reach such dynamical behavior: (i) sigmoidal growth kinetics of α, (ii) inhibition strength of γ on the autocatalyst node, and (iii) delay response between inhibitor and autocatalyst node.

1.2.2 Experimental conditions of the Oligator

Each node of the Oligator topology is composed of a species and its corresponding template. We list the templates of the Oligator used by Montagne et al. [26] in Table 1.2. In the notation used here the superscripts indicate the input and the output species ($T^{\alpha\beta}$ takes α as an input and generates β as an output). P2 stands for two phosphorothioate (PTOs) modifications, which are necessary for protection from $RecJ_f$ degradation. Because $RecJ_f$ degrades ssDNA processively from 5' to the 3' end by hydrolyzing the phosphate bond, two phosphorothioate in the 5' protect from degradation (Fig. 1.8A).

Table 1.2 – **Sequences of the three nodes of the Oligator.** Node-1 template autoreplicates α , node-2 template takes α to produce β which then triggers node-3 template to output γ. P2 stands for two phosphorothioates (P2 = **).

Name	**Template sequence 5'→3'**	**Name**	**Node sequence 5'→3'**
$T^{\alpha\alpha}$(P2)	A*A*CAGACTCGAAACAGACTCGA	α	TCGAGTCTGTT
$T^{\alpha\beta}$(P2)	G*C*ATGACTCATAACAGACTCGA	β	ATGAGTCATGC
$T^{\beta\gamma}$(P2)	T*T*ACTCGAAACAGACTGCATGACTCAT	γ	AGTCTGTTTCGAGTAA

The Oligator was originally configured under certain experimental reaction conditions to display an oscillating behavior. For example, chemical modifications to the template and selection of buffer components were carefully planned to ensure enzyme compatibility, such as enzyme thermostability and prevention of undesirable reactions. The Oligator buffer (buffer O), listed in Table 1.3, contains a high concen-

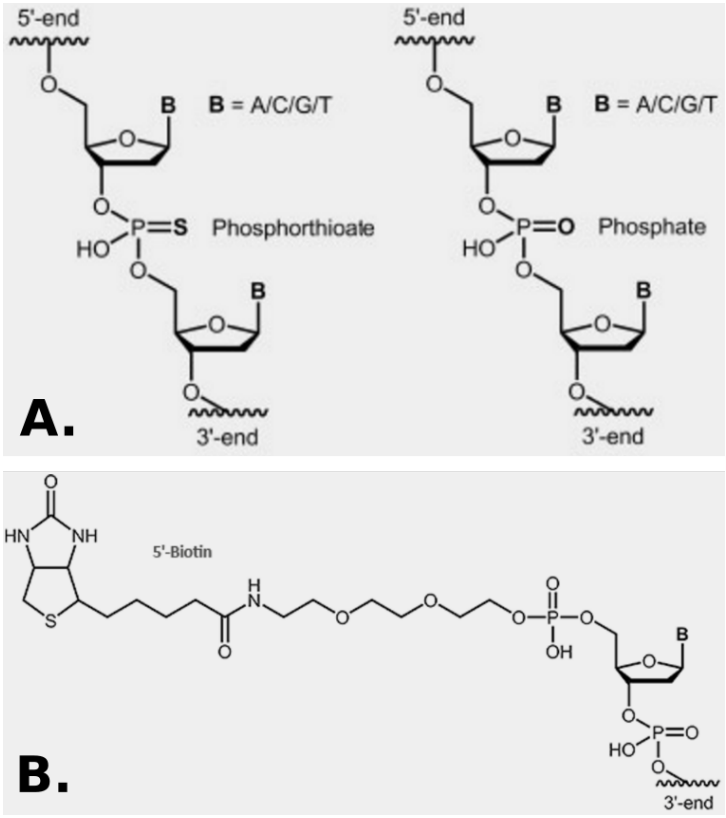

Figure 1.8 – **Chemical modification to template as a protection against exonuclease degradation. (A)** Backbone modification by phosphorothioate bond on 5'-end of templates; this involves the replacement of a sulfur atom by an oxygen on the phosphate group. **(B)** Biotin is linked to the final phosphate base of a template on its 5'-end via an aminoethoxy-ethoxyethanol linker. *Images adapted from www.biomers.net*

tration of trehalose (400 mM) in order to stabilize RecJ$_f$ exonuclease [34]. RecJ$_f$ is stabilized this way for experiments at 38.5°C, otherwise, RecJ$_f$ deactivates above 37°C. The addition of trehalose strongly influences the hybridization thermodynamics of DNA strands, increases the viscosity of the solution and keeps the activity of RecJ$_f$ only therefore preventing further exploration and tuning of this interesting reaction network at higher temperatures. For these reasons, in subsequent works [31, 32], Recj$_f$ was replaced by thermostable full-length exonuclease ttRecJ that can work at high temperatures in the absence of trehalose.

However, replacing RecJ$_f$ by ttRecJ results in the loss of oscillatory behavior of the Oligator. This can be due to different reasons. First and obviously, due to the higher

Table 1.3 – **Comparison of the Oligator buffer (Buffer O) [26] with buffers used in other reaction networks:** Bistable buffer (Buffer BS) [31] and Predator-Prey buffer (Buffer PP) [32]. Components marked (-) are not contained.

Component	Buffer O	Buffer BS	Buffer PP
Thermopol B DF	10 v/v%	10 v/v%	10 v/v%
Tris-HCl,pH =8	45 mM	45 mM	20
Mg^{2+}	7 mM	7 mM	8 mM
NaCl	50 mM	50 mM	50 mM
KCl	10 mM	10	10
$(NH_4)SO_4$	10 mM	10	10
dNTP	0.1 mM	0.4 mM	0.4 mM
Trehalose	410 mM	(-)	(-)
Dithiothreitol (DTT)	6 mM	6 mM	4 mM
Bovine serum albumin (BSA)	100 µg mL^{-1}	500 mgL^{-1}	500 mgL^{-1}
Synperonic F108	(-)	1 g/L	1 g/L
Netropsin	(-)	0.2 µM	0.2 µM

activity of ttRecJ. Second, because the higher activity of ttRecJ implies that undesired degradation of templates occurs if these are not additionally protected by three 5'-PTO backbone modifications instead of two. This extra PTO can increase or decrease the dissociation constant between templates and complementary species, thus, altering the design parameters. Third because removing the trehalose from the buffer strongly changes the hybridization thermodynamics. Fourth, our collaborators realized that if 3 PTO on the 5' end of a ssDNA inhibit the degradation activity of ttRecJ, they do not preclude its binding. As a result ssDNA templates with PTOs in 5' strongly inhibit exo activity but this activity is restored when the input is in high concentration and the 5' end of the template is majority double stranded. This feature lakes that the activity of the exonuclease strongly changes with the node concentration, thus hindering the programmability. In order to address this latter problem, biotin linking on the 5'-end coupled to streptavidin, instead of PTO modifications, can be used to protect templates from exonuclease degradation without inhibiting exonuclease (Fig. 1.8B).

As a result in this chapter we seek to obtain oscillations in the Oligator in conditions that are physico-chemically very different from the work of Montagne et al. [26]. We had two options, to first obtain oscillations in the original conditions and gradually

change conditions. Or to change all the conditions at once and build the network again step by step following similar experiments proposed by Baccouche et al. [35]. We decided to follow the latter strategy. We have sketched a working plan in Fig. 1.9. We will first test the autocatalytic node, then the inhibition on this node. Lastly, we will close the loop and search for oscillations by varying concentrations of templates and enzymes.

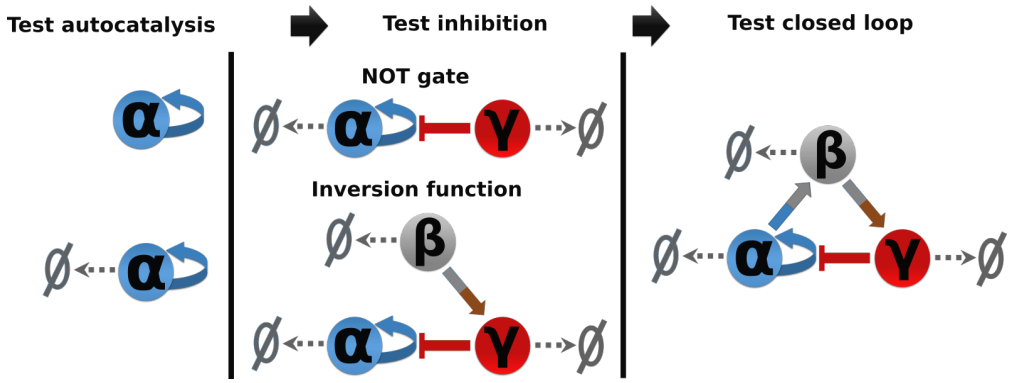

Figure 1.9 – **Experimental scheme to test the Oligator.** Autocatalysis is characterized with and without degradation, then inhibition is tested by introducing γ to an activated autocatalyst and by addition of activator β. In a final stage, the looped is closed and tested under different template and enzyme concentrations.

In this chapter we will perform reactions containing exonuclease ttRecJ, thus, we will use templates with either three 5'-PTOs or 5'-biotin/streptavidin modifications. We list the modified templates that are used in this work in Table 1.4. We also use a second set of sequences (Table 1.5) to create also an Oligator. This second set came from a numerical study of the Oligator done by the group of Tom de Greef at Technische Universiteit Eindhoven. He provided us with the sequences, and we have adapted them by adding DNA modifications. Also, we do not need to include trehalose in the buffer reaction since we do not used RecJ$_f$. For this reason, we test similar buffers before replacing the Oligator buffer with one of these buffers, which are used in the Predator-Prey and bistable networks (Table 1.3).

Table 1.4 – **Modified templates of the original Oligator network.** In our notation, internal modifications are in parenthesis whereas molecules covalently linked (such as dyes and biotin) on the 5'-end or the 3'-end of template are written before T or after (-) respectively. P3 stands for three phosphorothioates (P=*) and U for deoxy-ribo-Uridine, which substitutes a thymine. Dy and Cy refer, respectively, to dyes Dy530 and Cy3.5. Biotin and Biotin-TEG are indicated, respectively, by bt and Teg.

Name	Sequence 5'→3'
$T^{\alpha\alpha}$(P3,U)	A*A*C*AGACUCGAAACAGACTCGA
$T^{\alpha\alpha}$(P3)-Dy	A*A*C*AGACTCGAAACAGACTCGA-Dy
$T^{\alpha\alpha}$(P3,U)-Dy	A*A*C*AGACUCGAAACAGACTCGA-Dy
bt$AAT^{\alpha\alpha}$(U)-Dy	bt-AAAACAGACUCGAAACAGACTCGA-Dy
$T^{\alpha\beta}$(P3)	G*C*A*TGACTCATAACAGACTCGA
$T^{\beta\gamma}$(P3)-Cy	T*T*A*CTCGAAACAGACTGCATGACTCAT-Cy
Teg$AAT^{\beta\gamma}$-Cy	Teg-AATTACTCGAAACAGACTGCATGACTCAT-Cy

1.3 Assessment of an autocatalytic node

In this section, we characterize the basic reactions of the PEN-DNA toolbox: autocatalytic growth and degradation. We will first compare the kinetics of autocatalytic growth reactions in different buffers. Then, we will perform autocatalysis in dNTPs limited reactions to assay the turnover kinetics of pol and nick for a given template, and these also in different buffers. Finally, we will address the issue of possible sequestration of exo by 5-phosphorothioate or 5-biotin modified templates.

1.3.1 Autocatalytic reactions in different buffers

So for the PEN-DNA toolbox has been used in three different buffers. The initial oligator buffer (O) had a high concentration of trehalose to stabilize Rec_J exonuclease, as already discussed. Later the bistable buffer (BS) [31] was optimized for one particular nicking enzyme, Nt.BstNBI, and the Predator-Prey buffer (PP) [32] was optimized for another nicking enzyme, Nb.BsmI (Table 1.3). Here, we study the effect of different buffers on the autocatalytic growth of the PEN-DNA toolbox. We assay this effect by performing autocatalytic reactions of species α using template $T^{\alpha\alpha}$(P2) without exo in the three buffers listed in Table 1.3.

Table 1.5 – **Sequences of an in silico-designed Oligator by van Roekel et al. [36].** Node-1 template autoreplicates α_2 , node-2 template takes α_2 to produce β_2 which then triggers node-3 template to output γ_2. In this naming notation, internal modifications are in parenthesis, whereas molecules covalently linked (such as dyes and biotin) on the 5'-end or the 3'-end of template are written before T or after (-) respectively. U stands for deoxy-ribo-Uridine, which substitutes a thymine. Dy and Cy refer, respectively, to dyes Dy530 and Cy3.5. Biotin is indicated by bt.

Name	**Sequence 5'→3'**
btAAT$^{\alpha_2\alpha_2}$(U)-Dy	bt-AACATTGACUCTGCATTGACTCTG-Dy
btAAT$^{\alpha_2\beta_2}$(U)	bt-AATACCGACUCCACATTGACTCTG
btAAT$^{\beta_2\gamma_2}$-Cy	bt-AAACACTCTGCATTGACTTACCGACTCCA-Cy3.5
α_2	CAGAGTCAATG
β_2	TGGAGTCGGTA
γ_2	AGTCAATGCAGAGTGT

We activated the growth of α with the autocatalytic template $T^{\alpha\alpha}$(P2) at 60 and 200 nM in the three different buffers. In Fig. 1.10A we see their growth profile in the presence of EvaGreen. At 60 nM $T^{\alpha\alpha}$(P2), the initial profile is similar for all three buffers with a small reaction time delay of 4 min in the buffer PP. Although the maximum green fluorescence shift (ΔF) is different between buffers, values fell within a similar range. Interestingly, at 60 nM template a steady state in fluorescence is reached in buffer PP, but not in buffer BS nor in buffer O. In contrast at 200 nM template such steady state is reached in all three buffers.

It is important to note that we talk here about a steady state in EvaGreen fluorescence and not in concentration of species α. Indeed in our conditions α does not fluoresce in its single stranded form but only when it hybridizes to its template $T^{\alpha\alpha}$(P2). As a result the EvaGreen fluorescence is proportional to the total concentration of α only if $T^{\alpha\alpha}$(P2) is not saturated. Thus, the horizontal lines in Fig. 1.10A do not mean that the dynamic system has reached a steady state in concentration but that $T^{\alpha\alpha}$(P2) has reached saturation.

To quantify the initial growth kinetics (i.e. when α is at low concentration) of the autocatalysis we calculate the time for half growth ($t_{1/2}$). To do so, we plot the derivative of the fluorescence shift ($\frac{d(\Delta F)}{dt}$) as a function of time (Fig. 1.10B). Its maximum

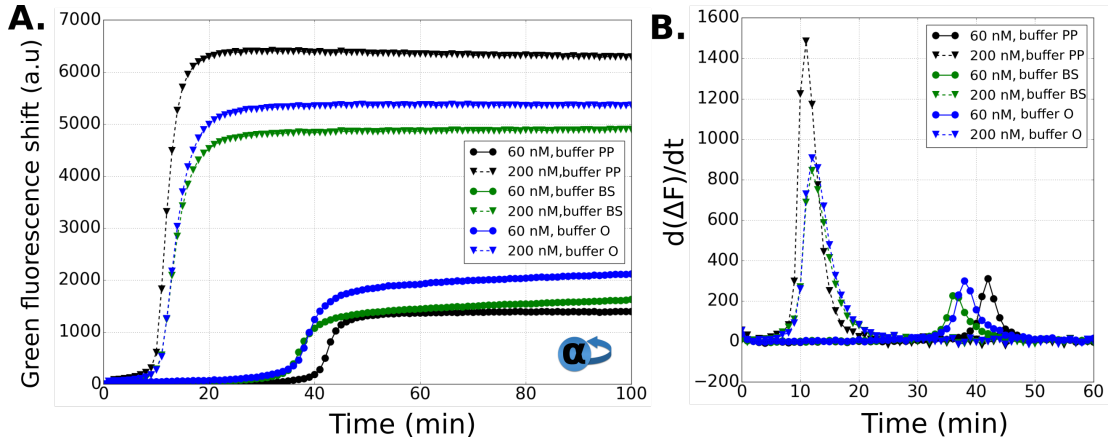

Figure 1.10 – **Autocatalytic growth of α in buffers PP, BS and O. (A)** The green fluorescence shift (ΔF) from EvaGreen is recorded over time. $T^{\alpha\alpha}$(P2) was 200 nM for $\bigtriangledown$ markers while 60 nM for $\bigcirc$. Reactions were performed with 3% pol and 2% nick, and triggered with 5 nM α at 38.5 °C. **(B)** Numerical differentiation of data from A versus time.

corresponds to $t_{1/2}$. We observe no significant differences between buffers BS and O, but a small difference exists for buffer PP. An exponential fit using Eq. (1.8) reveals the value of the rate constant (κ) is in fact the same for Buffer O and Buffer BS and about 1.5 times larger for the buffer PP (Table 1.6). Moreover κ, within the same buffer, seems to scale with $\sqrt{[T^{\alpha\alpha}]}$, but this needs to be confirmed by having more experimental points.

Table 1.6 – **Exponential rate constant of autocatalytic growth of α in different buffers.** The fits were performed for the data in Fig. 1.10. The kinetic rate constant κ is reported within two standard deviations.

Buffer	**Exponential Fit**	
	κ (min^{-1}) 60 nM T$^{\alpha\alpha}$(P2)	κ (min^{-1}) 200 nM T$^{\alpha\alpha}$(P2)
Buffer O	0.25 ± 0.03	0.50 ±0.06
Buffer BS	0.28 ± 0.04	0.49 ± 0.06
Buffer PP	0.44 ± 0.04	0.71 ± 0.09

We can conclude that the autocatalytic growth is indistinguishable between buffers BS and O. The major difference in their compositions is a higher concentration of dNTPs and the absence of trehalose in buffer BS and O. We know from the experiment

in Fig. 2.23 that increasing the concentration of dNTPs slows down growth. This would suggest that trehalose would also slow down growth so that both effects are balanced. Comparing BS and PP buffers, PP has half the concentration of Tris-HCl and 1 mM more of Mg^{2+}. Knowing the much greater influence that di-cations have both in DNA hybridization kinetics and in enzymatic activity it is possible that the concentration of Mg^{2+} is the main source of difference in kinetics between BS and PP. Further experimentation is required to verify this, but it is more practical to simply adopt buffer BS.

1.3.2 Effect of buffer on the turnover profile

A turnover experiment is a method to quantify the capacity of a given autocatalyst template to consume dNTPs, and this gives a qualitative view of the kinetics of all three enzymes (pol, nick and exo). In these experiments we see first an exponential growth of fluorescence then a plateau, and finally an exponential decay due to the degradation of the autocatalyst when all the dNTPs have been consumed (Fig. 1.11). We adjust the concentration of the dNTPs to be able to see the turnover profile in a reasonable time. For a given template sequence the reaction time (Δt) between growth and decay depends on the concentrations of the template and dNTPs. The shorter Δt the more efficient is a template to consume dNTPs and thus the faster pol and nick work with it.

To further assay the effect of the buffer on the enzymatic kinetics we study the turnover profile of template $T^{\alpha\alpha}$(P3,U) in the buffers BS and O (Fig. 1.11). Despite a small different of 10 minutes in Δt the exponential growth rate were comparable, so we turn to compare their decay regions. A linear fit of the initial decay shows that the rate constant k_{decay} for buffer BS (-0.045± 0.001 min^{-1}) was around 40 % smaller than for buffer O (-0.063± 0.002 min^{-1}) but Δt was comparable for buffer BS and buffer O, 170 and 160 min, respectively. At the end of the decay, the fluorescence goes slowly to zero; such slow decay rate can be explained by invoking the inhibition of ttRecJ with the 5' end of the templates. As α is consumed, the concentration of single-stranded template carrying phosphorothioates on its 5' end increases, and exo gets strongly

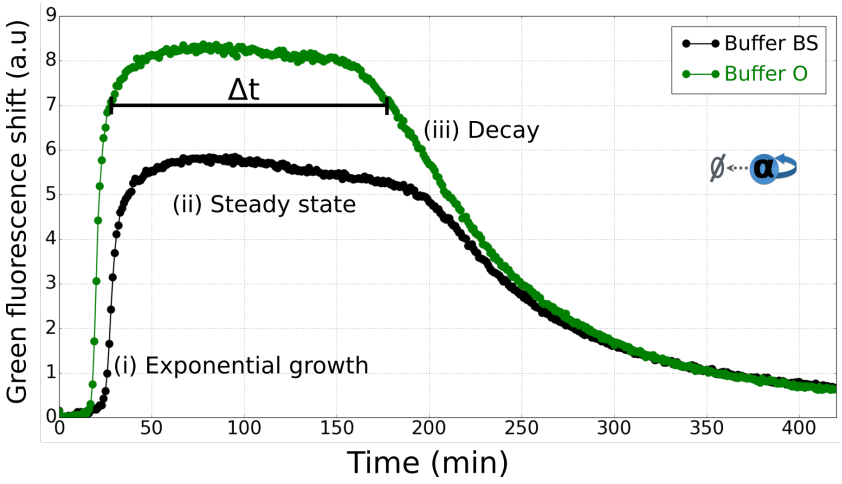

Figure 1.11 – **Turnover of autocatalyst α in two different buffers (BS and O).** The green fluorescence shift from EvaGreen is recorded over time. The turnover profile has a positive skewed-bell shape with three regions: (i) exponential growth, (ii) steady state and (iii) decay. Δt is the time it takes the profile to turn from steady state to decay. The reactions were performed at 42 °C with $T^{\alpha\alpha}$(P3,U) = 100 nM, 0.5% pol, 1% exo, 1% nick and 40 µM dNTPs. The activation was triggered with α = 0.1 nM.

inhibited. Although this linear activity of exo was reduced in buffer BS, the overall profiles were similar, thus, this turnover experiment further supports the idea that buffer BS can be used to replace buffer O in the Oligator network.

1.3.3 Inhibition of ttRecJ by the templates: phosphorothioate vs biotin/streptavidin modified templates.

Exo can bind unproductively to the 5' end of a template carrying phosphorothioates, thus decreasing its degradation activity towards α. Here, we will characterize this effect indirectly by performing turnover experiments and we will compare templates protected with three phosphorothioates versus templates carrying a biotin/streptavidin modification in their 5' end. We will use template $T^{\alpha\alpha}$(P3,U)-Dy in the first case and btAAT$^{\alpha\alpha}$(U)-Dy in the second case. Both templates have dye 530 covalently linked to its 3' side, so we can monitor the concentration of α by fluorescence quenching of Dy-530 upon binding of α to the input side of the template [37].

First, we perform turnover experiments with different concentrations of $T^{\alpha\alpha}$(P3,U)-

Dy (Fig. 1.12). We see that Δt increases with template concentration above 50 nM $T^{\alpha\alpha}$(P3,U)-Dy. Also, we observe that the decays become less steep as the concentration of template increases. This tells us that as the template concentration increases, exo is less efficient in degrading α. To quantify this, we linearly fit the initial decay (Fig. 1.13). It seems that there is a linear relationship between k_{decay} and template concentration. This indicates that phosphorothioate-modified templates can sequester exo, thus resulting in a lower exo activity.

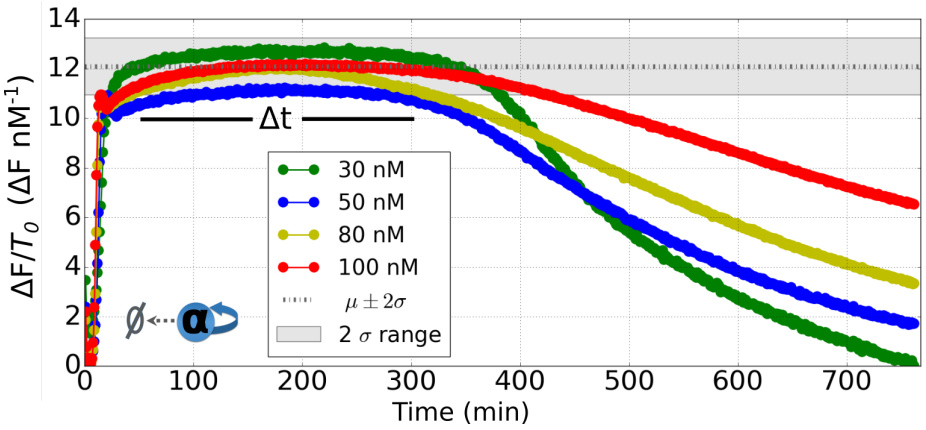

Figure 1.12 – **Turnover of phosphorothioate-modified template $T^{\alpha\alpha}$(P3,U)-Dy. (A)** A profile is the yellow fluorescence shift (ΔF) divided by its template concentration. $T^{\alpha\alpha}$(P3,U)-Dy was varied from 30 to 100 nM. Maximums fall within average max ± two standard deviations (displayed in shaded gray). The reactions were performed at 42°C with 1% pol, 1% exo, 2% nick and 40 µM dNTPs in buffer BS.

For the biotin/strepatvidin modified template case we used template btAAT$^{\alpha\alpha}$(U)-Dy in turnover experiments at 30 to 100 nM (Fig. 1.14). Their turnover profiles are similar when the fluorescence shift (ΔF) is normalized by template concentration (T_0). Even their ΔF maximums are within two standard deviation from their mean. The turnover time is independent of template concentration. Most of dNTPs consumption happens during the plateau of fluorescence, i.e. when concentrations of the substrates of pol (T_{in} in Fig. 1.3) and nick (T_{ext}) in the range of template concentration used here are one or both high. Our results thus indicate that enzymes are saturated. To determine if exo is inhibited by the biotin modification in btAAT$^{\alpha\alpha}$(U)-Dy, we search for differences in the decay region in the turnover profiles. We confirm this by linearly fitting the initial decay (Fig. 1.13). The decay rate does not depend on the template concentration

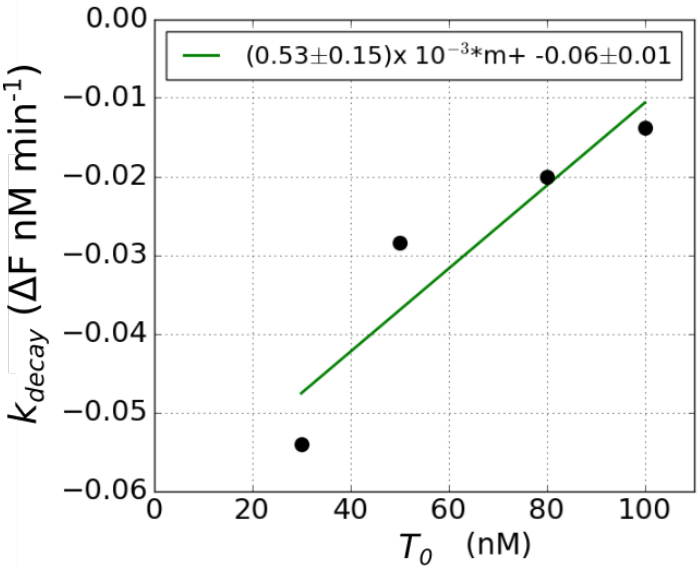

Figure 1.13 – **Rate decay constant from turnover experiments with phosphorothioate vs biotin/streptavidin modified templates.** A linear fit of the initial decay as function of template concentration from data in Fig. 1.12 and Fig. 1.14 is plotted here.

when the fluorescence has been normalized by template concentration. The fact that they are all similar tells us that there is less inhibition of exo from the biotin modification. From the results presented here, we conclude that phosphorothioate-modified templates inhibit strongly exo, whereas biotinylated/streptavidin templates inhibit exo less.

In the Oligator network, it is important that exo is available to degrade species. For example during the oscillations of the Oligator, if the autocatalyst α is being inhibited, exo must be able to first degrade most of α, and also when α recovers its ON state, it must degrade the inhibitor. Thus, the sequestration of exo by the templates can potentially destroy the dynamics and no oscillations are produced. After testing biotinylated and phosphorothioate-modified templates, we conclude that the former modification should be used if the sequestration of ttRecj negatively impacts the dynamics of the system.

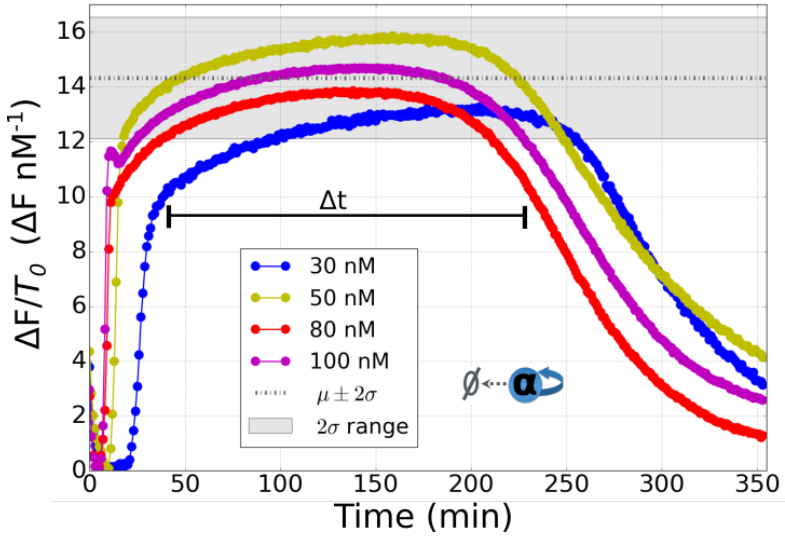

Figure 1.14 – **Turnover of biotin modified template btAAT$^{\alpha\alpha}$(U)-Dy. (A)** A profile is the yellow fluorescence shift (ΔF) divided by its template concentration. btAAT$^{\alpha\alpha}$(U)-Dy was varied from 30 to 100 nM. Maximums fall within average max ± two standard deviations (displayed in shaded gray). The reactions were performed at 42°C with 1% pol, 1% exo, 2% nick and 40 μM dNTPs in buffer BS

1.4 Autocatalyst growth in the presence of an inhibitor

An inhibitor must be designed such that it is able to slow down the autocatalyst growth. Here, we test the growth of an autocatalyst in the presence of an inhibitor. As we see in the sketch from Fig. 1.15, there is no degradation of either species.

We trigger the growth of autocatalyst α_2 in the presence of different concentrations of inhibitor γ_2 (Fig. 1.16). By increasing the concentration of γ_2 the activation of the autocatalyst is delayed, and the initial rate growth seems to slows down also with increasing γ_2. We see in this experiment (Fig. 1.16) that this inhibitor is strong enough to delay the autocatalyst for hundreds of minutes. We will test the inhibition when the autocalyst is already activated (i.e. ON state) in the following sections.

Figure 1.15 – **Sketch of an autocatalyst in the presence of an inhibitor.** Neither of the species are degraded since no exo is added.

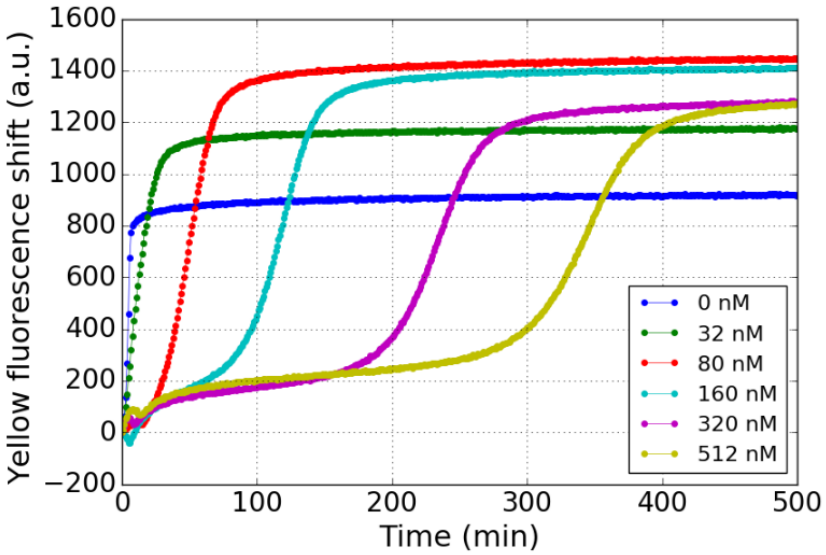

Figure 1.16 – **Autocatalyst growth in the presence of an inhibitor.** The inhibitor γ_2 is varied from 0 to 512 nM. The autocatalyst growth was activated with 0.5 nM of α_2. The reactions were performed at 42°C with 0.5% pol, 3% nick and 60 nM btAAT$^{\alpha_2\alpha_2}$(U)-Dy.

1.5 Inhibition of the autocatalyst in the ON state: NOT gate assay

The inhibition of the autocatalyst is an essential part of the Oligator, if it is too weak the stable state is an autocatalyst that is always ON, whereas if it is too strong, the autocatalyst is switched OFF and a weakly responding network is obtained.

In this section we assay the inhibition of an autocatlyst that is activated, then we analyze the inhibitory effectiveness. We call this assay a *NOT gate* due to its analogy to the corresponding logic gate (Fig. 1.17). In this assay the autocatalyst is first activated reaching an ON state. Then to test the inhibition, we inject in the reaction solution the inhibitor γ. If the inhibition is effective, the autocatalyst growth of α is stopped. Eventually, γ is degraded and α goes back to its ON state.

We remind the reader that we use a different exonuclease from the one reported in the original Oligator publication, hence we must determine the concentrations of templates and enzymes to adequately balance the inhibition. We perform NOT gate

experiments to determine the right experimental conditions at which the autocatalyst is effectively first inhibited to reach the OFF state and later able to recover to the ON state.

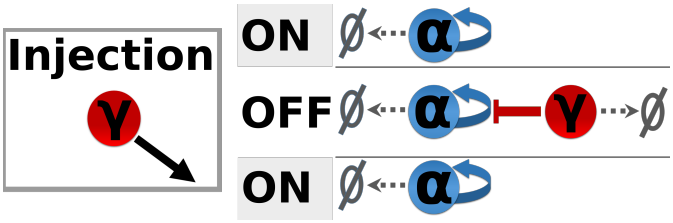

Figure 1.17 – **Sketch of the inhibition of an autocatalyst in the ON state: NOT gate assay.** An autocatalyst in the ON state is switched off by the addition of an inhibitor (γ). The inhibitor is degraded and the ON state is recovered.

1.5.1 Effect of inhibitor concentration on a NOT gate assay

We first study the impact of different inhibitor concentrations on an α autocatalyst that has already grown on its template btAAT$^{\alpha\alpha}$(U)-Dy in standard enzymatic conditions.

We let the growth of α reach a fluorescence steady state, which we call the ON state in Fig. 1.18. Once in the ON state, the reaction tube (that contains 20 µL) is removed from the fluorometer. Then, 2 µL of a solution containing the inhibitor in water is added to the activated reaction solution, which is subsequently mixed by vortexing for 15 seconds. The solution is placed back into the fluorometer to continue measuring the yellow fluorescence shift.

In the experiment in Fig. 1.18 we injected an inhibitor γ at a final concentration from 0 to 10 µM. We see that at $\gamma < 1$ µM the autocatalyst remains in the ON state. A partial inhibition is achieved at $\gamma = 1$ µM. A stronger inhibition seems possible at $\gamma = 10$ µM, but the ON state is then recovered within 300 minutes. The experimental conditions do not seem to be at the correct balance for effective inhibition. The fact that the autocatalyst can only be switched off at very high concentration of γ indicates that the autocatalyst is too strong.

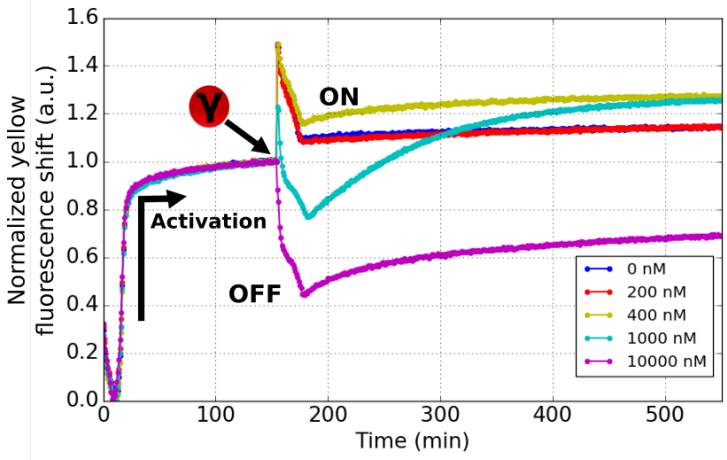

Figure 1.18 – **NOT gate experiments in which the inhibitor γ is injected at different concentrations.** Inhibitor was injected once the autocatalyst was activated (min = 154) at γ = 0-10000 nM. The experiment was performed at 42°C with 1% pol, 1% exo, 2% nick and 50 nM of btAAT$^{\alpha\alpha}$(U)-Dy.

1.5.2 Slowing down the autocatalyst: effect of nickase concentration on a NOT gate assay

In Section 1.5.1 we saw that the autocatalyst was too strong to be inhibited in the NOT gate experiment. We know that increasing the concentration of nick decreases the strength of the autocatalyst through a competition between nick and pol. Using this idea, we perfom NOT gate experiments at different concentrations of nick and expect to be able to inhibit the weaker autocatalyst.

We activate an autocatalyst at nick = 2%, 3% and 4%, then at steady state we inject either 0 or 1 µM of inhibitor γ (Fig. 1.19). We see that the inhibition is more effective as the concentration of nick increases. We numerically derivate this data as a function of time to determine if the autocatalyst indeed weakens as the concentration of nick (*nick*) increases (Fig. 1.19). The higher peak for 2% nick tells us that the autocatalyst inital growth rate is larger at this nick concentration. The amplitude of the peak decreases with *nick* confirming the weaking of the autocatalyst. Although we successfully inhibited the autocatalyst in Fig. 1.19, the recovering of the ON state still was too slow. This means that the inhibtor is not quickly degraded, and this is probably due to the low concentration of exo.

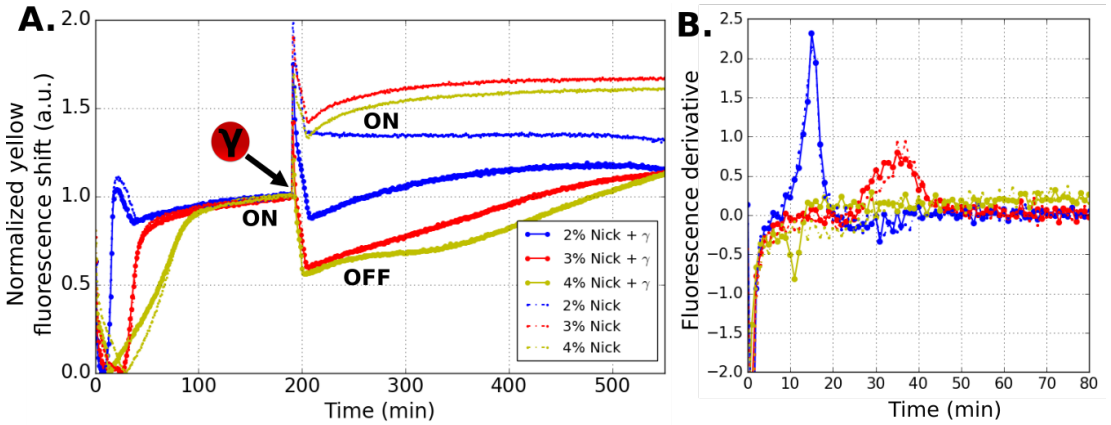

Figure 1.19 – **NOT gate experiments at different nick concentrations. (A)** The initial growth was activated at *nick* = 2, 3, 4%. In the legend (γ) means that 1 µM is injected but if the sample is not labeled with γ, then only water is injected. The experiment was performed at 42°C with 1% pol, 1% exo, 2% nick and 50 nM of btAAT$^{\alpha\alpha}$(U)-Dy. **(B)** Numerical differentiation of data over from A versus time.

1.5.3 Slowing down the autocatalyst: effect of exonuclease concentration on a NOT gate assay

Here, we perform NOT gate experiments at different concentrations of exo for two reasons: (i) to slow down the autocatalyst and (ii) to study how the recovery of the ON state after inhibition depends on *exo*. In Fig. 1.20 we show NOT gate profiles of an autocatalyst that is activated at *exo* = 2, 4 and 8%. Injecting 0.5 µM of inhibitor γ is able to partially switch the autocatalyst off. We see that the inhibition becomes more effective as *exo* increases. We conclude that that the ON states are not identical but the total α concentration on the ON state decreases as *exo* increases, thus making easier its inhibition. However, the recovery time from the OFF back to the ON state seems to be independent of *exo*. This may indicate that exo is saturated, thus leading to identical recovery times.

1.5.4 Forced oscillations in a NOT gate assay

We have learned from the NOT gate experiments that there must be a balance between the strengths of the autocatalyst and the inhibitor to stop the autocatalyst, which must

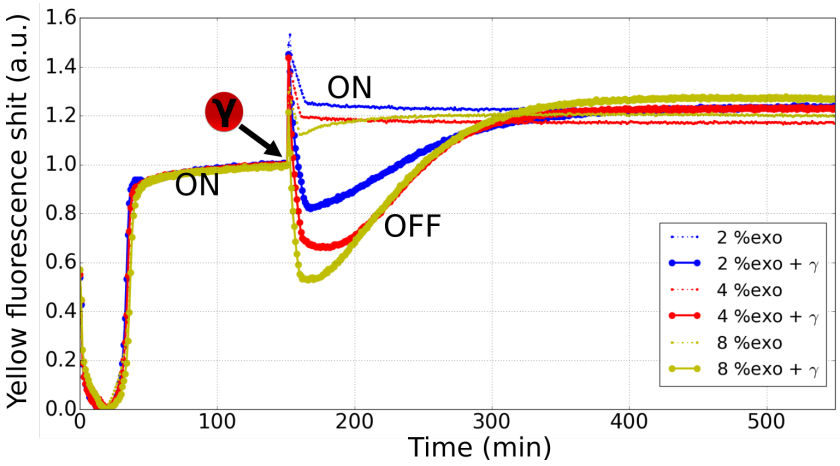

Figure 1.20 – **NOT gate experiments at different exo concentrations.** Activation of template $T^{\alpha\alpha}$(P3)-Dy was performed in a reactions solution containing *exp* = 2, 4 and 8%. We injected 2 µL of inhibitor γ at final concentration of 0.5 µM at min = 150, and 2 µL of water was added as a negative control (thinner dotted lines). The reactions were performed at 42°C, 1% pol, 2% nick and 50 nM $T^{\alpha\alpha}$(P3)-Dy, which was activated with 1 nM α.

be able to recover its ON state. If the NOT gate experiments are successful, with each inhibitor injection the autocatalyst can be forced to oscillate with periods related to the time it takes the autocatalyst to recover its ON state. We demonstrate this here. We show here only an experiment using template btAAT$^{\alpha_2\alpha_2}$(U)-Dy and not with template $T^{\alpha\alpha}$(P3)-Dy since we did not continue studying this latter design because we identified a problem with it as we will explain later in Section 1.6.1.

In Fig. 1.21 an autocatalyst is first activated (ON), which is indicated by the fluorescence value of 1, then we inject different concentrations of inhibitor γ. The higher the concentration of γ that we inject the closer we get to a complete OFF state. Injecting 20 nM of γ only deactivates the autocatalyst between 5-10%, whereas, 512 nM of γ inhibits up to 70%. This ON and OFF cycle can be repeated by injecting the inhibitor several times. At each injection of γ, its inhibitory efficiency decreases. This could be because we are injecting a solution that contains only γ in water, thus diluting by ~10% the activated reaction solution with every injection. At the fourth injection the salt concentration has been divided by a factor 1.4 and the binding affinity of γ_2 towards btAAT$^{\alpha_2\alpha_2}$(U)-Dy has probably decreased strongly. However, this hyphothesis should

be verified in the future by injecting γ_2 in the proper buffer. Another hypothesis is that the reaction mixture ages over time making the autocatalyst stronger, for example by partially consuming dNTPs.

Making the autocatalyst to manually oscillate gives information on how well the autocatalytic template can recover. Here, we demonstrate that we can find reasonable experimental conditions of an autocatalyst and inhibitor pair to force the oscillations.

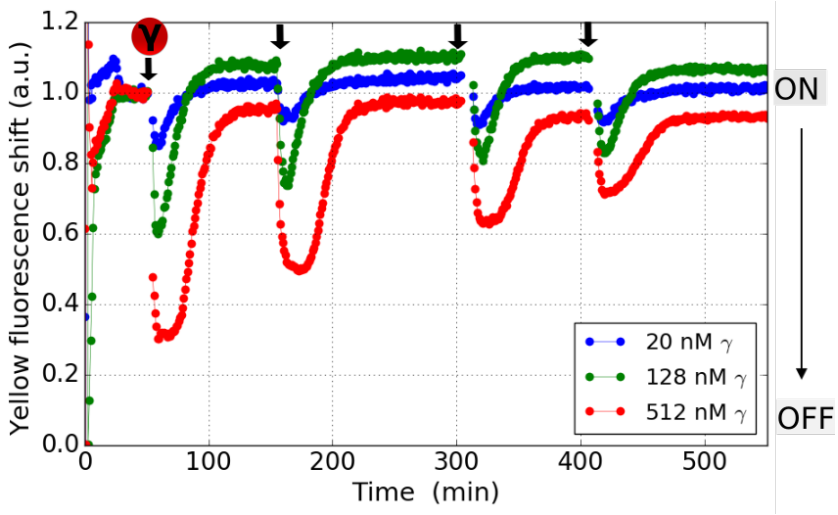

Figure 1.21 – **Oscillations in a NOT gate assay by periodically injecting inhibitor γ.** The yellow fluorescence here is the normalized fluorescence with respect to the ON state. Activation is indicated by a fluorescence level of 1. An autocatalyst was activated, and once activated 2 µL of inhibitor γ_2 was injected at 20, 128 and 512 nM. The reactions were performed at 42°C, 0.5% pol, 5% exo, 3% nick and 30 nM btAAT$^{\alpha_2\alpha_2}$(U)-Dy, which was activated with 1 nM α_2.

1.6 Inhibition of the autocatalyst in the ON state: inversion function

A further step towards the integration of the Oligator network is the *inversion function* assay, in which both the autocatalyst and inhibitor template are present. In Fig. 1.22 we sketch the inversion function assay: (i) the autocatalyst is activated with a small concentration of α in the presence of the inhibitor template, which is dormant because β is not present, (ii) the activated autocatalyst α is switched off by injecting β, which

activates the production of the inhibitor γ, and (iii) the ON state is recovered after degradation of β and γ. This assay allows us to test the effectiveness of activating the production of the inhibitor in the presence of the activated autocatalyst.

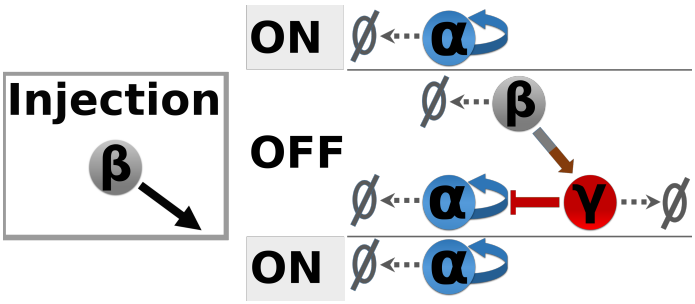

Figure 1.22 – **Sketch of the inhibition of an autocatalyst in the ON state: inversion function assay.** An autocatalyst in the ON state is switched off by the addition of an inhibitor (γ). The inhibitor is degraded and the ON state is recovered.

1.6.1 Effect of the inhibition activator on an inversion function

Here, we perform the inversion function assay by injecting species β, which activates the production of the inhibitor, at different concentrations (Fig. 1.23). As expected, the autocatalyst deactivation increases by increasing the concentration of β. Injecting 50 nM of β reaches a maximum deactivation of the autocatalyst in about 30 min, and it has a flat OFF state of Δt_{inhib} = 100 min. At 10 and 20 nM of β the maximum deactivation occurs, respectively, in 70 and 50 minutes without reaching a flat OFF state. In all cases, β is gradually degraded, thus stopping the production of the inhibitor γ, and the ON state is recovered upon the complete degradation of γ. However the level of fluorescence in the recovered ON state is not the same in all cases. At low α the inital and recovered ON states appear identical. As α grows the system does not seem to completely recover.

For the experiment in Fig. 1.23 we only succeeded to make an efficient inversion function by using the inhibitor template $T^{\beta\gamma}$(P2) that carries two PTOs and no dye, but not with $T^{\beta\gamma}$(P3)-Cy nor TegAAT$^{\beta\gamma}$-Cy that carry either 3 PTOs or a biotin/streptavidin in 5' and both labeled with dye Cy3.5 in 3'. We noticed that the autocatalyst would

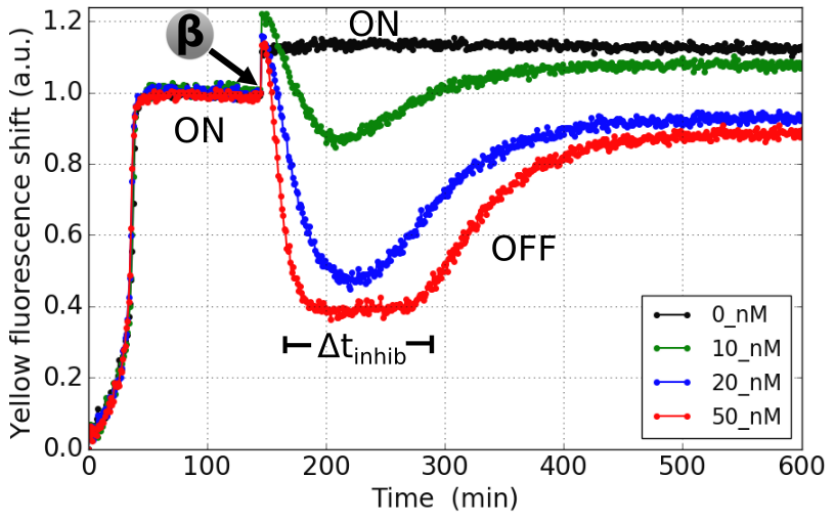

Figure 1.23 – **Inversion function at injections of different concentrations of the activator (β) of the inhibitor module.** An autocatalyst was activated with 1 nM α, and once activated 2 µL of β was injected at 0, 10, 20, 50 nM. The reactions were performed at 42°C, 1% pol, 4% exo, 2% nick, 30 nM $T^{\alpha\alpha}$(P3)-Dy and 80 nM $T^{\beta\gamma}$(P2).

grow to the ON state then deactivate by itself in the presence of $T^{\beta\gamma}$(P3)-Cy without adding β. A control experiment suggested that the Cy3.5 poisoned the system in an unknown way. This was problematic since we cannot use template $T^{\beta\gamma}$(P2) in the full network because this sequence has only two phosphorothioates, thus exo can slowly degrade it. We decided to stop using this design.

1.6.2 Forced oscillations in an inversion function assay

Since the oligator designed by the de Greef and co-workers (α_2, β_2 and γ_2) (Table 1.5) produced good results for the forced oscillations in the NOT gate assay from now on we will show experiments using these sequences. As in Section 1.5.4 we can manually trigger oscillations. Here, we do so by injecting multiple times the activator β of the inhibitor module. In this experiment we test if the inhibitor module can be activated efficiently multiple times.

We inject β to an activated autocatalyst at different concentrations (Fig. 1.24). We see that the level of OFF state increases by increasing β as expected. Interestingly, very small differences in concentration seem to produced highly different OFF state levels.

For example, from 8 nM to 10 nM we go from 50% inhibition to 90%. This suggests that the γ_2 more efficiently inhibits template btAAT$^{\alpha_2\alpha_2}$(U)-Dy that α_1 did with T$^{\alpha\alpha}$. In the full network we will have thus to choose a concentration of the template producing β_2 that it is not too high such that the maximum concentration of β_2 is about 10 nM.

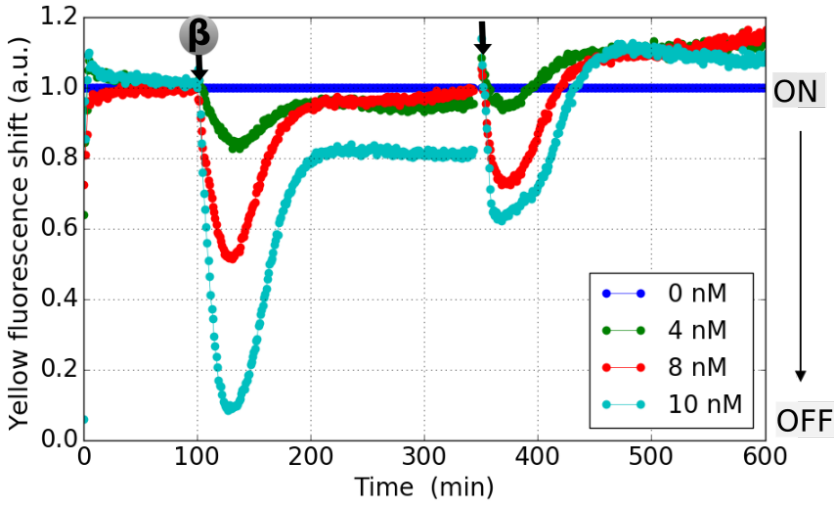

Figure 1.24 – **Oscillations in an inversion function assay by periodically injecting β_2.** The yellow fluorescence here is the normalized fluorescence with respect to the ON state. Activation is indicated by a fluorescence level of 1. An autocatalyst was activated with 1 nM α_2, and once activated 2 µL of β_2 was injected at 0, 4, 8 and 10 nM. The reactions were performed at 42°C, 0.5% pol, 5% exo, 3% nick, 30 nM btAAT$^{\alpha_2\alpha_2}$(U)-Dy and 80 nM btAAT$^{\beta_2\gamma_2}$-Cy.

However, when we inject a second time the level of OFF state seems much less than the first time. Again, this could be due to the dilution of the activated solution with each injection. A second injection of 10 nM β_2 is actually an injection of β_2 at 9 nM. Because the system is very sensitive to the concentration of β_2 in the injection solution (see the difference between β_2 = 8 and 10 nM at 100 min), this could explain at least part of the weaker inhibition with the second injection.

1.7 Testing the fully connected Oligator network

In this section we explore the Oligator network completely connected (Fig. 1.25). We have chosen to test this network with the sequences from Table 1.5 since we have succeeded to produce forced oscillations using the NOT gate and inversion function

networks with these sequences.

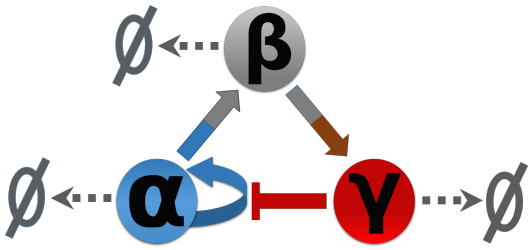

Figure 1.25 – **Scheme of the fully connected Oligator network.**

1.7.1 Effect of the template concentration on the Oligator network

We start by fixing the concentrations of the autocatalyst template btAAT$^{\alpha_2\alpha_2}$(U)-Dy and intermediate node template btAAT$^{\alpha_2\beta_2}$(U), but we change the concentration of the inhibitor template (Fig. 1.26). We keep the conditions where the forced oscillations were observed with the inversion gate (Fig. 1.24) except for nick that was reduced from 3 to 2%. We set the the intermediate template btAAT$^{\alpha_2\beta_2}$(U) to a low concentration of 0.5 nM to try to limit the maximum concentration of β_2 and increase the delay from btAAT$^{\alpha_2\alpha_2}$(U)-Dy. We monitor the concentrations of species α by recording the yellow fluorescence shift.

We see in Fig. 1.26 that at 4 nM of inhibitor template, the autocatalyst grows sigmoidally and remains fully activated (ON). By increasing the inhibitor template we see a deactivation of the autocatalyst between minutes 50-80. Once a maximum deactivation is achieved the autocatalyst starts to grow again. However, we just see half-oscillating cycles damping. At 128 nM inhibitor template the autocatalyst remains mainly inhibited, whereas at 64 nM the final state is probably a mixed state of inhibitors and autocatalysts. The fact that the inhibitor template concentration needed to deactivate an activated autocatalyst is (> 64 nM) larger than that of the autocatalyst template (30 nM) suggests the autocatalyst is too strong.

To decrease the strength of the autocatalyst we reduced its concentration from 30 to 20 nM and performed a similar experiment (Fig. 1.27). At 20 nM inhibitor template the autocatalyst remains in its ON state, but at greater concentrations we start to

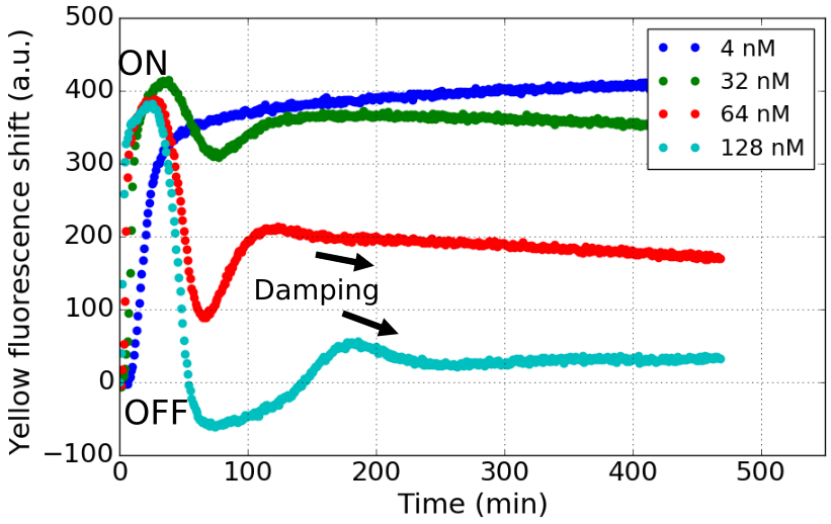

Figure 1.26 – **Oligator network at different inhibitor template concentrations and 30 nM autocatalyst template.** The reaction solutions contained 4, 32, 64 and 128 nM inhibitor template btAAT$^{\beta_2\gamma_2}$-Cy. The autocatalyst was initially activated with 0.5 nM α_2. The reactions were performed at 42°C, 0.5% pol, 5% exo, 2% nick, 132 nM streptavidin, 30 nM btAAT$^{\alpha_2\alpha_2}$(U)-Dy and 0.5 nM btAAT$^{\alpha_2\beta_2}$(U).

see its deactivation. At 50 nM inhibitor template we reach almost, at minute 130, a full deactivation, and from this maximum the growth resumes but never decays again. It seems that the system is trapped between two possible steady states: (i) weak inhibition such that the autocatalyst remains activated (at low btAAT$^{\beta_2\gamma_2}$-Cy) or (ii) mixed zone of activator and inhibitor.

The intermediate node serves as a delay between the growth of the autocatalyst and the production of the inhibitor. On the one hand, if the inhibitor is produced too early the autocatalyst has not grown sufficiently and is inhibited permanently. On the other hand, if the inhibitor is produced too late the autocatalyst has grown to a very strong state and is never inhibited.

To test this we varied the concentration of the intermediate node template btAAT$^{\alpha_2\beta_2}$(U) while fixing the concentrations of the autocatalyst and the inhibitor templates (Fig. 1.28). Decreasing the concentration of the intermediate node template delays the deactivation. Although with < 1 nM concentration of this template we can escape from the permanently inhibited state, the system remains in a mixed state of inhibitors

and autocatalysts. We repeated this experiment at several other concentrations of inhibitor template and similar results were obtained. This suggests that our system is trapped in that state, so a different strategy is needed.

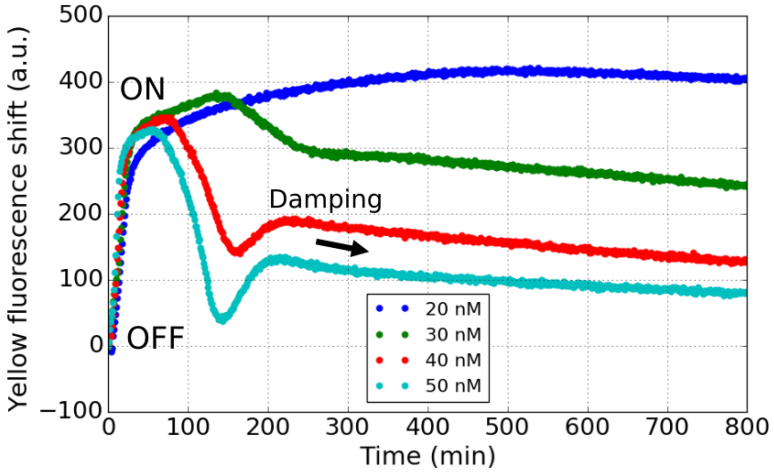

Figure 1.27 – **Oligator network at different inhibitor template concentrations and 20 nM autocatalyst template.** The reaction solutions contained 20, 30, 40 and 50 nM inhibitor template btAAT$^{\beta_2\gamma_2}$-Cy. The autocatalyst was initially activated with 0.5 nM α_2. The reactions were performed at 42°C, 0.5% pol, 3% exo, 2% nick, 20 nM btAAT$^{\alpha_2\alpha_2}$(U)-Dy and 0.5 nM btAAT$^{\alpha_2\beta_2}$(U).

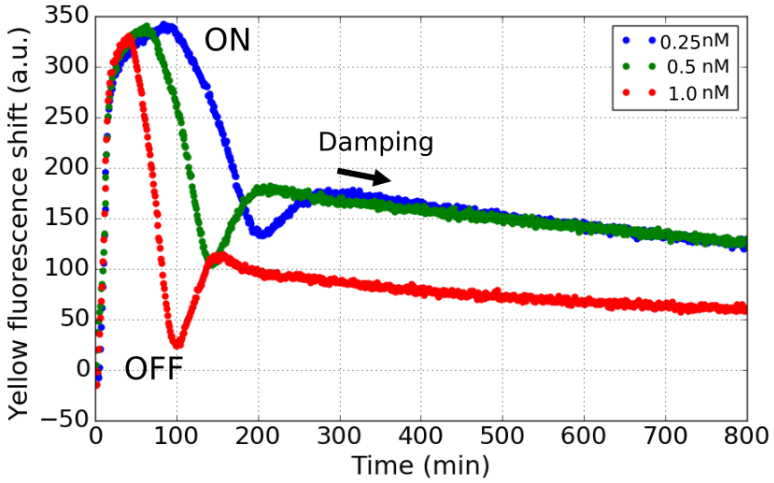

Figure 1.28 – **Oligator network at different concentrations of the intermediate node template.** The reaction solutions contained 0.25, 0.5, and 1 nM intermediate node template btAAT$^{\alpha_2\beta_2}$(U). The autocatalyst was initially activated with 0.5 nM α_2. The reactions were performed at 42°C, 0.5% pol, 3% exo, 2% nick, 30 nM btAAT$^{\alpha_2\alpha_2}$(U)-Dy and 45 nM btAAT$^{\beta_2\gamma_2}$-Cy.

1.7.2 Numerical simulations of the Oligator at different concentrations of enzymes

To guide our next experiments we explore our system numerically using the DNA Artificial Circuits Computer Assisted Design (DACCAD)[33], which is a dedicated software for simulating PEN-DNA toolbox networks. The rate constants are extracted from [31]. We want to know if by changing the concentrations of enzymes we can move our system towards oscillations.

We set enzymatic and DNA thermodynamic parameters at similar values to those reported in [26, 36]. In each plot in Fig. 1.29 exo is varied from 0.1 to 10 %, then nick and pol increase, respectively, from top to bottom and from left to right. We are able to find oscillations even when a system is stuck in a state of mixed inhibitors and autocatalysts (not shown here), for example this is done by increasing the concentration of exo in the right bottom plot. Increasing the concentration of nick, going from the top left to the bottom left plot, increases the number of oscillation periods. In the plots shown in Fig. 1.29 it seems that decreasing pol moves the system towards oscillations at the lower concentrations of nick. Although we have not performed an exhaustive search in the parameter space, we find in general that nick and exo are important parameters to obtain oscillations.

We learn two other things from the simulations in Fig. 1.29. The first autocatalyst peaks is much longer than the others and (ii) an oscillating system always goes through a phase where the concentration of α is close to zero. So far in our experiments we were never able to reach a very low level of α after the first peak. This suggests that in all our experiments either the autocatalyst loop is too strong or the inhibition loop is weak, or both.

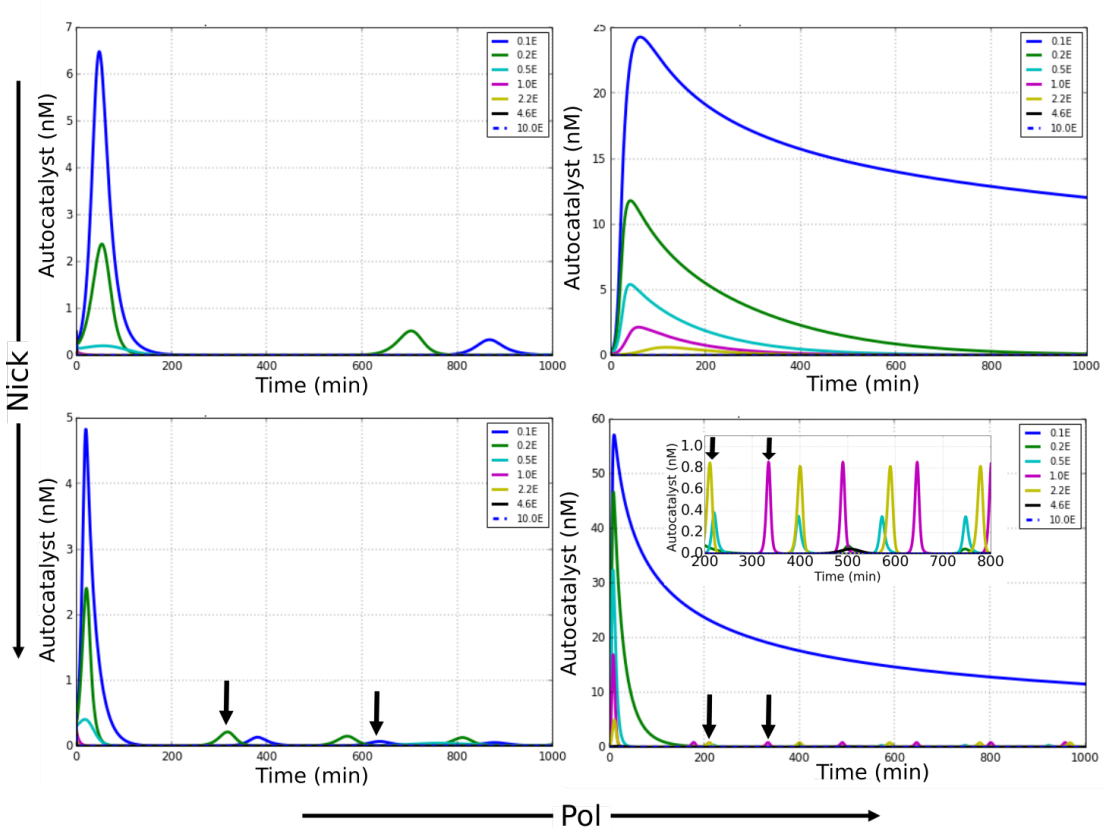

Figure 1.29 – **Numerical simulations of the Oligator at different concentrations of enzymes.** In the legends **E** stands for percent exo concentration. From left to right pol is 0.5 and 5%, and from top to bottom nick is 0.2 and 4.6%. The inset in the bottom right hand side plot is zooming on the y-axis of the larger plot. We set the dissociation constant of each species individually to: $K_d^\alpha = 36$ nM, $K_d^\beta = 41$ nM and $K_d^\gamma = 3$ nM.

1.7.3 Effect of the concentrations of enzymes on the Oligator network

Exploring experimentally a wide a range of enzyme concentrations requires a large number of experiments. Thus, we did simple tests to gain insights of how the enzymes affect the overall dynamics of the Oligator.

We performed an experiment at constant template concentrations and we varied the concentration of nick (Fig. 1.30). Increasing *nick* delays the inhibition of the autocatalyst since the autocatalyst is weaker at higher concentrations of nick. Eventually all curves go into damped oscillations. Nick weakens the autocatalyst favoring the

inhibition, however, even at low *nick* the autocatalyst is eventually fully inhibited.

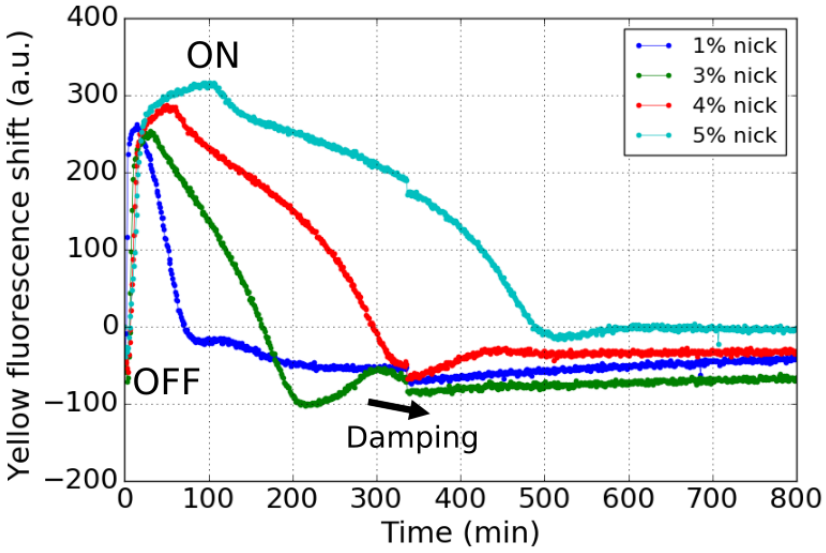

Figure 1.30 – **Oligator network at different concentrations of nickase.** The reaction solutions contained 1, 3, 4 and 5% nick. The autocatalyst was initially activated with 0.5 nM α_2. The reactions were performed at 42°C, 0.5% pol, 3% exo, 20 nM btAAT$^{\alpha_2\alpha_2}$(U)-Dy, 0.5 nM btAAT$^{\alpha_2\beta_2}$(U) and 50 nM btAAT$^{\beta_2\gamma_2}$-Cy.

If the inhibitor is not degraded the autocatalyst remains inhibited. We test in the following if increasing the concentration of exo can help the autocatalyst to resume its growth after being inhibited. In Fig. 1.31 we vary the concentration of exo while keeping all the concentrations of the templates, nick and pol constant. At 1% exo the inhibition of the activated autocatalyst is very slow but eventually reaches a complete inhibition. At higher concentrations of exo the activated autocatalyst is switched off more efficiently than at 1%. However, increasing exo between 3 and 5% increases the steady state concentration of γ_2 and thus moves the system away from an oscillatory state.

1.7.4 Effect of the inhibition template concentration on the Oligator network at higher temperature (45°C)

To explain the mixed state of inhibitors and autocatalysts we hypothesize that the species remain hybridized to their templates too long, thus they are not efficiently

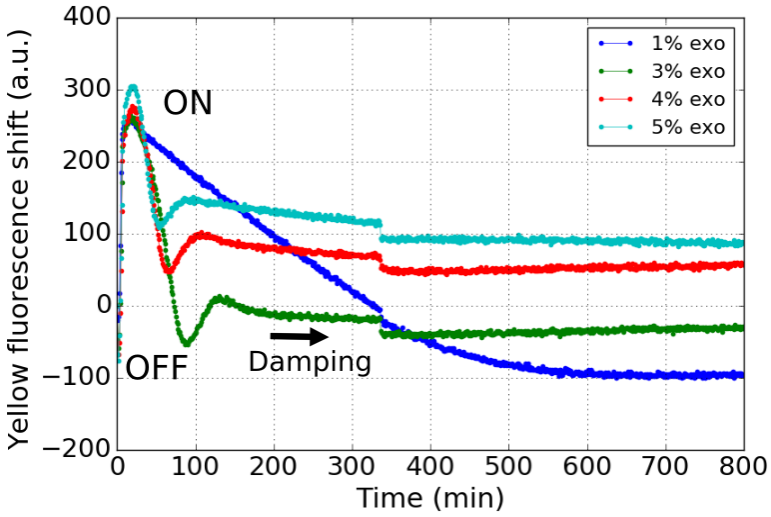

Figure 1.31 – **Oligator network at different concentrations of exonuclease.** The reaction solutions contained 1, 3, 4 and 5% exo. The autocatalyst was initially activated with 0.5 nM α_2. The reactions were performed at 42°C, 0.5% pol, 2% nick, 20 nM btAAT$^{\alpha_2\alpha_2}$(U)-Dy, 0.5 nM btAAT$^{\alpha_2\beta_2}$(U) and 50 nM btAAT$^{\beta_2\gamma_2}$-Cy.

degraded. Increasing the reaction temperature increases the dissociation constant of all the species, consequently spending less time on their templates. If the species are not on the template they are available for degradation. However, increasing the temperate also changes the activities of all the enzymes and the system is on a completely different state. Nonetheless, we experimentally test this situation as a last alternative.

We increased the temperate from 42°C to 45°C and we varied the concentration of the inhibitor template in the Oligator network (Fig. 1.32). Increasing the inhibitor template increases the OFF level of the activated autocatalyst. However we are never able to complementary inhibit the autocatalyst. We always face the same problem: the autocatalyst loop is too strong and/or the inhibiting loop too weak.

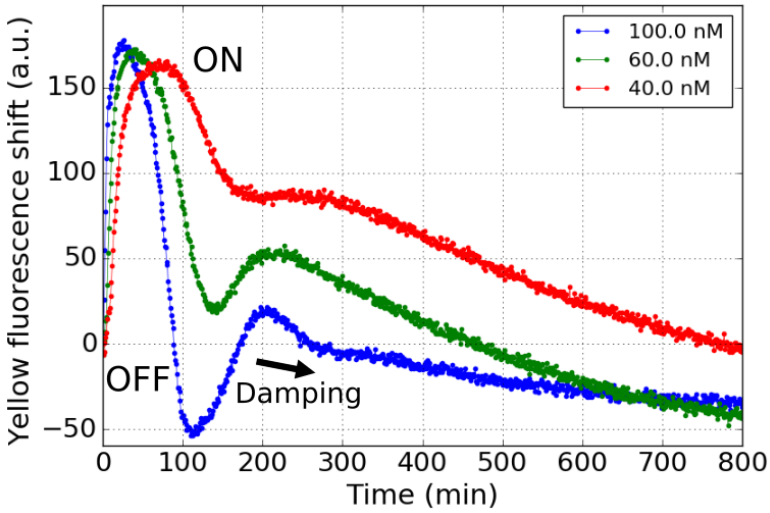

Figure 1.32 – **Oligator network at different inhibitor template concentrations at 45°C.** The reaction solutions contained 40, 60 and 100 nM inhibitor template btAAT$^{\beta_2\gamma_2}$-Cy. The autocatalyst was initially activated with 0.5 nM α_2. The reactions were performed at 45°C, 0.5% pol, 3% exo, 2% nick, 15 nM btAAT$^{\alpha_2\alpha_2}$(U)-Dy and 0.2 nM btAAT$^{\alpha_2\beta_2}$(U).

1.8 Conclusions and perspectives

We have tested systematically the kinetics of an activator-inhibitor reaction network as a candidate network to explore in the future Turing patterns. To do, so we have taken as a model the Oligator oscillating network designed by Montagne et al. [26]. Although oscillations are not needed for a network to be able to display a Turing instability we took oscillations as a design goal to learn how to test PEN-DNA networks. First, we evaluated the autocatalytic node in the absence and in the presence of its inhibitor. Then, we generated logic functions by injecting the inhibitor in the NOT gate experiment and the activator of the inhibitor module in the inversion function.

We aimed to recover the oscillatory behavior by testing each node in an incremental manner. Notably we obtained forced oscillations with an inversion function network with sequences that were designed in silico in [36] but never before tested experimentally. Once the Oligator network was fully connected the system always finished in a steady state with nonzero concentration of autocatalyst.

We have discovered that modifying key parameters such as the template and exonuclease concentration requires extensive experimentation that is very time consuming. In this network, the number of possible parameters that we can vary to search for oscillations is indeed large. Perhaps, this type of research can be complemented in the future with High Throughput Screening (HTS) methods such as the one implemented by Genot et al. [38], in which the reaction solutions are encapsulated in thousands of micro-droplets allowing to explore many experimental conditions in a single experiment. Although the PEN-DNA toolbox is programmable it is still hard and time-consuming to obtain the designed dynamic behavior. Nevertheless, another important conclusion is that the testing of reaction networks allowed me to learn the experimental techniques necessary for the work presented in the following chapters. Here, we have covered temporal dynamics, but in the next chapters we will expand the computation capabilities of the PEN-DNA toolbox from time to time and space.

2 Controlling diffusion: wave propagation with immobilized DNA strands

Turing patterns emerge from an activator-inhibitor reaction network in which the diffusion coefficient of the activator must be much smaller than that of the inhibitor (see Fig. 2 in the Introduction). In this chapter, we explore how to meet this condition for activators based on the PEN-DNA toolbox. After reviewing the literature concerning the redction of diffusion for Turing patterning, we focus on developing a strategy to tune the diffusion coefficient, D_{A_i}, of DNA autocatalytic species, A_i. Our strategy is based on the fact that the autocatalytic species, as seen in Chapter 1, hybridizes to its complementary template, thus forming a complex. Molecular drags linked to the templates, or their complete immobilization, should result in the reduction of the effective diffusion coefficient ($D_{A_i eff}$) of the activation species due to the complexation. We use biotinylated templates that can be linked to various substrates via a streptavidin-biotin interaction. We investigated two types of substrates: (i) ~30 µm diameter porous agarose beads and (ii) ~200 nm diameter magnetic nonporous beads. As a means to test these two strategies we study traveling fronts of an autocatalytic node. Reducing $D_{A_i eff}$ should result in lower front velocities, and by measuring the velocity of the fronts we can estimate $D_{A_i eff}$. We achieved a reduction of $D_{A_i eff}$ by up to 4.3 fold using a diluted dispersion of agarose beads in an agarose gel and of 2.4 fold with a dispersion of the magnetic beads in solution. When the agarose beads were closely packed the fronts gave a low fluorescence signal and tended to vanish after propagating only for short distances.

2.1 State of the art: a complexation reaction as a strategy to reduce the diffusivity

In this section we focus on how the reversible complexation of a genetic activator species with an immobile ligand reduces the effective diffusion coefficient of the activator, thereby assisting in the emergence of Turing patterns. First, we go over the theoretical aspects of complexation in an activation-inhibitor model. Subsequently, we review the first research works on Turing patterns, which were possible because of the complexation of the activator species with starch. Lastly, we introduce the Belousov–Zhabotinsky (BZ) reaction in a water-in-oil Aerosol OT (AOT) microemulsion, a system developed in the early 2000s where a difference in diffusion between the activator and inhibitor in an aqueous and oil phase gives rise to a rich diversity of patterns.

2.1.1 Theoretical aspects of complexation in Turing patterns

Turing patterns are steady-state concentration structures with well-defined wavelength that emerge in a reaction-diffusion system where all the concentrations are initially homogeneous across space. The first criterion for Turing patterning is that the system has temporally uniform steady state that is stable in the absence of diffusion [39]. The second criterion is that in the presence of diffusion there is at least one spatially inhomogeneous infinite-small perturbation to the uniform steady state that is bistable, i.e. it grows instead of decaying. Turing patterning is thus a symmetry-breaking process.

The first experimental demonstrations of chemical Turing patterns by Castets et al. [18] and Ouyang and Swinney [19] used the chlorite–iodide–malonic acid (CIMA) reaction in an open gel reactor in the presence of starch as iodide indicator. In this system, the activator and the inhibitor are, respectively, I^- and ClO_2^-. However, their expected diffusivities in solution are not drastically different as required for Turing patterning. These works led to theoretical [40–42] and further experimental

[43] studies that aimed to explain how the requirements for the criteria for Turing instability were met in such experiments. Lengyel and Epstein [40] proposed that the complexation of the activator I^- with the starch indicator results in the reduction of its effective diffusivity. To illustrate how complexation facilitates the Turing instability the authors first consider a reaction-diffusion (RD) system of two chemical species (A and I) with rate constants (k),

$$\frac{\partial A}{\partial t} = f(A, I, k) + D_A \frac{\partial^2 A}{\partial z^2} \tag{2.1}$$

$$\frac{\partial I}{\partial t} = g(A, I, k) + D_I \frac{\partial^2 I}{\partial z^2},$$

where D_A and D_I are the diffusion constants, t is the time and z the spatial variable. f and g are functions providing the rate of creation and destruction of A and I, respectively. The jacobian matrix of Eq. (2.1) is defined as,

$$J = \begin{pmatrix} a_{11} & a_{12} \\ a_{21} & a_{22} \end{pmatrix} \tag{2.2}$$

where

$$a_{11} = \frac{\partial f}{\partial A}, \quad a_{12} = \frac{\partial f}{\partial I}, \quad a_{21} = \frac{\partial g}{\partial A}, \quad a_{22} = \frac{\partial g}{\partial I}. \tag{2.3}$$

The first criterion for Turing patterning is that X has a steady state that is spatially uniform to perturbations. Linear stability analogous tells us that this criterion is verified if and only if [39]

$$\mathrm{tr}(J) = a_{11} + a_{22} < 0 \tag{2.4}$$

and

$$\det(J) = a_{11}a_{22} - a_{12} + a_{21} > 0. \tag{2.5}$$

The second criterion for Turing patterning is that the steady state of Eq. (2.1) is unsta-

ble to as spatially inhomogeneous perturbation. This implies [39] that

$$a_{11}D_I + a_{22}D_A > 0 \tag{2.6}$$

Equations (2.4) and (2.5) are the necessary and sufficient constraints for a two-variable system to display Turing patterns. From Eq. (2.4) $a_{11} + a_{22}$ should be negative but Eq. (2.6) implies that a_{11} and a_{22} have opposite signs. This means that one species promotes its own production (the activator, $a_{22} < 0$). In this situation for Eq. (2.6) to hold we need

$$|a_{11}| < |a_{22}|. \tag{2.7}$$

From Eqs. (2.6) and (2.7) we have

$$\frac{D_A}{D_I} < 1, \tag{2.8}$$

that activator must diffuse slower than the inhibitor. These criteria are summarized in the expression by Gierer and Meinhardt [14] *short-range activation and long-range inhibition*. Let's see now how adding complexation to an immobile species modifies this equation. In the presence of a binding partner (S) of the activator the formation of the complex (C) at equilibrium is given by,

$$\mathrm{A} + \mathrm{S} \underset{k_-}{\overset{k_+}{\rightleftharpoons}} \mathrm{C}, \quad K = \frac{C}{AS} = \frac{k_+}{k_-}, \tag{2.9}$$

where k_+ and k_- are, respectively, the forward and backward rate constants. The concentration of the binding partner is much larger than A such that the concentration of S is considered constant ($S \approx S_0$) and grouped into $K' = KS_0$. Adding the

complexation reaction to the RD system in Eq. (2.1) yields,

$$\frac{\partial A}{\partial t} = f(A,I,k) - k_+ S_0 A + k_- C + D_A \frac{\partial^2 A}{\partial z^2} \tag{2.10a}$$

$$\frac{\partial I}{\partial t} = g(A,I,k) + D_I \frac{\partial^2 I}{\partial z^2} \tag{2.10b}$$

$$\frac{\partial C}{\partial t} = k_+ S_0 A - k_- C \tag{2.10c}$$

Note that C is immobile and thus its diffusivity is zero. We can substitute C by $K'A$ in Eq. (2.10c),

$$K' \frac{\partial A}{\partial t} = k_+ S_0 A - k_- C. \tag{2.11}$$

Then, we can cancel the terms on the right hand side of Eq. (2.11) by adding it to Eq. (2.10a),

$$\sigma \frac{\partial A}{\partial t} = f(A,I,k) + D_A \frac{\partial^2 A}{\partial z^2} \tag{2.12}$$

$$\frac{\partial I}{\partial t} = g(A,I,k) + D_I \frac{\partial^2 I}{\partial z^2},$$

where $\sigma = (1 + K')$. What Eq. (2.12) tells us is that the complexation separates the time scales for changes in the concentrations of the inhibitor and activator by a factor of σ in the same way as a difference in diffusion coefficient does. This is perhaps easier to analyze when the system is rescaled by setting $t = t'/\sigma$ and $z = D_A^{1/2} z'$,

$$\frac{\partial A}{\partial t'} = f(A,I,k) + \frac{\partial^2 A}{\partial z'^2} \tag{2.13}$$

$$\frac{\partial I}{\partial t'} = \sigma \left(g(A,I,k) + \psi \frac{\partial^2 I}{\partial z'^2} \right),$$

where $\psi = D_I / D_A$. Hence, the greater the σ, i.e. the more stable the complex, the larger the difference in the time scale of diffusion between the two chemical species: $\sigma\psi$. From Eq. (2.13) we can rewrite the equivalent of the Turing constraints Eqs. (2.4)

to (2.6),

$$\frac{a_{11}}{\sigma} + a_{22} < 0 \tag{2.14}$$

$$a_{11}a_{22} - a_{12}a_{21} > 0 \qquad (\sigma \text{ vanishes}) \tag{2.15}$$

$$\frac{D_A}{\sigma D_I} < 1. \tag{2.16}$$

We recall that in the activator-inhibitor system $a_{11} > 0$ and $a_{22} < 0$. Complexation of A with an immobile ligand has thus two important consequences for Turing patterning:

1) It increases the range of stability of the uniform steady state (Eq. (2.15)).

2) It reduces the apparent diffusivity of A Eq. (2.16).

From Eq. (2.4) for example, if the system has a unique unstable steady state displaying oscillatory dynamics without complexation ($\sigma = 1$), then the presence of complexation ($\sigma > 1$) can stabilize the homogeneous steady state, and Turing instabilities occur in this expanded region. σ simply enlarges the range of the stability area of the steady-state (Fig. 2.1). This tells us that diffusion-driven instabilities for Turing patterning are possible now at parameter values that were inside the stable oscillatory region of the system without complexation [40].

Pearson [41] extended this analysis to conditions outside the regime of the quasi-steady state approximation. His findings are similar to those of Lengyel and Epstein [40], and he concludes that the main role of complexation is to stabilize a steady state which would be unstable for the case without complexation [41]. The analysis tells that by taking into account complexation, the Turing conditions can be satisfied even if both, the activator and inhibitor, have equal diffusivity [42].

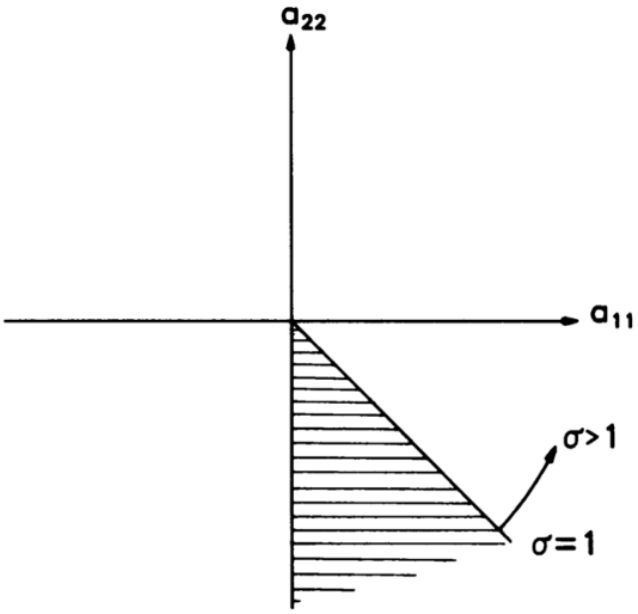

Figure 2.1 – **Stability analysis for a general activator-inhibitor system in the presence of a ligand binding to the activator.** The y-axis and x-axis are the jacobian elements in Eq. (2.3). The shaded area is the stable steady state of the an inhibitor-activator model $\sigma = (1 + K')$ where K' is the apparent equilibrium constant for the association of the activator and the ligand. When $\sigma > 1$ the shaded area increases thus making easier to obtain Turing patterns. This figure was taken from [40].

2.1.2 Turing patterns by complexation in inorganic reactions

As mentioned in Section 2.1.1 the activator in the CIMA reaction (I^-) forms a complex with the starch resulting in the reduction of its effective diffusivity relative to that of the inhibitor (ClO_2^-). The starch was completely immobilized in the gel [18]. Using this system a rich set of Turing patterns were found by Ouyang and Swinney [19]: Fig. 2.2 shows (a-b) hexagons, (c) stripes, and (d) mixture of hexagons and stripes. The brighter regions in Fig. 2.2 correspond to activator concentration that is detected upon binding to the starch indicator.

In a numerical study [44] of this system, Ouyang and Swinney [19] point out that a diffusion ratio between the inhibitor and activator $D_{ClO_2^-}/D_{I_3^-}$ of at least 10 is required. Also Lengyel and Epstein [44] estimated $D_{ClO_2^-}/D_{I_3^-} \approx 15$, which results from the complexation of the activator in a gel with excess binding partners. The reduction of

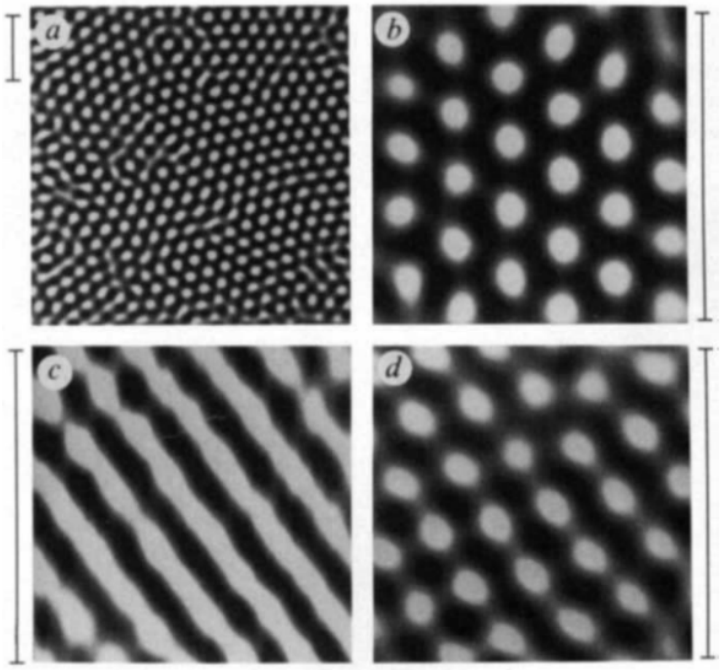

Figure 2.2 – **Chemical Turing patterns in an open gel reactor.** The following patterns of activator (I^-) were found: **(a-b)** hexagons, **(c)** stripes, and **(d)** mixture of hexagons and stripes. The patterns are visualized in transmitted light (580 nm). The scale bars are 1 mm. This figure was borrowed from [19], and the complete experimental conditions are found in FIG.1 of this publication.

the diffusivity is proportional to the fraction of time that the activator is trapped in the complex [13].

The starch serves two different purposes to reduce the effective diffusion of the activator and as an indicator. If that is the case any other immobilized agent that forms a complex with the activator might yield similar results. This was demonstrated by Noszticzius et al. [45] using polyvinyl alcohol to reduce the diffusion coefficient of I_3^- (Fig. 2.3B). In a more recent study, Asakura et al. [43] employed polymers with a quaternary alkyl ammonium cationic side chain and micelles of quaternary alkyl ammonium cationic amphiphiles to lower the effective diffusivity of I^-, and Turing patterns were also observed.

The complexation of the activator has allowed meeting the Turing instability condition in the CIMA reaction. However, this approach has been limited to this system and to

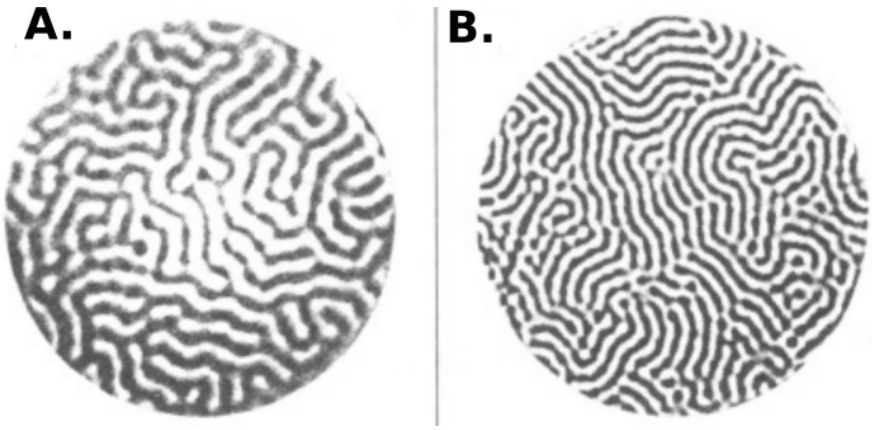

Figure 2.3 – **Chemical Turing patterns using (A) poly(vinyl alcohol) and (B) soluble starch.** The patterns have different wavelengths (λ) : **(A)** λ = 0.32 mm for poly(vinyl alcohol) at 15 g/L and **(B)** λ = 0.21 mm for soluble starch at 2.5 g/L. The disk reactors are 6 mm in diameter. This figure was extracted from [45].

the ferrocyanide-iodate-sulfite (FIS) reaction [46]. Only another approach has been successful in achieving the reduction in diffusivity needed for Turing patterning, as we will see in the following text.

2.1.3 Modifying the effective diffusivity by solubility difference between two phases

Here, we present a approach to obtain Turing patterns introduced by Vanag and Epstein [47]. It modifies the effective diffusivity by using the difference in solubility of the activator and inhibitor in a medium with two-phases. They used the Belousov–Zhabotinsky (BZ) reaction in a water-in-oil microemulsion stabilized with the surfactant Aerosol OT (AOT). In this system, the BZ reaction solution is encapsulated in nanometer sized water droplets dispersed in an oil (octane) phase. Since the initial BZ reagents are polar, they remain in the droplets. Then, the reaction starts and produces the inhibitor species (Br_2), which can diffuse into the oil phase due to its nonpolar nature. In this two-phase system the difference in diffusivity is achieved by the higher solubility of Br_2 in the oil phase making its effective diffusion coefficient much larger than that of the activator ($HBrO_2$) that is confined in the water micro-droplets and its diffusivity is given by the diffusivity of the droplets.

In homogeneous reaction conditions, the oscillating BZ system spatially organizes into traveling waves: either outwardly moving spirals or concentric circles [15, 48]. However, when this reaction is constrained into water-in-oil AOT microemulsion droplets, a new class of patterns emerges: Turing structures, standing waves, accelerating waves and inwardly moving spirals [47, 49].

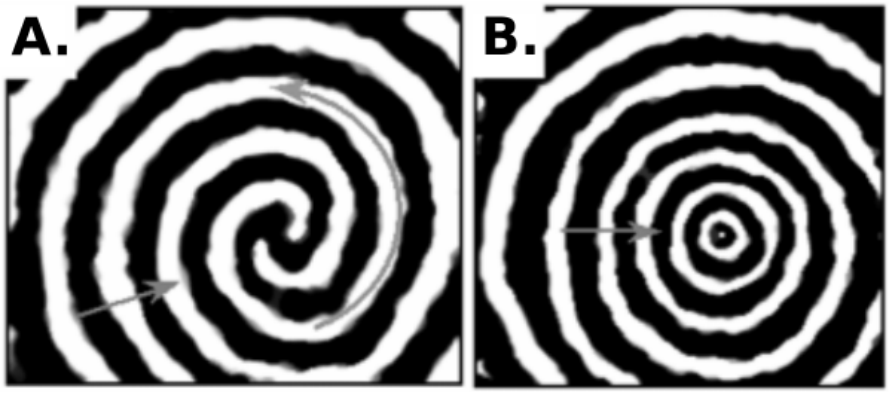

Figure 2.4 – **Inwardly rotating spiral (A) and concentric circle (B) BZ waves in AOT microemulsion droplets. (A)** Antispirals formed at a volume fraction of droplets ϕ_d = 0.55. Frame size was 1.8 × 3.75 mm^2. **(B)** Concentric circles were obtained at ϕ_d = 0.59. Frame size was 2.7 × 2.5 mm^2. Figures compiled from [49]

Inwardly-moving spirals emerge because of the ability of the waves to accelerate. From an initial pattern, the waves move towards the center of their arc, and consecutive waves increase in size. The free space between the waves allows a faster wave end to curl up around the end of the next outer wave. The velocity, v, is proportional to the diffusion coefficient of the activator: $v \sim (D_A)^{1/2}$. The change of velocity comes from the different diffusivity of the activator in water and in oil. The velocity of a spiral of short wavelength is driven by the diffusion coefficient of the activator in water, but a spiral of long wavelength is driven by the diffusion coefficient of the activator in oil, D_{oil}.

It is important to note that after 35 years of active research only three chemical systems are capable of generating Turing patterns. The CIMA and the FIG systems do so in an open gel reactor while the BZ-AOT reaction is capable of generating them in a closed reactor. This underlies the great experimental challenges to create a new system capable of Turing patterns.

We have discussed how complexation can reduce the effective diffusivity of the activator in the CIMA reaction, however, the implementation of this approach to other inorganic reaction systems capable of generating Turing patterns is far from trivial. The issue comes from the fact that most inorganic molecules have similar diffusion coefficients and a ligand for reversible complexation of the activator must be found. Whereas the usage of the two-phase approach is limited reaction systems that can be kept out of equilibrium in a closed reactor for a limited time. The problem is that the only such system made of inorganic reactions in the BZ reaction. A promising reaction system that can benefit from both of the approaches covered in this section must: (i) operate out-of-equilibrium in a closed reactor and (ii) involve chemical species that can easily from complexes with immobile or slowly diffusion ligands.

2.2 Strategies to control the diffusivity of short DNA strands

As we have seen in Section 2.1.1 controlling the diffusivity of the activator is not straightforward, and it has been achieved only in a few cases. A system that is capable of pattern formation in which the diffusivity of the activator and inhibitor species can be methodically tuned is needed. We believe that the PEN-DNA toolbox is such system, and the achievement of tuning diffusivity will open the possibility of engineering Turing patterns in a rational manner.

In the PEN-DNA toolbox, the activator and inhibitor are short DNA strands as we have described in Chapter 1. Our goal is to search for an experimental approach that allows us to reduce the diffusion coefficient of short DNA strands with a specific sequence. Such methodology must be compatible with the PEN-DNA toolbox, in other words, it must not negatively interfere with the enzymatic machinery of the toolbox. In this section, we first review the literature related to controlling the diffusivity of short DNA strands. Subsequently, we present our experimental approach.

2.2.1 DNA covalently attached to polyacrylamide gels

Allen et al. [50] developed a methodology to control the mobility of a desired DNA strand by immobilization of a DNA binding partner in a polyacrylamide-DNA gel. The binding partner templates are acrydite-modified DNA oligonucleotides. This modification allows their incorporation into the polyacrylamide gel matrix during polymerization of the gel. Figure 2.5 shows how the authors use DNA base-paring to control the hybrization degree of a short DNA strand (**L**) to the binding partner (***B**). The hybridization reaction is favored by increasing the number of paired bases, which increases the Gibbs free energy (-ΔG°) of the reaction. Their experiment was carried out as follows: the immobilized binding partner is evenly distributed in the gel, then the **L** strand is loaded into the gel. In a reference experiment, the ***BL** complexes are also loaded into a gel without immobilization. The diffusivity of the species with an immobilized binding partner is normalized by its diffusivity without immobilization as a function of -ΔG° (Fig. 2.6). Increasing -ΔG° reduces the mobility of **L**. If we take the last point from the plot in Fig. 2.6 to be $\mu/\mu_{native} \sim 0.125$, we can calculate a maximum reduction of diffusivity of 8 fold.

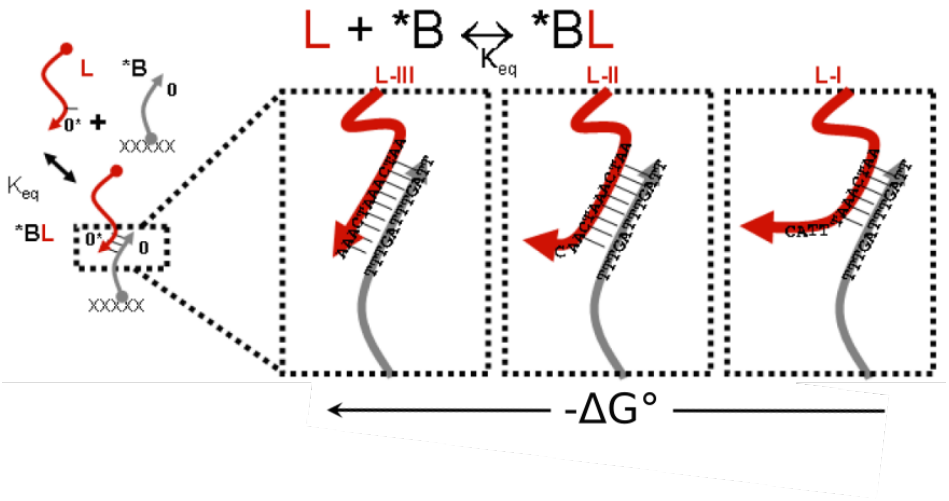

Figure 2.5 – **Controlled hybridization by controlling base-pairing of DNA strand L to its immobilized binding partner (*B).** The xxxx on ***B** indicate its immobilization. Increasing the number of paired bases increases the Gibbs free energy (-ΔG°) of the hybridization reaction. This sketch was taken from [50].

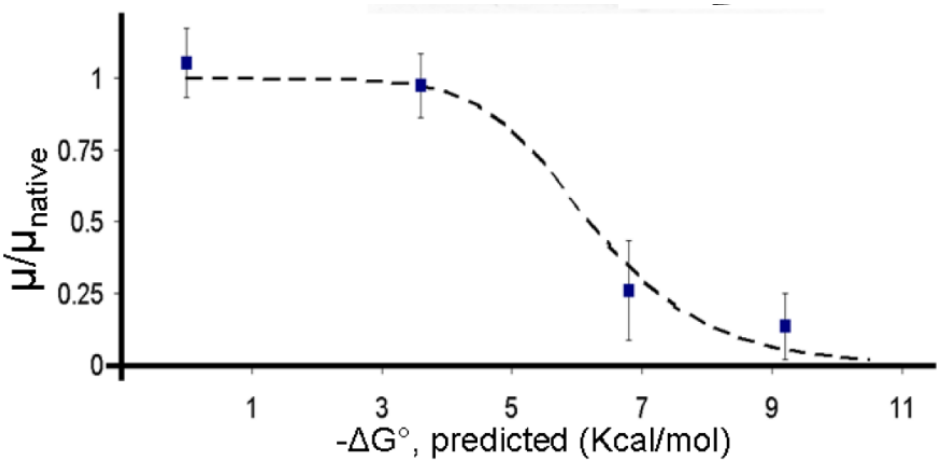

Figure 2.6 – **Diffusivity of a DNA strand decreases with the -ΔG° of complex formation with an immobilized DNA partner.** The y-axis is the fraction between the mobility from binding to immobilized partner and the mobility without immobilization. This figure was taken from [50].

2.2.2 Strategy to control the diffusivity of DNA in the PEN-DNA toolbox

Anton Zadorin in our group profited from the fact that a PEN-DNA autocatalyst A needs to bind to its template T (Fig. 2.7) to control its diffusivity. Indeed if T is attached to a hydrodynamic drag (Fig. 2.8) the diffusivity of the A:T will be similar to that of the T. Using this idea, Zadorin et al. [29] utilized triton X-100 micelles of 5.5 nm in radius as hydrodynamic drags. Templates had a cholesteryl modification on their 3' (Table 2.1). The templates interacted with the micelles through hydrophobic interactions between the chrolesteryl and the micelles. This resulted in the reduction of the mobility of the template (D_{T}), therefore, decreasing D_{eff}. In this strategy the interactions with the micelles were not permanent, additionally, the micelles, themselves, were mobile. Yet, this strategy achieved a reduction of the diffusion coefficient of up to 2.7 fold. In this chapter we build upon the work of Zadorin et al. [29] by using completely immobilized templates to control diffusion.

Table 2.1 – **Results obtained by Zadorin et al. [29].** Estimated hydrodynamic radius, R_h, measured diffusion coefficient, D_i, growth rate, $r'(0)$, front velocity, v, and an inferred diffusion coefficient associated to the front propagation, $D_{eff}(0)$. Template concentration 200 nM, pol = 16 U/mL, nick = 300 U/mL, 10 g/L triton X-100. All measurements were performed at 38°C. Where applicable, values are accompanied by the confidence interval with the confidence probability of 0.95. The intervals are calculated for samples of n = 5 both for $r'(0)$ and v, $D_{eff}(0)$ was treated as a function of these variables.

Species	$\mathbf{R_h}$ (nM)	$\mathbf{D_i}$ ($10^3 \mu m^2 min^{-1}$)	***r'(0)*** ($10^{-2} min^{-1}$)	**v** ($\mu m\ min^{-1}$)	$\boldsymbol{D_{eff}}$**(0)** ($10^3\ \mu m^2\ min^{-1}$)
A	-	16 ± 3	-	-	-
T:trit	1.5[1]	10.7 ± 0.7[2]	7.7 ± 1.3	65 ± 5	14 ± 3
T-ch:trit	5.5[3]	4.0 ± 0.3[4]	7.8 ± 0.5	40 ± 4	5.1 ± 1.1

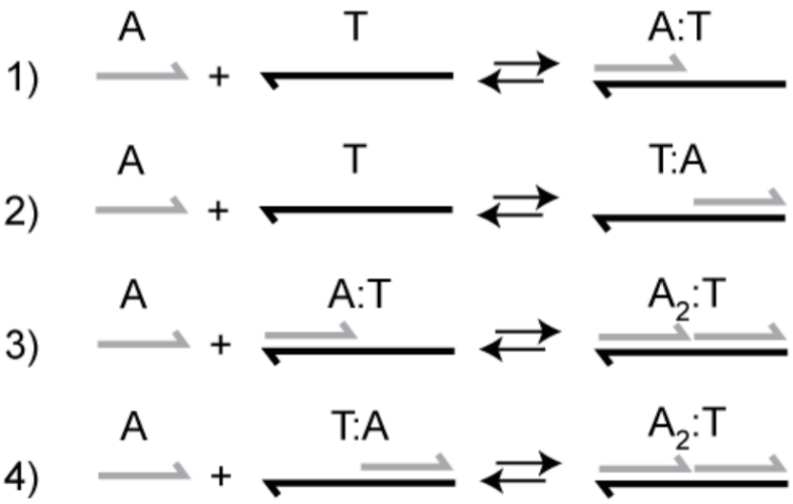

Figure 2.7 – **DNA-DNA hybridization reactions of species A to its template T.** In the PEN-DNA toolbox autocatalytic templates have identical sequences in the input and output site.

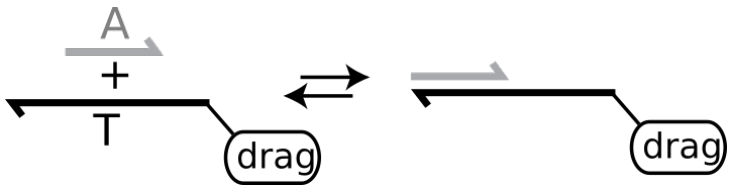

Figure 2.8 – **Sketch of the diffusion control strategy.** The template (T) is attached to a hydrodynamic drag, while the active species (A) reversibly hybridizes to it.

Let's now introduce a model to evaluate the effective diffusivity of an autocatalytic species in the presence of its template. Species A can be free or bound to T, and at equilibrium the effective diffusion coefficient of A depends on all the species involved (Fig. 2.7)

$$D_{eff}(A) = \eta_{\mathrm{A}} D_{\mathrm{A}} + \eta_{\mathrm{A:T}} D_{\mathrm{A:T}} + \eta_{\mathrm{T:A}} D_{\mathrm{T:A}} + \eta_{\mathrm{A_2:T}} D_{\mathrm{A_2:T}}, \tag{2.17}$$

where A is the concentration of species A. And η_{i} and D_{i} are, respectively, the molar fraction and diffusivity of the species i.

If $D_{\mathrm{T}} < D_{\mathrm{A}}$ it is reasonable to expect that $D_{\mathrm{A:T}} \approx D_{\mathrm{T:A}} \approx D_{\mathrm{A_2:T}} \approx D_{\mathrm{T}}$, thus

$$D_{eff}(A) \approx \eta_{\mathrm{A}} D_{\mathrm{A}} + (\eta_{\mathrm{A:T}} + \eta_{\mathrm{T:A}} + \eta_{\mathrm{A_2:T}}) D_T. \tag{2.18}$$

Equation (2.17) tells us that if we want to reduce $D_{eff}(A)$ we must decrease the effective diffusivity of the template. Although all the species in Fig. 2.7 should in principle be considered, at low concentrations[5] of A we can consider only reaction (1) and (2) in Fig. 2.7,

$$\mathrm{A} + \mathrm{T} \underset{k_d}{\overset{k_a}{\rightleftharpoons}} \mathrm{A:T} \tag{2.19}$$

$$\mathrm{A} + \mathrm{T} \underset{k_d}{\overset{k_a}{\rightleftharpoons}} \mathrm{T:A}$$

where K_d is the dissociation constant. We assumed that hybridization of A in the input and output side of T has identical K_ds. Because we have considered that both reactions have identical K_d, then the concentrations $A:T = T:A$, which we can group as a single complex C of concentration $C = 2A:T$. We thus have,

$$\eta_{\mathrm{A}} + \eta_{\mathrm{C}} \simeq 1, \tag{2.20}$$

where η_{C} is the molar fraction of C. Using the definition in Eq. (2.20), Eq. (2.17)

[5] This is the case at the edge of a traveling front.

becomes,

$$D_{eff}(A) \approx \eta_{\mathrm{A}} D_{\mathrm{A}} + (1-\eta_{\mathrm{A}}) D_{\mathrm{C}}. \tag{2.21}$$

In this context η_A is defined as,

$$\eta_{\mathrm{A}} = \frac{A_{tot} - C}{A_{tot}}, \tag{2.22}$$

where A_{tot} is the combined concentration of free and bound A. Combining both equilibrium reactions from Eq. (2.19) yields,

$$\frac{K_d}{2} \approx \frac{(A_{tot} - C)(T_0 - C)}{C}, \tag{2.23}$$

where T_0 is the initial template concentration. If T_0 is much larger than A_{tot}, therefore $T_0 \gg C$. Then, we can simplify Eq. (2.23) to,

$$\frac{K_d}{2} \approx \frac{(A_{tot} - C) T_0}{C}. \tag{2.24}$$

Solving for C in Eq. (2.24) gives,

$$C \approx \frac{A_{tot} T_0}{T_0 + \dfrac{K_d}{2}}. \tag{2.25}$$

This definition of C can be substituted into Eq. (2.22),

$$\eta_{\mathrm{A}} \approx \frac{K_d}{2T_0 + K_d}. \tag{2.26}$$

Then, to get an approximation of the diffusivity that can give us an insight on what physical parameters are important we substitute in Eq. (2.26) into Eq. (2.21),

$$D_{eff}(0) = \frac{K_d}{2T_0 + K_d} D_{\mathrm{A}} + \frac{2T_0}{2T_0 + K_d} D_{\mathrm{T}}. \tag{2.27}$$

The diffusion coefficient of free A cannot be changed. Thus, from Eq. (2.27) reducing the effective diffusivity of A is done by reducing the diffusivity of the template D_T.

2.2.3 Our strategy: porous and non-porous microparticles to control the diffusivity of DNA in the PEN-DNA toolbox

Here, we discuss our strategy to tune the diffusivity of the autocatalytic species A. Our approach allows us to test several technologies. For this reason, templates are biotinylated and linked to different substrates via streptavidin-biotin binding (Fig. 2.9). As discussed in the previous paragraph, we expect the diffusivity of A to be controlled by the hybridization to its template. Primarily, we tested 200 nm diameter magnetic beads and 34 µm diameter crosslinked agarose beads, but we also considered an oil-in-water emulsion with oil droplets of 4 µm in diameter (Table 2.2).

These three different drags were considered for several reasons. First because they cover a quite large range of sizes (2 orders of magnitude) and because of their low diffusivities. Second because they are physiochemically very different and one objective of our work (as it will be shown in Chapter 3) was to explore the behaviour of the PEN-DNA toolbox with different materials. Indeed the magnetic beads could be in the future used to control the position of the template-bound beads with an external magnetic field. Magnetic beads and microdroplets are non-porous to DNA and enzymes, while agarose beads are, which possibly has an impact in the diffusion of DNA. Moreover, droplet size can be modified and the streptavidin on their surface can move and concentrate on some areas, in contrast with the magnetic beads where streptavidin is homogeneously distributed.

If they are homogeneously dispersed in the solution, in the case of the magnetic beads and the oil droplets, the effective diffusion of A is given by Eq. (2.27). This is fundamentally the same strategy as the one covered in Section 2.2.2 since the templates are attached only to the surface of the supports. The beads and the droplets act as molecular drags that reduce the diffusivity of the template. We expect a larger reduction of diffusivity of A, than using the 5-nm triton X-100 micelles (D_T = 4000 $\mu m^2 min^{-1}$), because of the smaller diffusion coefficient of the magnetic beads (D_T = 600 $\mu m^2 min^{-1}$) and the oil droplets (D_T = 30 $\mu m^2 min^{-1}$). We did not have the opportunity to test in diffusion control the oil droplets due to time limitations, thus

we leave this open for future research.

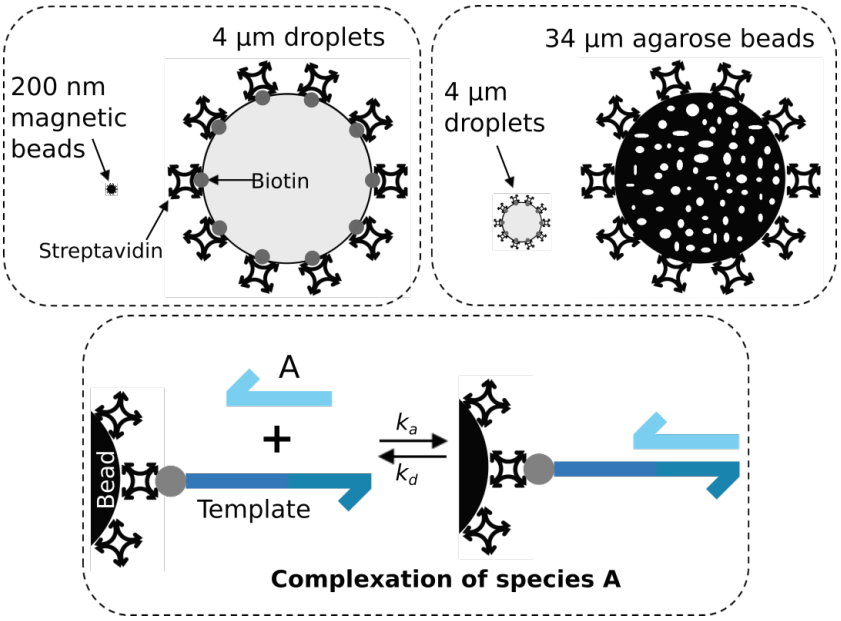

Figure 2.9 – **Biotinylated templates can be attached to streptavidin-coated magnetic beads, oil droplets and agarose beads.** Superparamagnetic beads (ademtech streptavidin *plus*), lipid-stabilized emulsion droplets [51], and crosslinked agarose (Sepharose GE Healthcare) beads are, respectively, 200 nm, 4 µm and 34 µm in diameter. Complexation of A is formed by the hybridization to its template strand.

Table 2.2 – **Physical parameters of magnetic beads, oil droplets and agarose beads.** Diffusion coefficients were estimated from van Ommering [52] for the (‡) magnetic beads at 40°C and from Feng et al. [51] for the (†) droplets at 25°C.

	Magnetic beads	**Droplets**	**Agarose beads**
Diameter (µm)	0.2	4	34
Porous	No	No	Mesoporous
Beads/µL in stock	1.2×10^9	1.9×10^7	1.5×10^4
Binding sites/bead	4.2×10^3	5.2×10^6	1.2×10^{10}
Diffusivity ($\mu m^2 min^{-1}$)	$\sim 600^{\ddagger}$	$\sim 30^{\dagger}$	~ 0

2.2.4 Theoretical aspects of diffusion in packed agarose beads

The templates within the agarose beads have no mobility, and if they are homogeneously distributed we can set Eq. (2.27) to,

$$D_{eff}(0) = \frac{K_d}{2T_0 + K_d} D_{\mathrm{A}}. \tag{2.28}$$

However, we cannot approximate the distribution of templates within agarose beads that are discretely positioned as a homogeneous system. The diffusivity reduction using templates attached to agarose beads needs a different analysis. This leads to packing agarose beads as closely as possible to be closer to such a homogenous system. To understand such system we will develop next a model based on the geometrical distribution of closely packed agarose beads. We have two regions of distinct diffusivity in such system. We see in Fig. 2.10 that even though beads are closely packed, regions without beads appear at the interfaces. Templates are immobilized within the agarose beads (inside region), but in the outside region there are no templates.

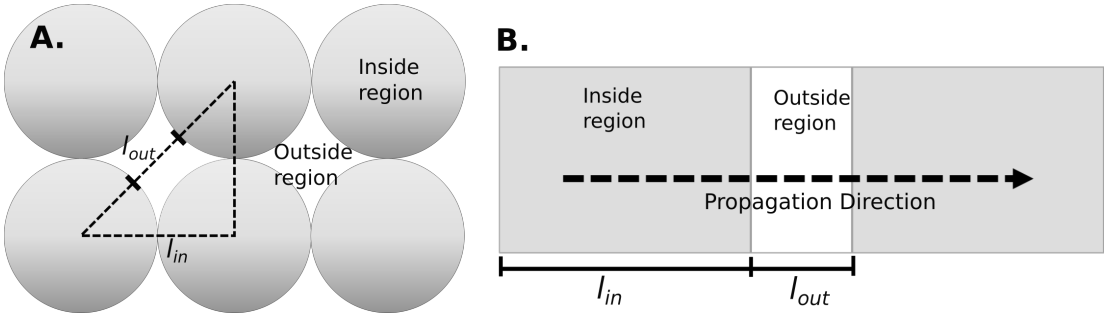

Figure 2.10 – **DNA species diffuse differently in the inside and the outside regions of packed agarose beads. (A)** Sketch of packed beds with labeled regions. l_{in} and l_{out} are characteristic diffusion lengths in the inside and outside regions. **(B)** A wavefront of DNA species travels through inside and outside regions of the beads.

Thus, A diffuses differently in these two regions. In this case, the average diffusion coefficient ($D_{\langle t \rangle}$) depends on the fraction of the time (χ_τ) that A spends on the inside region, where the effective diffusion is D_{in}, or in the outside region, where the effective diffusion is D_{out}. We have

$$D_{\langle t \rangle} = \chi_{\tau_{in}} D_{in} + \chi_{\tau_{out}} D_{out} \tag{2.29}$$

$$\chi_{\tau_{in}} = \frac{\tau_{in}}{\tau_{in} + \tau_{out}}, \quad \chi_{\tau_{out}} = \frac{\tau_{out}}{\tau_{in} + \tau_{out}},$$

where $\chi_{\tau_{in}}$ and $\chi_{\tau_{out}}$ are, respectively, the fraction time that A spends in the inside and outside regions. τ is calculated as the characteristic time of diffusion over a length

l_{in}/l_{out}, which is the size of each region,

$$\tau_{in} = \frac{l_{in}^2}{D_{in}}, \quad \tau_{out} = \frac{l_{out}^2}{D_{out}}. \tag{2.30}$$

Using the triangle from the sketch in Fig. 2.10 we can determine for each region,

$$l_{in} = 2r, \quad l_{out} = 2r(\sqrt{2}-1), \tag{2.31}$$

where r is the radius of the agarose beads. Now, we have all the variables to develop a diffusion model for the packed beads, and such equation becomes,

$$D_{\langle t \rangle} = \frac{1+\Upsilon}{\frac{1}{D_{in}} + \frac{\Upsilon}{D_{out}}}, \tag{2.32}$$

where Υ = 3 - $2\sqrt{2} \approx 0.17$. Interestingly, Eq. (2.32) does not depend on the radius of the beads. Thus, this equation applies to any system in which the beads are closely packed. Note that $D_{\langle t \rangle}$ goes to zero if $D_{in} \to 0$.

The diffusivity of the templates is considered zero (i.e. $D_T = 0$) for this system, and D_{out} is the same diffusivity of the free species (D_A). So, the expression for the diffusivity of A inside the beads is Eq. (2.27) without the second term on the right hand side as in Eq. (2.28). Thus, inputting Eq. (2.28) for D_{in} and D_A for D_{out} into Eq. (2.32) gives the effective diffusion equation in packed agarose beads in 2D,

$$D_{\langle t \rangle_{eff}} = \frac{D_\mathrm{A} K_d \Theta}{T_0 + K_d \Theta}, \quad \Theta = (1+\Upsilon)\frac{1}{2} \approx 0.6. \tag{2.33}$$

This results only applies to a two-dimensional (2D) space. If the diffusion coefficient inside the bead is zero and the beads are packed in a 2D space we cannot find a path to go through without passing inside a bead. In a three-dimensional space this is not true as a molecule could find a path through the interfaces of the beads. In the 3D

case the calculation is more complicated [53]. It yields

$$D_{\langle t \rangle} = \frac{\pi}{4} D_y + \left(1 - \frac{\pi}{4}\right) D_{in}, \tag{2.34}$$

where

$$D_y = \frac{2 D_{in} D_{out}}{D_{in} - D_{out}} \left(\frac{D_{in}}{D_{out} - D_{in}} Ln\left(\frac{D_{in}}{D_{out}}\right) - 1 \right) \tag{2.35}$$

when $D_{in} \to 0$ and $D_{\langle t \rangle} \to 0.2\ D_{out}$.

In this experimental setting, increasing T_0 or decreasing K_d decreases $D_{\langle t \rangle_{eff}}$ sigmoidally. Interestingly Eq. (2.33) is very similar to Eq. (2.28), which is in fact the case of complete immobilization with homogeneous (ideal case) distribution of templates. At $\Theta = 0.5$ Eq. (2.33) becomes Eq. (2.28) meaning that the existence of outside regions are just slightly less favorable for reducing diffusivity. This difference is small enough to conclude that it is worth using agarose beads closely packed. Additionally, agarose beads are very attractive because of their experimental advantages: high versatility, quick binding and the possibility of adjusting the density of beads.

2.2.5 Relating the front propagation velocity to the diffusivity

Throughout this chapter we have chosen to measure the effective diffusivity of an autocatalyst by measuring its front propagation velocity. The reaction-diffusion equation for an autocatalytic species A is,

$$\frac{\partial A}{\partial t} = R(A) + \frac{\partial}{\partial x}\left(D_{eff}(A) \frac{\partial A}{\partial x} \right), \tag{2.36}$$

where $R(A)$ is the reaction term. As demonstrated by Zadorin et al. [29], provided that the function $R(A)$ respects certain conditions[6], Eq. (2.36) has a traveling front solution

[6] (a) Bounded growth, i.e., there exists $A_{max} > 0$ such that $r(A_{max}) = 0$, (b) $r(0) = 0$, (c) $r'(0) > 0$, and on $(0, A_{max})$ (d) $r(A) > 0$, (f) $r'(A) < r'(0)$.

$A(x,t) = A(x - vt)$ which minimal velocity, v, is given by

$$v = 2\sqrt{R'(0)D_{eff}(A)}, \tag{2.37}$$

where $R'(0)$ is the derivative of R at $A = 0$[7]. This is known as the velocity of Fisher-KPP [1]. In this chapter we will employ this equation to relate measured values of v to D_{eff}. To do so we need in addition to determine the reaction kinetics $R'(0)$ of our DNA-based reaction system. We spatialize the system by generating propagating fronts of species A. As a result D_{eff} will be calculated by

$$D_{eff} = \frac{v^2}{R'(0)}. \tag{2.38}$$

We note that Eqs. (2.37) and (2.38) are only valid for *pulled* propagating fronts [54]. Pulled fronts are those whose dynamics are controlled by what happens at the tip of the front where $A \to 0$. Fisher-KPP fronts are a class of pulled fronts. *Pushed* fronts, in contrast, are controlled by the dynamics behind the front where $A \neq 0$. For pushed fronts only the scaling $v \sim \sqrt{R'(0)D_{eff}(A)}$ holds. As a rule of thumb, fronts due to monostable kinetics tend to be pulled while those relying on bistable kinetics maybe expected to be pushed. Despite this fundamental difference, in the next sections we will use Eqs. (2.37) and (2.38) for analyzing fronts due to monostable and bistable networks. We should consider them just as scaling laws though.

2.3 The bistable network and its experimental procedure

Zadorin et al. [29] encountered a problem of measuring the velocity of propagation of a simple PEN-DNA autocatalyst: self-start. An autocatalyst template with pol and nick but without its input finds the way to self start and still produce an autocatalytic growth of the input. This is very annoying for generating traveling fronts because the system grows uniformly across space before a front is observed. We selected a reaction network that displays bistability since this property allows us to eliminate

[7] We remind the reader that this is the case at the edge of a traveling front.

self-start, which is the self-triggering of autoreplication in the absence of an input. This DNA bistable network designed by our collaborator Y. Rondelez is composed of an autocatalytic node and a repression node Fig. 2.11. The activation node involves the autocatalytic production of the species A. In the repression node, the activation species is captured by a repressor template and converted into a waste species (W). Both, species A and W can be eliminated by exo.

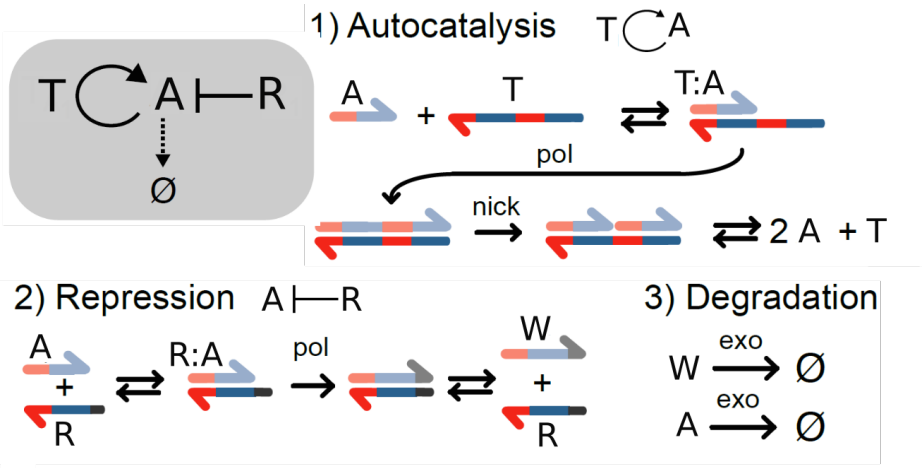

Figure 2.11 – **The mechanism of the DNA bistable network.** This network is composed of an autocatalytic node and a repression node with enzymatic degradation. ***Activation.*** The activation species (A) binds to the activation template (T). The T:A complex is extended by the polymerase (pol). Subsequently, the double strand complex is cut by the nickase (nick) enzyme producing two As. ***Repression.*** Activation species is captured by the repressor template. The complex R:A is extended by pol producing the waste species (W). ***Degradation.*** Activation species and waste species are degraded by the exonuclease (Exo) enzyme.

The bistability arises from the fact that the activation species has a higher affinity towards binding to the repressor template. This results in the repression node to be a more favored reaction. Then, we can expect that A grows sigmoidally only when the activation growth rate surpasses the repression rate.

2.3.1 DNA oligonucleotides

For the most part of this chapter we utilize two independent sets of DNA sequences (Table 2.3) that can be put together into a bistable network. We named these two

independent sets: bistable network 1 and 2. Each network is composed of: an activation species (A_i), an activation template (T_i), and a repressor template (R_i). All the templates carry a biotin modification except T_{2N} and R_{2N}. These non-biotinylated templates bear the same design as T_2 and R_2, so they are not treated as a different network. The absence of biotin allows us to test for potential differences in the behavior of biotinylated sequences and non-biotinylated ones.

Table 2.3 – **DNA sequences of the two bistable networks.** The two independent bistable networks are numbered 1 and 2. Each network contains its own set of autocatalytic (A_i) species, autocatalytic template (T_i), and repressor template (R_i). All templates contain a biotin covalently linked, except T_{2N} and R_{2N}. Phosphorothioate backbone modifications are indicated by an asterisk (*).

Network	**Name**	**Template sequence 5'→3'**
Bistable network 1	A_1	CATTCAGGATCG
	T_1	bt-*A*A* G*ATCCTGAATGCGATCCTGAAT
	R_1	bt-AAAAAACGATCCTGAATG
Bistable network	A_2	CATTCTGACGAG
	Biotinylated	
	T_2	C*T*C*G*TCAGAATGCTCGTCAGAAAAAAA-bt
	R_2	T*T*T*T*CTCGTCAGAATGAAAAA-bt
	Non-biotinylated	
	T_{2N}	C*T*C*G*TCAGAATGCTCGTCAGAA
	R_{2N}	T*T*T*T*CTCGTCAGAATG

As we can see from the hybridized structures in Fig. 2.12 (Page 79) the design in the bistable network 1 has one unpaired base on A_1 in the T_1:A_1 structure, but no unpaired bases in R_1:A_1. In the case of the bistable network 2, two bases in T_2:A_2 are unpaired instead of one. R_2:A_2 has no unpaired bases on A_2. The absence of the unpaired bases in R_i:A_i results in the preferential hybridization of A_i to R_i rather than to T_i. This preferential affinity towards R_i:A_i can be reprogrammed by changing the number of unpaired bases. To estimate the affinity of A_i to the templates, we calculate the thermodynamic parameters for the hybridization reactions between A_i/T_i and A_i/R_i (Table 2.4). We can see in this table that the hybridization reactions A_i/R_i have higher melting temperatures and more negative changes in enthalpy due to the absence of unpaired bases, so they are slightly more favored than the A_i/T_i reactions.

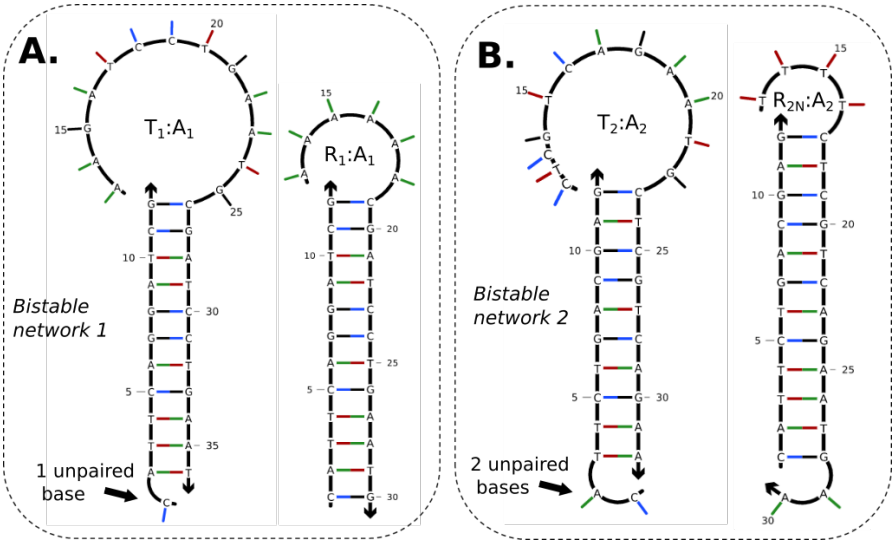

Figure 2.12 – **Double strand DNA structures for the bistable (A) network 1 and (B) network 2.** The structures were calculated using the NUPACK web application [55]. The parameters were set at 38°C, Na^{+} = 0.05 M, and Mg^{++} = 0.006 M.

Table 2.4 – **Thermodynamic parameters for the hybrization reactions.** The melting temperature (Tm), ensemble enthalpy (ΔH), and ensemble entropy (ΔS) were calculated using DINAMelt web server [56]. The concentrations of A_i, T_i, and R_i were 1 µM, and Na^{+} = 0.05 M and Mg^{++} = 0.006 M.

	Tm (°C)	**ΔH (kcal/mol) at 38°C**	**ΔS (cal/mol/K) at 38°C**
A_1/T_1	48.2	-94.1	-293.6
A_1/R_1	49.1	-103.6	-322.0
A_2/T_2	50.6	-101.9	-316.9
A_2/R_2	52.2	-105.0	-324.9

2.3.2 Determination of the dissociation constant

As we discussed in Section 2.2.2, the dissociation constant (K_d) has a strong influence in the effective diffusivity. Here, we characterize K_d in the formation of the double strand complexes T_1:A_1 and R_1:A_1 at different temperatures. We evaluate this formation during DNA-DNA hybridization reactions at equilibrium.

The experiment consisted of titrating R_1 = 50 nM with A_1 = 0-400 nM (Fig. 2.13). This same protocol was repeated to titrate T_1 = 50 nM (Fig. 2.14). The green fluorescence level increases by increasing A_1 since the concentration of double strand

DNA increases. We use Eq. (1.3) to relate the fluorescence to the concentration of A_1, and Eq. (1.5) to extract the dissociation constant (K_d) by fitting the data in Figs. 2.13 and 2.14. At every temperature K_d is larger for T_1/A_1 than for R_1/A_1. This means that the formation of the R_1:A_1 complex is more likely than the T_1:A_1 complex.

For our system to maintain bistability the K_d of the activator template T_1 must be larger than that of the repressor template R_1. The experiments here tells us that indeed K_d is larger for T_1:A_1 in a temperature range of 37-45°C. Secondly, we have obtained an experimental value of K_d that can be used to estimate the D_{eff}. We expect that the templates in the bistable network 2 have similar K_d values since their thermodynamic parameters are comparable (Table 2.4).

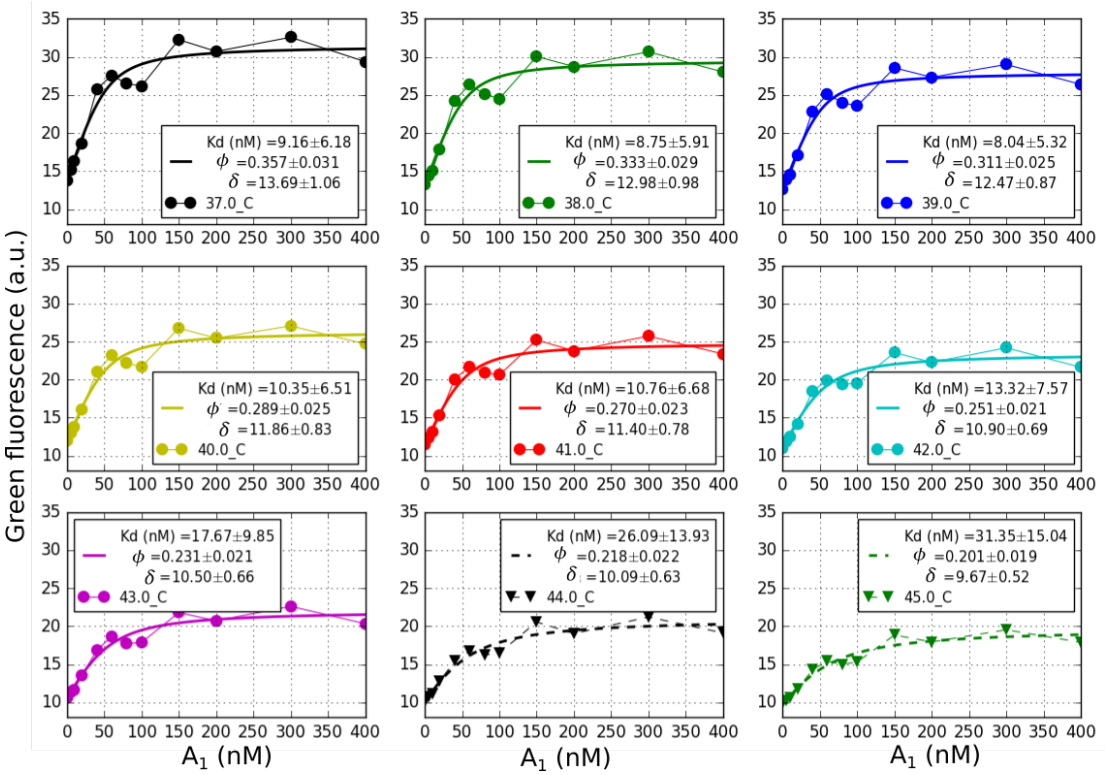

Figure 2.13 – **Determination of the dissociation constant of R_1:A_1 complex.** Isothermal titration of R_1 = 50 nM was titrated with A_1 = 0-400 nM at different temperatures. The data was fitted to Eq. (1.5) to determine the dissociation constant (K_d).

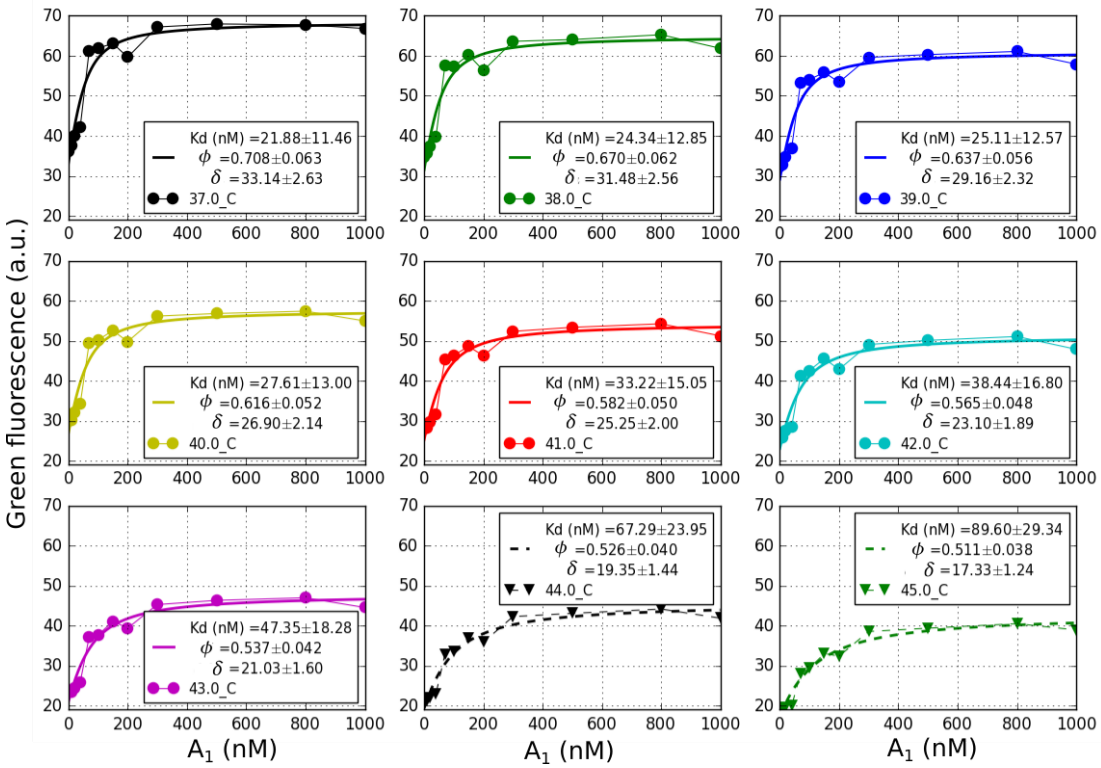

Figure 2.14 – **Determination of the dissociation constant of T_1:A_1 complex.** Isothermal titration of T_1 = 50 nM was titrated with A_1 = 0-1000 nM at different temperatures. The data was fitted to Eq. (1.5) to determine the dissociation constant (K_d).

2.3.3 Experimental procedure

In this chapter we use the Predator-Prey buffer listed in Table 1.3. Subsequently, a reaction mixture is prepared containing the buffer and the required enzymes. For the most part in this chapter, the concentrations of the enzymes are as reported in Table 2.5, unless otherwise stated. We also included in the buffer 5% v/v of EvaGreen

Table 2.5 – **Enzyme concentration used in this chapter.** The enzyme concentrations are reported in dimensionless formats: $exo_n = exo/exo_0$ with exo_0 = 12.5 nM, $pol_n = pol/pol_0$ with pol_0 = 16 U/mL, and $nick_n = nick/nick_0$ with $nick_0$ = 80 U/mL. The concentrations listed here are the final values in the reaction tube.

Enzyme	Concentration
Exonuclease ttRecJ (exo)	0.5
Bst large fragment DNA polymerase (pol) (NEB)	1
Nb.BsmI nicking enzyme (nick) (NEB)	5

(Biotium) dye to monitor the concentration of the DNA species. Kinetic experiments were performed in a real-time PCR machine (Biorad CFX96 or Qiagen Rotor-Gene Q) in plastic PCR tubes. Front propagation experiments were conducted in borosilicate glass capillaries (VitroCom) of 0.5 x 0.5 mm (outside dimensions) and monitored in an inverted Zeiss Axio Observer Z1 microscope (see the microscope specifications in Page 201). To perform a front experiment, a glass capillary was filled with the reaction solution containing the autocatalytic and the repressor templates, the enzymes and the buffer but not containing the input species A (Fig. 2.15). Then, to trigger the front of species A, 2 µL of the reaction solution containing A = 400 nM were added to one of the sides of the capillary.

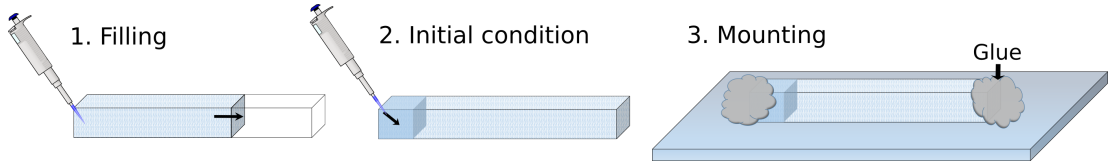

Figure 2.15 – **Setting up a front propagation experiment in a glass capillary. 1.** The capillary is filled with the reaction buffer and templates. **2.** An initial condition is injected only on one side. The initial condition is the reaction solution additionally containing $A_{(t=0)}$ = 400 nM. **3.** The capillary is mounted on a glass slide and its open ends shut with two part-epoxy adhesive (Araldite).

2.4 Reactions with templates diffusing freely in solution

This section consists of two major subsections: (1) characterization of the kinetics of activation species and (2) characterization of the front propagation of activation species. Here we present reactions of the two DNA-based bistable networks in which the templates diffuse freely in solution.

2.4.1 Kinetics of the DNA bistable network

Autocatalytic DNA nodes tend to suffer from self-start. To eliminate the self-start from the activation node, we use the repressor node of the bistable network. Afterwards, we characterize the kinetics at bistable conditions by determining the reaction rate law.

Lastly, we compare the kinetics in plastic PCR tubes to the kinetics in glass capillaries.

2.4.1.1 Repressor node eliminates self-start

First, we test the activation node, and simultaneously, we assay its self-start (Fig. 2.16). The sigmoidal growth of A_2 species starts by adding an initial concentration of A_2, but it is also self-started after 200 min. Increasing R_2 to 5 nM delays the self-start (blue curve). The self-start is eliminated at R_2 = 10 nM. Tuning the repressor template concentration in these bistable networks successfully eliminates self-start.

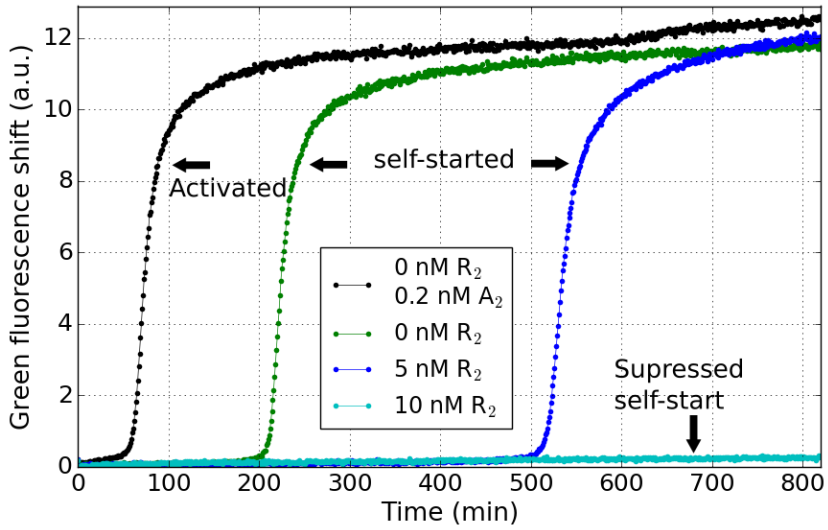

Figure 2.16 – **Increasing the concentration of repressor template R_2 eliminates self-start.** The sigmoidal growth of the A_2 activation species was triggered with 0.2 nM A_2 or self-started. The reaction was performed at 45°C and T_2 = 100 nM.

We also tested the elimination of the self-start on the T_1 template by increasing R_1 (Fig. 2.17A). Self-start at R_1 = 0 nM starts around 90 min, which is delayed by increasing R_1. From Fig. 2.17B we determine that the time delay in the reaction starting time is somewhat linear before the self-start is completely eliminated at R_1 = 30 nM.

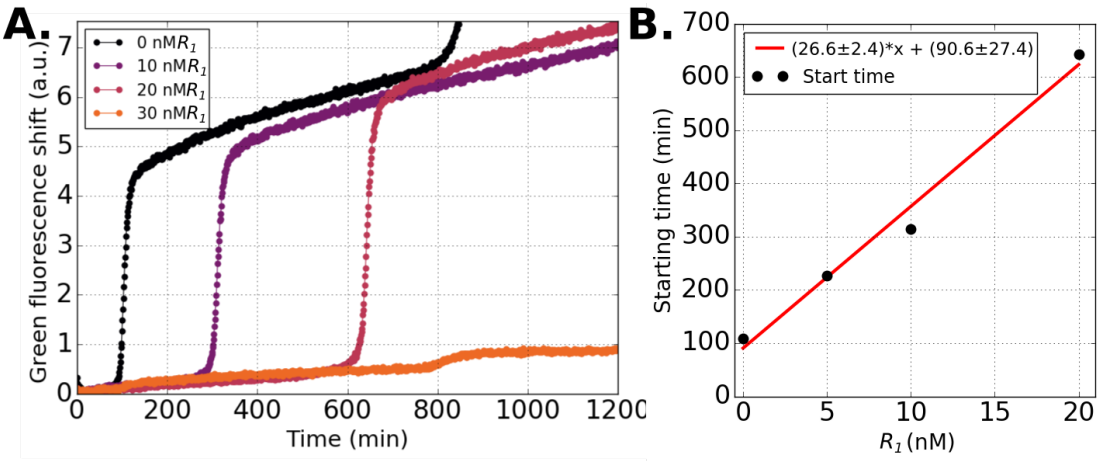

Figure 2.17 – **Increasing the concentration of repressor template R_1 eliminates self-start. (A)** The sigmoidal growth of the A_1 species was triggered with $A_{1(t=0)}$ = 0.2 nM or self-started. **(B)** Linear fit of the starting time as a function of R_1. The reaction was performed at 45°C, streptavidin = 40 nM, and T_1 = 100 nM.

2.4.1.2 DNA-based reaction system at bistable conditions

We are interested in characterizing the bistability of these networks to later determine the growth kinetics of A_i. The concentration of T_1 was reduced to 50 nM, and in these conditions R_1 = 10 nM suppressed self-start. Then, we tested the bistability of the system at R_1 = 10 nM and T_1 = 50 nM (Fig. 2.18). The OFF state means that there is no sigmoidal growth of A, which can be switched to the ON state by adding an initial concentration of A_1 ($A_{1(t=0)}$).

The bistable networks were designed to work at 45°C, but we were interested in working at a lower temperature to decrease the dissociation constant, K_d, between templates and activation species (Figs. 2.13 and 2.14). First, we determined if our system displays bistability at lower temperatures. Instead of first determining the concentration of R_1 needed to suppress the self-start and then doing the bistability test, we add $A_{1(t=0)}$ = 0.2 nM to the reaction solution and increase R_1 until it suppresses the activation. Figure 2.19 shows this bistability test at 41.1°C and 38.4°C. The activation of A_1 is suppressed with R_1 = 8 nM and R_1 = 16 nM, respectively, at 41.1°C and 38.4°C. Additionally, the autocatalytic growth was compared by extracting a rate growth constant R' (Table 2.6). At R_1 = 0, R' increases 10% by lowering the temperature from

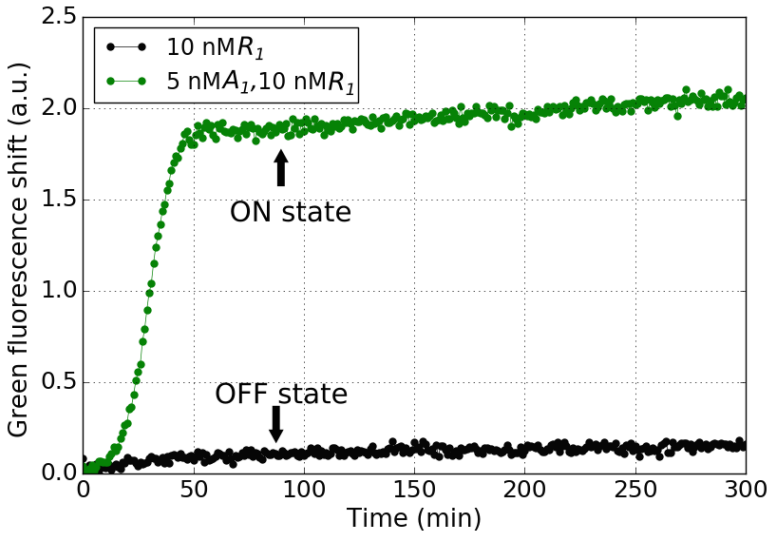

Figure 2.18 – **Illustration of the bistability of bistable 1.** The OFF state can be switched to the ON state by including $A_{1(t=0)}$ = 5 nM in the reaction solution. The reactions were performed at 45°C, R_1 = 10 nM and T_1 = 50 nM.

41.1°C to 38.4°C. Whereas, at 38.4°C increasing R_1 from 0 to 8 nM decreases R' by 1.37 fold.

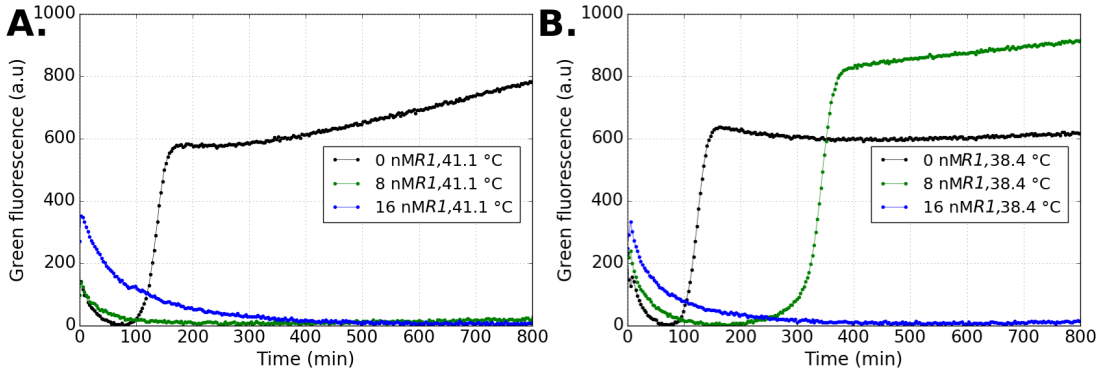

Figure 2.19 – **Bistability at 41°C and 38.5°C.** R_1 was varied from 0-16 nM. The reaction solution contained $A_{1(t=0)}$ = 0.2 nM, T_1 = 50 nM, and streptavidin = 80 nM. The reaction was performed at **(A)** 41°C and **(B)** 38.5°C.

These results demonstrate that although the bistability of this network is designed to function at 45°C, bistability is displayed also at lower temperatures. The robustness of the bistability probably comes from the fact that the difference in the dissociation constant between R_1/A_1 and T_1/A_1 is large enough even at lower temperatures, as we see in the K_d measurements in Figs. 2.13 and 2.14.

Table 2.6 – **Rate growth constant R' at 41.1°C and 38.4°C for bistable system 1 with T_1 = 50 nM.** R's were extracted from the data in Fig. 2.19.

Temperature (°C)	R_1 **(nM)**	R'_{growth} (min^{-1})
41.1	0	0.10
38.4	0	0.11
38.4	8	0.04

2.4.1.3 Determination of the rate order of reactions

To measure the reaction kinetics in the bistable network we perform experiments in which we activate a system at bistable conditions at increasing concentrations of A_1. In Fig. 2.20 we fix the T_1 and R_1, and we vary the initial concentration of A ($A_{1(t=0)}$). The activation occurs above a threshold value of $A_{1(t=0)}$. The activation happens at $A_{1(t=0)}$ = 0.4 nM, and at higher values of $A_{1(t=0)}$ the activation time is reduced.

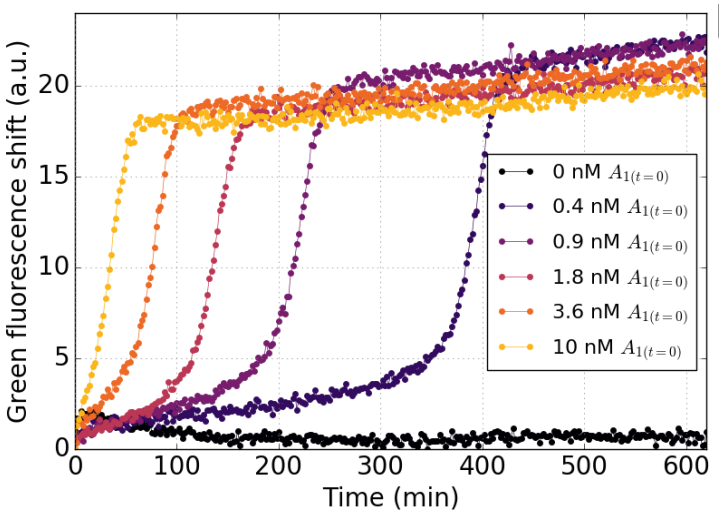

Figure 2.20 – **The sigmoidal activation of A_1 occurs above a threshold.** The initial concentration of $A_{1(t=0)}$ is varied from 0 nM to 10 nM. The reaction was performed at 38.5°C, T_1 = 50 nM and R_1 = 20 nM.

Then, to determine the rate law at these experimental conditions we consider the overall reaction of the activation node: $A \longrightarrow 2A$. We propose testing for first and second order rate. A first order rate law is given by,

$$\frac{dA}{dt} = kA, \tag{2.39}$$

with solution,

$$A(t) = A(t=0)e^{kt}, \tag{2.40}$$

where k is the reaction rate coefficient. We call $t_{1/2}$ the time at which the concentration of A has reached a certain $A_{1/2}$. We have

$$t_{1/2} = \frac{1}{k}\ln(A_{(t=0)}) - \frac{1}{k}\ln(A_{1/2}). \tag{2.41}$$

The time taken by a first order rate law to reach a given concentration scales with the logarithm of the initial concentration.

If the growth kinetics are second order, we have

$$\frac{dA}{dt} = kA^2 \tag{2.42}$$

with solution

$$A(t) = \frac{1}{\frac{1}{A(t=0)} - kt}, \tag{2.43}$$

and thus

$$t_{1/2} = \frac{1}{kA_{(t=0)}} - \frac{1}{kA_{1/2}}. \tag{2.44}$$

To determine what order rate law our data in Fig. 2.20 displays we extract the half-life $t_{1/2}$ for which the fluorescence reaches half its maximum value. In Fig. 2.21 we plot $t_{1/2}$ as a function of $\ln(A_{(t=0)})$ or $\frac{1}{A_{(t=0)}}$ following Eqs. (2.41) and (2.44).

The linear regression fits the second order rate law better than a first order one (except for the point at $1/A(t=0) = 2.5\ \mathrm{nM}^{-1}$, i.e. $A(t=0) = 0.4$ nM). Thus, this indicates that our system follows a second order rate law. From the inverse of the slope in Fig. 2.21B we obtain a reaction rate coefficient of $k = 5\times10^{-3}\ \mathrm{min}^{-1}\mathrm{nM}^{-1}$.

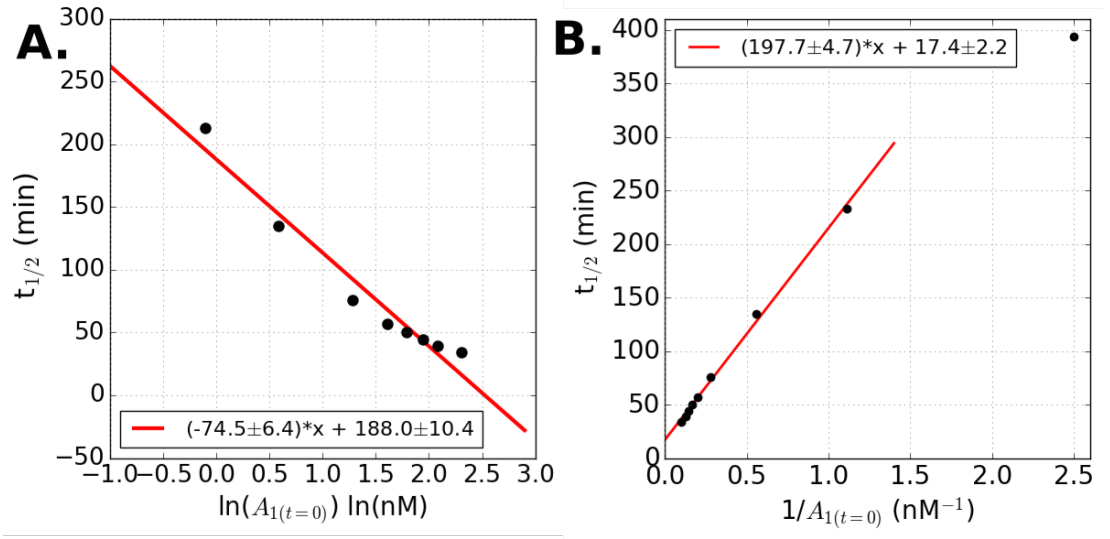

Figure 2.21 – **Testing for (A) first and (B) second order rate laws.** The time in Fig. 2.20 at which A_1 reaches half of maximum growth is plotted as function of **(A)** $\ln(A_{1(t=0)})$ or **(B)** $1/A_{1(t=0)}$.

2.4.1.4 Kinetics in glass capillaries

Once the kinetics of the bistable network were characterized in plastic tubes in the fluorometer, we checked whether the kinetics were similar in the glass capillaries, where the front propagation experiment will be performed. We soon discovered that the reactions in the capillaries lasted for shorter times than in plastic tubes. Here, we present our efforts to find the right experimental conditions to prolong the reactions in the capillaries.

Figure 2.22 shows the autocatalytic growth of A_2 using template T_2 at 45°C with the standard concentration of dNTPs (400 µM). The reactions were carried out simultaneously in a glass capillary and in a plastic tube. The most striking difference is the behavior at long times. In the plastic tube we observe a strong increase in fluorescence that we have interpreted as a parasitic reaction. In the glass capillary the intensity drops to the initial value before increasing again slightly and dropping back to zero. The second difference is that growth is delayed in plastic tubes compared with glass capillaries, although the apparent growth rate is identical as we can see when we normalize the curves and shift the time. Finally, the plateau of fluorescence is really

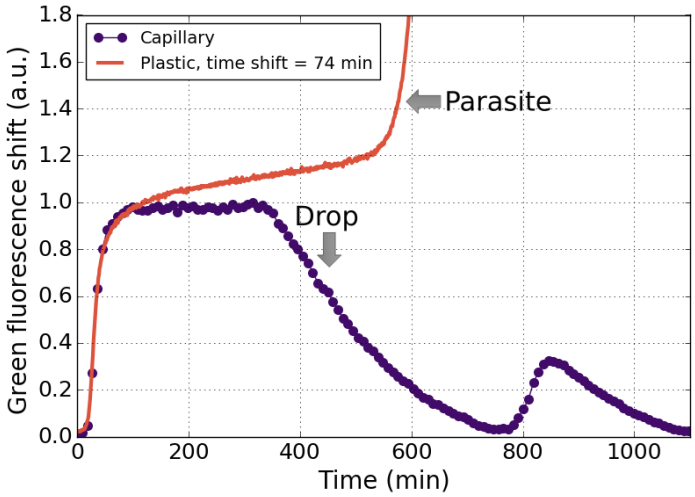

Figure 2.22 – **Autocatalyst growth in a glass capillary and a plastic tube.** The reaction solution was split to simultaneously carry out the reactions in a plastic PCR tube and a glass capillary. The green fluoresce signal was normalized and the time shifted for the plastic tube reaction to superimpose the curves. The reactions were carried out at 45°C.

flat in glass capillaries but it grows linearly in the tubes. The third difference is the emergence of a side reaction (parasite) that produces a parasitic species with high fluorescence in the presence of EvaGreen. The high intensity in fluoresnce indicates the formation of a large amount of double-stranded DNA. Although such parasitic reactions may occur in isothermal amplification schemes [57] and are not uncommon in the PEN-DNA toolbox [35], they tend to appear after more than 500 minutes and do not affect the initial growth kinetics.

These observations suggest that some of the enzymes have a different activity between the capillaries and the tubes. This is probably not the case for pol as the growth rate is similar in both situations (and we know that in our conditions pol is limiting the growth compared to nick). We could hypothesize that either nick or exo is more active. In the first case the autocatalyst turns over faster when it is saturated (on the plateau) and thus dNTPs are consumed rapidly, the decay of intensity will be indicative of an exhausting of the dNTPs.

To test this hypothesis, we increased the concentration of dNTPs (Fig. 2.23A). We see in this plot that all the curves have a similar decay. Since the decay rate seems to be independent of *dNTPs* we conclude that our first hypothesis (increase of the activity of nick consumes dNTPs) is not verified. However, the effect of *dNTPs* is in the initial rate growth, which decreases by increasing *dNTPs*. Additionally, the starting time is delayed by *dNTPs*. For example, at *dNTPs* = 0.8 mM the initial starting time was delayed by around 50 minutes and by more than 100 minutes at *dNTPs* = 1.2 mM. The addition of dNTPs changes the kinetics and does not prolong the reactions in glass capillaries. To make sure this effect on the initial growth rate by the increase of *dNTPs* was not only unique to the glass capillaries, we perform the same reactions in plastic tubes (Fig. 2.23B). We also observed a delay in starting time and a decrease in the initial rate growth.

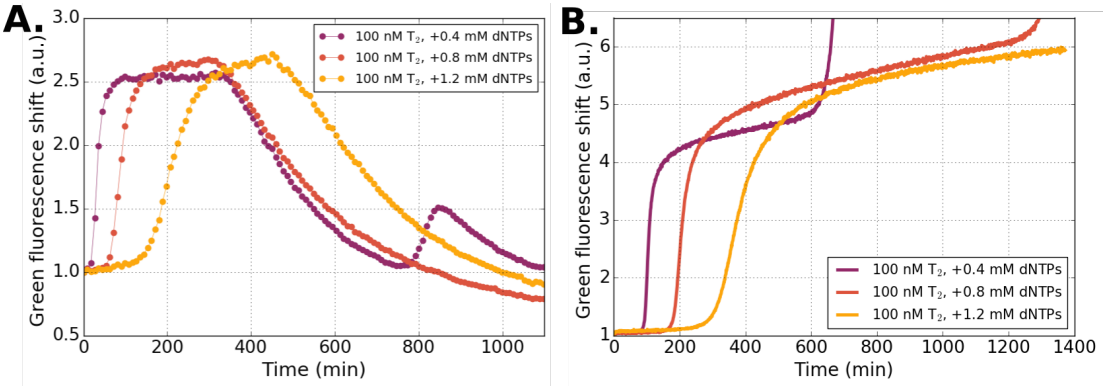

Figure 2.23 – **Effect of *dNTPs* on the reaction time in (A) glass capillaries and (B) plastic tubes.** The green fluoresce signal was divided by its value at time = 0 min. The reactions were carried out at 45°C.

Since the results in Fig. 2.23 do not point to an increase of nick activity, a second hypothesis is that an increase of the exo activity in the capillaries is coupled to strong inhibition of exo in the presence of free template with phosphorothioates in the 5' end. We proposed the following speculative interpretation. This could explain the growth/plateau/decay observed temporal pattern as follows. At initial time the concentration of single stranded T_2 with phosphorothioates in the 5' end is high and exo is completely inhibited by binding to it. As the autocatalyst is produced it binds to T_2 and the concentration of the 5' decreases, and thus exo is activated. At some

point all exo are liberated from the 5' end of T_2 and it happens that degradation > production, the grown state becomes unstable and the signal decays. At this point most of the free 5' ends belong to A_2 and not to T_2 and thus during the decay phase, exo is not inhibited. Later A_2 is so low that all the 5' ends belong to T_2, exo is inhibited again and the system starts to grow again.

Although we could not test this second hypothesis fully, we tested it partially by decreasing the concentration of T_2 in the capillary (Fig. 2.24). From T_2 = 100 nM to T_2 = 50 nM the decay is strongly reduced. This seems to support our second hypothesis.

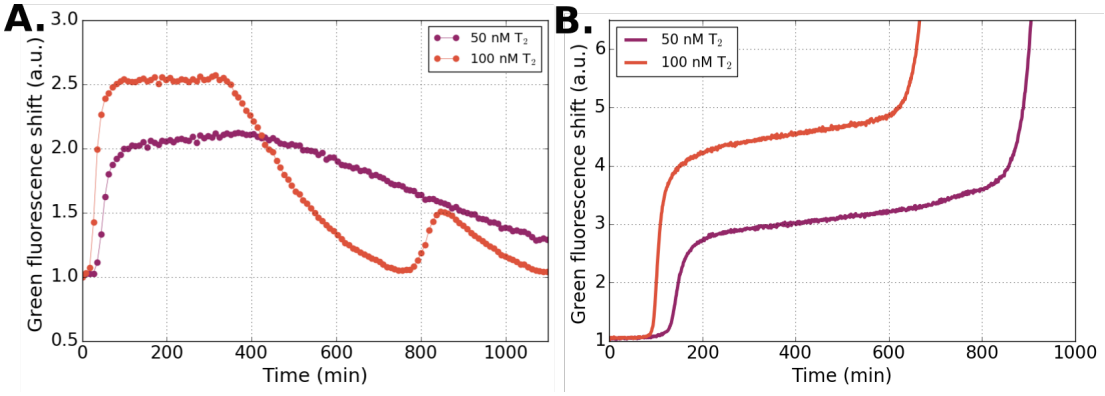

Figure 2.24 – **Effect of T_2 on the reaction time in (A) glass capillaries and (B) plastic tubes.** The green fluoresce signal was divided by its value at time = 0 min. The reactions were carried out at 45°C.

The inhibition of exo with high concentration of template is critical in this system. This could be used in the future to engineer interesting non-linear dynamics. For our purposes of having stable fronts in glass capillaries the lowest concentration of T_2 seems better.

2.4.2 Fronts with templates diffusing freely in solution: Bistable network 2

Here, the bistable network 2, previously discussed in Section 2.4.1, is spatialized in the form of traveling fronts of activation species A_2. Front propagations occur with templates (with steptavidin attached) that diffuse freely in solution in a closed microreactor, thus there is no hydrodynamic flow.

A glass capillary was filled with the reaction buffer containing T_2 = 100 nM and R_2 = 10 nM, and the front propagation triggered with A_2 = 400 nM. The kymograph[8] of this experiment in Fig. 2.25A shows the front of fluorescence due to EvaGreen traveling along a glass capillary. The front propagates from left to right. The front velocity can be extracted by a linear fit through the border between the low and high fluorescence as indicated with the long white arrows. The fluorescence profile along the channel for different times is plotted in Fig. 2.25C to give an idea of the propagation dynamics.

In the top kymograph in Fig. 2.25A the velocity is constant (46.2±2.3 µm min^{-1}) for about 10 mm before slowing down to 39.2±0.6 µm min^{-1}. In a replicate experiment (kymograph in Fig. 2.25B) the front velocity is 49.2±1.8 µm min^{-1}, which is constant over the whole experiment. The initial velocity in Fig. 2.25A and the velocity in Fig. 2.25B are identical within experimental precision. However, we have no explanation for the sudden change in the velocity in Fig. 2.25A. Another variation is that sometimes we observe black regions appearing on the kymograph as the front progresses. We can see these areas where reactions are not sustained in Fig. 2.25B. The appearing time is around 350 minutes. This time agrees well with the duration time at which reactions were sustained in well-mixed conditions in capillaries in Fig. 2.23. Generally, the unsustained reaction areas do not seem to interfere with the front propagation.

Following the conclusion in Section 2.4.1.4 that reducing T_2 may remove the decay of fluorescence generated a front at a lower concentration of T_2 (T_2 = 50 nM and R_2 = 20 nM). In this experiment, the velocity is 35.4±0.2 µm min^{-1} (Fig. 2.26). Self-start occurred on the right hand side of the capillary around 500 min. We can compare experiments from Figs. 2.25 and 2.26 by using Eq. (2.37), in which we can assume that the effective diffusivity of A_2 is the same in both experiments to get the ratio of rate

[8] From now on we will use a kymograph to represent the dynamics of the front. A kymograph is a fluorescence vs time vs space 3D plot. At each time point the fluorescence profiles along the longitudinal axes of the capillary are averaged long the transversal axis to make one horizontal line in the kymograph. Time goes vertically from top to bottom and the distance along the longitudinal axis of the capillary goes horizontally. See Fig. 4.32 for more details.

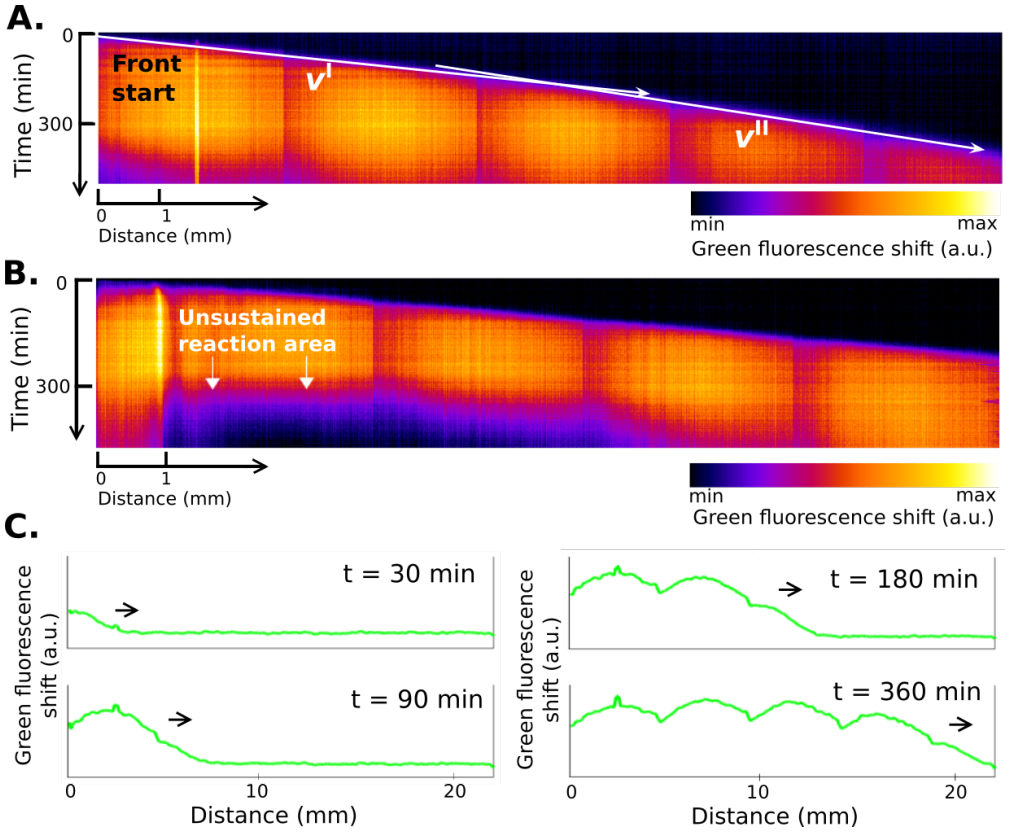

Figure 2.25 – **Front propagation of A_2 with templates (T_2 = 100 nM, R_2 = 10 nM) diffusing freely in solution.** Kymographs of the front propagation of A_2 species. **(A)** The front velocities are $v^I = 46.2 \pm 2.3$ µm min^{-1} and $v^{II} = 39.2 \pm 0.6$ µm min^{-1}. The velocities are obtained by fitting linearly through the edge of low and high fluorescence as the white arrows indicate. **(B)** Replicate experiment with $v = 49.2 \pm 1.8$ µm min^{-1}. **(C)** The front profiles were extracted by plotting the profile across space at different times from the kymograph in (A). The fronts were triggered with 2 µL of reaction solution containing A_2 = 400 nM. The reactions were carried out at 45°C and streptavidin = 100 nM.

growth between these two experiments,

$$\frac{v_1^2}{v_2^2} = \frac{R_1'}{R_2'} = R'_{ratio}. \tag{2.45}$$

With $v_1 = 47.7$ µm min^{-1} and $v_2 = 35.4$ µm min^{-1} we get $R'_{ratio} = 1.8$. This factor is in good agreement with the factor 2 expected from a scaling $R' \sim T_2$ shown by Zadorin et al. [29].

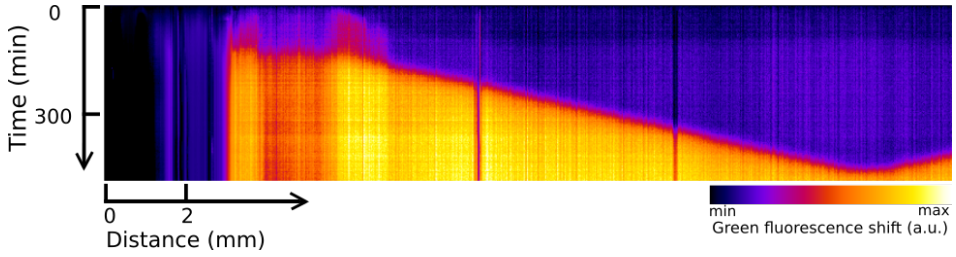

Figure 2.26 – **Front propagation of A_2 with templates (T_2 = 50 nM, R_2 = 20 nM) diffusing freely in solution.** Kymograph of the EvaGreen fluorescence. We found v = 35.4±0.2 µm min^{-1}. The front was triggered with 2 µL of reaction solution containing A_2 = 400 nM. The reactions were carried out at 45°C and streptavidin = 100 nM.

2.4.3 Fronts with templates diffusing freely in solution: Bistable network 1

We also tested the bistable network 1 in front propagation experiments. The activation template was fixed at T_1 = 50 nM but R_1 was varied. We first generate fronts at T_1 = 50 nM and R_1 = 10 nM. From the kymograph in Fig. 2.27A we compute a front velocity of 40.5±0.2 µm min^{-1}. This velocity remains constant until self-start occurs at around 450 minutes. When we include additional *dNTPs* (0.4 mM) and keep the same template concentrations (Fig. 2.27B), the front velocity decreases (32.7±0.2 µm min^{-1}) and self-start is eliminated. This observation is coherent with a small inhibition of growth by *dNTPs* (as observed in Fig. 2.23 for template T_2). In these two experiments we expect the diffusivity of A_1 to be identical but not the kinetics, thus, solving for the rate constant in Eq. (2.37) and we get the fraction of rate growth between these two experiments,

$$\frac{v_1^2}{v_2^2} = \frac{R_1'}{R_2'}. \tag{2.46}$$

Inputting the values for velocities in Eq. (2.46) we get $R'_{noExtra}/R'_{dNTPs}$ = 1.5. Velocity decreases by approximatelty 20% by adding additional *dNTPs* possibly because the rate growth is 1.5 times larger in the absence of additional *dNTPs* = 0.4 mM. In Table 2.6 R'$_{growth}$ = 0.04 min^{-1} for R_1 = 8 nM so $D_{eff} = v^2/(4R')$ = 10^4 µm^2 min^{-1}. When R_1 is increased at 0.4 mM of DNTPs from 10 to 20 nM (Fig. 2.28) the initial front velocity

was reduced to 31.3±0.9 µm min^{-1}. After 550 min the velocity is further reduced to 23.3±0.5 µm min^{-1}.

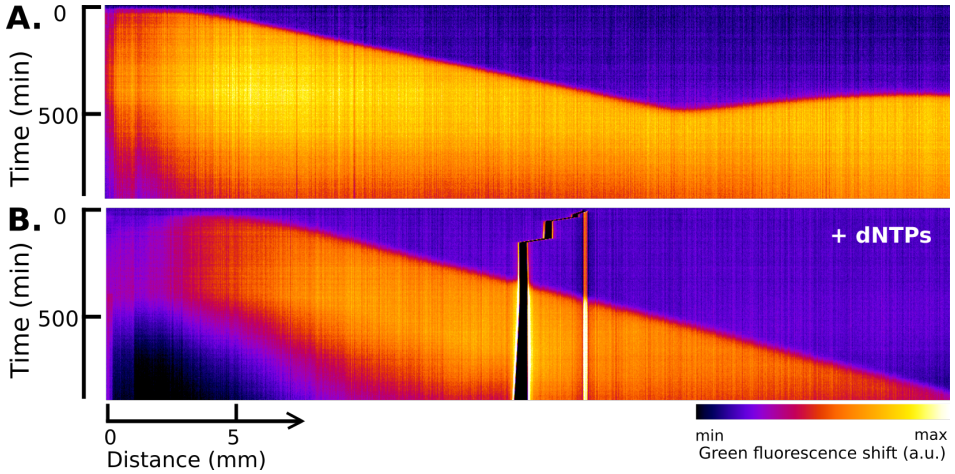

Figure 2.27 – **Front propagation of A$_1$ with templates (T_1 = 50 nM, R_1 = 10 nM) diffusing freely in solution.** Kymograph of the EvaGreen fluorescence. **(A)** The concentration of dNTPs was, as usual, 0.4 mM. We found: v = 40.5±0.2 µm min^{-1}. **(B)** The concentration of dNTPs in the reaction solution was increased to 0.8 mM. We found: v = 32.7±0.2 µm min^{-1}. The fronts were triggered with 2 µL of reaction solution containing A_1 = 400 nM. The reactions were carried out at 45°C. The black lines are bubbles that appeared and grew without disturbing the experiments.

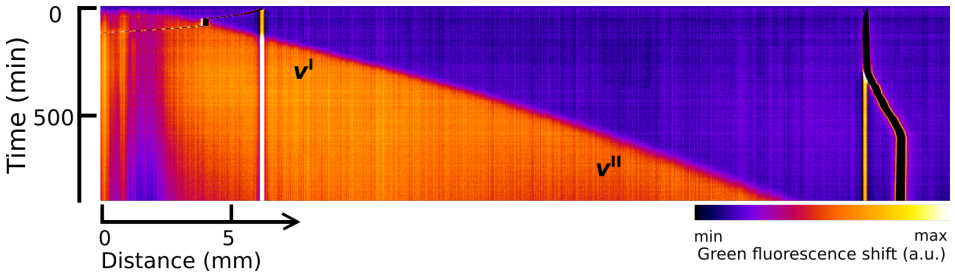

Figure 2.28 – **Front propagation of A$_1$ with templates (T_1 = 50 nM, R_1 = 20 nM) diffusing freely in solution.** Kymograph of the EvaGreen fluorescence. We found: v^I = 31.3±0.9 µm min^{-1} and v^{II} = 23.3±0.5 µm min^{-1}. The concentration of dNTPs was, as usual, 0.4 mM. The front was triggered with 2 µL of reaction solution containing A_1 = 400 nM. The reactions were carried out at 45°C and streptavidin = 100 nM.

In Section 2.3.2 we saw that achieving a low D_{eff} is critically dependent on a low dissociation constant K_d which, as shown in Fig. 2.14, happens at lower temperature. For this reason we reduced the temperature from 45°C to 38.4°C and measured the velocity (Fig. 2.29). The front velocity remains constant (32.9±0.9 µm min^{-1}) for the

time of observation. Interestingly, the front velocity does not change significantly even though the temperature is reduced by 6.6°C. This can probably be explained by an increase of the rate growth R' and a decrease of the effective diffusivity of A_1 by decreasing the temperature. For example, in Table 2.6 we saw that R' at $R_1 = 0$ increased 1.1 fold by decreasing the temperature from 41.1°C to 38.4°C.

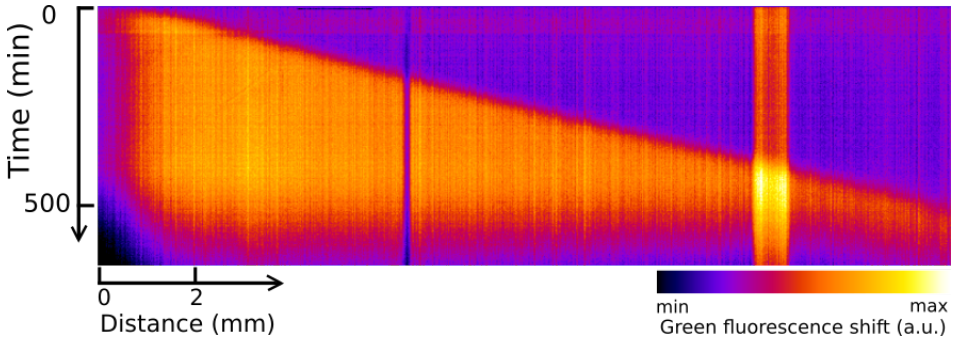

Figure 2.29 – **Front propagation of A_1 with templates (T_1 = 50 nM, R_1 = 20 nM) diffusing freely in solution at 38.4°C.** Kymograph of the EvaGreen fluorescence. The front velocity is $v = 32.9 \pm 0.9$ µm min^{-1}. The reaction solution contained 80 nM of streptavidin. The front was triggered with 2 µL of reaction solution containing A_1 = 400 nM.

In conclusion, we obtained here for the first time propagating fronts in a DNA bistable network with templates freely diffusing in solution. We found experimental conditions that suppress self-start (by increasing the repressor concentration) and that reduce the decay of the growth at longer times (by reducing template concentration). In most cases the velocity of the front was constant over time but in two occasions decreased significantly (10 to 30%). This observation could indicate that they system takes long to reach a steady state. Finally fronts were observed at 45 and 38.4°C without a detectable change in velocity.

2.5 Reactions with templates immobilized in agarose beads

In this section we utilize crosslinked agarose beads to immobilize templates (see the protocol in Appendix A.1). As we discussed in Section 2.2.3, these beads are porous, hence allowing reactions to be carried out within the beads. We explore two experimental settings: (i) closely packed agarose beads and (ii) a diluted dispersion of

agarose beads in an agarose gel.

In the first case, the beads are as closely packed as possible in a glass capillary. We have to point out that the packing does not cover the entire capillary but only about half of the bottom of the capillary (see protocol 2 in Appendix A.2 for details), yet we refer to this system as 'closely packed'[9]. First, we study the kinetics in the packed beads. Subsequently, we study the front propagation and how this pertains to the reduction of the diffusivity of the activation species.

In the second experimental setting, the concentration of the beads is much lower than in the first case. The agarose beads can sediment within a few hours, so we embedded them in an agarose gel. The agarose gel solidifies and fixes the beads spatially within the microreactor (see representation in Fig. A.2, Appendix A.2). In this case we also study first the kinetics followed by the front propagation dynamics.

2.5.1 Templates within packed agarose beads

We utilize the bistable network 2 with templates T_2 and R_2 immobilized within agarose beads that are closely packed.

2.5.1.1 Growth kinetics within packed agarose beads

First, the autocatalytic growth of A_2 in the absence of R_2 is investigated. For this we prepare a reaction solution containing T_2 attached to the agarose beads (see protocol in Appendix A.1) at half the desired concentration in the reaction buffer with/without enzymes. We let the porous agarose beads soak in the solution with enzymes for 15 minutes; the solution is vortexed frequently during this time. The solution is centrifuged to sediment the beads to the bottom, and half of the liquid removed using

[9] We did not quantify the impact of autocatalyst species diffusing freely in the upper part of the capillary where beads are not present on the front propagation. However, since there are no autocatalyst templates in this upper region of the capillary there is no growth of the autocatalyst species. We can hypothesize that the contribution to the front propagation of the autocatalyst species in the region without beads can be neglected since there is degradation of the autocatalyst species but no growth in this region.

a folded piece of absorbing paper. We illustrate this protocol in Fig. 2.30A, in which the red arrows point to the air-liquid interface before being removed and after.

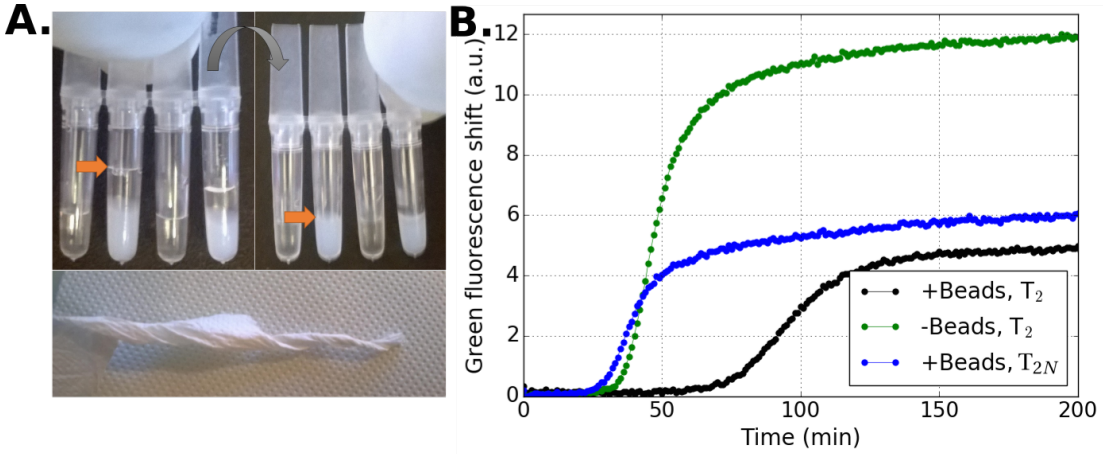

Figure 2.30 – **Autocatalytic growth of A_2 with templates either attached (T_2) or not attached (T_{2N}) to agarose beads.** **(A)** Sample preparation of the packed agarose beads: solutions are initially prepared at 50% (v/v) beads then liquid is removed before reaction with a piece of folded paper. **(B)** Fluorescence profile of the growth of A_2 with either T_2 = 100 nM or T_{2N} = 100 nM. The symbols (-) and (+) mean that agarose beads are absent and present, respectively. The reactions were carried out at 45°C and activated with A_2 = 0.2 nM.

Table 2.7 – **Rate growth constant R' in agarose packed beads.** R's were extracted from the data in Fig. 2.30.

Beads	**Template**	R' (min^{-1})
Beads	T_2	0.08
Beads	T_{2N}	0.17
No beads	T_2	0.19

The activation of A_2 with T_2 within the packed agarose beads is possible as demonstrated by the black markers in Fig. 2.30B. To assay the effect of packing agarose beads we repeat this protocol for the template that cannot be attached to the beads (T_{2N}). In this case because templates are not attached they go in and out of the agarose beads. The activation of A_2 with T_{2N} (blue markers in Fig. 2.30B) shows a faster sigmoidal growth than with T_2. To quantify this, we normalized the data and fitted an exponential model to the data. And we obtained growth rate constant: $R' = 0.08\ min^{-1}$

for T_2 attached to the beads, and $R' = 0.17$ min^{-1} for T_{2N} not attached to the beads. The rate growth constant of the template not attached is about twice of that to the template attached. The slower growth might be explained by arguing that templates inside the beads are less accessible by the enzymes. Another hypothesis is that the enzymes did not have enough time to diffuse into the beads tot reach a homogeneous concentration during the pre-incubation time of 15 min. This is however unlikely. Indeed, for a typical diffusivity of an enzyme of 50 μm^{2}s^{-1} the diffusion timescale occurs 30 μm beads in only 10s.

A second control experiment compares the growth kinetics on T_2 in a solution with no beads (Fig. 2.30B). The growth kinetics with T_2 ($R' = 0.19$ min^{-1}) without beads is comparable to that of T_{2N} ($R' = 0.17$ min^{-1}) with beads. Growth with T_2 in the absence of the beads reaches a larger fluorescence shift. The smaller fluorescence is probably due to light scattering since beads are highly packed.

Finally, we verified that R_2 was functional in the packed beads (Fig. 2.31). Indeed, self-start occurs at 280 minutes in the absence of the repressor template (R_2), but it is eliminated with $R_2 = 5$ nM.

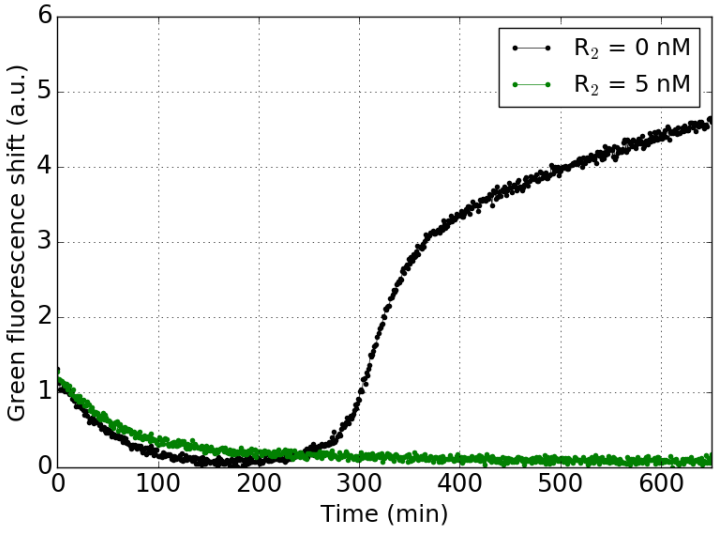

Figure 2.31 – **Self-start with T_2 = 100 nM attached to packed agarose beads is suppressed with R_2 = 5 nM.** The reactions were carried out at 45°C.

2.5.1.2 Front propagation with templates immobilized in packed agarose beads

We spatialized the system, as in Section 2.4.2, with both templates T_2 and R_2 attached to the agarose beads and generated traveling fronts. Figure 2.32 shows the kymograph of this experiment. Initially a front of low fluorescence propagates at a velocity of 27.4±1.5 µm min^{-1}. The fluorescence of the front decreases as it propagates further into the channel. Then, after 2 mm the velocity of this low intensity front decreases to 18.8±1.1 µm min^{-1} and is eventually caught up by the second front.

A second front with high fluorescence is triggered at time = 400 min. Below the original kymograph in Fig. 2.32, we show a treated version using a fluorescence threshold to facilitate the identification of the low and high intensity fronts. The high fluorescence front has a velocity two times higher than the low intensity one (54.6±2.8 µm min^{-1}) and it remains constant throughout the length of the channel. We think that the low fluorescence front corresponds to the propagation of A_2 while the high intensity one is due to the parasite.

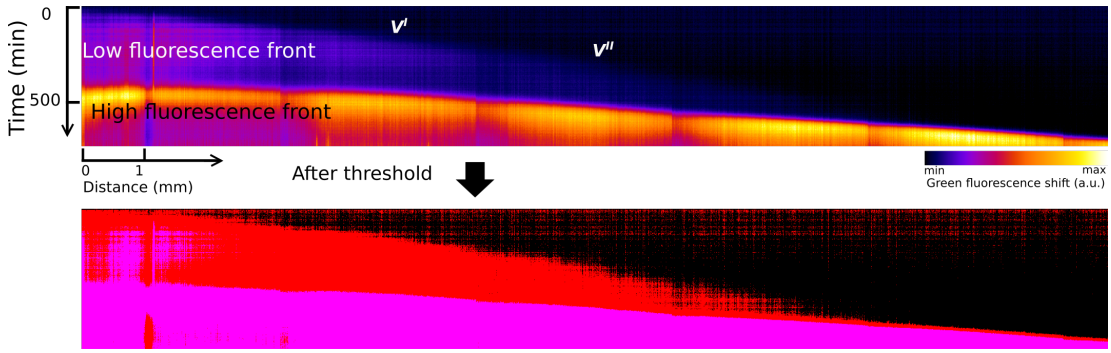

Figure 2.32 – **Front propagation of A_2 with templates (T_2 = 100 nM and R_2 = 10 nM) immobilized in agarose beads.** Kymograph of the EvaGreen fluorescence. The low fluorescence has two fronts with velocities of v^I = 27.4±1.5 µm min^{-1} and v^{II} = 18.8±1.1 µm min^{-1}, whereas the high fluorescence front velocity is 54.6±2.8 µm min^{-1}. Bottom kymograph is the top kymograph after thresholding. The front was triggered with 2 µL of reaction solution containing A_2 = 400 nM. The reaction was carried out at 45°C.

We repeated the previous experiment but increasing T_2, from 100 nM to 200 nM, to get a larger signal (Fig. 2.33). We again observed a low fluorescence front followed by a high fluorescence one, however both fronts display this time a similar velocity 34 and

37 µm min^{-1}, respectively. The velocity increases to 34.0±2.7 µm min^{-1} by increasing T_2. The front eventually vanishes as the green fluorescence tends to decrease as the front progresses. Again, a high fluorescence front appears at time = 500 min and propagates at a constant velocity of 37.3±1.0 µm min^{-1}.

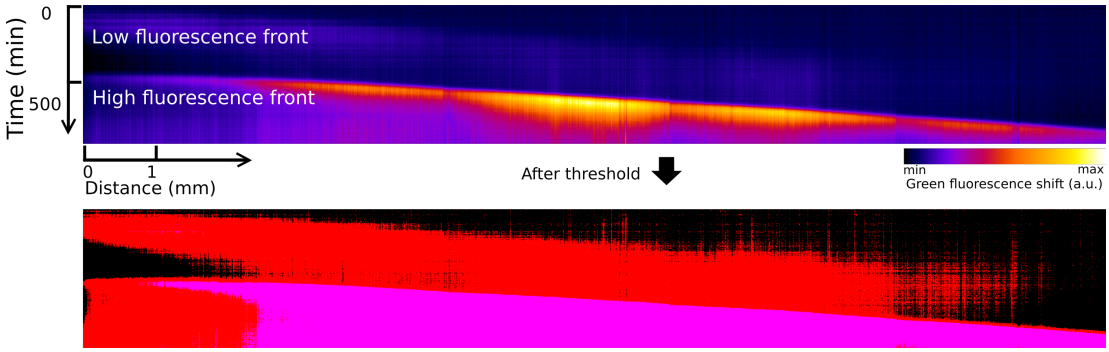

Figure 2.33 – **Front propagation of A_2 with templates (T_2 = 200 nM and R_2 = 10 nM) immobilized in agarose beads.** Kymograph of the EvaGreen fluorescence. The low fluorescence front velocity is v = 34.0±2.7 µm min^{-1}. The high fluorescence front velocity is 37.3±1.0 µm min^{-1}. Bottom kymograph is the top kymograph after thresholding. The front was triggered with 2 µL of reaction solution containing A_2 = 400 nM. The reaction was carried out at 45°C.

We can now to estimate the reduction of diffusion by comparing the velocities in Figs. 2.25 and 2.32 and given that the reaction kinetics in beads are 2-fold faster with templates free in solution or not attached to the beads,

$$\frac{R'_{packed}v^2_{free}}{R'_{free}v^2_{packed}} = \frac{D_{free}}{D_{packed}} = \Gamma_D, \quad R'_{free} = 2R'_{packed}, \tag{2.47}$$

where Γ_D is the ratio of how much the effective diffusion coefficient has been reduced. We get only Γ_D = 1.5. This result is significantly lower than what was achieved with micelles (Γ_D = 2.7) by Zadorin et al. [29] even though the templates are completely immobilized. Although the packing bead strategy requires further investigation the capacity of this system to reduce diffusion seems poor. To verify this result it would be interesting to measure D_{eff} in the absence of a traveling front, for example using fluorescence recovery after photobleaching.

It would be also interesting to performed these experiments at a lower temperature, such as 38°C, to decrease K_d. At 45°C the K_d between A_1 and T_1 is 90 nM. Taking D_T in the beads equal to zero we can use Eq. (2.27) to estimate Γ_D as

$$\Gamma_D \frac{D_A}{D_{eff}(0)} = \frac{2T_0 + K_d}{K_d} \approx 3. \tag{2.48}$$

This is actually not so far from the obtained values of $\Gamma_D = 1.5$. If the experiments were to be performed at 38°C where $K_d = 24$ nM we expect $\Gamma_D = 9$, which is an important gain. This could be interesting in future studies. In any case, we were successful in obtaining reproducible fronts in a particularly complex porous medium.

2.5.2 Templates immobilized in agarose beads in agarose gel

In this section templates are immobilized in the same crosslinked agarose beads, but now these are diluted at 5% v/v in an agarose medium. The results were obtained in collaboration with Olivier Languin, an undergraduate student that I supervised. First, we study the growth kinetics, then in a similar manner as seen in the previous sections we investigate the dynamics of front propagation.

2.5.2.1 Experimental system

Due to historical reasons [29] we do not use a bistable system as the one we have used in the previous sections but merely an autocatalytic node. The DNA sequences are given in Table 2.9. We use the same buffer as before, however the nicking enzyme is Nt.Bst NBI instead of Nb.BsmI (Table 2.8). Agarose beads are used at 5% v/v in the solution. Then, the final solution is assembled by mixing the master mix with either a 4 g/L agarose solution gel or a water solution. The gel solidifies within minutes avoiding the sedimentation of the beads.

Table 2.8 – **Enzyme concentration in the experiments of Section 2.5.2.** The enzyme concentrations are reported in dimensionless formats: $pol_n = pol/pol_0$ with pol_0 = 16 U/mL and $nick_n = nick/nick_0$ with $nick_0$ = 80 U/mL. The concentrations listed here are the final values in the reaction tube.

Enzyme	Concentration
Bst large fragment DNA polymerase (pol) (NEB)	1
Nt.Bst NBI nicking enzyme (NEB)	various concentrations

Table 2.9 – **DNA sequences of the self-activation node used here.** This node is composed of an activation (α) species and an activation template ($T^{\alpha\alpha}$(P2)), which exists in two versions: biotinylated (-bt) and nonbiotinylated. Phosphorothioate backbone modifications are indicated by (*).

Name	Template sequence 5'→3'
α	TCGAGTCTGTT
$T^{\alpha\alpha}$(P2)T5-bt	A*A*CAGACTCGAAACAGACTCGATTTTT-bt
$T^{\alpha\alpha}$(P2)	A*A*CAGACTCGAAACAGACTCGA

2.5.2.2 Growth kinetics in a diluted dispersion of agarose beads

The system in this section is simply an activation node, its growth kinetics are known to be first order [29], and they were studied in Chapter 1. First, we compare the growth kinetics of α over $T^{\alpha\alpha}$(P2)T5-bt and $T^{\alpha\alpha}$(P2) and extract a growth rate constant (Fig. 2.34). We obtain a growth rate constant of R' = 0.13 min^{-1} identical for both templates. This is somewhat expected since these two templates bear the same replication sequence, however, chemical modifications, such as biotinylation, can modify the kinetics in these DNA systems. In contrast the delay before growth is significantly different and α grows later with $T^{\alpha\alpha}$(P2)T5-bt than with $T^{\alpha\alpha}$(P2).

We tested if the agarose medium influences the growth kinetics. To investigate this we analyze the growth of α in the absence or presence of a 4 g/L agarose gel medium. Figure 2.35 shows that the curves are superimposable in both media. However, the growth activation started 110 minutes earlier in agarose. Before going into front propagation experiments in agarose, we also determine the kinetics in the presence of the agarose beads with the template that can be linked ($T^{\alpha\alpha}(P2)$A5-bt) to the beads and with the one ($T^{\alpha\alpha}(P2)$) that cannot be linked (Fig. 2.36). The initial growth rate is

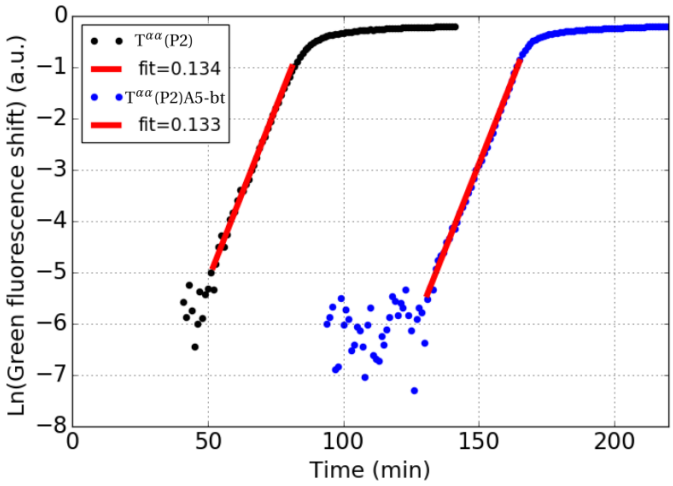

Figure 2.34 – **Growth kinetics of α with T$^{\alpha\alpha}$(P2)T5-bt and T$^{\alpha\alpha}$(P2).** The natural logarithm of the fluorescence shift was taken and the data linearly fitted. The fit is the growth rate constant (R'). The reactions were performed at 38°C, $nick_n$ = 3, $T^{\alpha\alpha}(P2)A5-bt$ or $T^{\alpha\alpha}(P2)$ = 50 nM, and triggered with 1 nM α.

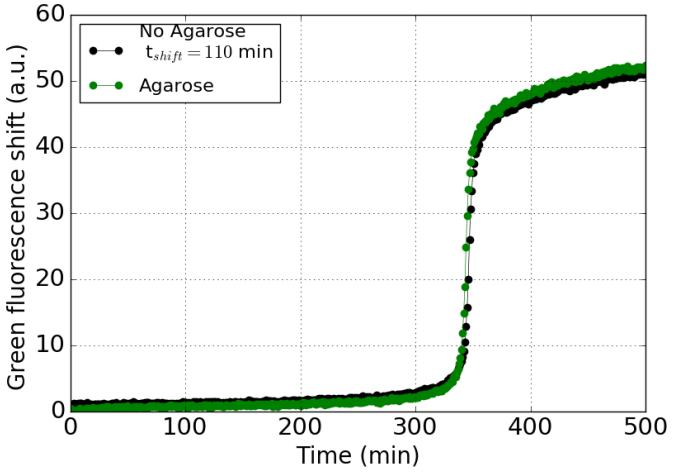

Figure 2.35 – **Sigmoidal growth of α in agarose or water medium.** The curve for no agarose is shifted to superimpose the two curves. The activation was self-started. The concentration of agarose was 4 g/L. The reactions were performed at 38°C, $nick_n$ = 3, and $T^{\alpha\alpha}(P2)A5-bt$ = 100 nM.

very similar for both templates, however, in the case of T$^{\alpha\alpha}$($P2$)A5-bt the fluorescence intensity is more than 40% higher. The negative control shows no growth, when the solution with beads and templates is washed, since the template is not linked to the beads. We obtained a rate growth constant R' for T$^{\alpha\alpha}$($P2$) that was 10% larger than for T$^{\alpha\alpha}$($P2$)A5-bt (Table 2.10).

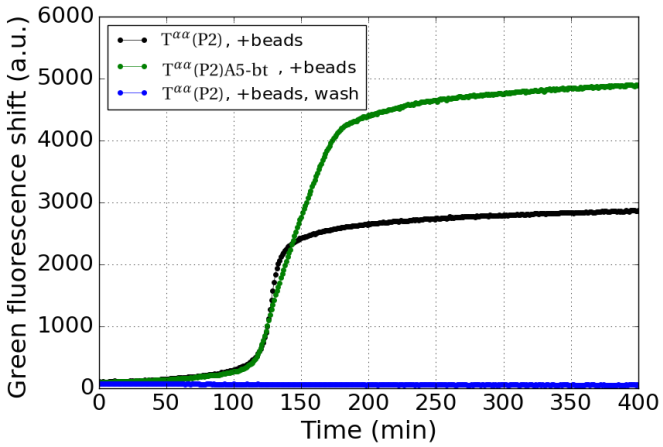

Figure 2.36 – **Growth kinetics of α in the presence of agarose beads in an agarose gel.** Templates $T^{\alpha\alpha}(P2)$ cannot be attached to the agarose beads, so in a negative control, which is indicated by the word *wash*, the solution with beads was washed three times. The concentration of agarose gel was 4 g/L. The reactions were performed at 38°C, 5 % v/v agarose beads, $nick_n$ = 4, and $T^{\alpha\alpha}(P2)A5-bt$ or $T^{\alpha\alpha}(P2)$ = 100 nM.

Table 2.10 – **Rate growth constant R' in agarose beads in an agarose gel.** R's were extracted from the data in Fig. 2.36.

Beads	**Template**	R' (min^{-1})
Beads	$T^{\alpha\alpha}$(P2)	0.101
Beads	$T^{\alpha\alpha}$(P2)A5-bt	0.091

2.5.2.3 Front propagation in a diluted dispersion of agarose beads

We perform front experiments in which $T^{\alpha\alpha}$(P2)T5-bt templates are attached to agarose beads as in Section 2.5.1.2, but here the beads are not packed. An aqueous reaction solution is prepared at 10% (to make a final 5%) v/v agarose beads using a 2x master mix (Table 2.8) at 4°C, then this solution is added to a 8 g/L agarose solution (at 50°C) to make a final 1x reaction solution. Before the gelification of the resulting solution, it is introduced into polystyrene/parafilm microfluidic channels (see Section 4.3.1).

Figure 2.37 shows the kymograph of an experiment following this protocol. Visible vertical stripes in the kymograph come from the discrete distribution of the beads. We calculate a front velocity of v = 18.3±0.1 µm min^{-1}. Replicate experiments yield velocities that vary around 15% from 15.9 to 18.8 µm min^{-1}.

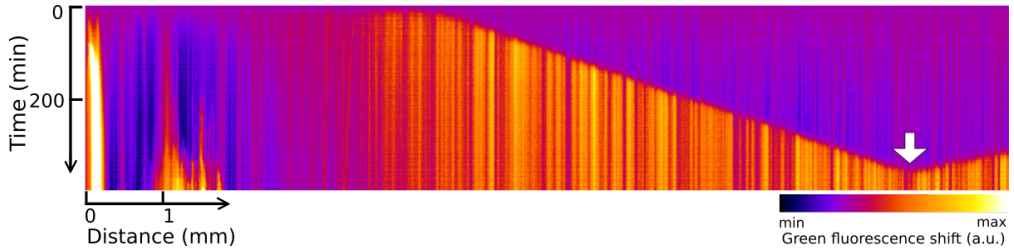

Figure 2.37 – **Front propagation of α with templates ($T^{\alpha\alpha}(P2)A5-bt$ = 100 nM) immobilized in agarose beads within an agarose gel.** Kymograph of the EvaGreen fluorescence. The front velocity is v = 18.3±0.1 µm min^{-1}. The white arrow points to the self-start. The front was triggered with 1 µL of reaction solution containing α = 1 µM. The reaction was carried out at 38°C with 5 % v/v agarose beads, $nick_n$ = 4 and $T^{\alpha\alpha}(P2)A5-bt$ = 100 nM.

Several attempts were required to obtain valid experiments. This is because many times fronts were self-triggered from the sides, i.e. the parafilm walls, of the channel. We can see this in the Fig. 2.38, in which two time frames were taken to demonstrate how the self-triggered fronts appear.

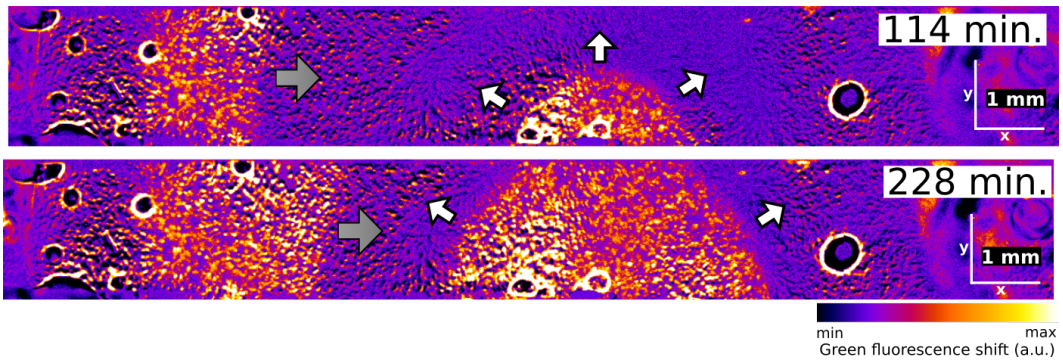

Figure 2.38 – **Two time frames displaying a triggered front (grey arrows) and a self-triggered front (white arrows).** The frames were taken from an experiment similar to the one presented in Fig. 2.37.

To compare and understand our results we perform similar front propagation experiments with template T$^{\alpha\alpha}$(P2), which cannot be attached to the agarose beads since this template does not bear a biotin modification. Figure 2.39 shows the front propagation of α in the presence of agarose beads within a gel agarose. Initially, multiple fronts developed colliding with each other then becoming one front, so we measured the velocity once the front traveled uniformly as one front. The front velocity in this

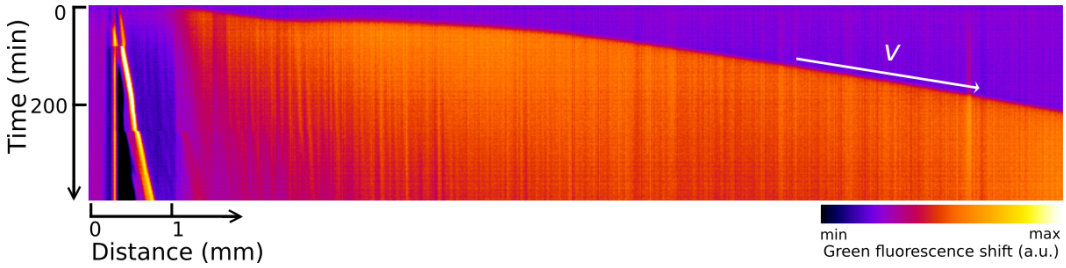

Figure 2.39 – **Front propagation of α with templates ($T^{\alpha\alpha}(P2)$ = 100 nM) in the presence of agarose beads within an agarose gel.** Kymograph of the EvaGreen fluorescence. The front velocity is v = 37.7±1.2 µm min^{-1}. The reaction solution contained $T^{\alpha\alpha}(P2)$ = 100 nM and 5 % v/v agarose beads. The front was triggered with 1 µL of reaction solution containing α = 1 µM. The reaction was carried out at 38°C with $nick_n$ = 4.

experiment is v = 37.7±1.2 µm min^{-1}, which is about twice than the one calculated when $T^{\alpha\alpha}(P2)A5-bt$ is attached to the beads.

To compare our results from Figs. 2.37 and 2.39 we use again Eq. (2.37) and the rate growth values from Table 2.10 for each respective condition. The diffusivity ratio is thus given by,

$$\Gamma_D = \frac{D_{free}}{D_{attached}} = \frac{v_{free}^2 R'_{attached}}{v_{attached}^2 R'_{free}}. \tag{2.49}$$

Thus, using Eq. (2.49) we obtained Γ_D = 4.3±0.3. From replicate experiments, D_{ratio} varied between 3.7-4.3. We obtained more satisfactory results when the beads are not packed. However, we must point out that the reaction conditions were different, not only we used different sequences but the temperature was also lower. The dissociation constant for T$^{\alpha\alpha}$(P2)T5-bt:α (K_d ~ 3 nM at 38°C) is lower than for the system used in Section 2.5.1 (K_d ~ 80 nM at 45°C).

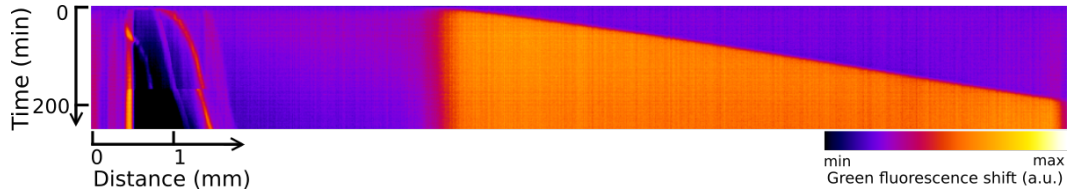

Figure 2.40 – **Front propagation of α with templates ($T^{\alpha\alpha}$(P2)) diffusing freely in the presence of agarose beads in an aqueous solution.** Kymograph of the EvaGreen fluorescence. The front velocity is v = 37.5±0.2 µm min^{-1}. The front was triggered with 1 µL of reaction solution containing α = 1 µM. The reaction was carried out at 38°C with 5 % v/v agarose beads, $nick_n$ = 4 and $T^{\alpha\alpha}(P2)$ = 100 nM.

2.6 Reactions with templates attached to magnetic beads

In this study we use again the bistable network 1 with templates T_1 and R_1 attached to 200 nm beads. We first study the kinetics, then we generate propagating fronts and measure their velocities.

2.6.1 Growth kinetics with templates attached to magnetic beads

We attached the templates to the surface of 200 nm magnetic beads (ademtech bio-Adembeads strept plus) using a binding and washing (B&W) buffer (2 M NaCl, TE 10 mM and 0.2% tween). The templates T_1 and R_1 were not attached to the same bead, so we created repressor beads and activation beads. The magnetic beads binding sites were never saturated since we covered only 1/3 of the sites with templates. The final concentration of beads was 0.02% v/v of beads/solution for 100 nM of templates.

The kinetics of the autocatalytic growth of A_1 with the templates attached to the magnetic beads were assayed in glass capillaries (Fig. 2.41). Both curves grow sigmoidally reaching a maximum that then decreases. We extracted the rate growth constant R' to use it in the calculation of the effective diffusivity of A_1 (Table 2.11). We list these values in the next subsection to group them with the front velocities. The R' for T_1 = 100 nM in Fig. 2.41 is 1.16 fold larger than for T_1 = 80 nM.

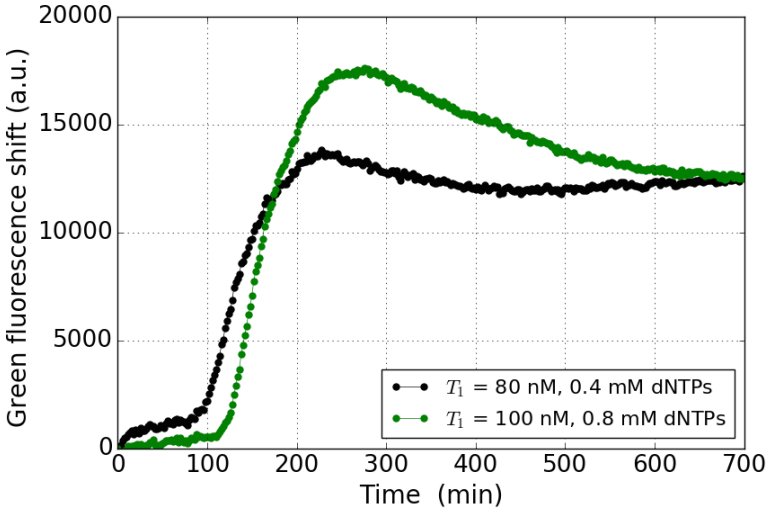

Figure 2.41 – **Kinetics with templates attached to magnetic beads in glass capillaries.** T_1 and *dNTPs* were varied but the repressor template R_1 was fixed to 20 nM. The reactions were performed at 45 °C and triggered with A_1 = 4 nM.

2.6.2 Front propagation with templates attached to magnetic beads

We generated a propagating front in which the concentration of templates was T_1 = 100 nM and R_1 = 20 nM (Fig. 2.42). The front velocity was constant and equal to 32.4±0.7 µm min^{-1}.

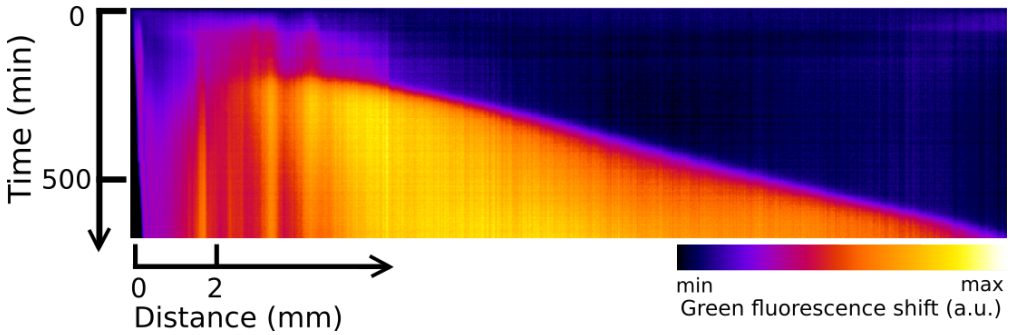

Figure 2.42 – **Front propagation of A_1 with templates (T_1 = 100 nM and R_1 = 20 nM) attached to magnetic beads.** Kymograph of the EvaGreen fluorescence. The front velocity is v = 32.4±0.7 µm min^{-1}. The front was triggered with 2 µL of a reaction solution containing A_1 = 400 nM. The reaction was carried out at 45°C with 0.8 mM *dNTPs*.

Figure 2.43 shows the kymograph of a similar experiment in which the activation template is reduced to T_1 = 80 nM, but the repressor template concentration remains at R_1 = 20 nM. We obtain a similar front velocity (33.4±0.6 µm min^{-1}) to that at T_1 = 100 nM even though T_1 = 80 nM. For an unknown reason the front started after a delay of 300 minutes.

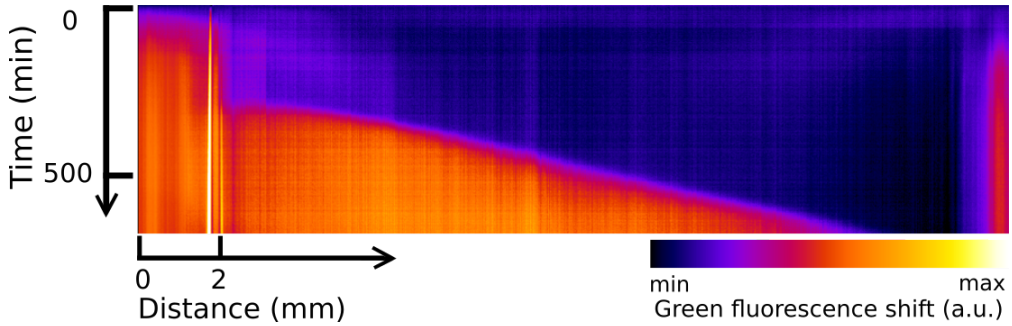

Figure 2.43 – **Front propagation of A_1 with templates (T_1 = 80 nM and R_1 = 20 nM) attached to magnetic beads.** Kymograph of the EvaGreen fluorescence. The front velocity is v = 33.4±0.6 µm min^{-1}. The front was triggered with 2 µL of a reaction solution containing A_1 = 400 nM. The reaction was carried out at 45°C.

We summarize the results from Figs. 2.42 and 2.43 in Table 2.11. Additionally we estimated the values of $D_{eff}(0)$ and the predicted velocity using this and the measured $R'(0)$. First, we determine the validity of the model, $v = 2[R'(0)D_{eff}(0)]^{1/2}$ by comparing the model velocity (v^{mod}) to the measured velocity (v^{exp}). The model tends to overestimate the velocity between 10-15%, which is reasonable since Zadorin et al. [29] reported similar variations.

To get an estimate of the efficiency of our strategy we compare the values of $D_{eff}(0)$ with the predicted value when the templates are not attached ($D_{eff}(0) \sim$ 12400 µm^{2}min^{-1}). The diffusion of A_1 is only reduced by up to = 2.4 fold. This strategy does not yield strong diffusion control despite low diffusivity of the magnetic beads. We believe this is again due to the much high dissociation constant ($K_d \sim$ 80 nM at 45°C) of the network used here whereas Zadorin et al. [29] benefit from the lower K_d ($\sim$ 3 nM at 38°C).

Table 2.11 – **Data on fronts of A_1 with templates attached to magnetic beads.** The symbols (†) and (‡) indicate the experiments contained, respectively, *dNTPs* = 0.4 mM and 0.8 mM. v^{exp} and v^{mod}, respectively, stand for experimentally measured and predicted from the model. v^{mod} is calculated using: $2\sqrt{D_{eff}(0)R'(0)}$. $D_{eff}(0)$ is estimated at the corresponding conditions using Eq. (2.27) at: K_d = 80 nM, D_A = 16000 µm^{2}min^{-1} and D_T = 600 µm^{2}min^{-1}. Templates not attached to the magnetic beads yield $D_{eff}(0) \sim$ 12430 µm^{2}min^{-1} using D_T =11000 µm^{2}min^{-1} [29].

Conditions (Templates in nM)	v^{exp} (µm min^{-1})	v^{mod} (µm min^{-1})	$D_{eff}(0)$ (µm^{2}min^{-1})	$R'(0)$ (min^{-1})
T_1 = 100, R_1 = 20, ‡	32.4	37.0	5000	0.069
T_1 = 80, R_1 = 20, †	33.4	37.1	5730	0.059

Working at 38.4°C the bistability is maintained (as seen in Fig. 2.19) and $K_d \sim$ 24 nM Fig. 2.14. However we were unable to generate fronts in these conditions. Only few attempts were done due to time limitations. Inhomogeneous and very low fluorescence signals were obtained. It can be interesting that future experiments are performed at intermediate temperatures from 38.4°C to 42°C.

2.7 Conclusions and perspectives

In this chapter we used 200 nm magnetic nanoparticles and 34 µm agarose beads to immobilized DNA-PEN templates in order to reduce the effective diffusion coefficient of an activator. We studied the growth kinetics and front propagation dynamics for a bistable network in packed agarose beads (case 1) and diluted magnetic beads (case 2) and for an autocatalytic network in diluted agarose beads (case 3). Finding the correct experimental conditions to obtain stable propagating fronts for the bistable network in both situations was time-consuming. Our results yielded a reduction factor in the effective diffusivity of the activation species of: 1.5, 2.4, 4.3 for the cases 1, 2 and 3 respectively. Clearly the propagation of fronts in these complex porous media requires further investigation.

To get further insight, the determination of diffusivities in these media for a non-reactive system (only DNA complexation without enzymes) appears as a critical step. Furthermore, K_d, the dissociation constant between the active species and templates

with the hydrodynamic drag, appears as a critical parameter. In the future, decoupling the control of diffusion from the reactive templates seems an attractive solution, for example by designing a ligand of the autocatalyst that does not act as a template and can be used a a larger concentration.

3 Material morphogenesis: self-assembly of beads directed by DNA patterns

In Chapter 2 we found the conditions for coupling a biochemical system capable of generating spatiotemporal patterns, the PEN-DNA toolbox, with a variety of material supports. These supports were both physico-chemically diverse and spanned two orders of magnitude in size. Our goal was then that these material supports influence the chemical patterns via a reduction of diffusion. We now focus on the complementary objective: that chemical patterns determine the shape of a material. We have called this approach material morphogenesis [58] by analogy to embryo morphogenesis where chemical pattern formation in a field of pluripotent cells results in the structuration of this initially homogeneous *material*. As a proof of principle we have chosen to use DNA-decorated colloids as their capacity to aggregate in the presence of complementary strands is well described [59]. In particular, we demonstrate that DNA patterns can control the conditional aggregation of magnetic beads in two situations: (i) a traveling front of A_i that directs a front of aggregating beads and (ii) a stationary front of A_i that induces the assembly of a fixed pattern of aggregated beads.

The work of this chapter is the result of three contributions: (i) my work on front propagation with templates attached to magnetic beads described in Chapter 2, (ii) the work of Vadim Dilhas, a master student in our group, that I contributed to mentor for controlling the aggregation of beads and (iii) the work of Anton Zadorin, a postdoctoral researcher in our group, to generate stationary DNA patterns. Therefore, this chapter

is shorter than the other experimental chapters. This work has been submitted and the preprint appears in Appendix B.

3.1 Experimental system

In contrast with Chapter 2 we have used 1 µm and not 200 nm diameter paramagnetic beads (except on Section 3.3.2). A similar protocol, with slight variations, to the one reported by Leunissen et al. [60] was used to prepare DNA-functionalized beads. It took however several months to achieve a stable dispersion of beads that did not aggregate non-specifically. The use of pluronic, a hydrophilic and neutral polymer that adsorbs on the surface of the beads, solves most of these issues. We decorated 1 µm diameter, streptavidin-coated (5 µM biotin binding sites and 10 mg/mL of beads) Dynabeads (MyOne Streptavidin C1) with the biotinylated DNA. Two types of beads (B_1 and B_2) were created by changing the sequence attached to the bead (Fig. 3.1). We have listed the DNA sequences in Table 3.1.

Table 3.1 – **DNA sequences for the functionalization of beads capable of material morphogenesis.** B_1 and B_2 are biotinylated (bt). Phosphorothioate backbone modifications are indicated by an asterisk (*).

Name	Template sequence 5'→3'
B_1	G*G*A*TGAAGATGAGCATTACTTTCCGTCCCGAGAGACCTAACTGACACGC ... TTCCCATCGCTA-bt
B_2	bt-AGCATTACTTTCCGTCCCGAGAGACCTAACTGACACGCTTCCCATCGCT ... AGGATGAAGATG
S	T*A*G*CGATGGGAAGCGTGTCAGTTAGGTCTCTCGGGACGGAAAGTAATGC
T_L	T*T*G*GATGAAGATGGGATGAAGATGGAATG'CGATCCTGAATG
L	CATCTTCATCCCATCTTCATCCAA

Complexes B_i:S are linked to the beads. The two types of beads are assembled in the presence of a linker strand L. The linker has 2 thymine extra bases (drawn in red in Fig. 3.1) on its 3' end to prevent polymerase extension and the subsequent strand displacement of S on B_1 beads by the polymerase. The detailed protocol to assemble the two bead types is as follows:

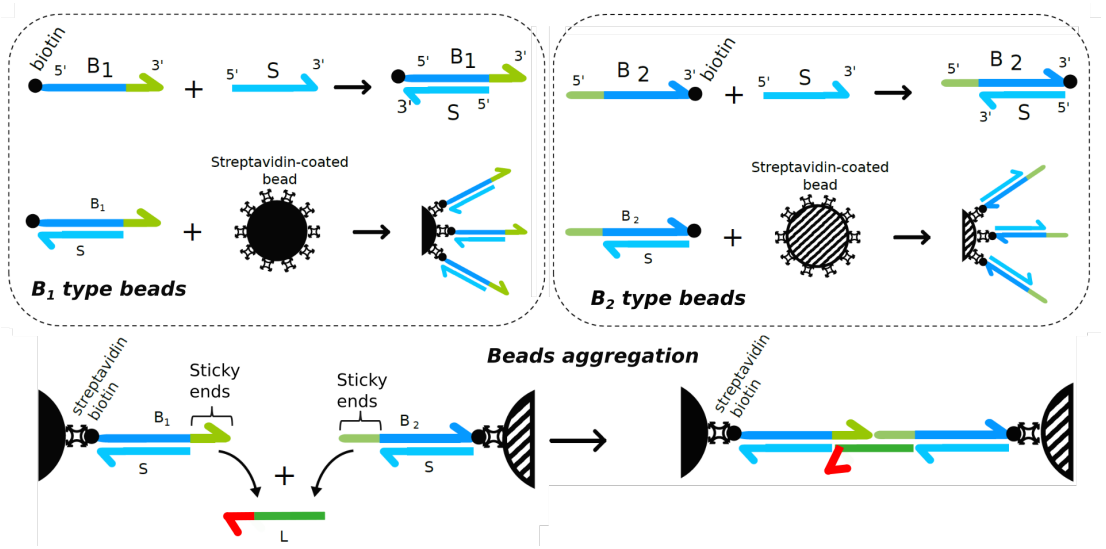

Figure 3.1 – **Scheme of DNA-decorated magnetic beads capable of aggregation in the presence of a linker L.** Two types of beads are created depending on the sequence used for the functionalization of the beads. Biotinylated templates B_1 and B_2 hybridize to S to form a rigid DNA complex, which is linked to streptavidin coated beads of 1 µm in diameter. A linker strand L assembles the two type of beads by hybridization to the sticky ends in the B_i:S complexes.

1. The solutions containing the B_i:S complexes are prepared at a final concentration of 8 µM in the suspension buffer (10 mM phosphate, 50 mM NaCl and 0.1% w/w Pluronic surfactant F127, Sigma-Aldrich).

2. The beads are rinsed 3 times in the suspension buffer and split into two aliquots.

3. The functionalization of the beads is done by removing the bead supernatant and adding the corresponding B_i:S complexes solution to each bead aliquot. The resulting solutions are incubated at room temperature for 30 min under gentle mixing. The final concentration of the beads is 10 mg/mL.

4. The two bead solutions are mixed and rinsed 3 times in the suspension buffer followed by an incubation period of 30 minutes at 55°C for 30 min. Afterward, the solution is rinsed again 3 times to eliminate the non-grafted strands. The solution is stored at 4°C.

To carry out an experiment, the master solution is assembled as in Section 2.3.3. However, before adding the beads to the master solution, the bead solution is pre-heated at 55°C for 30 min, then added at 0.5 mg/mL of beads to the final reaction mix.

The bistable network topology that we have presented in Fig. 2.11 was modified to include the linear production of the linker (L) (Fig. 3.2). This way the aggregation of the beads is only started by triggering first the production of the activation species A. Here we use the sequences of the bistable network 1 (Table 3.2).

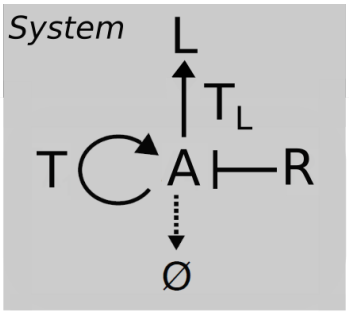

Figure 3.2 – **Network topology of a bistable system with linear production of a linker (L).** The production of the linker L needs the template that takes species A as an input and produces L as the output.

Table 3.2 – **DNA sequences of the bistable network used here:** autocatalytic species A_1, autocatalytic template T_1, and repressor template R_1. Phosphorothioate backbone modifications are indicated by an asterisk (*). T_1 has dye CY3.5 on its 5' end.

Network	Name	Template sequence 5'→3'
Bistable	A_1	CATTCAGGATCG
network 1	T_1	CY3.5-C*T*C*G*TCAGAATGCTCGTCAGAA
	R_1	T*T*T*T*TCGATCCTGAATG

3.2 Propagating front of aggregated beads

In this section we present a propagating front of aggregated beads directed by a front of DNA. First, a DNA front is triggered, as in Fig. 2.25 of Chapter 2, in the presence of the unaggregated beads (Fig. 3.3). The traveling front of A_1 is followed by a front of L (yellow arrows), which then induces the aggregation of the beads. Initially, the beads

are able to move by Brownian motion and are homogeneously distributed. As the front propagates it produces the linker and the beads aggregate into heavy, immobile clusters, which we can see in the zoom area at the bottom of Fig. 3.3. The front of aggregating beads travels at a velocity of 30± 3 µm min^{-1}.

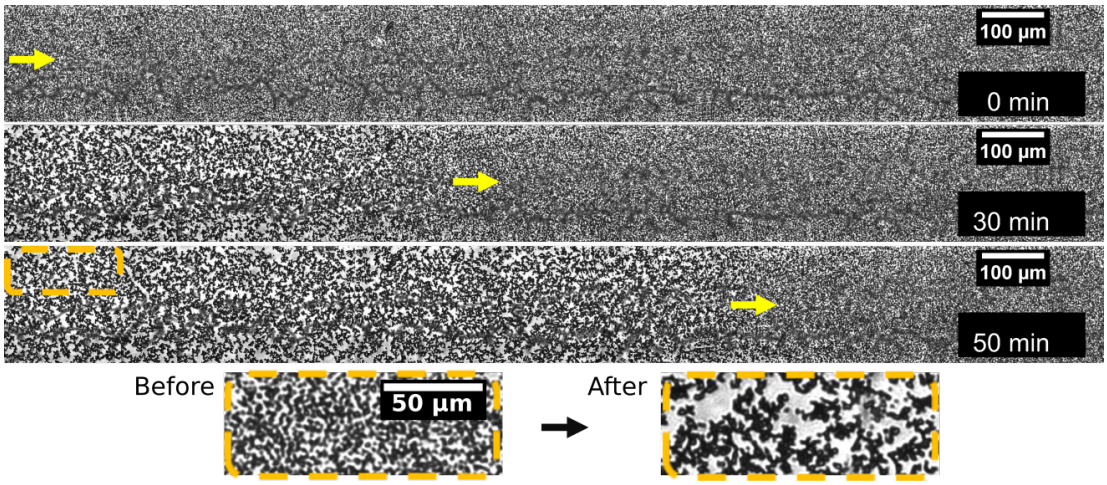

Figure 3.3 – **A propagating front of beads is induced by a front of DNA.** Yellow arrows indicate the direction of the propagation of the front. Green squares are zoom areas. The front velocity was 30± 3 µm min^{-1}. This experiment was performed at 45°C at T_1 = 25 nM, R_1 = 10 nM, T_L = 50 nM and triggered with $A_{1_{(t=0)}}$ = 100 nM.

This demonstrates that patterns generated by the PEN-DNA toolbox systems can be coupled to materials leading to directed assembling, or material morphogenesis. We use this interesting conclusion in Section 3.4 to transfer a stationary DNA pattern to beads, but first we will cover in Section 3.3 how the stationary DNA patterns are generated and how we can use again the beads as in Chapter 2 to control a stationary pattern.

3.3 DNA stationary patterns based on positional information

Before going into the experimental part, we will introduce briefly how to engineer stationary spatial DNA patterns using a positional information approach. The resulting pattern is composed of two chemically-distinct regions separated by a sharp border,

which we will refer in this chapter as a *Polish flag*. Subsequently, we will use the low diffusivity of 200 nm beads for the generation of sharp gradients of templates attached to these beads. Finally, the sharp gradients of repressor template (R_1) attached to magnetic beads are used in the generation of a Polish flag of species A_1.

3.3.1 Introduction to the mechanism of positional information

As we have seen in the Referencesch:intro, one of the most influential ideas in embryonic development is Lewis Wolpert's positional information (PI) [4]. In this mechanism, a pre-pattern composed of a morphogen concentration gradually increasing across space is differentiated into chemically distinct zones with sharp borders, a situation that Wolpert named the *French flag* problem (Fig. 3.4). This differentiation is based simply on morphogen differences in concentration. The growth of a first chemical species in a zone can be inhibited above or below a concentration of morphogen, thus allowing the activation of a second species in this region. This process occurs in other zones resulting a pattern such as the French flag presented in Fig. 3.4.

We use the principle of positional information patterning to generate a spatial DNA pattern. Initially, a gradient of morphogen (repressor template) is generated along the longitudinal axis of the capillary (Figs. 3.5 and 3.6). Also, a homogeneous distribution of the activation species A_1 is at low concentration everywhere in the channel. This is very different to the fronts, in which A_1 is initially present only as a Heaviside initial condition that triggers the propagation of the front. We see in Fig. 3.5 that the repressor gradient is constant over time, but the concentration of A_1 changes from the initial to the final state. The autocatalytic production of A_1 is triggered by the initial presence of A_1. And because we use a bistable network, A_1 only grows below a threshold concentration of the repressor template. The resulting Polish flag pattern is a region of species A_1 and a second region without it.

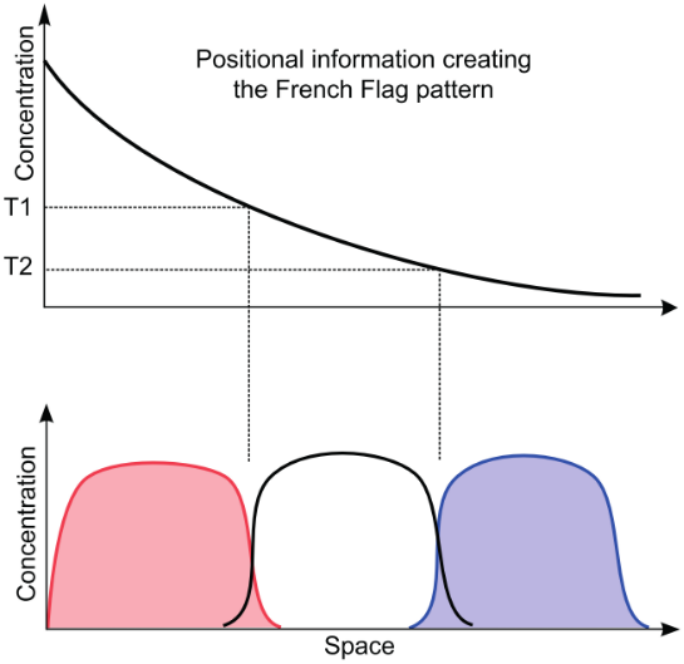

Figure 3.4 – **French flag pattern.** A morphogen gradient is interpreted into three chemically distinct zones, thus giving rise to a French flag pattern. There is a threshold concentration at which the growth of a chemical species occurs while repressing the other two chemical species. This figure was taken from [10].

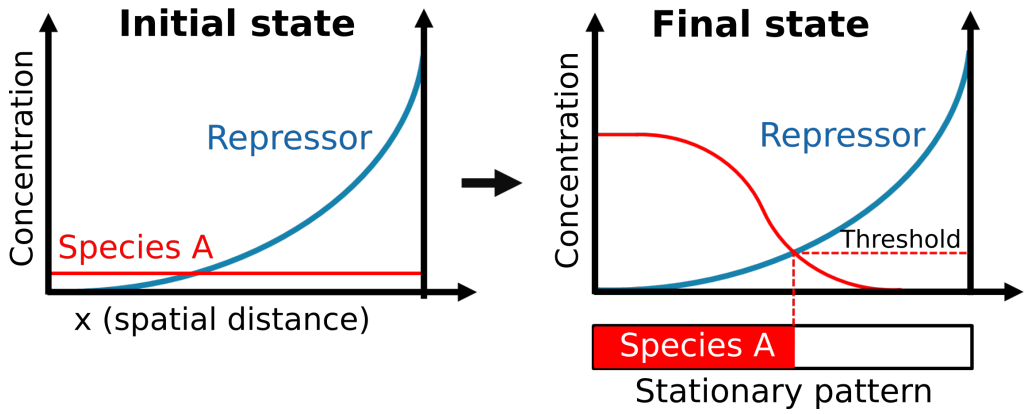

Figure 3.5 – **A Polish flag pattern emerges by the positional information mechanism.** Species A grows only below a threshold concentration of the repressor, thus resulting in a two-region pattern. The final pattern is stable over time.

3.3.2 Generating sharp gradients of DNA-decorated beads

Anton Zadorin was the first one to obtain a Polish flag pattern in our group. He generated the shallow gradient by mixing inside the capillary by Taylor dispersion

a solution containing no repressor, coming from one side, and a solution with high repressor concentration coming from the other side. For the gradient to be stationary the duration of the experiment (20 h) he had to use 5 cm long capillaries. Our objective here was to show that 200 nm beads can be used to create sharp gradients of repressor template. But, first we will describe how the gradients are manually produced.

We prepare a solution containing 0.4 µM repressor template R_1 and a second solution without the represssor. Both solutions contain the buffer, the dNTPs, A_1, T_1 and the three enzymes: pol, nick and exo. We first fill completely a capillary using a micropipette and a custom-made connector with the solution without the repressor. Then, a pipette is inserted being in the 'push' position into the connector. The other end of the capillary is dipped into the reaction solution containing the repressor template. We pump 10 times 4 µL of liquid in and out of the capillary to generate a gradient by Taylor dispersion. In Fig. 3.6 we show an image of gradients of methylene blue dye as a demonstration. We see the high concentration of methylene blue dye on the right hand side and the low concentration on the left hand side.

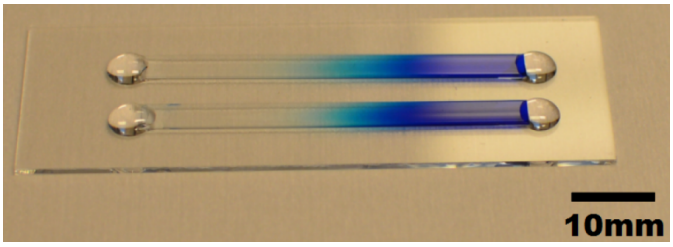

Figure 3.6 – **Gradients of methylene blue dye generated by Taylor dispersion.** The gradients are created by pipetting back and forth a constant volume of dye. Subsequently, each extremity of the capillary is sealed with a droplet of glue that serves also to attach it to a glass slide. The glass capillaries have inside 50 ×4×0.2 mm^3 dimensions.

We create two gradients with templates: (i) attached to 200 nm beads and (ii) not attached. Templates are attached at half the binding capacity of the beads (bead properties in Table 2.2) following a similar protocol to the one described in Section 2.6.1. The 0.4 µM template-bead solution results in a concentration of 0.025% v/v of beads/-solution. The gradients were done using the same pipetting protocol, nonetheless the gradient with templates attached to the beads is sharper than the one without beads

(Fig. 3.7). The gradient with templates attached to the beads sharpens quickly at 32 mm. Whereas, the sharpening of the gradient of templates not attached is slower and starts at 25 mm. To quantify the sharpness of the gradients we fitted an exponential to the gradients, and we obtained a characteristic length of 2.5 mm for the case with the templates attached and 15 mm for not attached.

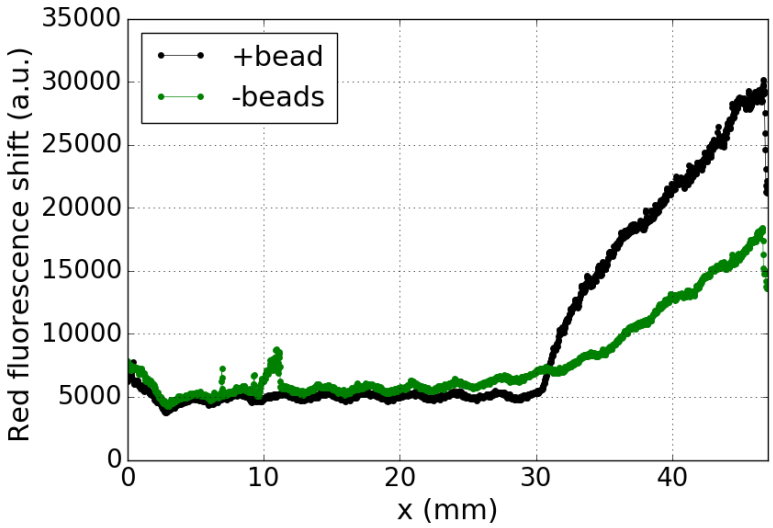

Figure 3.7 – **Gradients with templates attached (+beads) or not attached (-beads) to 200 nm beads.** The red fluorescence shift comes from the fluorophore (Cy3.5) modification on the 5' end of the templates.

When we are creating the gradients by 'Taylor dispersion'[1] the smearing out of the high concentration of repressor into the lower concentration depends on the diffusivity of the templates. Thus, we are able to create sharper gradients of repressor template by attaching them to magnetic beads, which have a diffusion coefficient of around 18 fold smaller than the templates alone.

[1]The Taylor dispersion concerns the spreading of a solute A in a solution flowing in a capillary, typically with a Poiseuille (quadratic) velocity profile across the transversed direction of the capillary. The effective dispersion coefficient is given by $D_{disp} = D_A + D_{Taylor}$ where D_A is the Brownian diffusivity of species A and $D_{Taylor} \sim \frac{1}{D_A}$. Our group has thoroughly characterized the spreading of a free DNA template during the generation of the morphogen gradient and it follows a Taylor dispersion mechanism. The fact that the DNA templates attached to beads with 18-fold smaller Brownian diffusivity generate a sharp gradient implies that they do not follow a Taylor mechanism, thus the quotes.

3.3.3 Stationary patterns with a gradient of morphogen attached to beads

The work of Zadorin in our group demonstrated that French and Polish flag patterns can be generated with DNA repressor templates that diffuse freely in solution (see Appendix B for details). And, we just saw that we can create sharp gradients due to the low diffusivity of the 200 nm beads. Here, we combine both expertises to generate a Polish flag pattern with repressor templates attached to these beads. We use biotinylated templates so that they can be attached to the beads (listed in Table 2.3) instead of the ones listed in this chapter (Table 3.2). Two reaction solutions are prepared as indicated in Section 2.3.3. One solution contains 400 nM of R_1 linked to the beads and the other contains no R_1. Then, we create a morphogen gradient of R_1 along the capillary, which is subsequently closed. Figure 3.8A shows the kymograph of the emergence of a Polish flag pattern following our protocol. Initially, we see that a front of A_1 propagates from left to right. However, the front velocity decreases as it approaches higher concentrations of the repressor template until it stops at a threshold concentration of R_1. Once the stationary pattern develops, it is stable for at least 3 hours. The fluorescence profile of the stable pattern in Figure 3.8B shows the sharp border between a region of A_1 and a region without A_1. For this particular experiment we did not monitor the gradient profile, but because we followed the same protocol as in Fig. 3.7 we expect a sharp gradient.

For unknown reasons, our control experiment seeking to generate a Polish flag pattern in the same conditions in the 22 mm long capillary but without the beads did not work. However, we can compare our experiment of the repressor template attached to the beads with a Polish flag generated in a 50 mm long capillary without beads (Fig. 3.9). The stationary fluorescence profile with beads is 2 fold sharper than the one without beads. This probably comes from the sharper gradient in the case of the experiment with beads. However, it needs to be studied further how the gradients affect the final pattern.

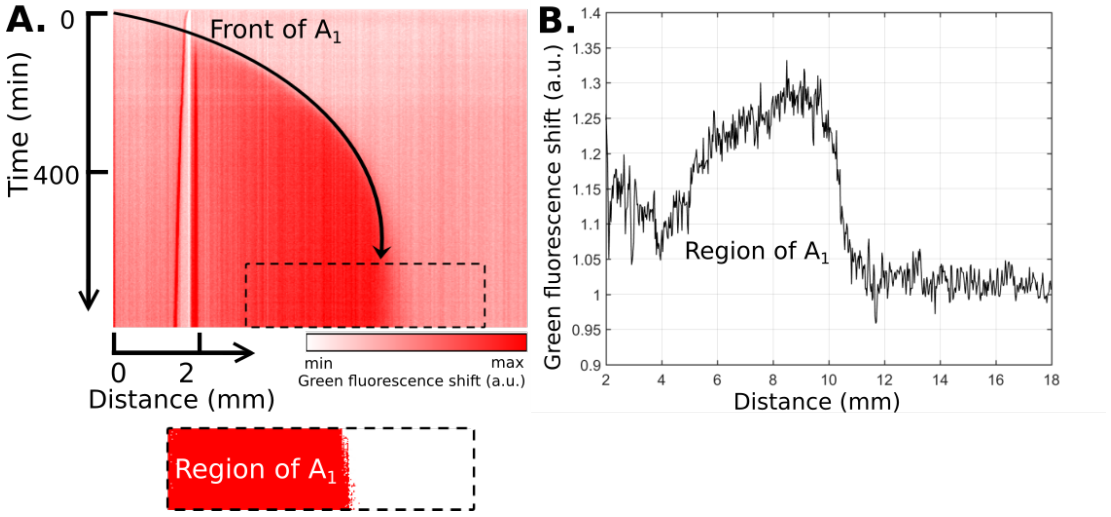

Figure 3.8 – **Polish flag pattern using a gradient of repressor template linked to magnetic beads. (A)** Kymograph of EvaGreen fluorescence. We thresholded the zoom region to emphasize the pattern. **(B)** Green fluorescence shift spatial profile at 600 min. The repressor template R_1 template was varied between 0 nM and 400 nM. White crosses point to fluoresce increase coming from around the edges of the capillary channel, so we do not attribute this to DNA fluorescence. The reaction was performed at 45°C, T_1 = 25 nM, $A_{1_{(t=0)}}$ = 1 nM with a repressor template of 0 to 400 nM. Enzyme concentrations were as listed in Table 2.5.

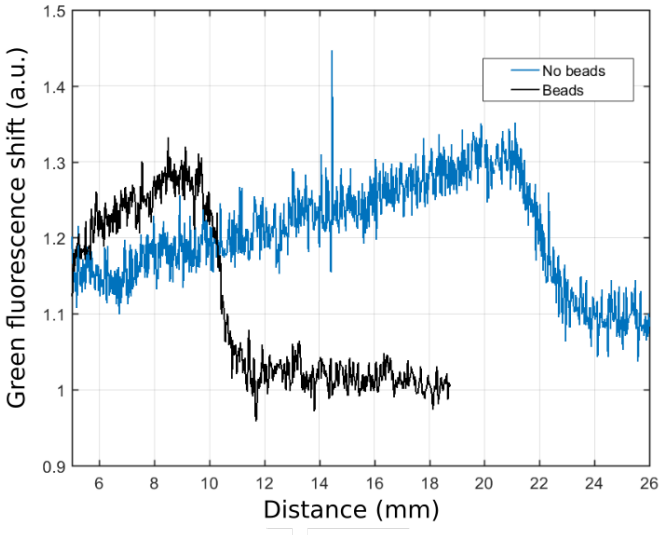

Figure 3.9 – **Fluorescence profiles of Polish flag patterns with repressor templates attached and not attached to 200 nm beads.** The reactions were performed at 45°C, T_1 = 25 nM, $A_{1_{(t=0)}}$ = 1 nM with a repressor template gradient of 0 to 400 nM. The enzyme concentrations were as listed in Table 2.5.

The experiment in Fig. 3.9 is a preliminary result that confirms that 200 nm magnetic beads are compatible with DNA stationary patterns and that sharp gradients can also be used to generate a Polish flag pattern. However, even without a sharp gradient a Polish flag pattern develops, as shown in the recent work of our group (Appendix B), in which steady-state patterns based on positional information, including a French flag pattern, were observed for the first time in a chemical system.

3.4 Stationary front of aggregated beads

Here, we transfer a Polish flag pattern of DNA into a Polish flag pattern of aggregated beads. As opposed to Section 3.3.3 the repressor template is not linked to the beads, so we create a gradient of R_1 less sharp, to focus on material morphogenesis instead. The beads that aggregate in this section are the same we presented in Section 3.2. As in Section 3.2 the beads B_1 and B_2 are initially homogeneously dispersed in the capillary. As in Section 3.3.1 a bistable network is present in the capillary with a gradient of R_1 along the capillary. As in Section 3.2 the bistable network produces the linker L that aggregates the beads (Fig. 3.1).

We show in Fig. 3.10A a brightfield image of the central part of the capillary after 40 h of the experiment showing the materialization of the Polish flag. On the left side of the image the beads are aggregated, but not on the right side. We observe on the left hand side that the beads are farther from each other because they have clustered into larger aggregates. The level of aggregation is quantified by determining the average size of the aggregates (Fig. 3.10B). The aggregated bead clusters were between 250-400 μm^2 in size. We see in the zoom in Fig. 3.10C the aggregated and non-aggregated beads. On the right hand side of the image the beads formed much smaller aggregates of about 50 μm^2 in size. These small aggregates could be due to non-specific assembly of the beads in the absence of L or due to a leak on the reaction producing L. Interestingly, the pattern of beads was stable for up to a month at room temperature (Fig. 3.11).

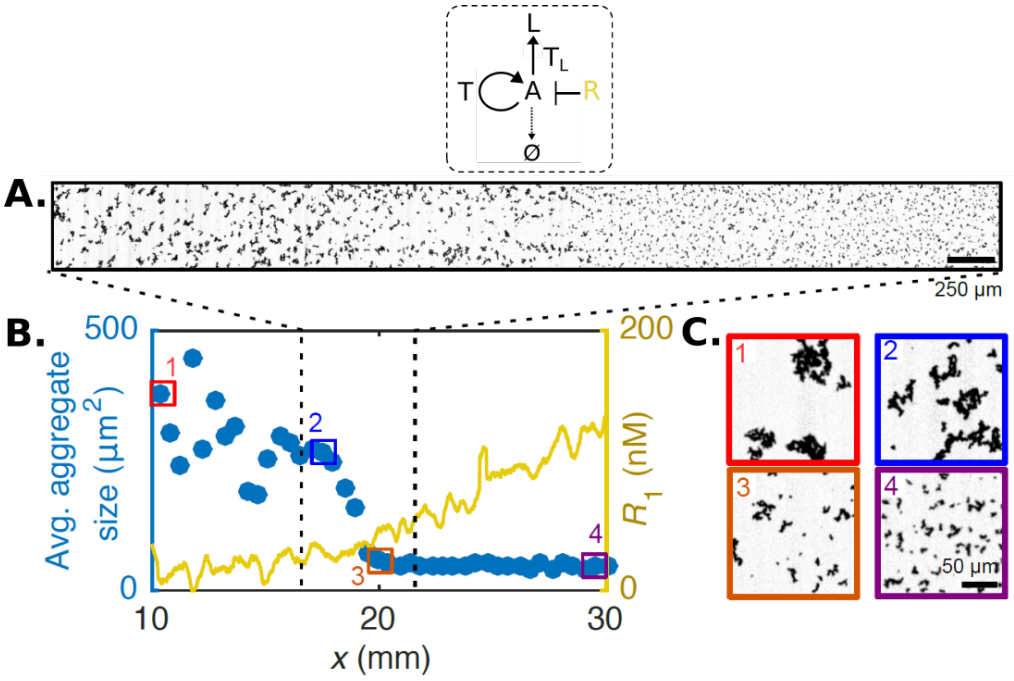

Figure 3.10 – **Polish flag pattern of aggregated beads.** **(A)** Brightfield image at the center of the capillary channel. **(B)** Average size of particle aggregates (blue disks, left axis) and initial concentration of R_1 (yellow line, right axis) along the channel. The colored squares indicate the positions at which the brighfield images in **(C)** were recorded. The dashed lines correspond to the position where (A) was recorded. The reaction was performed at 45°C, T_1 = 25 nM, $A_{1_{(t=0)}}$ = 1 nM. Enzyme concentrations were as listed in Table 2.5.

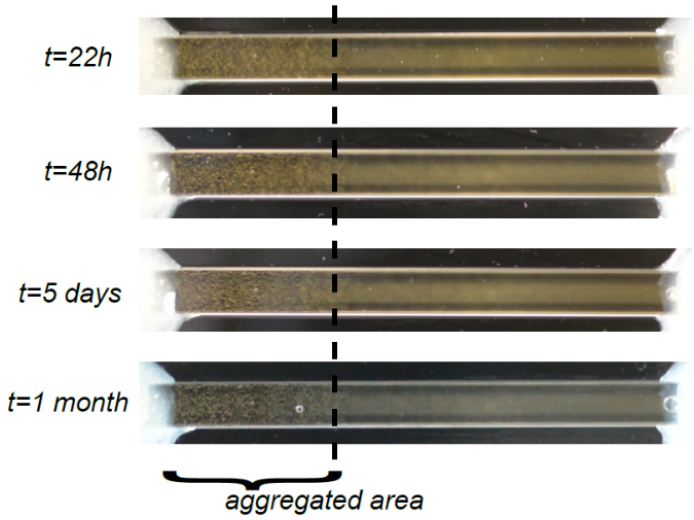

Figure 3.11 – **A Polish flag pattern of aggregated beads is stable for a month.** The aggregated beads are seen on the left hand side of the capillary. The photos were taken in brightfield with a Nikon D600 camera equipped with a 35 mm lens.

3.5 Conclusions and perspectives

Our efforts in controlling the interaction of DNA strands with microparticles for controlling diffusion (Chapter 2) found here an application in material morphogenesis. We have demonstrated that DNA concentration patterns can be transferred into patterns of bead aggregation. This is shown in two different cases: a traveling and a stationary front. This DNA model of morphogenesis mimics two key stages of embryo development: (i) the generation of chemical patterns and (ii) the transfer of patterns into a material (the initial homogeneous development of beads can be seen as an embryo mode of pluripotent cells). We foresee the continuation of this research to create more complex morphogenetic materials . The rational design of DNA patterns together with responsive materials are an opportunity to explore the capabilities of material morphogenesis.

Furthermore, in the case of the Polish flag patterns the influence of the sharpness of the gradients on the dynamics and shape of the patterns should be studied. For instance, a stable pattern can be perturbed externally with a magnetic field if the templates are attached to magnetic beads. This can be an interesting contribution for understanding the physical aspects of pattern formation. In the positional information mechanism the initial and boundary conditions impact greatly the final pattern, as it happens in many other patterning mechanisms except for Turing patterns. In the next chapter, our goal will be to develop a method compatible with the PEN-DNA toolbox to control the patterning boundary conditions.

4 Propagation of DNA waves in microreactors of tailored geometry

After attempting to control network topology in Chapter 1 and diffusion in Chapter 2, and coupling of reaction-diffusion patterns with materials in Chapter 3, here we address the problem of imposing the boundary conditions over a DNA-based reaction-diffusion system. More precisely, we developed a microfluidic technique to study the propagation of DNA waves in microreactors with controlled geometry. As an example we investigated the dynamics of propagation of a modified Predator-Prey network [32]. This network consisted in the autocatalytic replication of a prey species subsequently consumed by an autocatalytic predator reaction. In a microreactor with spatially homogeneous concentrations of both species, the network produced a concentration pulse of preys followed by a sigmoidal growth of predators. We quantified its kinetics as a function of the concentration of polymerase (pol) and nicking (nick) enzymes and of predator. These reactions occurred at 44°C and to bring them into microfluidic devices we needed a technology that reduced evaporation. We tested three technologies. PDMS devices were compatible with our reaction, however, evaporation remained too high despite our efforts in reducing it. Microfluidic stickers made of photocurable glue were, alike PDMS devices, optically transparent and capable of replicating submicron size features but, in addition, were less porous and thus evaporation was strongly reduced. We also explored a low-cost fabrication method that consisted in embedding pre-cut parafilm channels between two polystyrene (or glass) slides. Finally, we studied wave propagation in these devices. In straight channels, we observed that

the relative velocity of the pursuing predator wave compared with the velocity of the evading prey depended on the state of the propagation dynamics and on the material of the channel. To test the capacity of our microfluidic technique to investigate geometry-related phenomena we studied two cases: front propagation along a 90° turn and computing the optimal path in a maze. Moreover, during this work, an alternative microfluidic method to control the initial condition of the wave was developed using PDMS valves. In summary, we have explored microfluidic tools compatible with the investigation of DNA-based reaction-diffusion systems. Although evaporation is still a challenge, we believe that this work allows the control of geometry in such systems. This work was published in *J. Phys. Chem. B* (Appendix C).

4.1 State of the art

Living cells must be capable of sensing their dimensions by continuously mapping their surroundings to adapt to physical constraints. This sensing of space needs a molecular ruler for decision making. Such a molecular ruler would involve transportation of molecules across cells, often at much larger distances than that of the size of molecules. Diffusion alone only drives chemical processes into homogeneity, hence the emergence of spatiotemporal organization requires also locally interacting out-of-equilibrium processes [8]. Reaction-diffusion (RD) processes could act as these molecular rulers and programs because they have an intrinsic characteristic length (L_c), which is given by the diffusion coefficient of molecules (D) and their reactivity (k): $L_c = (D/k)^{(1/2)}$. Traveling waves are RD processes that can transmit chemical information across space within cells and operate in an out-of-equilibrium manner. Some biological examples of the functionality of traveling waves are: calcium waves [61, 62] that are involved in the activation of cellular processes, Min CDE protein waves [63] that oscillate from pole to pole in *E. coli* to determine the division site, or traveling waves of cyclic AMP [64] in cell-to-cell communication in the amoebae *Dictyostelium discoideum* [65]. These traveling waves propagate within the boundary-limited and crowded intracellular world in the living cell. However, due to the complexity of living systems, it is experimentally challenging to study the effect of geometry on the spa-

tiotemporal organization of chemical waves in vivo. To circumvent this problem, wave propagation studies have been performed under controlled conditions in artificial systems.

In this section, we review several works that have studied the effect of geometry on the propagation dynamics of traveling waves. First, we review the effects of curvature on Belousov-Zhabotinsky (BZ) waves [15]. Second, we will give examples in which enclosures give rise to new spatiotemporal patterns and other cases where physical obstacles impact the original pattern. We focus on the propagation of chemical waves and how they react to lateral and two-dimensional geometrical constraints. Finally, we emphasize the use of microfluidic technology to control initial and boundary conditions.

4.1.1 Effect of curvature on the wave propagation velocity

The first experimental approach to study the effect of curvature on a BZ chemical wave was done by Foerster et al. [66]. The temporal evolution of the collision of circular waves propagating from opposite directions was recorded. The collisions formed cusplike structures of high curvature, for which velocities were measured (Fig. 4.1). The normal velocity, $v_\perp$, depended on the front curvature, γ, according to an eikonal relation,

$$v_\perp = v_0 + \gamma D, \tag{4.1}$$

where v_0 is the planar wave velocity and D is the diffusivity. From the term γD in Eq. (4.1) we see that the effect of curvature is relevant only in the length scales of the order of a diffusion length [67]. Indeed, the normal velocities of the chemical waves increased linearly with the curvature (Fig. 4.1B). These experiments validated Eq. (4.1) since D, the slope of the linear regression, was in good agreement with the expected diffusion coefficient of the propagator species.

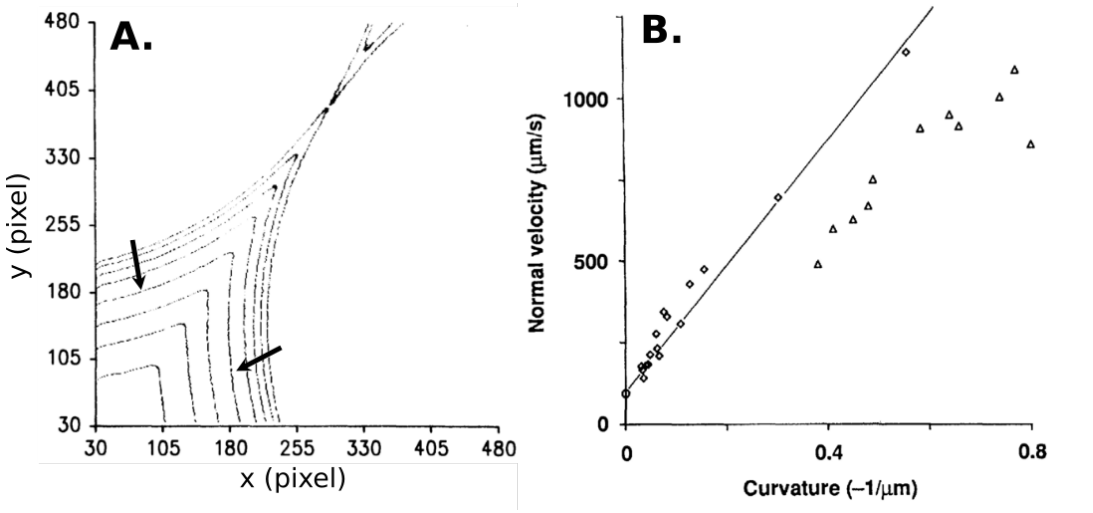

Figure 4.1 – **The normal velocity of a traveling wave depends on its curvature. (A)** Cusplike structures put into a montage of successive contour maps with time increasing in the direction of black arrows. The time of the entire sequence is 5 s. The spatial resolution is 4.5 μm per pixel. **(B)** The normal velocity and curvature were determined from the cusplike structures produced during the collision of circular BZ-chemical waves. The computed slope of the linear fit is 1996 $\mu m^2/s$ with an intercept of 95 μm/s. The slope is the calculated diffusion coefficient of $HBrO_2$, and this value can be compared to the estimated value (1800 $\mu m^2/s$) in [68]. This figure was reprinted from [66].

The propagation of chemical waves in the previously described experiments (Fig. 4.1) was not performed under geometrical constraints. But the theory from Eq. (4.1) and the experimental validation inspired subsequent works on wave propagation experiments with boundary conditions.

The effect of curvature and geometrical constraints was exploited to create logic gates using BZ waves in capillaries as input [69, 70]. The experimental set-up consists of two open capillaries with their open ends facing each other with a gap in-between. The input is a BZ wave traveling in the capillary towards the gap and the output is a propagation of a wave in the gap. As an example, we present an implementation of an AND and an OR gate in Fig. 4.2. A BZ wave was triggered from the right side of the capillary. The wave traveled along the capillary reaching the exit. In the case of the OR gate (Fig. 4.2A), the conditions were such that the wave can further propagate through the gap between the two capillaries. The authors also demonstrated that as long as a

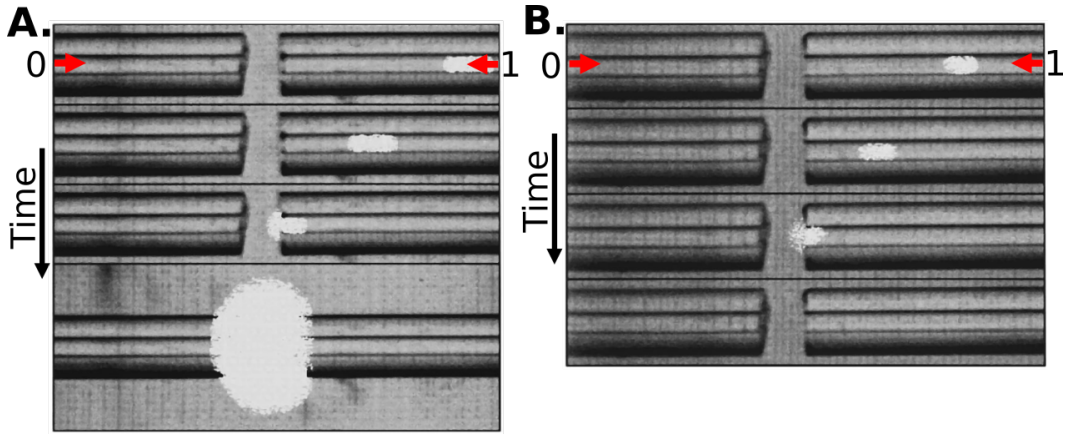

Figure 4.2 – **OR (A) and AND (B) logic gates in capillaries with Belousov–Zhabotinsky waves.** **(A)** Images of the traveling wave at 10 s intervals in a capillary tube of 50 µm radius. The wave was only triggered from the right tube (red arrow 1), then in the OR gate the wave reached the exit and propagated into the gap. No wave was triggered from the left tube (red arrow 0). The size of the field view is 0.38 × 2.42 mm^2 for top three panels and 0.82 × 2.42 mm^2 for the bottom panel. The gap between the tubes is 180 µm. And BrO_3^- = 0.14 M. **(B)** In the AND gate the wave reached the exit but it did not propagate into the gap. The same conditions were used as in (A) except that BrO_3^- = 0.1085 M. The size of the field view is 0.38 × 2.58 mm^2 for the three panels. These figures were reprinted from [69].

wave was triggered from either capillary, the OR gate was successful. In the case of the AND gate, the wave reached the exit but it did not propagate into the gap (Fig. 4.2B). BZ waves propagated only through gaps above a critical size. The observations can be explained as follows. For the OR gate the concentration of BrO_3^- was tuned to have a high value of v_0 while in the AND gate v_0 was lower. When the wave gets out of a capillary of radius r the front is convex with also radius r. A convex front has $\gamma < 0$ (Fig. 4.3) and thus there is a critical value $\gamma_c = \frac{1}{r_c}$, give by $r_c = D/v_0$ for which $v_\perp = 0$ and the front stops. In the AND gate a single wave at the exit of one capillary had $v_\perp$ but when two waves combined $\gamma > \gamma_c$ and thus $v_\perp > 0$.

The effect of the curvature was later used to sense door sizes using BZ-waves in labyrinths [71]. Door sizes and optimal trajectories were determined in geometries with large and small doors positioned at different locations (Fig. 4.4). The curvature effects lead to speeding up or slowing down of waves that otherwise would travel at constant velocities in the bulk. The wave propagation velocity was highly reduced

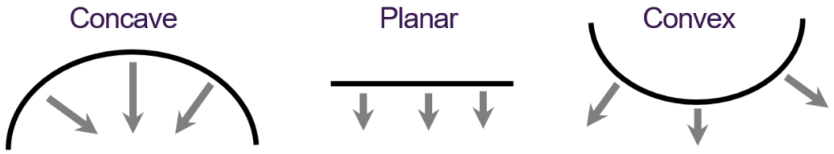

Figure 4.3 – **Value of curvature depends on the shape of the propagation front.** The curvature , γ, values in Eq. (4.1) for the three front shapes are: (1) $\gamma > 0$ (concave), (2) $\gamma = 0$ (planar) and (3) $\gamma < 0$ (convex).

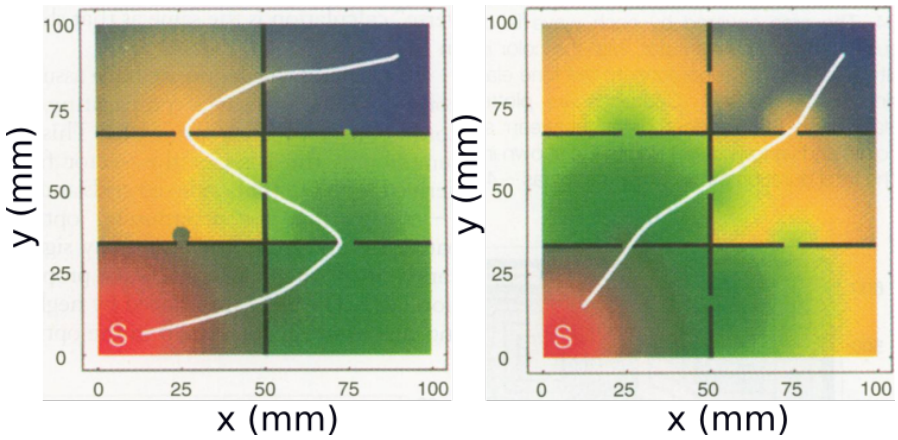

Figure 4.4 – **Belousov–Zhabotinsky waves interrogate door sizes in labyrinths.** Waves traveled faster through larger doors and slower through smaller ones. White lines are the optimal paths. Total time, dimensionless, was 24.15 and 14.60 for left and right plots respectively. Time lapses were color coded, time increasing in the following order: red, green, yellow and blue. This figure was taken from [71].

when exiting narrow doors and enhanced at larger ones. In the same publication [71] a more complex labyrinth was mapped by the BZ waves (Fig. 4.5). The propagating waves solved this labyrinth by finding the minimum path length between two points.

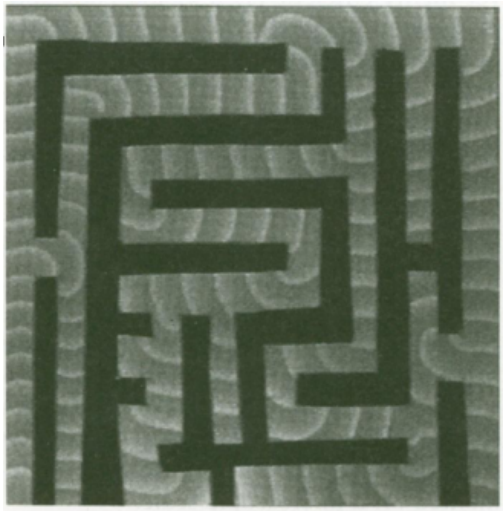

Figure 4.5 – **Belousov–Zhabotinsky waves map the geometry of a labyrinth.** 50 images at 50 s intervals were superimposed of the propagating waves. Total area of the labyrinth was 3.2 × 3.2 cm^2. This figure was obtained from [71].

4.1.2 Effect of spatial confinement on wave propagation

In a more recent study, traveling waves were assembled [72] by purifying the MinCDE protein system, which is involved in cell division in *E. coli* [73]. Min protein waves on planar lipid bilayers organized into spirals when no geometrical constraints existed. Spirals switched to aligned waves in reactors of size similar to the characteristic length scale of the protein waves, l_c (50-100 µm) (Fig. 4.6A). In the absence of obstacles, traveling waves of Min proteins with wavelength 50 µm and 100 µm were observed on supported lipid bilayers. Propagation always oriented along the largest distance as illustrated by the experiment within a rectangular region (Fig. 4.6B) in which the protein waves traveled diagonally.

In the presence obstacles, of size around l_c, influenced the outcome pattern. When the obstacles were larger than l_c, see Fig. 4.7A, waves did not influence each other, whereas when the size of the obstacles were $\approx l_c$, irregular patterns were formed (Fig. 4.7B). When the obstacle size was reduced, propagation was unaffected once again, see Fig. 4.7C. Definitely, Min-protein waves sensed and responded to geometry, but to extend this conclusion and to expose the principles of spatiotemporal organization under geometrical constraints will require further investigations with other reactive

systems and the use of microfluidics, for precise liquid handling and definition of the boundary conditions.

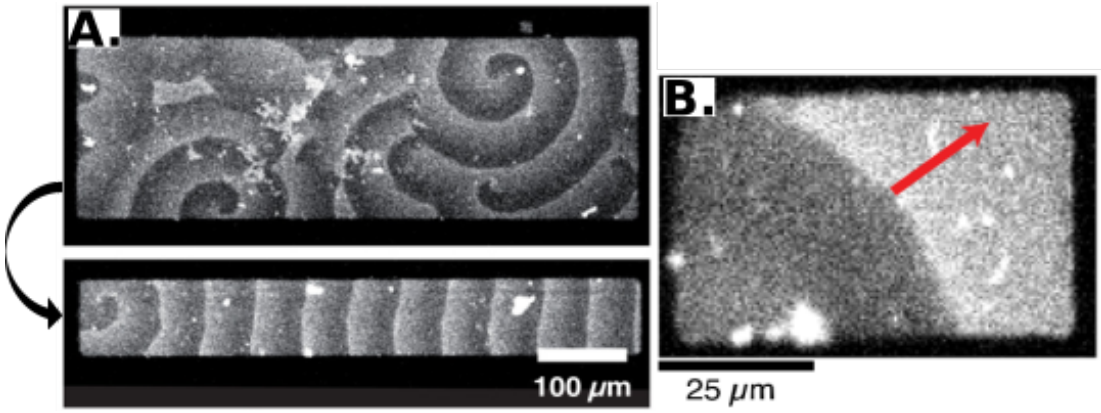

Figure 4.6 – **Min Protein waves oriented along the longest path when geometrically constrained. (A)** Min protein waves propagated on membranes without (upper) and with (bottom) geometrical confinement. **(B)** Waves propagated diagonally (red arrow) in a rectangle patched. Figures compiled from [72]. The concentration of the proteins were: 0.8 µm MinD, 0.5 µm MinE with 10% Cy5-labeled MinE.

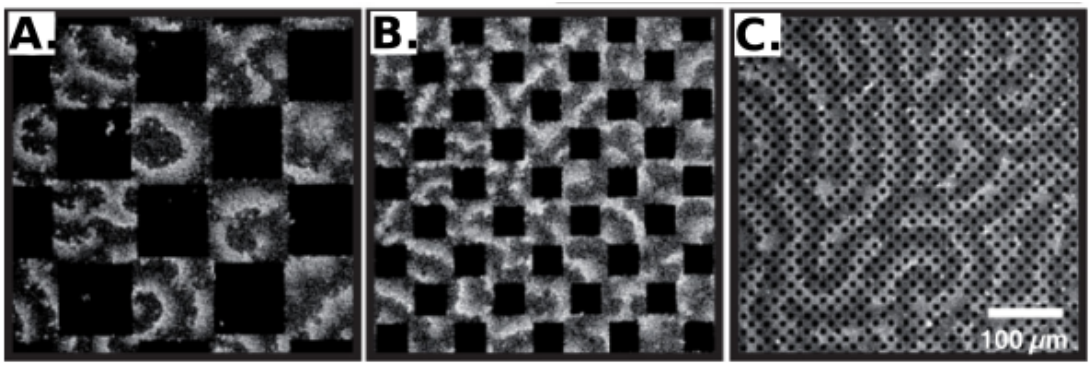

Figure 4.7 – **Min Protein waves are influenced by obstacles of (B) characteristic length scale but not by (A) larger or (C) smaller ones.** Min protein waves propagated on membranes in the presence of obstacles (black patches). The concentration of the proteins were: 0.8 µm MinD, 0.5 µm MinE with 10% Cy5-labeled MinE. Figures compiled from [72].

4.1.3 Microfluidic approaches to control reaction-diffusion patterns

Recent advances in microfluidic technology allowed to control boundary conditions and to explore BZ waves in micrometer size channels. Ginn et al. [74] illustrated how

the curved shape of the front was affected by the geometrical confinement (Fig. 4.8). In 1 mm regions, the BZ waves propagated with a curved shape. When these waves went through a channel of 50 µm width they lost the curved shape. But when the waves exited the narrow channel the original shape was recovered.

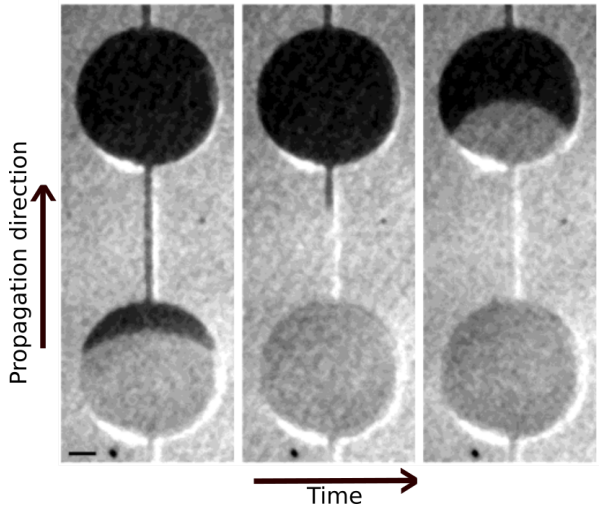

Figure 4.8 – **Propagation of an oxidation wave through a BZ system in a microreactor.** The time interval between the snapshots is 10 s. Bright and dark regions represent the oxidized and reduced states of the ferroin-catalyzed CHD-BZ system, respectively. The dimension of the channel are 80 µm height and 50 µm width. The circular regions of the microreactor is 1 mm in diameter (reference bar is 200 µm). Initial BZ concentrations are 1.50 M H_2SO_4, 0.15 M CHD, 0.10 M $NaBrO_3$, and 3.1 mM ferroin. This figure was taken from [74].

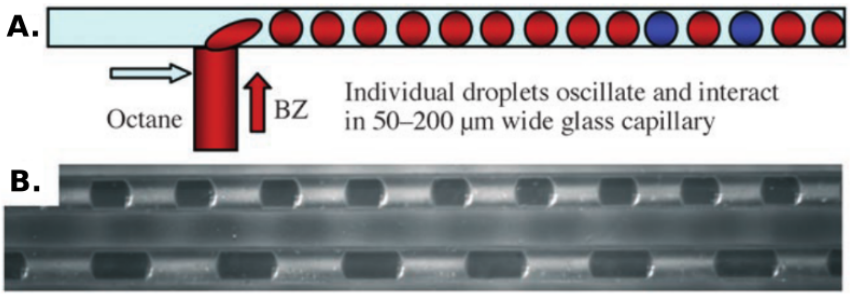

Figure 4.9 – **Belousov–Zhabotinsky droplets spaced by octane solution in a glass capillary. (A)** Drawing of the microfluidic device. Red and blue droplets correspond, respectively, to the reduced catalyst (ferroin) and to the oxidized form (ferriin). **(B)** Snapshot of microfluidic device with droplets. BZ droplets with convex surfaces are dark due to ferroin. The capillary is 150 µm in diameter and 4.8 mm in length. Figure was taken from [75].

Microfluidics was also used to study the level of communication between oscillating systems. This was achieved by the comparmentalization of the BZ system in droplets within glass capillaries (Fig. 4.9). BZ water-in-oil droplets were created by flowing, normal to each other, octane and BZ-solutions, see Fig. 4.9A. The spacing with octane allows for communication between droplets through the hydrophobic intermediate Br_2. The authors were capable of finding stationary Turing structures that emerged from an initial state of oscillations (Fig. 4.10). In a latter publication this technology was extended to control the droplet size and the octane gaps, and six of the Turing-type instabilities were found [20]. By constructing two-dimensional arrays of droplets, the authors elegantly demonstrated the suitability of microfluidics to study spatiotemporal organization.

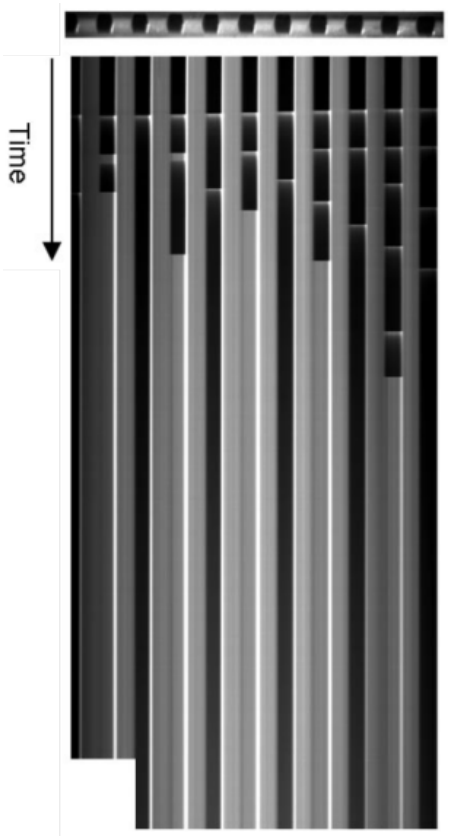

Figure 4.10 – **The Turing structures of BZ in water-in-oil droplets were generated from an initial oscillatory state.** Space-time plot showing emergence of stationary Turing structures with alternating oxidized and reduced states. The total time is 180 min. The capillary is 150 µm in diameter and 4.8 mm in length. Figure was taken from [75].

We have seen that the propagation of chemical waves is strongly affected when geometrical constraints are of the order of magnitude of the wavelength, which has been used to create, among other things, logic gates in the BZ system. In order to be able to impose geometrical constraints in the PEN-DNA-toolbox systems, it was needed to develop specific microfluidic devices, which we will present in the following sections.

4.2 Kinetics of Predator-Prey reactions

Here, the Predator-Prey DNA network, previously published by Fujii and Rondelez [32], is adapted by removing the enzymatic degradation (exonuclease) of DNA species, but all other reactions remain. In the absence of exonuclease, the Predator-Prey temporal dynamics change from oscillations to a pulse of preys that grows exponentially then decays sigmoidally during predation. Because it is sufficiently complex but robust this is a good network to test for the compatibility of our microfluidic techniques with PEN- DNA-toolbox systems in general.

In this section we will study how the dynamics of the degradation-free Predator-Prey system depend on the concentration of pol, nick and the initial predator.

4.2.1 Predator-Prey mechanism without enzymatic degradation

The DNA-based degradation-free Predator-Prey system involved three DNA species (sequences listed in Fig. 4.11A): prey (N), grass (G) and predator (P). G was a hairpin and P had a palindromic design. The Predator-Prey network was based on two overall reactions: (i) $N \longrightarrow 2N$, autocatalytic prey growth, and (ii) $N + P \longrightarrow 2P$, predation. In the prey growth, depicted in Fig. 4.11B, N hybridizes to G and pol extends the G:N complex. This is followed by a nicking step of I_N, which dehybridizes into two N and one G. In the predation reaction, N binds to P, then the P:N complex is extended to produce two P.

In this chapter we used the buffer PP (listed in Table 1.3), which contained two enzymes: Nb.BsmI nicking enzyme (nick) and Bst large fragment DNA polymerase (pol).

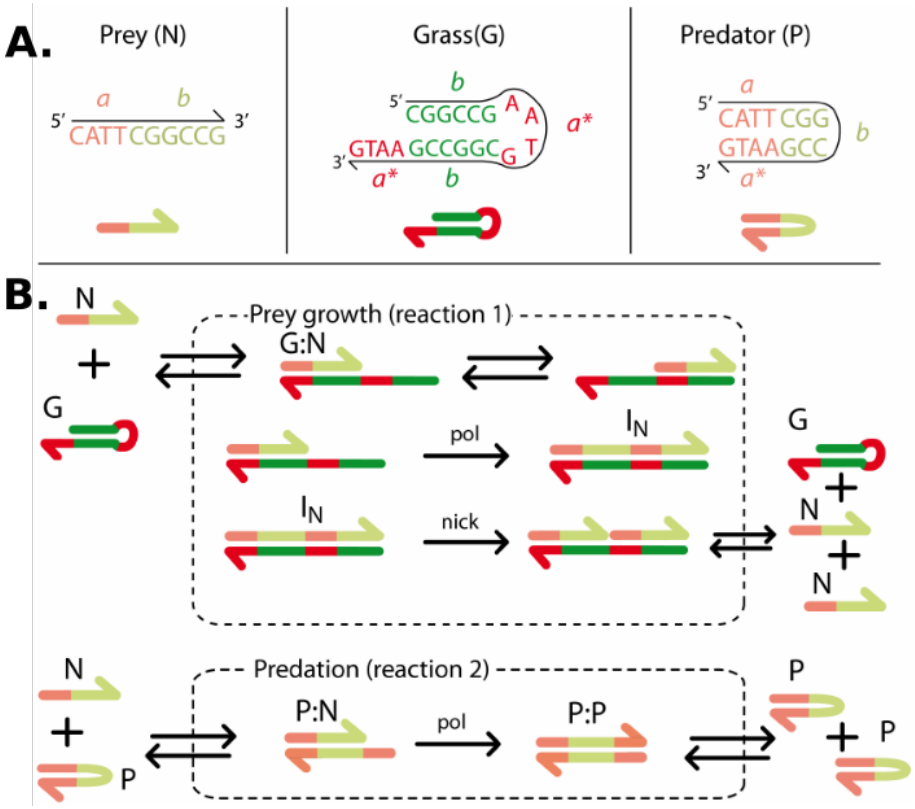

Figure 4.11 – **The Mechanism of the DNA-based degredation free Predator-Prey system. (A)** Harpoon-ended arrows represent single strand DNA. Their sequences are given in uppercase. a and b are sequence domains CATT and CGGCCG respectively, and a* and b* are their complementaries. **(B)** Autocatalytic prey growth over grass template G involves two enzymes, pol and nick. The predation reaction consumes N to produce two copies of P.

Our stock concentration of nick and pol were 8000 and 160 U/mL respectively, but their concentrations in the reaction mixture were varied according to the experiment. Throughout this chapter the enzyme concentrations are reported in dimensionless formats: $pol_n = pol/pol_0$ with pol_0 = 16 U/mL and $nick_n = nick/nick_0$ with $nick_0$ = 80 U/mL.

4.2.2 Experimental probing of the DNA-based Predator-Prey network

The Predator-Prey dynamics are monitored using two fluorophores as in Section 1.1.3. The fluorescence of DY530, which is attached to the grass template (G), is quenched

(quantum yield, $\phi_N = 0.70$) upon hybridization with N near the 3', Fig. 4.12A. P contains the sequence of N, so it is able to hybridize to G as well. However, the quenching quantum yield of P ($\phi_P = 0.23$) is three times smaller than that of N. The determination

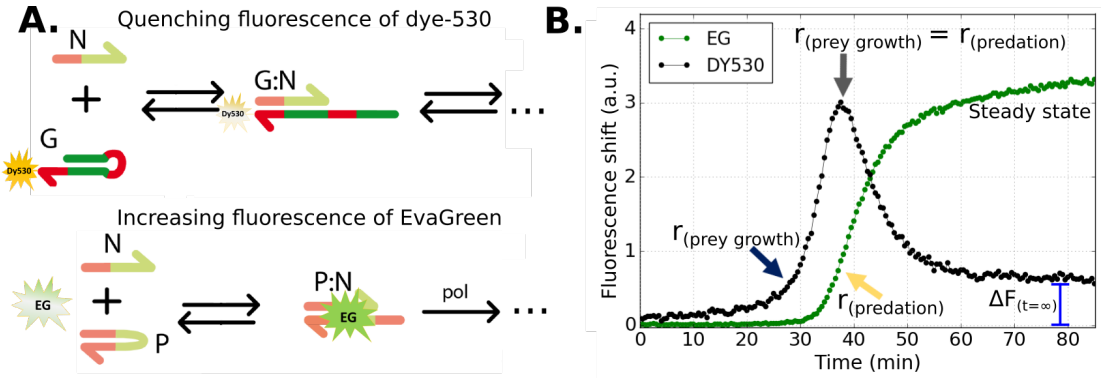

Figure 4.12 – **Monitoring description of the extent of Predator-Prey dynamics. (A)** DY530 dye attached to G and DNA-binding dye EvaGreen are used as reporters. **(B)** Predator-Prey dynamics are followed by the fluorescence shift of EvaGreen (EG) and DY530. The main stages of the dynamics are labeled.

of fluorescence quantum yields is performed in titration experiments, in which the initial concentration of grass template (G_0) is fixed at 200 nM and either P or N is added to a series of tubes at increasing concentrations from 0 to 3.5 µM (Fig. 4.13). When the concentration of N increases, the fluorescence of DY530 decreases. As in Chapter 1 to facilitate the reading we plot the fluorescence shift of DY530, which is the absolute value of the fluorescence change such that it is always proportional to N. The dependence of the fluorescence change is fitted to a model derived from equilibrium reactions as previously described in Eq. (1.5) , Page 18.

EvaGreen (EG) fluorescence is proportional to the concentration of double strand DNA (Fig. 4.12A). Consequently, in the monitoring of the Predator-Prey dynamics we expect a contribution to the fluorescence shift from all species. However, when observing the experimental data, the fluorescence shift of EvaGreen seems to correlate only to the predation. For example in Fig. 4.12B, the increase in EvaGreen fluorescence does not start simultaneously with the prey growth, instead there is a start delay of around 10 minutes. The signal increases steadily even during the prey decay, then it reaches a steady-state. In addition, previous works reported that EvaGreen preferentially stains

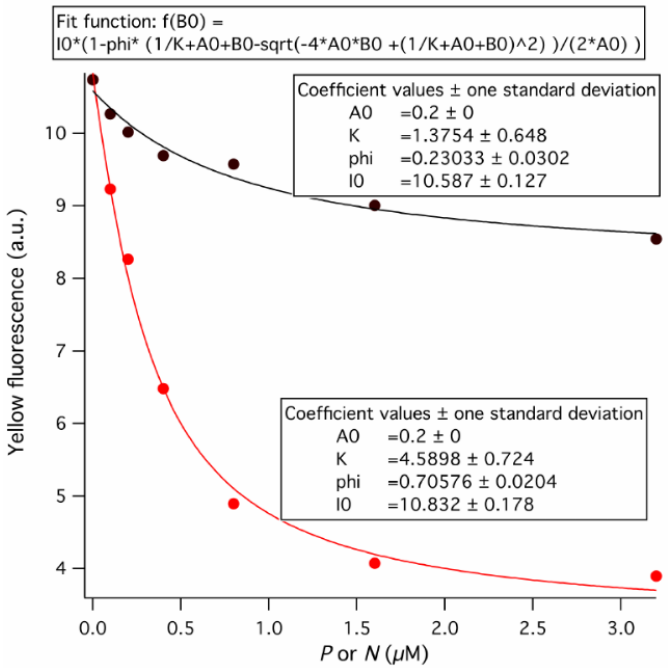

Figure 4.13 – **Dependence of yellow fluorescence on N (red) or P (black).** Fluorescence of DY530 as a function of P or N. Reaction mixtures contained 200 nM G and usual buffer, with the exception of enzymes, and were incubated at 44°C for 10 minutes. Then the fluorescence of each individual tube was recorded and the data fitted to the equation shown above the plot.

the predator [28, 32]. From these clues, we assume P is monitored by EvaGreen and N by DY530.

Both temporal reactions and wave propagations are monitored using DY530 and EvaGreen which are later referred in the text as yellow and green fluorescence shifts respectively. Kinetic experiments are carried out in test tubes and monitored in a real-time PCR machine (Biorad CFX96 or Qiagen Rotor-Gene Q) as in previous chapters.

The Predator-Prey dynamics are always first studied in 0D experiments, in which by vortexing before introducing the tubes into the real-time PCR machine we obtain a system that is spatially homogeneous in concentration of all the chemical species. In a typical Predator-Prey 0D experiment, as seen in Fig. 4.12B, the fluorescence shift of DY530 increases during prey growth up to a maximum, where the prey growth rate equals the predation rate, then after this point the signal decreases reaching a

steady state. This maximum corresponds to N_{max} and the steady state to $P = P_{max}$ and $N_{(t=\text{inf})} \approx 0$. The signal of DY530 does not go back down to zero at steady state, $\Delta F_{t=\text{inf}}$, due to the quenching contribution of P.

4.2.3 Effect of polymerase concentration

The pol enzyme participates in both prey growth and predation reactions (see the mechanism in Fig. 4.11B), so we first study the effect of pol concentration on the Predator-Prey dynamics. In Fig. 4.14 we plot the Predator-Prey dynamics for pol_n = 0.5-4. Increasing pol_n increases the maximum fluorescence shift and reduces the temporal width (w_t) of the bell-shaped curves.

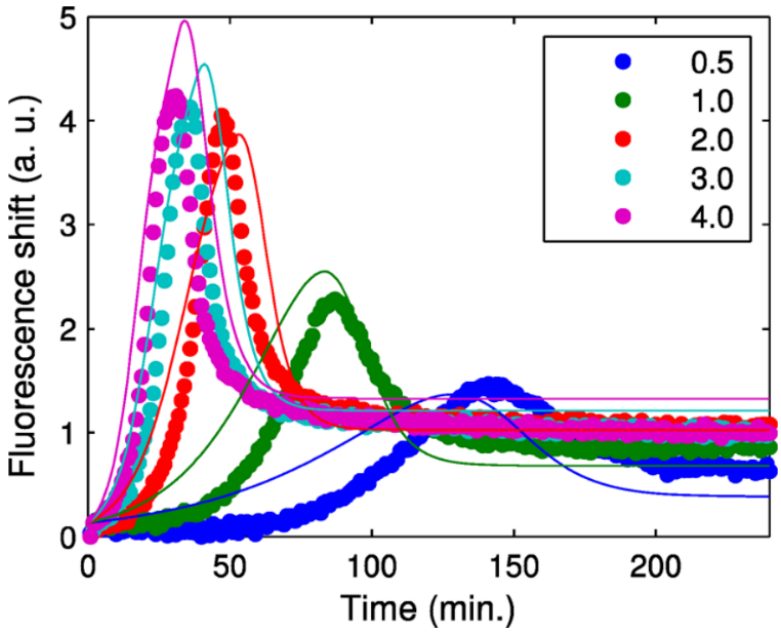

Figure 4.14 – **Predator-Prey dynamics at different pol concentrations.** Yellow fluorescence shift vs time for pol_n = 0.5-4. Solid circles and lines correspond, respectively, to experiments and to fits to the model in Eq. (4.2).

A simplified model, adapted from the model proposed by Fujii and Rondelez [32], is used to fit the experimental data. The autocatalytic prey growth and predation reaction rates, r_i, are described by saturable Michaelis-Menten equations, Eqs. (4.2)

and (4.3) respectively,

$$N \xrightarrow{r_1} 2N \qquad r_1(N) = \kappa_1 pol_n \frac{N}{1+bN} \tag{4.2}$$

$$N + P \xrightarrow{r_2} 2P \qquad r_2(N,P) = \kappa_2 \frac{NP}{1+bP}. \tag{4.3}$$

The system of equations ruling the dynamics is thus

$$\frac{dN}{dt} = r_1 - r_2 \tag{4.4}$$

$$\frac{dP}{dt} = r_2,$$

where N and P are the prey and the predator concentrations, respectively. κ_1, which is proportional to the initial concentration of grass template, and κ_2 are rate constants, pol_n is a normalized concentration of pol enzyme and b is a saturation term. In these equations, the autocatalytic growth rate of prey depends explicitly on κ_1 and pol_n, which is experimentally accessible. In the case of predation, pol_n is not explicit in Eq. (4.3). However, N_{max} depends on pol_n, so the apparent predation rate, r_p, also depends on it. Using the data of the dependence of fluorescence on N and P previously discussed (Fig. 4.13), we could relate the data from Fig. 4.14 to concentrations of N and P, then fit and solve for the other parameters in Eq. (4.4). The values obtained were $\kappa_1 = 0.05 \pm 0.02$ min^{-1}, $\kappa_2 = 0.5 \pm 0.1$ min^{-1}μM^{-1} and $b = 1.0 \pm 0.5$ μM^{-1}. This phenomenological model, Eq. (4.4), captured both the maximum and final fluorescence dependence on pol_n, as well as quantitatively the observed experimental bell-shaped dynamics.

To compare quantitatively the experiments with the model we use two phenomenological rates, r_g and r_p, corresponding to the prey growth and predation respectively. These are obtained by fitting functions $e^{r_g t}$ and $e^{-r_p t}$, respectively, at short and long times to the curves in Fig. 4.14. The prey growth rate, r_g, depends linearly on pol_n,

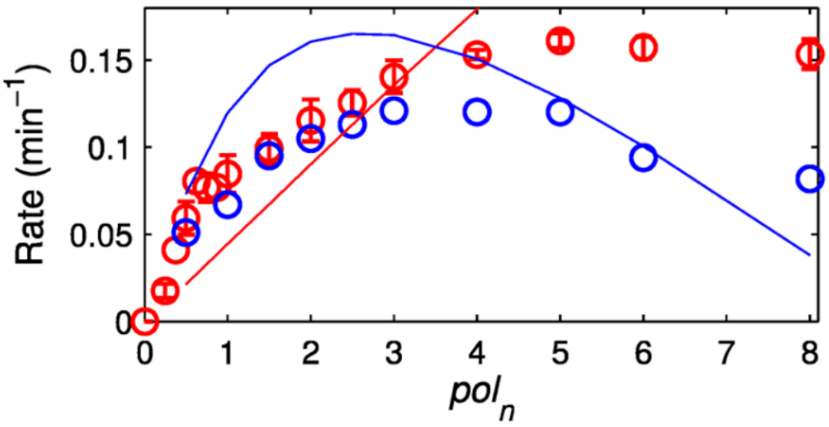

Figure 4.15 – **Dependence of the phenomenological rates, r_g (red), and r_p (blue), on pol_n.** Lines correspond to simulations and circles to experimental data from Fig. 4.14 and fig. S4 in section 1.4 of SI Appendix C.2. The values of the parameters in Eqs. (4.2) and (4.3) for the simulations were: $\kappa_1 = 0.05$ min^{-1}, $\kappa_2 = 0.5$ min^{-1}µM^{-1} and $b = 1.0$ µM^{-1}.

experimentally and in the simulations, in the range of pol_n = 0.5-4 (Fig. 4.15). However, the r_g saturation above $pol_n > 4$ is not captured. The model also captures well the dependence of r_p on pol_n. In conclusion, the simplified three-parameter model (Eqs. (4.2) to (4.4)) and growth rate assumptions are sufficient for describing the essential dynamics of the Predator-Prey system presented here.

4.2.4 Effect of nickase concentration on self-start

The autocatalytic loop of the Predator-Prey reactions suffered from self-start, which is defined as the activation of a template even in the absence of input as we have seen in Section 2.4.1. During the self-start, N is produced by the pol enzyme even at $N_{(t=0)} = 0$, then the same dynamics are obtained as in the case of $N_{(t=0)} > 0$. This limited the time window at which wave propagation could be monitored as self-start destroyed the waves. When these experiments were performed the bistable network used in Chapter 2 was not yet available. We turn our attention to the nicking step to study the possible effect of $nick_n$ on the self-start. In the full mechanism proposed in Fig. 4.11, a nicking step follows the production of intermediate species, I_N. In our hands, a change of nick in the range $nick_n$ = 1-10 had a negligible influence in the

Predator-Prey dynamics. We thus concluded that the nicking reaction was not the kinetically limiting step.

In Fig. 4.16 we see the Predator-Prey dynamics at $nick_n$ = 10, 12, 16. The delay in reaction start time motived us to explore the self-start as function of $nick_n$. We performed a similar experiment but without an initial concentration of N (Fig. 4.17). In this figure, we see that the growth prey rate and the width of the pulse are independent of $nick_n$, but self-start is delayed by increasing $nick_n$.

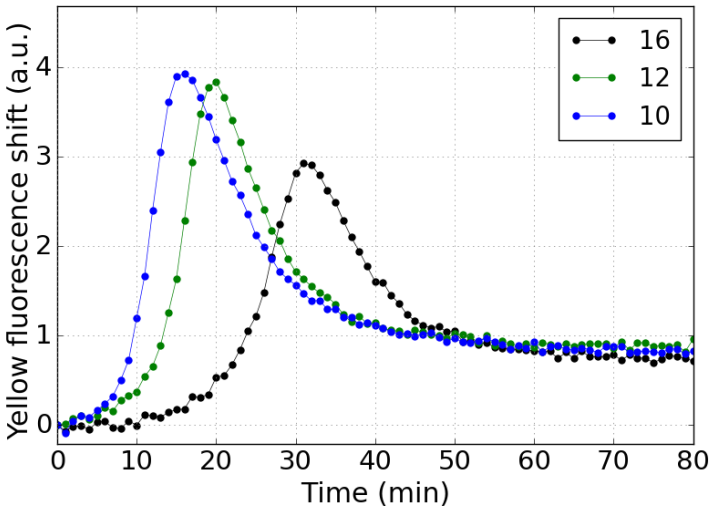

Figure 4.16 – **Predator-Prey dynamics at different nick concentrations.** Yellow fluorescence shift vs time for $nick_n$ = 10, 12 and 16. Reactions were performed at 44°C, pol_n = 1, $P_{(t=0)}$ = 2 nM, $N_{(t=0)}$ = 10 nM and G_0 = 200 nM.

The data from Figs. 4.16 and 4.17 were normalized to extract a start time at the same value of fluorescence. This value was chosen to be 0.1. Then, a linear fit (Fig. 4.18) of the reaction start time as function of $nick_n$ was performed. And although only three data points were available, it can be concluded that nick strongly delays self-start while only slightly changes the dynamics in the presence of N.

In conclusion, prey growth is independent of $nick_n$ when pol_n is limiting and $nick_n$ is in excess. Moreover a large excess of $nick_n$ can be used to reduce self-start. We can propose a mechanism to explain the delay of the self-start (Fig. 4.19). In fact, the G:N complex contains a specific sequence site for the nick to bind on. if the nick

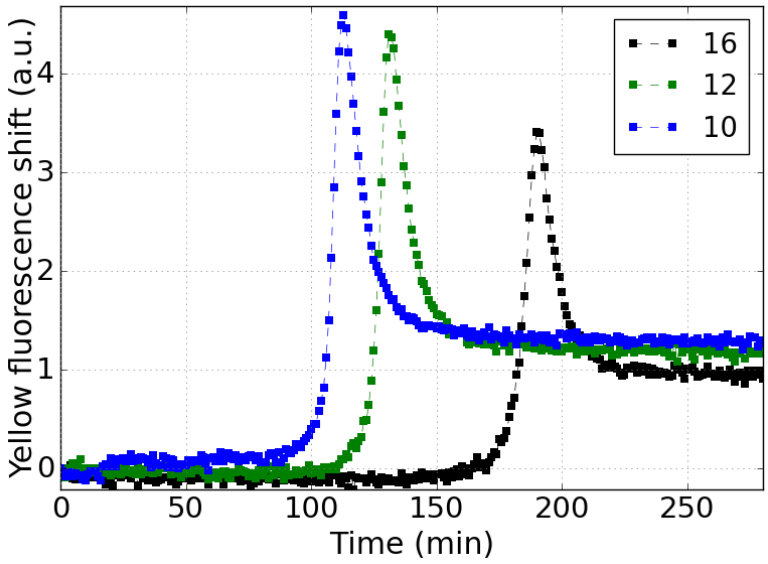

Figure 4.17 – **Predator-Prey dynamics without an initial *N* at different nick concentrations.** Yellow fluorescence shift vs time for $nick_n$ = 10, 12 and 16. Reactions were performed at 44°C, pol_n = 1, $P_{(t=0)}$ = 2 nM, $N_{(t=0)}$ = 0 nM and G_0 = 200 nM.

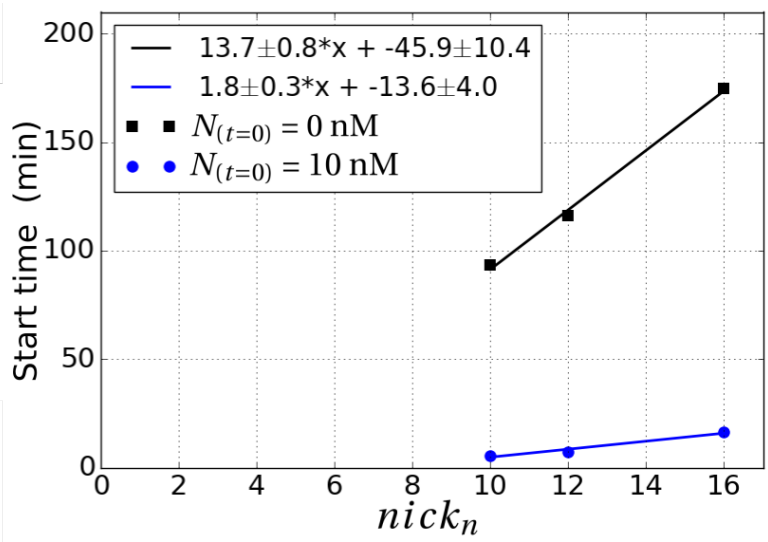

Figure 4.18 – **Linear fit of the reaction start time as a function of nick concentration**. Data from Figs. 4.16 and 4.17 were normalized. And the reaction start time, $t_{(F_{Normalized}=0.1)}$, was extracted and linearly fitted as a function of $nick_n$.

is bound, pol cannot bind and extend the upper strand. This competition for the G:N substrate could result in a partial inhibition of the polymerization reaction. The inhibition should be enhanced by increasing the concentration of nick. So we expect this inhibition to be mostly effective in the case of $G : N \ll nick_n$.

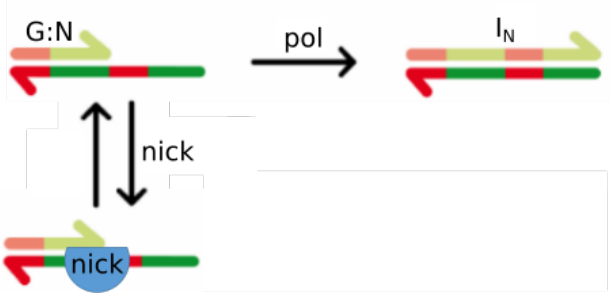

Figure 4.19 – **Schematic description of the inhibition of the pol step by competition with nick for a template.** The template G:N can be extended by pol to produce I_N or nick can bind unproductively to G:N. Nick can target G:N because this complex contains a recognition nick site (5'...GAATGC...3').

4.2.5 Effect of initial predator concentration

The dynamics of the Predator-Prey pulse at different initial concentrations of predator serve to explore the state at which the predation overtakes the prey growth. In Fig. 4.20 we monitored N and P, respectively, by yellow and green fluorescence. We also observe that at $P_{(t=0)} = 0$, the prey pulse reaches a maximum at t = 20 min and then decreases over time. This maximum and subsequent decrease correlates with the increasing in the green fluorescence shift (black arrow in Fig. 4.20), which implies that this decrease in the prey signal is due to a predator self-start.

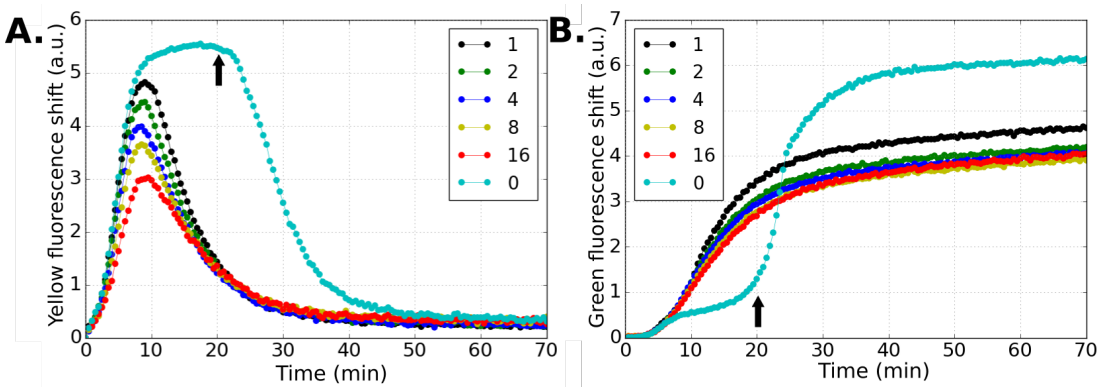

Figure 4.20 – **Predator-Prey dynamics at different initial predator concentrations.** **(A)** Yellow fluorescence shift vs time for $P_{(t=0)}$ = 0-16 nM. **(B)** Green fluorescence shift vs time. Black arrow points to self-start of the predation. Reactions were performed at 44°C, $nick_n = 5$, $pol_n = 1$, G_0 = 200 nM and $N_{(t=0)}$ = 10 nM.

This means that our system is able of producing P even if it is initially absent. We

speculate that a truncated polymerization of N on a G template is possible. In this case, since G also contains a region that is partially complementary to P, it is not unlikely that an incomplete polymerization could result in the production of a tiny amount of P which could then exponentially grow due to its autocatalytic nature in the system. In Fig. 4.20A the height of the fluorescence yellow shift decreases with $P_{(t=0)}$. This maximum N_{max} corresponds to $dN/dt = 0$. From Eqs. (4.2) to (4.4), we find

$$N_{max} = \frac{\kappa}{bP} + \kappa - \frac{1}{b}, \tag{4.5}$$

where $\kappa = \kappa_1 pol_n \kappa_2^{-1}$ and $P = P_{t=0} + P_{produced}$. From Eq. (4.5) we expect that N_{max} decreases as P increases and in a qualitative manner we see that our experimental results follow this tendency.

The data in Fig. 4.20 was normalized (analysis not shown here) and the curves were almost superimposable for $P_{(t=0)}$ = 1-16. To be more quantitative, we extracted the phenomenological prey growth rate (r_g) and plotted it as a function of $P_{(t=0)}$ (Fig. 4.21). r_g decreases somewhat linearly with $P_{(t=0)}$. At low $P_{(t=0)}$ the initial growth rate of the prey can be approximated by developing r_2 to the first order in P. From Eqs. (4.2) to (4.4) we have

$$r_g \approx \frac{dN}{dt}|_{P\to 0} = \kappa_1 pol_n \frac{N}{1+bN} - \kappa_2 N P_{(t=0)}. \tag{4.6}$$

From Eq. (4.6) we see that r_g decreases linearly with $P_{(t=0)}$ as we have observed in Fig. 4.21.

We also tried to reduce the prey self-start by increasing $P_{(t=0)}$ further. For this, the Predator-Prey dynamics were studied in reactions without an initial concentration of N at different $P_{(t=0)}$. Figure 4.22A shows that the pulse decreases with $P_{(t=0)}$ as previously observed in Fig. 4.20A. In the case of the green fluorescence (Fig. 4.22B), the final level tends to decrease with $P_{(t=0)}$ with the exception of $P_{(t=0)}$ = 32 nM. Also, increasing $P_{(t=0)}$ introduces a linear delay in the reaction starting time, as we see in Fig. 4.22C. However, a complete suppression of self-start through $P_{(t=0)}$ is theoretically impossible as this remains monostable regardless of $P_{(t=0)}$. As before, we extracted r_g

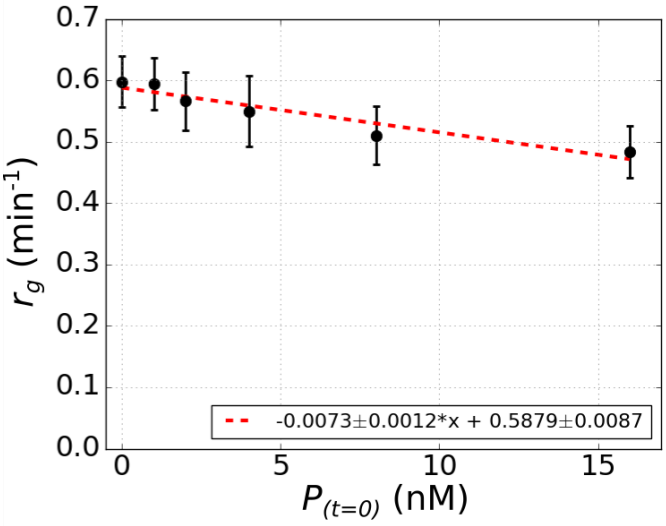

Figure 4.21 – **Dependence of the experimental growth rate r_g on the initial predator concentration of P.** r_g was calculated from the data in Fig. 4.20A. Error bars correspond to one standard deviation. Red dotted line is a linear fit of the data.

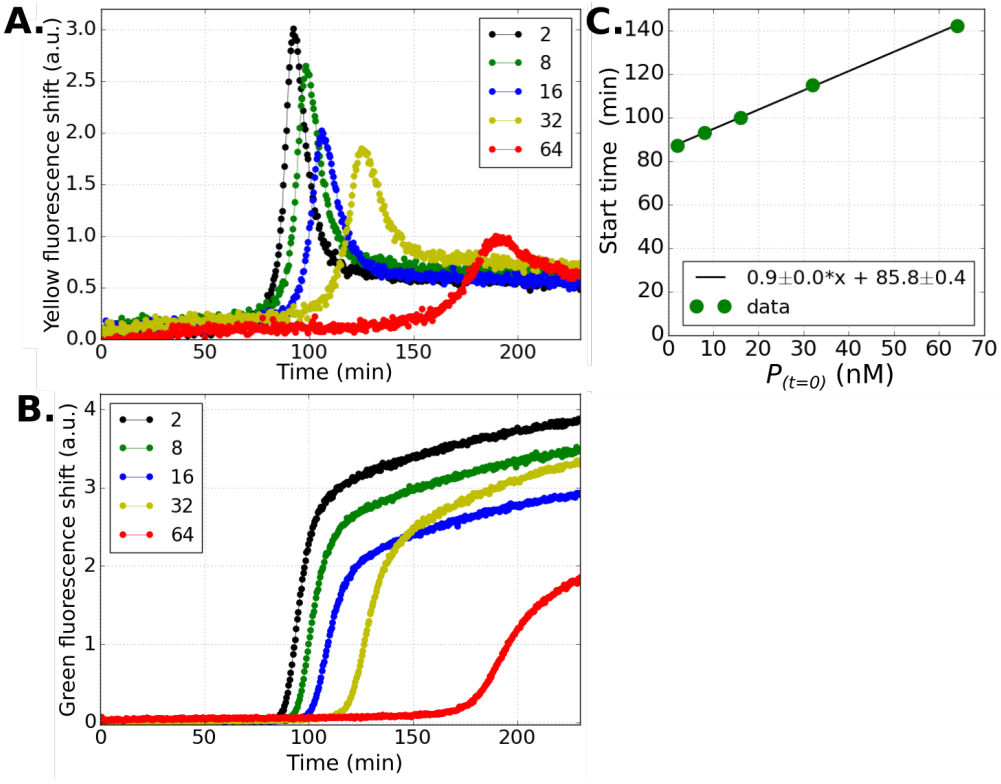

Figure 4.22 – **Predator-Prey dynamics without an initial N at different initial predator concentrations. (A)** Yellow fluorescence shift vs time for $P_{(t=0)}$ = 0-64 nM. **(B)** Green fluorescence shift vs time for $P_{(t=0)}$ = 0-64 nM. Reactions were performed at 44°C, $nick_n = 5$, $pol_n = 1$, $G_0 = 200$ nM and $N_{(t=0)} = 0$ nM.

and plotted it as a function of $P_{(t=0)}$ (Fig. 4.23). r_g decreases linearly with $P_{(t=0)}$. This agrees with our estimation of the linear contribution of $P_{(t=0)}$ on r_2 using Eq. (4.6).

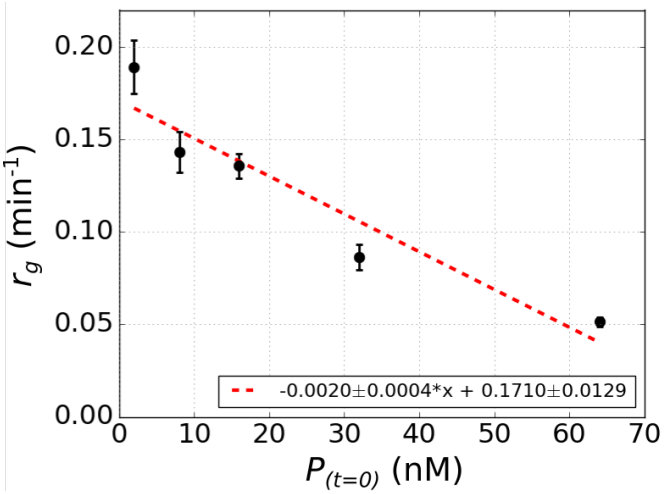

Figure 4.23 – **Dependence of the experimental growth rate r_g on the initial predator concentration of P.** r_g was calculated from the data in Fig. 4.22A. Error bars correspond to one standard deviation. Red dotted line is a linear fit of the data.

In conclusion, it can be said that $P_{(t=0)}$ determines the concentration of N at which $dN/dt = 0$. And the phenomenological rate growth of the prey linearly depends on $P_{(t=0)}$. Also autocatalytic nodes as we have already seen suffer from self-start. Although increasing $P_{(t=0)}$ introduces a time delay, it is not a powerful parameter to control self-start because it changes the growth kinetics.

4.3 Microfluidic devices used for spatiotemporal reactions

Microfluidic devices have emerged due to their capability to manipulate small volumes of liquid in the range of µL-pL with high-precision. One of the earliest work that demonstrated that elastomers are practical for the formation of well-defined and stable µm-sized capillaries as well as for the liquid handling was done by Delamarche et al. [76]. In this work polydimethylsiloxane (PDMS)-based devices were employed to pattern biomolecules on gold, glass, and polystyrene. PDMS has many advantages as a material to build microfluidic chips. The low Young's modulus of PDMS makes

incorporation of active elements such as valves and pumps possible [77]. In addition, its porosity makes PDMS permeable to gases thus allowing removal of air, which is trapped during the filling of the channel. However, it is this same property that causes evaporation when working above room temperature for several hours [78, 79]. The evaporation rates are in the scale of $\mu L\, h^{-1}$. In batch reactors of typical volume of 0.1-1 µL, evaporation precludes the use of PMDS devices at temperatures above ambient.

In order to prevent evaporation, the authors in [80] placed their batch PDMS devices in a humidified incubator and antievaporation channels were incorporated around the channels within the device. Another group reported submerging the entire device into a water bath [81]. Microfluidic devices have also been fabricated from nonporous materials, such as metal and silicon, but the fabrication techniques are often complicated and at much higher costs [79]. Poly(methyl methacrylate) (PMMA) has also been used in microfluidic devices because it is both nonporous and transparent. Evaporation-free PMMA devices were fabricated by direct-write laser micromachining [82]. But the fabrication required extra bonding time and surface smoothness at high temperatures.

In this section, we first describe the fabrication process for each of the microfluidic devices that we used in this chapter. Also, we present our efforts to find practical solutions to avoid evaporation within our experimental microfluidic setups. We explore a possible solution to the evaporation issue in PDMS devices. We also report the use of low-evaporation devices that were assembled from three nonporous materials: (1) photocurable glue/glass, (2) polystyrene/parafilm, and (3) glass/parafilm.

4.3.1 Fabrication and testing of microfluidic devices

Our PDMS devices are produced by casting a piece of PDMS on a silicon wafer containing a SU-8 mold, which is previously created by photolithography. The PDMS is prepared at a weight ratio of 10:1 base/curing agent and bubbles are removed by degassing in a vacuum desiccator for around 1h. The PDMS is cured at 70°C for 1h. Holes were drilled to access the channels. The PDMS used in the final device and a

glass slide are treated by O_2 plasma to allow permanent bonding when their surface are placed in contact.

As an effort to solve the evaporation issue in PDMS devices, an anti-evaporation water tank was incorporated into a device (Fig. 4.24). In this design the tank is placed on top of the fluidic channel. Also the thickness of the PDMS layer above the channel is reduced to 250 µm to minimize the evaporation. These PDMS microfluidic devices with embeded valves were compatible with DNA-based reactions networks (Fig. 4A in Appendix C, Page 203), however, evaporation remained an issue despite our efforts.

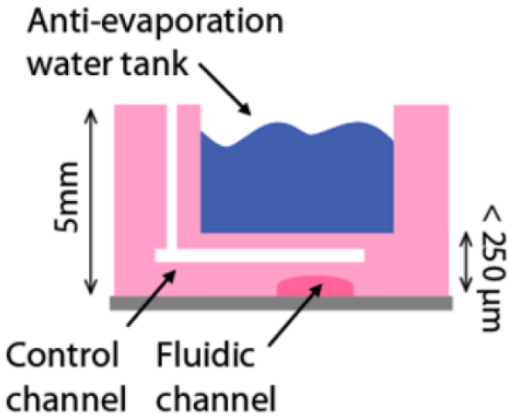

Figure 4.24 – **Schematic drawing of an anti-evaporation water tank on a PDMS device.** Side view of the PDMS device, with a fluidic channel, a control channel and an antievaporation tank (not to scale). (B)

Microfluidic stickers [83], or NOA devices as we will call them in this text, are made from a photocurable thiolene based resin NOA81 (Norland optical Adhesive), and contrary to PMDS devices, evaporation is strongly reduced. NOA devices, alike PDMS, allow for submicron size pattern replication and display a low autofluorescence above 500 nm [83]. These devices are simple and rapid to fabricate from a PMDS mold that was first made by replica-molding of a micro-milled PMMA pattern, as explained in Fig. 4.25. Once we have a PDMS mold, the fabrication takes around 15-20 minutes per chip and 5-20 channels could be accommodated on a single device depending on the dimensions of individual channels.

In order to quantify the evaporation in both NOA and PDMS devices, we filled channels

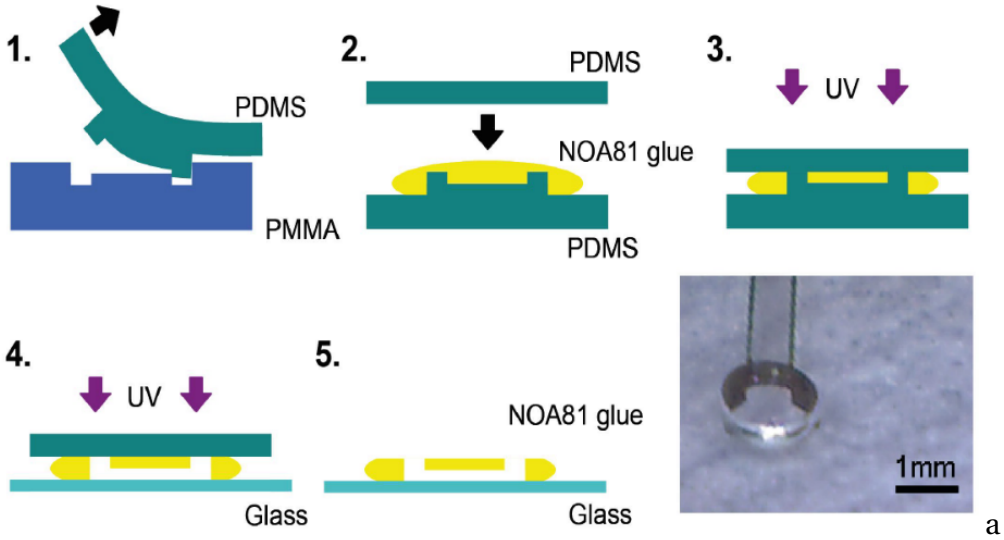

Figure 4.25 – **Step by step fabrication process of a NOA device. 1.** A PDMS mold is first obtained by replica-molding of a micro-milled PMMA sheet (Minitech Machinery Corporation). **2.** and **3.** A drop of NOA is pressed in between the structured PDMS and a flat layer, and then UV insulate. **4.** The structured PDMS is removed revealing a thin layer of non-cross-linked glue which is used to seal the device to a glass slide. **5.** Removing the flat PDMS is the final step. Photography is a closed view of a 1 mm-diameter inlet. Channel size is 300 µm width and 120 µm high. Total thickness of the glue is 300 µm.

with a fluorescein solution and imaged them over time (Fig. 4.26). Bubbles were spotted in PDMS devices after 2 h and significant evaporation within 5 h, making them impractical (Fig. 4.26A). From the calculated percent evaporation in Fig. 4.26B, we determined that complete evaporation in PDMS occurs in 25 h. In the case of NOA devices, small bubbles appeared in 5 h in the outlet but evaporation remained low for over 25 h. The resistance to in NOA devices comes from the fact that NOA is nonporous. The evaporation issue was thus dramatically reduced by using NOA devices. However, we detected in NOA devices a high autofluorescence in the green channel. Thus monitoring P with Evagreen could not be done in NOA device. Depending on the experiment this was or was not an issue since we could in any case monitor the pulse of preys in the yellow channel.

In contrast with NOA, glass and polystyrene are not autofluorescent. We used these materials to fabricate straight fluidic channels when we were interested in monitoring

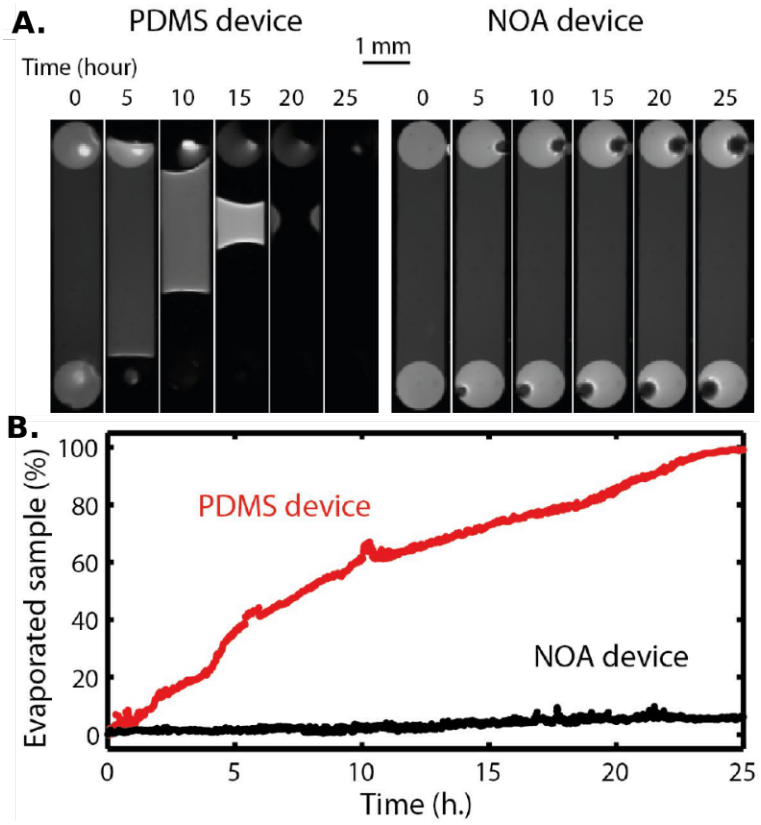

Figure 4.26 – **Comparison of the evaporation in PDMS and NOA devices. (A)** Channels, 120 µm high and 1mm width, were filled with 100 µM fluorescein and sealed with PCR adhesive film. The devices were mounted on a microscope heating stage (Tokai Hit thermoplate) at 44°C for 25 h. **(B)** Percentage of evaporated sample represents the thickness-corrected area for which there is no more fluorescence signal.

the predator front. For this type of devices we employed a simple and low-cost fabrication technique. Polystyrene devices were fabricated by embedding two layers of parafilm, with 1-mm width carved channels (Fig. 4.27A), between two polystyrene slides (Fig. 4.27B). Then they were placed on a hot plate at 50°C to glue the assembly. Prior to assembly, two holes of 1-mm diameter were drilled, in the upper slide, at the end of each side. The channels were filled by aspiration with a micropipette. A similar protocol used glass slides instead of the polystyrene slides, except that no holes were drilled. In this latter case the upper glass slide was a short glass coverslip, such that the parafilm channels were not completely covered, see Fig. 4.27C. The hydrophobic surface of polystyrene/parafilm devices or the absence of well-defined inlets in glass/parafilm devices make filling complex geometries very challenging

(Section 4.3.1). Parafilm-based devices were quick to assemble but they were limited to wave propagations in straight channels only.

To give a picture of the differences in material composition among the microfluidic devices, we show a photo and a scheme of each straight channel device (Fig. 4.28). Three of the devices are mounted on glass slides (Fig. 4.28A,B,D) and one on polystyrene slides (Fig. 4.28C).

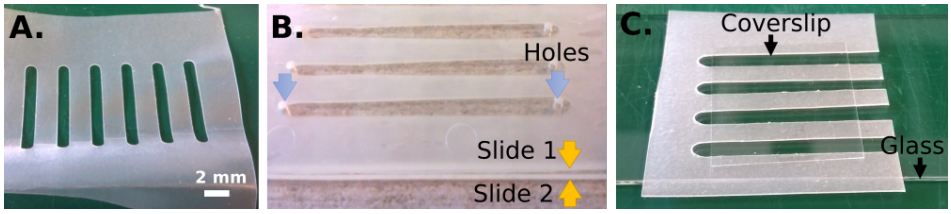

Figure 4.27 – **Low-cost fabrication of polystyrene and glass devices. (A)** Channels were cut in a parafilm sheet with a plotter cutter. **(B)** Two of these sheets were embedded between two polystyrene slides aligning the ends of the channels with the drilled holes on slide 1. Then the device was placed on a hot plate at 50°C for 45 s to glue the assembly. **(C)** A glass slide and a coverslip could be used instead of polystyrene slides. But no holes were drilled. The width of the channels were unevenly deformed upon heating but the height (≈ 200 µm) remained constant.

So far, we have described fabrication techniques and evaporation issues. To illustrate the fabrication intricacy of complex geometries in NOA devices we will discuss how we solved two technical issues. NOA devices greatly reduced the evaporation problem, yet, careful fabrication and usage steps were taken to overcome technical problems in these devices. For example, bubbles were produced (blue arrows in Fig. 4.29) when pouring the liquid NOA during step 2 in the fabrication, see Fig. 4.25. A possible solution was vacuum degassing after the pouring, but it was simpler and faster to carefully remove the bubbles with a needle. Bubble formation was also minimized by slow pouring of NOA over the PDMS mold. Another cause of channel failure was air-branched tunnels (golden dash lines in Fig. 4.29) produced when the NOA stamp was assembled with the glass slide in step 4 in Fig. 4.25. These tunnels were fed by empty spots that allowed air to branch to the channel border. Slowly pouring sufficient NOA from the center outward during the fabrication step 2 solved this problem.

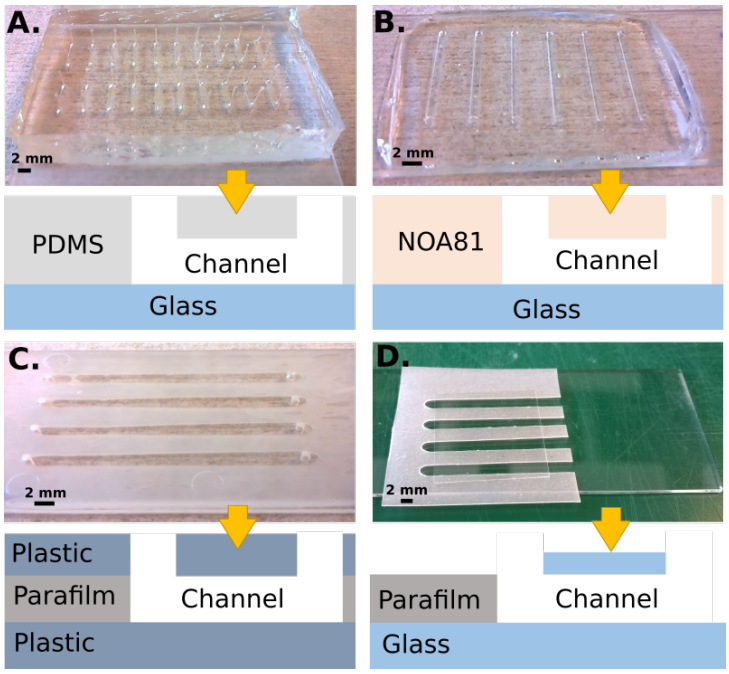

Figure 4.28 – **Channel structures in microfluidic devices used in this chapter. (A)** PDMS channels on a glass slide. **(B)** Channels made of photocurable glue NOA on a glass slide. **(C)** Embedded layers of parafilm formed channels between two polystyrene slides or **(D)** glass slides.

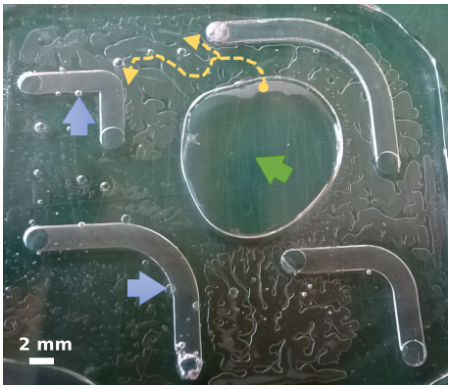

Figure 4.29 – **Technical issues upon fabrication in NOA devices.** Bubbles (blue arrows) formed when pouring liquid NOA on the PDMS mold before UV solidification and ended up inside the channels. Channel was destroyed by utilization of insufficient NOA, which produced large gaps (golden dash lines) fed by empty spot (green arrow).

Complex reactor geometries, as it was the case of NOA maze devices (Section 4.5), required step-by-step filling when setting up an experiment (Fig. 4.30, Page 156). This type of technical issue arises when reaction solution can flow from multiple

Table 4.1 – **Comparison of the microfluidic devices used in this work. 1.** The order of magnitude of the size of the features that can be replicated. **2.** The size at which the initial conditions can be controlled. **3.** Autofluorescence of channel material. **4.** Fabrication time (†) is longer because a reusable mold is first designed and fabricated. **5.** Filling difficulty of straight channels with the DNA reaction solution. **6.** Filling difficulty of turn and maze devices with the reaction solution. **7.** Evaporation was not tested for longer times (‡) in these devices. **8.** Type of geometry for which a microfluidic technology was found to be more practical.

	PDMS/ glass	**NOA/ glass**	**Polysterene/ parafilm**	**Glass/ parafilm**
1. Size features	Submicron	Submicron	Millimetre	Millimetre
2. Initial condition size	Micron	Micron	Millimetre	Millimetre
3. Autofluorescence	No	In green	No	No
4. Fabrication time	> 4 h$^{(\dagger)}$	> 20 min$^{(\dagger)}$	15 min	10 min
5. Filling 1D devices	Easy	Easy	Moderate	Moderate
6. Filling 2D devices	Easy	Moderate	Challenging	Challenging
7. Evaporation	< 2 h	> 25 h	> 3 h$^{(\ddagger)}$	> 3 h$^{(\ddagger)}$
8. Preferred for:	-	2D	1D	1D

directions to fill the same region, thus trapping air because NOA is impermeable to gases. Before filling, a layer of transparent PCR tape (premium Plate sealing film, Platemax, Axigen) was placed on top of the device to block all holes. Then, holes were opened by hole-punching hole$_n$ and hole$_{n+1}$, thus allowing reaction solution to flow into these channels. This was repeated in the numbered order until the entire device was filled, then the holes sealed with PCR tape.

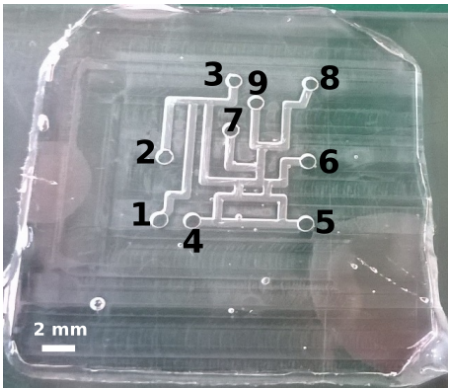

Figure 4.30 – **Filling steps of NOA maze devices.** Drilled holes of the maze device were taped temporally, then opened and filled with the reaction mixture in the numbered order. Then once the device was filled, all holes were sealed with PCR tape.

Of the four technologies considered so far —PDMS, polystyrene/parafilm, glass/-parafilm and NOA— each has advantages and disadvantages (Table 4.1). The porosity of PDMS is both a great advantage for filling a device with complex geometry, because bubbles entrapped during device filling disappear by simply increasing the pressure at the inlet, and a disadvantage when working at high temperatures, because, in our hands, we were unable to efficiently suppress evaporation. For this reason we discarded PDMS for our experiments. Both parafilm-based and NOA devices have low porosity and are thus suitable for working at high temperatures. Because parafilm-based devices are much simpler to fabricate, they were preferred for 1D geometries. However, they were impossible to fill for more complex geometries. Indeed, polystyrene being hydrophobic, these devices can only be filled with pressure. In contrast, NOA/glass devices are naturally hydrophilic and one can take advantage of capillary forces to carefully fill complex geometries minimizing bubbles. For these reasons we used only NOA/glass devices for studying front propagation in complex geometries.

4.3.2 Setting up a wave propagation experiment within a microreactor

Spatiotemporal or wave propagation experiments required preparing the microfluidic device in advance. During a typical experiment a microfluidic device was filled with a reaction mixture containing the PP-buffer, the grass (G) template and an initial concentration of predator, as depicted in Fig. 4.31. The filling was driven by capillary forces in the case of glass-based devices, but in the case of polystyrene-based devices, the liquid was pushed during the micropipette filling. As we did in Chapter 2, to selectively trigger wave propagation at one side of the channel, a second mixture containing an initial concentration of prey was introduced and mixed into a hole on one side of device. A small volume was removed from the other side in order to drive the trigger solution deeper into the channel. The device was completely sealed.

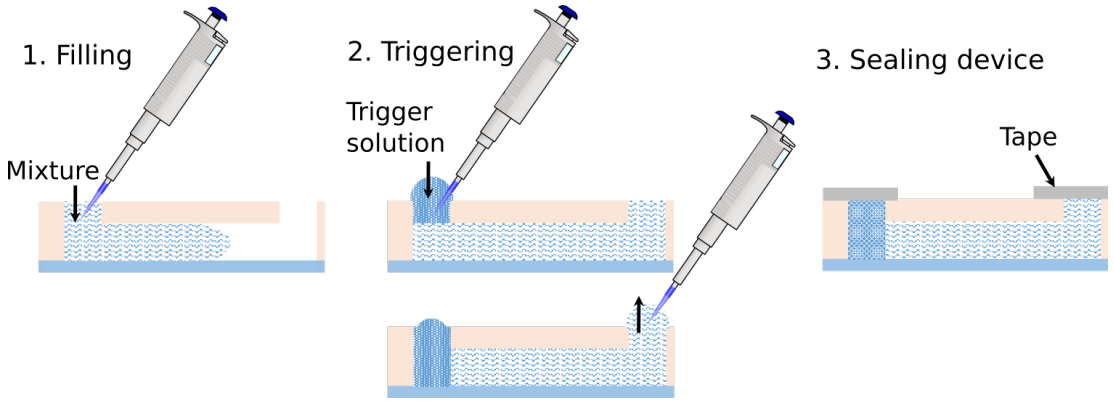

Figure 4.31 – **Experiment preparation in a microfluidic device. 1.** Channel is filled with a reaction mixture containing the PP-buffer (along with nick and pol), grass template and an initial concentration of predator. **2.** A trigger solution, mixture containing 100 nM of prey, was introduced and mixed. Then from the other side, 0.5 µL were removed to ensure the trigger was inside of the channel. **3.** Any extra liquid near the holes was displaced during the sealing of the device.

The microfluidic device in a wave propagation experiment was prepared as described in Fig. 4.31, then the reaction would take place at 44°C in a heating stage mounted on an inverted Zeiss Axio Observer Z1 microscope (see the microscope specifications in Page 201). As an example, the experimental data of a propagating pulse in a NOA device is displayed in Fig. 4.32. The fluorescence shift was recorded over time along the channel, see the time-lapse in Fig. 4.32A. In this figure the entire channel appears black at time zero because there is no prey present. For t > 0 min the prey leading front is displayed as the clear region in a gray scale and the darkening behind is the predator trailing front. From the profile plots we see that the resulting dynamics is a traveling pulse (Fig. 4.32B).

As we did in previous chapters, it is practical to represent the spatiotemporal data in a kymograph, in which the x-axis is the position along the channel and the y-axis is the time as shown in Fig. 4.32C. From this figure the velocities of the fronts can be extracted by fitting straight lines through the boundaries labeled prey front and predator front. Velocity is the inverse of the calculated slope. For this particular experiment, we see that the prey front has a constant propagation velocity (v_1) smaller than that of the predator front (v_2), so the spatial width (w_x) of the front decreases as

the pulse moves forward along the channel. In the upcoming sections, kymographs will be used to quantitatively analyze the front width and the velocities of the prey and predator fronts in wave propagations in straight channels (Section 4.4) and in more complex geometries (Section 4.5).

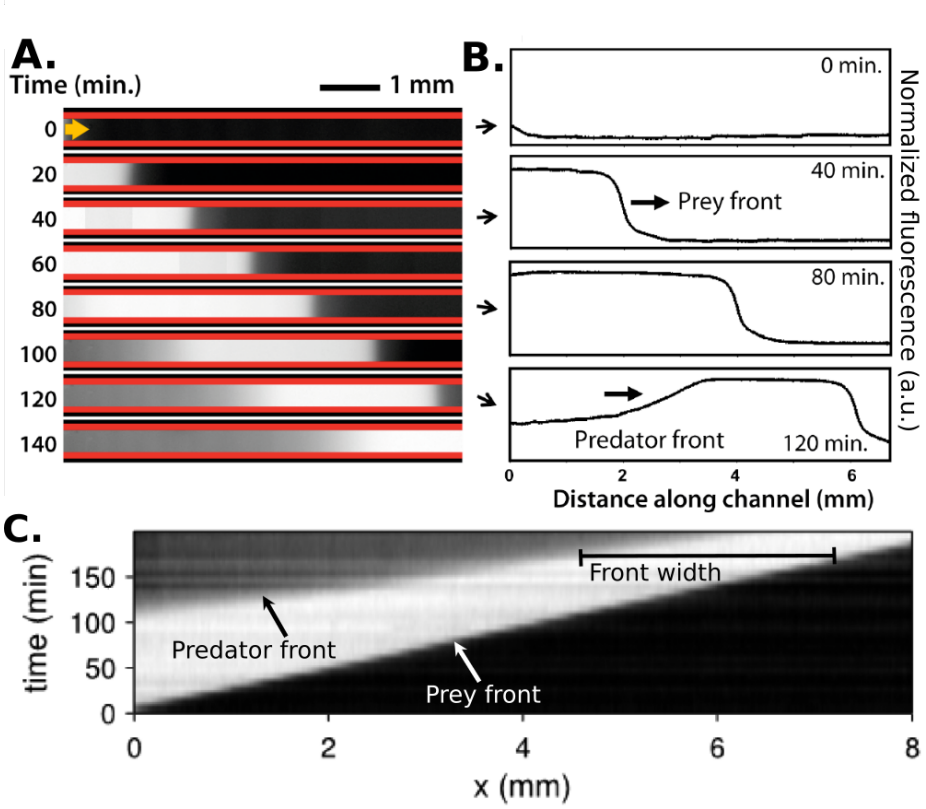

Figure 4.32 – **Predator-Prey waves propagating in a straight NOA channel.** **(A)** Time-lapse of fluorescent shift images. Wave propagation is triggered (golden arrow) from the left side by adding 100 nM prey. **(B)** Profiles of the prey and predator fronts along the channel. **(C)** Corresponding kymograph for a traveling pulse of preys. Reactions were performed at 44°C, $pol_n = 2$, $P_{(t=0)} = 2$ nM and $G_0 = 200$ nM.

4.4 Pulse propagation in straight channels

Note to the reader: The results are qualitatively similar to those already discussed in Sections 2.4.2 and 2.4.3. We have included them for completeness. The non-specialized reader may skip them and proceed to Section 4.5 in Page 170.

We shortly summarize the theoretical predictions concerning front propagation before discussing the experiments. In this case Eqs.4.4 become a set of two partial differential equations,

$$\frac{\partial N}{\partial t} = \kappa_1 pol_n \frac{N}{1+bN} - \kappa_2 \frac{NP}{1+bP} + D_N \Delta N \tag{4.7}$$

$$\frac{\partial P}{\partial t} = \kappa_2 \frac{NP}{1+bP} + D_P \Delta P,$$

where D_N and D_P are the diffusion coefficients of N and P, respectively, and Δ is the Laplace operator. In the propagation along a straight channel (x direction), as it is the case in this section, Δ becomes a second order partial derivative of the involved species with respect to x, such that

$$\Delta N = \frac{\partial^2 N}{\partial x^2} \qquad \& \qquad \Delta P = \frac{\partial^2 P}{\partial x^2}. \tag{4.8}$$

Initially, propagation starts with a Heaviside-type initial condition, i.e. large $(N_{(t=0)})_{(x=0)}$. So the leading wave of N propagates in a region where $P_{(t=0)} \approx 0$, such that $r_2 \approx 0$. Consequently the leading wave described by Eq. (4.7) is independent of the trailing front, and its solution is a Fisher-KPP front of constant velocity (derivation in Page 214), given by,

$$v_1 = 2\sqrt{r_1'(0) D_N}, \tag{4.9}$$

where $r_1'(0) = \kappa_1 pol_n$ is the derivative of r_1 at $N = 0$ and D_N is the diffusion coefficient of N. D_N was estimated by measuring the diffusion of 11 and 22 bases long ssDNA, and its value was found to be 15000 μm^2 min^{-1} at 44°C, G_0 = 200 nM and low N [29]. We can extract $r_1'(0)$ from well-mixed reactions to estimate the propagation velocity of the leading front (v_1). Then, we can validate the model by comparing the measured velocity of the prey to the estimated value.

To develop a similar expression to that in Eq. (4.9) for the predator front velocity we assume that N is independent of time when the prey front arrives, then

$$v_2 = 2\sqrt{r_2'(N(x),0)D_P}, \tag{4.10}$$

where $r_2'(0) = \kappa_2 N(x)$ is the derivative of r_2 at $(N,P) = (N(x),0)$. The value of the predator diffusion coefficient was taken to be $D_P \approx D_N$, since both N and P are of similar size, 11 and 14 bases respectively. We can use this model to guide our understanding on the propagation of the predator front.

In the following subsections, propagation experiments of Predator-Prey waves in straight channels — in NOA/glass, polystyrene/parafilm and glass/parafilm devices— are presented. In these experiments, the effects of pol_n and the initial concentration of predators on the propagation dynamics are investigated. Subsequently, we discuss the three relative velocities of prey front velocity (v_1) related to predator front velocity (v_2): (1) $v_1 < v_2$, (2) $v_1 > v_2$, and (3) $v_1 = v_2$.

4.4.1 Effect of polymerase on the propagation dynamics in NOA channels

The simple modeling in Eq. (4.7) predicts that the leading (prey) front is independent of the trailing (predator) front and we can describe the velocity of the prey front, v_1 using Eq. (4.9). This equation tells us that $v_1^2 \sim \kappa_1 pol_n$. To test the validity of the model we measured the effect of polymerase on the velocity of the prey. The reaction solutions were prepared at different pol_n, then we triggered the pulse of preys in separate channels in a single microfluidic device, as described in Fig. 4.31. This study was done in NOA devices to characterize the dynamics of 1D propagation and subsequently to study 2D propagation (Section 4.5.1) and complex geometries (Section 4.5.2).

In Fig. 4.33 we plot the kymographs of the Predator-Prey fronts at different pol_n. In all three concentrations of pol, the prey front velocity is always lower than the predator

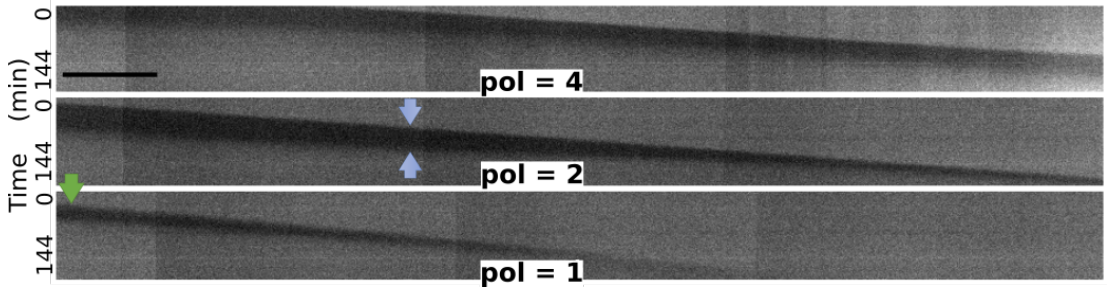

Figure 4.33 – **Wave propagation at different polymerase concentrations in NOA channels. (A)** Kymograph of the yellow fluorescence shift in a channel containing the Predator-Prey system with pol_n = 1, 2 or 4. Black scale bar is 1 mm. The reactions were performed at 44°C, $nick_n$ = 12, $P_{(t=0)}$ = 2 nM, G_0 = 200 nM and triggered with $N_{(t=0)}$ = 100 nM. Green arrow and blue arrows point to, respectively, the start time and the temporal width.

front velocity. In Fig. 4.34 we plot the velocity of the prey front as a function of pol_n. In this figure we see that a linear fit through the data describes well the dependency of v_1^2 on pol_n, as expected from our model ($v_1^2 \sim \kappa_1 pol_n$). In addition, this proportionally has also been demonstrated by Zadorin et al. [29], a posdoctoral researcher in our group, using a different PEN-DNA toolbox network. However, in the case of Zadorin the linear fit goes through $v^2 = 0$ at $pol_n = 0$, but not in our case. Zadorin explores values of $pol_n \leq 2$, whereas we have pol_n = 1-4. So a second linear regime below $pol_n \leq 1$ that goes through $v^2 = 0$ should exist in our system. This hypothesis needs to be tested with lower concentrations of pol_n.

Since $v_1 < v_2$ the spatial width (w_x) of the pulse width decreases along the channel in the wave propagations at the values of pol_n = 1, 2, and 4 (Fig. 4.33). In other words the distance between the leading front and trailing front gets smaller with time. Instead of quantifying w_x, directly it is simpler to get similar information by analyzing the temporal profile at each position along the channel. We analyze the profile by obtaining the difference in time between the predator and the prey fronts at any particular point over the length of the channel (one such location is indicated by the blue arrows on Fig. 4.33). We call this value the temporal width (w_t). In order to have a robust comparison of w_t for different channels and different experiments, we systematically normalized the fluorescence with respect to the maximum value. And,

we defined w_t as the width of the peak at 0.4 of the normalized fluorescence as shown in Fig. 4.33.

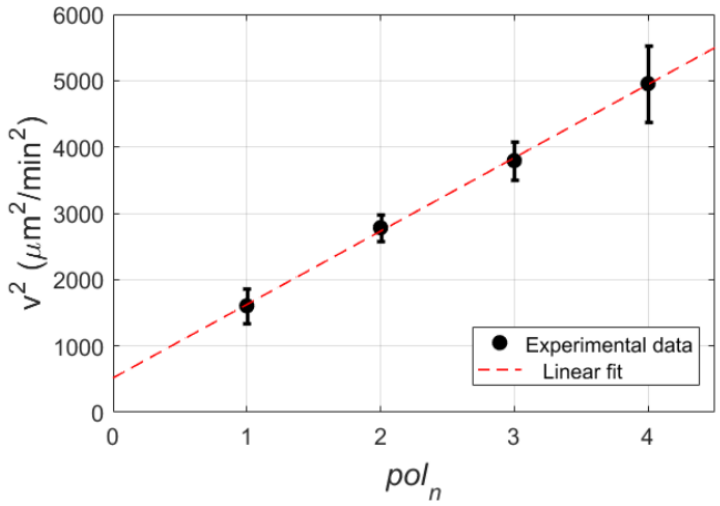

Figure 4.34 – **Square of the prey velocity as function of the concentration of polymerase.** The square velocity of the leading (prey) front is linearly fitted as a function of pol_n. The slope is 1100 μm^2 pol_n/min^2 and the intercept is 520 μm^2/min^2. Error bars come from one standard deviation.

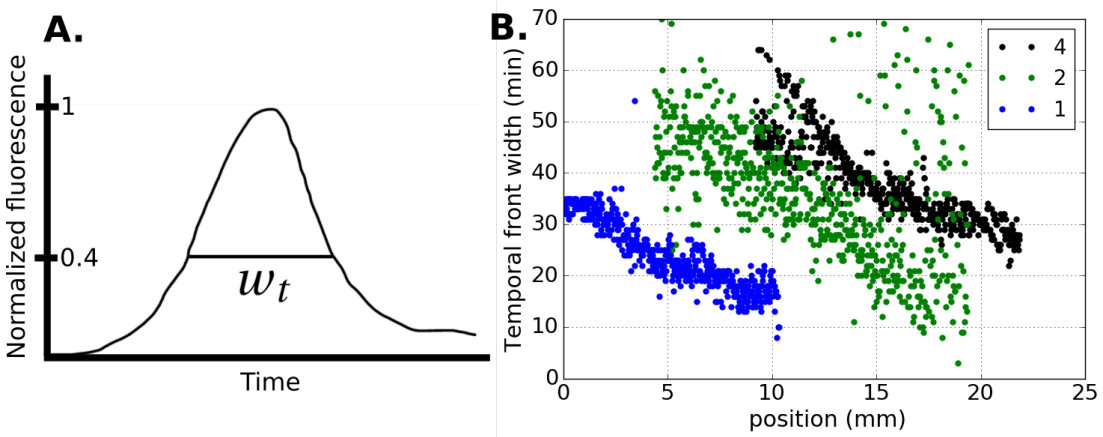

Figure 4.35 – **Temporal width as a function of position in a channel. (A)** The temporal profile was normalized and the temporal width, w_t, was taken to be at position 0.4. The profile is a sketch for illustration. **(B)** Temporal width as a function of position for wave propagation experiments at pol_n = 1, 2, and 4 in Fig. 4.33.

We computed w_t at every location along the channel for pol_n = 1, 2 and 4 (Fig. 4.33B). Since the predator front is faster than the prey front, we expect w_t to get smaller as the

propagation progresses along the channel, which is confirmed by our experiments (Fig. 4.33). Another interesting observation is that for a given position, w_t varies largely for the three different values of pol_n. We hypothesize that lower pol_n brings the reaction towards steady state faster. This implies that if the propagation at a certain value of pol_n is allowed to continue over a longer distance, w_t would get smaller and attain values comparable to those obtained at lower pol_n. In other words, the temporal width would be a function of space, $w_t(x)$, and the starting size would be given by pol_n. For $pol_n = 4$, w_t decreases initially as the propagation progresses along the channel. Then, at 15 mm, the slope decreases drastically. This change in slope might be an indication that eventually a steady state can be reached in a longer channel. The propagation dynamics at larger values of pol_n would have to be studied to see if $w_t(x)$ follows this tendency beyond $pol_n > 4$. For $pol_n < 4$, the slope dw_t/dx maintains a linear decay and this slope remains constant along the channel.

In summary, we can say that because experiments in Fig. 4.33 do not reach a steady state we do not know what is the final outcome of the instable situation, $v_1 < v_2$. Two outcomes are possible from such situation: (1) either the front is caught by the predator front and both fronts vanish, or (2) both fronts stabilize at at an equal velocity.

To gain further insight about the propagation of P we included EvaGreen in the reaction solution. To do so, we switched from NOA/glass devices to glass/parafilm devices. We carried out wave propagation experiments at pol_n = 0.25, 0.5, 1, and 2. Figure 4.36 shows the kymographs of the combined fluorescence shift profiles (blue for P, red for N) at different concentrations of pol. We found that $v_1 \geq v_2$ in all cases, so the predator front did not catch the prey front. Surprisingly we distinguished two propagation phases with distinct dynamics, in which the prey and predator fronts go through a velocity switch. In the case of pol_n = 0.25-0.5, the velocity of the prey front from phase I, v_1^I, decreases in phase II, i.e. $v_1^I > v_1^{II}$. And the predator front velocity follows the same tendency $v_2^I > v_2^{II}$. In the case of pol_n = 1-2, only v_1 decreases when going into phase II.

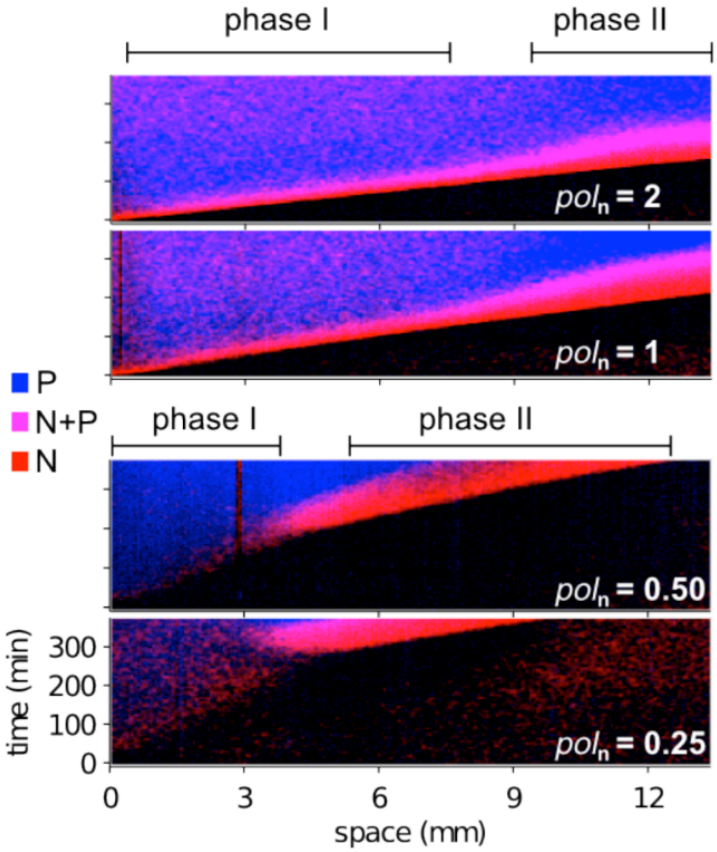

Figure 4.36 – **Predator-Prey waves display rich dynamics in a glass/parafilm device.** Composite kymographs with two overlaid channels: EvaGreen (blue) and DY530 (red) fluorescence shifts for different polymerase concentrations, pol_n. The blue and red channels mainly account for P and N, respectively. The reactions were performed at 44°C, $nick_n$ = 12, $P_{(t=0)}$ = 2 nM, G_0 = 200 nM and triggered with 100 nM N.

We then estimated that $r_1'(0) \approx r_g$ and $r_2'(N(x),0) \approx r_p$ (Fig. 4.15). Using this approximation, we can explain Phase I using Eqs. (4.9) and (4.10). In phase I we measured two distinct proportionality constants between the velocities and pol_n: (1) $v_1^I \approx v_2^I = 32 pol_n^{1/2}$ µm min^{-1} for pol_n = 0.25-0.50, and (2) $v_1^I = 58 pol_n^{1/2}$ µm min^{-1} and $v_2^I = 55 pol_n^{1/2}$ for pol_n = 1-2. This was not surprising since the difference in the proportionality constant is in good agreement with the variation observed for r_g and r_p in the same pol_n ranges (Fig. 4.15).

However, the propagation dynamics suddenly change and phase II takes over. In phase II the prey front is followed by a mixture of the two fronts (N + P), which are later followed only by a predator front. The switching times scale with $pol_n^{1/2}$. Phase II

shows a switching time that scales with $pol_n^{1/2}$: t_{switch} (150 ± 20)$pol_n^{1/2}$ min. Unlike phase I, phase II does not have a clear scaling law between v_i and pol_n. However, $v_1^{II} \approx v_1^I$ for pol_n = 1-2 while, in contrast, v_1^{II} is significantly larger than v_1^I for pol_n = 0.25-0.50.

A sudden switch in the propagation dynamics has already been observed in fronts of replicating RNA [84]. In that case a faster propagating mutant triggered the transition. Although a mutation cannot be entirely disregarded, the scaling $t_{switch} \sim pol_n^{1/2}$ points towards a deterministic process. We suspect that phase I and II may correspond, respectively, to pulled and pushed fronts [54]. This means that in phase I the dynamics are controlled by what happens ahead of the front where the autocatalyst concentrations are low. Whereas in the second phase the reaction term behind the front controls propagation.

4.4.2 Effect of initial predator concentration on the propagation dynamics

Here, we investigate the effect of the initial predator concentration ($P_{(t=0)}$) on the propagation dynamics. To do so, we use polystyrene/parafilm and glass/parafilm devices. Our motivation for this was to test if the velocity of the prey front, v_1, decreases with $P_{(t=0)}$. In fact, we saw in Fig. 4.23 that the phenomenological growth rate of the prey, r_g, decreases with $P_{(t=0)}$. Hence, we aim to test our model: $v_1 \sim \sqrt{r_g(P_{(t=0)})}$.

We let Predator-Prey waves propagate in polystyrene/parafilm devices at different $P_{(t=0)}$. Figure 4.37 shows the kymographs of the DY530 and EvaGreen fluorescence shifts at different $P_{(t=0)}$. In this figure, a high concentration of N appears dark in DY530, while a high P appears bright in EvaGreen. Contrary to the results obtained in Fig. 4.33, here the prey front velocity matches the velocity of the predator front. Hence the system is at steady state. Furthermore, the temporal width (blue arrows in Fig. 4.37) is constant (≈ 20 min) since $v_1 = v_2$. Once the prey pulse passes, the signal in DY530 is not well recovered for $P_{(t=0)} > 8$ nM (Fig. 4.37B) and we believe that it was due to the contribution of predators to the quenching of DY530 (Fig. 4.13). Unfortunately,

we discovered that self-start (golden arrow) happens around 50-60 minutes, which is much earlier than in NOA/glass or glass/parafilm (≈ 150 min). We decided to switch to glass/parafilm devices to continue our study.

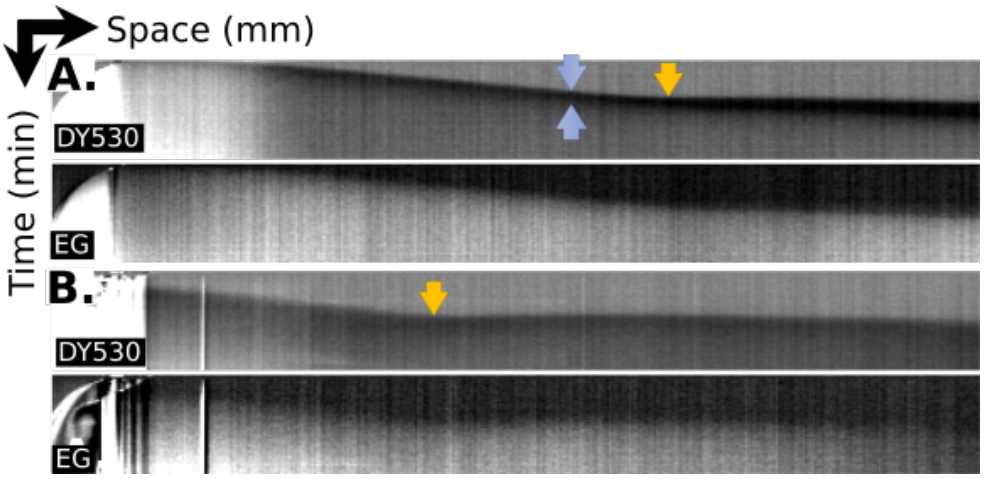

Figure 4.37 – **Predator-Prey wave propagation at different initial predator concentrations in polystyrene/parafilm channels.** Kymograph of the yellow (upper) and green (lower) fluorescence shifts in a channel containing the Predator-Prey system with (A) $P_{(t=0)}$ = 2 nM and **(B)** $P_{(t=0)}$ = 32 nM. Reactions were performed at 44°C, $nick_n = 5$, $pol_n = 1$, and triggered with 100 nM N. Self-start stopped wave propagation (golden arrow). Time and space arrows represent 100 min and 1 mm respectively.

The same experiment was repeated in glass/parafilm devices since self-start in these devices was less problematic. The initial concentration of the predator was also varied. The kymographs of these experiments are shown in Fig. 4.38. We observe that initially the prey front velocity is slightly bigger than the predator front velocity, i.e. $v_1 \gtrsim v_2$, but at around $t \approx 160$ min (blue arrow) v_2 decreases abruptly and v_1 remains constant. The same effects are observed for $P_{(t=0)} > 2$ nM. This is consistent with the two phase dynamics previously described in Fig. 4.36.

In Fig. 4.39 we plot the square velocity of the prey as a function of $P_{(t=0)}$. v_1^2 decreases by increasing $P_{(t=0)}$. In our model ($v_1 \sim \sqrt{r_g(P_{(t=0)})}$) and we have shown that r_g decreases linearly with $P_{(t=0)}$ in Section 4.2.5. Hence, we fitted the data with a linear regression and compared it with the predicted square of the velocity. Although v_1 is overestimated when using r_g from temporal studies to predict v_1, the estimation is within the correct order of magnitude. In Fig. 4.39 we see that the linear fit is

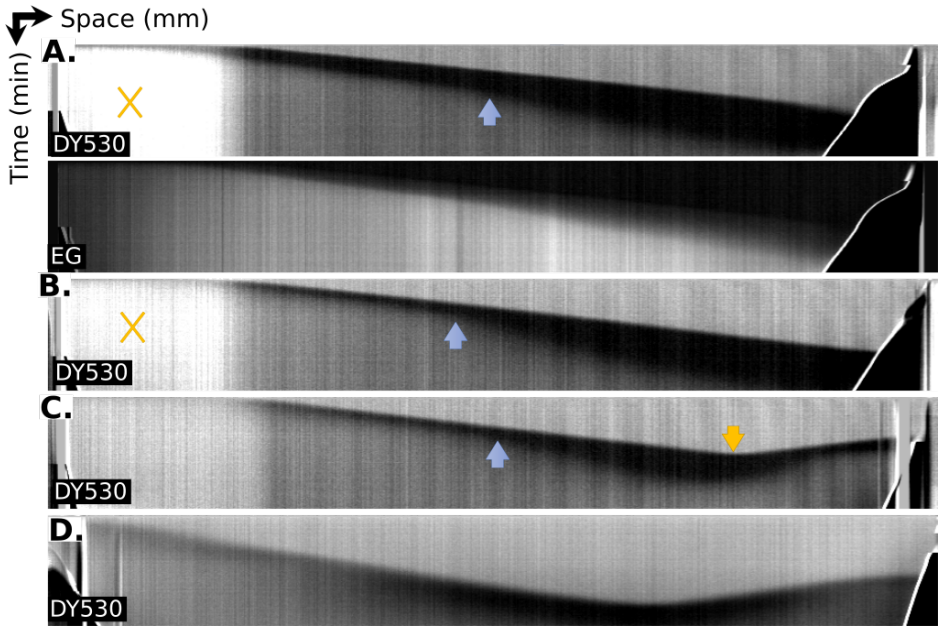

Figure 4.38 – **Predator-Prey propagating waves at different initial predator concentrations in glass/parafilm channels.** Kymograph of the yellow (upper) and green (lower) fluorescence shifts in a channel containing the Predator-Prey system with **(A)** $P_{(t=0)}$ = 2 nM, **(B)** $P_{(t=0)}$ = 8 nM, **(C)** $P_{(t=0)}$ = 16 nM, and **(D)** $P_{(t=0)}$ = 100 nM. The golden cross point to the area of autofluorescence from the sealing grease. Self-start stopped wave propagation (golden arrow). The velocity of the predator front abruptly slows down (blue arrows). Reactions were performed at 44°C, $nick_n$ = 5, pol_n = 1 and triggered with 100 nM N. Time and space arrows represent 100 min and 1 mm respectively.

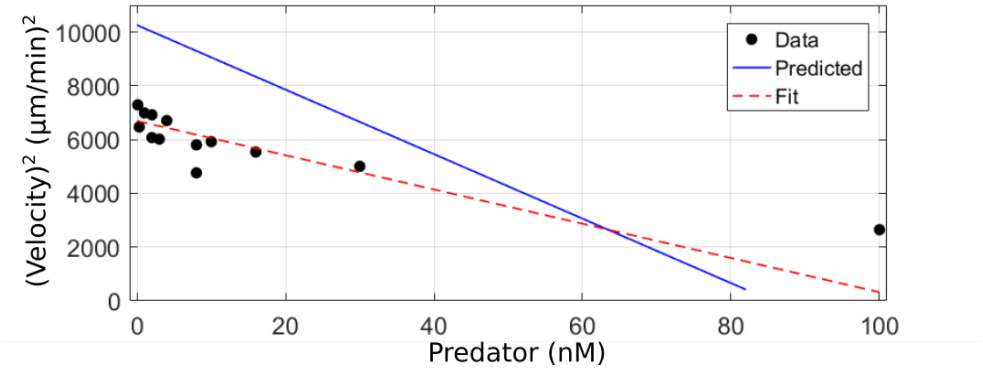

Figure 4.39 – **Prey front velocity as a function of initial concentration of predator.** The velocity of the prey front were determined from DY530 fluorescence shift from the kymographs in Fig. 4.38 and other experiments not shown here. Red dotted line is a linear fit of the data: slope = -63.7 ± 31.6 and intercept = 6690 ± 350. The blue solid line is the the predicted square velocity, which is calculated using the r_g from the linear fit in Fig. 4.23 and a diffusion coefficient of 15000 µm^2 min^{-1}.

noisy, but these variations in v_1 are within our measurement precision. In Page 203 (Appendix C.1), the standard deviation was determined to be 5% in a series of replicate experiments with identical reaction mixtures in a single chip, but this rose to ≈ 20% when comparing experiments performed in different days. Thus, it is not surprising that these variations, possibly coming from discrepancies of chip surfaces upon fabrication, make difficult to precisely quantify how v_1 is related to $P_{(t=0)}$ in Fig. 4.39.

It can be thus stated that the prey velocity depends linearly on $P_{(t=0)}$. Unfortunately, the early self-start in polystyrene/parafilm devices did not allow us to study the propagation dynamics over distances longer than 4 mm. Thus we might have missed a phase transition in the propagation dynamics in these devices. We can also speculate that the fact that $v_1 > v_2$ in glass/parafilm, but $v_1 = v_2$ in polystyrene devices, indicate that surface interactions due to the channel materials exist. If the discrepancies come from surface interactions, this must be tested further.

4.4.3 Discussion on the relative velocities of the prey and the predator fronts

In the numerical simulations in Appendix C Page 222, the width and shape of the front was predicted to be constant, and the front width to be regulated by κ_2. Also, both the velocities of the trailing front and the leading front, v_2 and v_1 respectively, were predicted to be identical, and equal to 70 μm min^{-1}. However, in contrast with the simulations, in the experiments we found three relative velocity regimes: (1) $v_1 < v_2$ (Fig. 4.33), (2) $v_1 > v_2$ (Figs. 4.36 and 4.38), and (3) $v_1 = v_2$, (Fig. 4.37). We have listed in Table 4.2 the experimental conditions at which we found each regime.

The first case was discussed in the article (Appendix C Page 204) in which it was argued that the trailing front had not reached steady state at the experimental conditions used. It was hypothesized that this came from pol sequestration during prey growth, which lowered κ_2. Once predation started, the non-saturated κ_2 was recovered. The second regime ($v_1 > v_2$) could be understood by analyzing the expression for the prey front velocity: $v_2 \sim \sqrt{r_2'(N(x),0)}$. Decreasing the derivative of the predation rate,

Table 4.2 – **The three relative velocity regimes and their experimental conditions.** **(1)** This regime was observed in the experiments in Fig. 4.33. **(2)** The regime had two subcategories of the propagation phases. One in which both v_1 and v_2 decreased in phase II, experiments in Fig. 4.36, for pol_n = 0.25-0.5. And a second one where only v_2 decreased for pol_n = 1-2 and $nick_n$ = 12, in Fig. 4.36, and pol_n = 1 and $nick_n$ = 5, in Fig. 4.38. **(3)** This regimec occurs at steady state, experiments in Fig. 4.37.

Regime:	**(1)** $v_1 < v_2$	**(2)** $v_1 > v_2$	$v_1 > v_2$	**(3)** $v_1 = v_2$
Device	NOA /glass	Glass /parafilm	Glass /parafilm	Polysteryne /parafilm
EvaGreen	No	Yes	Yes	Yes
Two propagation phases	No	Yes: $v_2^I > v_2^{II}$ $v_1^I > v_1^{II}$	Yes: $v_2^I > v_2^{II}$	No
pol_n	1-4	0.25-0.5	1, 1-2	1
$nick_n$	12	12	5, 12	5

$r_2'(N(x),0)$, lowers the value of v_2 while v_1 remains unaffected. We suggest that this is the case at the experimental conditions at which we observed this regime. Another interesting feature of this regime is the existance of two phases in the propagation dynamics. At $pol_n = 0.25 - 0.5$ both v_1 and v_2 decreased in the phase II, but only v_2 decreased in the phase II for $pol_n = 1 - 2$. Finally, in the third regime the system is at steady state, thus $v_1 = v_2$ as predicted by the model.

4.5 Wave propagation in different geometries

In the previous section the propagation of waves was confined to 1-dimensional reactors. Here we will focus on the propagation of the prey front in two dimensions. Complex 2D reactors could only be filled when fabricated in NOA/glass.For this reason we used only NOA/glass devices for complex geometries.

We tested two geometries, the simplest 2D geometry, a 90° turn, and quantified the effect of the turn radius in the propagation, and a complex one, a maze, and demonstrated that the Predator-Prey network can solve the classical problem of finding the optimal path between two points [71].

4.5.1 Predator-Prey propagation dynamics in a 90° turn

We have seen in Section 4.1.1 that curvature influences the propagation of fronts when it is of the order of the diffusion length $\sqrt{D/k}$, where k is the characteristic rate of the reaction. In Section 4.4 we demonstrated that the propagation velocity of the prey front, v_1, was constant in straight channels, were the curvature was zero. Here we investigated the effect of curvature in the propagation of Predator-Prey fronts.

To do so, we fabricated 90° turn channels with two different radii in NOA devices (see Page 204 in the article in Appendix C.1). Figure 4.40A shows DY530 fluorescence images during the propagation of a front in a turn with a 1.5 mm radius. At the entrance of the turn, the curvature of the front was practically zero[1]. When the front engaged into the turn its shape got curved. The curvature was not constant across the width of the channel: it was negative (the front was convex) along the inner path and became positive (the front was concave) close to the outer path. We measured v_1 along the inner and outer paths and observed that it respectively decreased and increased (Fig. 4.40B). v_1 decreased up to 75 µm min^{-1} and increased up to +120 µm min^{-1} from 150 µm min^{-1} at the entry (Table 4.3). A 90° turn with higher radius, 8 mm, induced front curvatures that were significantly smaller in absolute value (Fig. 4.41A-B) together with smaller changes in velocity (-18.6 and +6.2 µm min^{-1} from 62 µm min^{-1} at the entry).

Table 4.3 – **Measurement and precision of the front curvature.** Mean radius, R_c, of the circles fitted to propagating front on the inner and outer paths in a turn channel with inner curvature radius 1.5 mm at 21 (‡) and 26(∗) min. Front curvatures, γ, for the inner and outer sides of the front were measured by manually adapting a circle to the front shape, as seen in Fig. S11, Page 225.

	inner‡	outer‡	inner*	outer*
$\lvert R_c \rvert$ (10^3 µm)	1.2 ± 0.4	0.3 ± 0.1	1.2 ± 0.3	0.3 ± 0.1
$\lvert \gamma \rvert$ (10^{-3} µm^{-1})	0.9 ± 0.3	3.7 ± 1.2	0.9 ± 0.2	3.5 ± 1.3
γD (µm min^{-1})	-16 ± 5	+67 ± 22	-16 ± 4	+63 ± 23
measured "γD" (µm min^{-1})	-75	+120	-75	+120

[1] Indeed the curvature is not exactly zero because during the creation of the initial condition with the pipette we induce a slight curvature that remains.

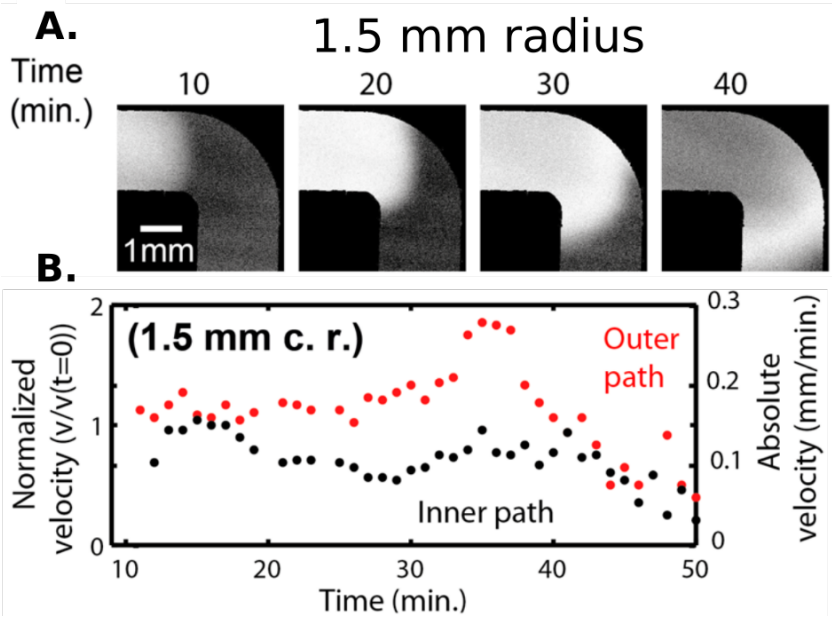

Figure 4.40 – **Propagation dynamics of a Predator-Prey wave in a 90° turn of small radius.** **(A)** Yellow fluorescence shift time-lapse images of a traveling pulse of N propagating through a 90°-turn channel with 1.5 mm curvature radius. **(B)** Normalized (left axis) and absolute (right axis) velocity of the prey front along the longitudinal coordinate of the channel at different times for the inner (black) and outer (red) path of the channel. The channel is 2 mm wide and 500 µm deep. The experiment was performed at 44°C, $nick_n = 10$, $pol_n = 0.5$, $P_{(t=0)} = 2$ nM, $G_0 = 200$ nM and triggered with $N_{(t=0)} = 100$ nM.

We recall (Section 4.1.1, Page 129) that the effect of curvature, γ, on the velocity is given by:

$$v_\perp = v_0 + \gamma D \tag{4.11}$$

where v_0 is the planar wave velocity and D is the diffusion coefficient. The curvature is given as the inverse of the radius of a circle tangent to the front line. To compare our results with this theoretical prediction we measured (see Fig. S11, Page 225) the maximum curvature along the inner and outer paths in our experiments (Table 4.3, Page 171). Although Eq. (4.11) underestimates by 2-fold and 6-fold, respectively, the experimental inner and outer velocities, the correct order of magnitude and the sign are in agreement.

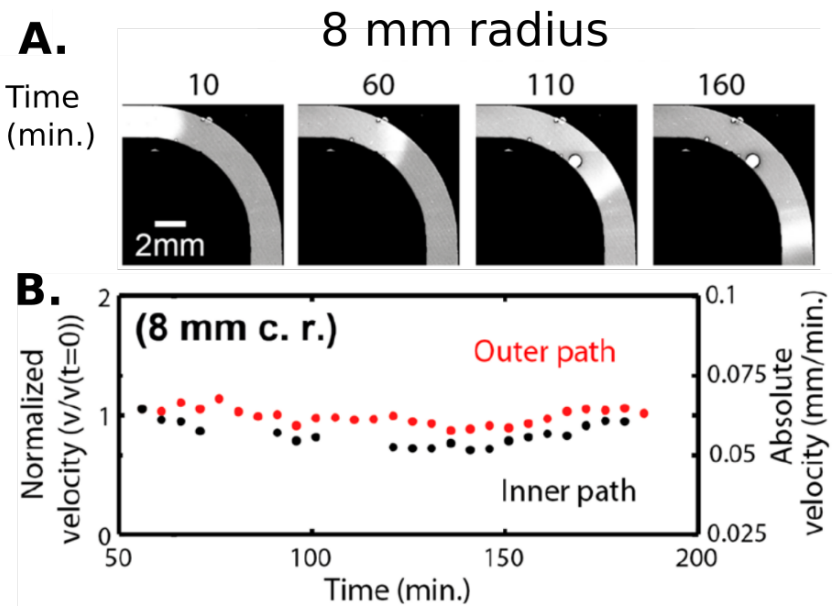

Figure 4.41 – **Propagation dynamics of a Predator-Prey wave in a 90° turn of large radius.** **(A)** Yellow fluorescence shift time-lapse images of a traveling pulse of N propagating through a 90°-turn channel with 1.5 mm curvature radius. **(B)** Normalized (left axis) and absolute (right axis) velocity of the prey front along the longitudinal coordinate of the channel at different times for the inner (black) and outer (red) path of the channel. The channel is 2 mm wide and 500 µm deep. The experiment was performed at 44°C, $nick_n$ = 10, pol_n = 0.5, $P_{(t=0)}$ = 2 nM, G_0 = 200 nM and triggered with $N_{(t=0)}$ = 100 nM.

4.5.2 A propagating pulse computes the optimal path in a maze

We tested the capability of the Predator-Prey waves to compute optimal paths within multi-branched channels. We fabricated a NOA maze device and allowed waves to explore the entire geometry (Fig. 4.42). The wave propagation was triggered from the upper-left corner of the maze. Waves propagated through all possible paths, splitting when multiple paths were available and vanishing at dead ends and upon collision with a counter-propagating wave.

The entire maze was 5.5 × 9 mm^2 and it was explored by the propagating waves in 150 minutes (Fig. 4.42B). We arbitrarily assigned the exit of the maze to outlet O in Fig. 4.42B. From this data, the shortest path between the starting point, I, and the exit, O, was computed. The algorithm to compute the shortest distance involved analyzing

the reverse front propagation. We started by the last recorded image at the position O and searched for the closest front on the previous image and so on until arriving to I. We obtained the white line which is in good agreement with the solution.

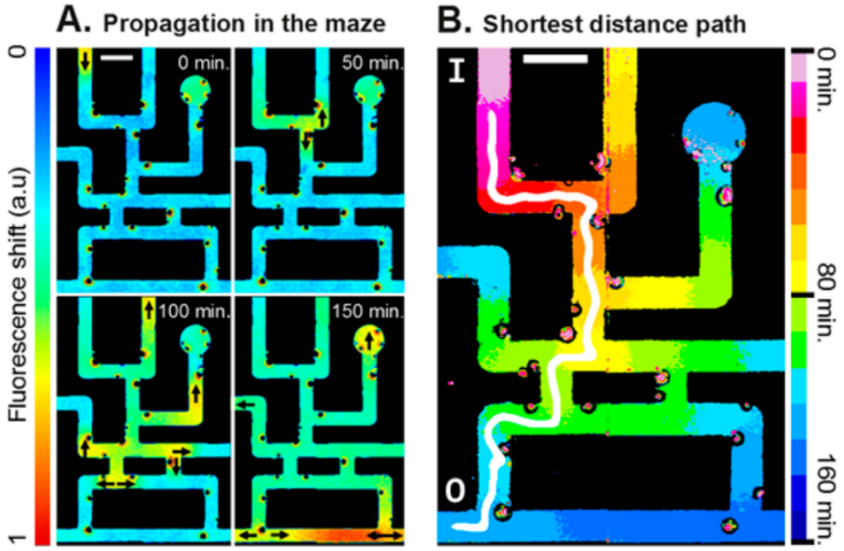

Figure 4.42 – **Pulse of prey computes the optimal path between the entrance and the exit of a maze.** **(A)** Time-lapse yellow fluorescence shift images, represented in a color scale. Black arrows indicate the propagation direction of the leading edge. Black circles are air bubbles. **(B)** Computation of the shortest path (white line) was done by tracking in time the position of the leading front and analyzing the reverse front propagation. Color indicates the time stamp of the leading edge of the pulse. The 5.5 × 9 mm^2 maze had 500 µm wide and 200 µm deep channels. The experiment was performed at 44°C, $nick_n = 10$, $pol_n = 0.5$, $P_{(t=0)} = 2$ nM, $G_0 = 200$ nM and triggered with $N_{(t=0)} = 100$ nM.

A maze with a 4-fold larger area was also tested, but the waves did not have sufficient time to explore the entire device because self-start triggered wave propagation at random positions within the maze. Shrinking the device was a technical solution but for future applications, the bistable network in Chapter 2 should be used. It was not available when the experiments were performed.

4.6 Conclusion and perspectives

In this chapter, microfluidic devices compatible with the PEN-DNA toolbox were developed and used: (1) to confine the wave propagation to 1-dimension and study the propagations dynamics of a prey front that is chased by a predator front, (2) to control the geometry of reactors to study reaction-diffusion waves in 2-dimensions, and (3) to explore the computation capability of chemical waves.

The methodology presented here allowed us to explore the intriguing dynamics of two interconnected waves. Rich dynamics, such as pulses of varying width, were produced by out-of-equilibrium reactions that arose from coupling two autocatalytic nodes into a Predator-Prey network topology. In addition, the influence of pol on front propagation was investigated. In straight channels, pol_n plays a role in the relative velocity of prey front velocity related to the predator front velocity. Two phases of propagation dynamics were observed when varying pol_n. Increasing the initial concentration of predators decreased the velocity of the prey front. We obtained prey and predator fronts that propagated at equal velocities in polystyrene-based devices but not in glass-based device. For this case, we observed that the velocity of the pursuing predator wave related to the prey velocity also depends on the material of the channel, but the causes were not determined. The pulse propagation in 90° turns revealed that the effect of curvature can be studied with our system. Finally, a traveling pulse of preys navigated a labyrinth, and we were able to determine the optimal path by tracing the front position. It can be concluded from this work that DNA-based programmable synthetic systems, coupled with microfluidic technology, are a promising experimental framework for investigating the influence of geometry on spatiotemporal organization.

By changing the concentration of the enzymes and the initial concentrations of its DNA components the Predator-Prey network presented here has been thoroughly characterized in temporal and spatiotemporal studies. Using this accumulated knowledge, future experiments can focus on the front propagation within highly complex geometries. For example, it would be interesting to create logic gates in channels

based on the PEN-DNA toolbox. The programmability of the PEN-DNA toolbox would be allow to generate a large amount of non-interacting gates by designing templates with orthogonal sequence. Dominic Scalise and Rebecca Schulman at Johns Hopkins University in Baltimore have already shown interest in bulding relatively large-scale analogue computers based on this technology. Another interesting direction concerns the propagation of waves across a bed of obstacles. Beyond the results review in Section 4.1.2 it is not known how a RD front propagates across randomly distributed obstacles close to percolation. A combination of the methods developed in this chapter with the packed agarose beads in Chapter 2 appears as an attractive solution to tackle this question. In this context, the complexity of the interactions between chemical species can be increased. DNA networks displaying higher level of connections that are related to the Predator-Prey network have already been design. For example the propagation dynamics of the Predator-Prey-mutualism and competition-bilateral symbiosis networks could be studied in the complex geometries. All these network behaviors are unfeasible using inorganic reactions such as the BZ system.

5 Conclusion and perspectives

During this PhD work, we have worked extensively on engineering reaction-diffusion systems based on the PEN-DNA toolbox that display spatiotemporal dynamics by aiming to control four key elements: (1) the topology of the network, (2) the reaction rates, (3) the diffusion coefficients and (4) the boundary conditions. We have shown that we can control all four elements within the PEN-DNA toolbox, but further research is required to gain full control of all these elements.

In Chapter 1 we have thoroughly characterized the kinetics of an activator-inhibitor network with a thermostable exonuclease in the search of its oscillatory behavior. We generated temporal logic functions by injecting the inhibitor in the NOT gate experiment and the activator of the inhibitor module in the inversion function. Notably, we obtained forced oscillations with an inversion function network with sequences that were designed in silico in [36] but never before tested experimentally. In particular, the autocatalyst will need to be weakened to get a functional oscillator. We have discovered that modifying key parameters such as the template and exonuclease concentration in a multi-node network such as the Oligator requires extensive experimentation that is very time consuming due to the large number of possible parameters that we can vary to search for oscillations. Although the PEN-DNA toolbox is programmable, dynamical behaviors are not obtained by plug and play. Thus, if the PEN-DNA toolbox is to be widely-adopted to design new networks and to modify existing ones with several nodes more efforts in developing computer-assisted design

tools are required.

In Chapter 2 we used 200 nm diameter magnetic nanoparticles and 34 µm diameter agarose beads to immobilized DNA-PEN templates in order to reduce the effective diffusion coefficient of an autocatalyst species. We studied the growth kinetics and front propagation dynamics for a bistable network in packed agarose beads (case 1) and diluted magnetic beads (case 2) and for an autocatalytic network in diluted agarose beads (case 3). Our results yielded a reduction factor in the effective diffusivity of the activation species of: 1.5, 2.4, 4.3 for the cases 1, 2 and 3 respectively. Although we were able to reduce the diffusivity of short DNA strands, clearly the propagation of fronts in these complex porous media requires further investigation. First of all, it is critical to determine the diffusivities in these media for a non-reactive system (only DNA complexation without enzymes) in the future. Furthermore, K_d, the dissociation constant between the autocatalyst species and templates with the hydrodynamic drag, appears as a crucial parameter. Secondly, we can also investigate in the future decoupling the control of diffusion from the reactive templates. This seems an attractive solution, for example by designing a ligand of the autocatalyst that does not act as a template and can be used a larger concentration.

The work from Chapter 2 provided the foundation for controlling colloidal aggregation with DNA patterns resulting in entirely new type of materials: morphogenetic materials in Chapter 3. To the best of our knowledge this constitutes the first demonstration of a morphogenetic material. We demonstrated that DNA concentration patterns can be transferred into patterns of bead aggregation. This was shown in two different cases: a traveling and a stationary front. This DNA model of morphogenesis resembles two key stages of embryo development: (i) the generation of chemical patterns and (ii) the transfer of patterns into a material. In the future more complex morphogenetic materials can be created using this research. Furthermore, in the case of the Polish flag patterns the influence of the sharpness of the gradients on the dynamics and shape of the patterns should be studied. In the future, if the templates are attached to magnetic beads, external forces can be applied to perturb the stable patterns investigate the physical aspects of pattern formation.

In Chapter 4 microfluidic devices compatible with the PEN-DNA toolbox were developed and used: (1) to confine the wave propagation to 1-dimension and study the propagations dynamics of a prey front that is chased by a predator front, (2) to control the geometry of reactors to study reaction-diffusion waves in 2-dimensions, and (3) to explore the computation capability of chemical waves. In 1-dimensional devices, two phases of propagation dynamics were observed when varying pol_n, and increasing the initial concentration of predators resulted in the decrease of the velocity of the prey front. We used 2-dimensional devices to quantify the effect of curvature. Finally, a traveling pulse of preys navigated a labyrinth, and we were able to determine the optimal path by tracing the front position. Future experiments can focus on the front propagation within highly complex geometries. For example, it would be interesting to create logic gates in channels based on the PEN-DNA toolbox. The programmability of the PEN-DNA toolbox would allow to generate a large amount of non-interacting gates by designing templates with orthogonal sequence. Another interesting direction concerns the propagation of waves across a bed of obstacles. Beyond the works review in crefsec:confi it is not known how a reaction-diffusion front propagates across randomly distributed obstacles close to percolation.

The methodology presented in this work allowed us to characterize the rich dynamics of traveling waves and stationary fronts. These spatiotemporal patterns were produced by out-of-equilibrium reactions that arose from three different network topologies: a bistable, an autocatalytic and a Predator-Prey network. We have shown that we can measure the growth kinetics and dynamic rates of DNA reaction networks and work towards rationally engineering spatiotemporal behaviors in this quantitative approach. Overall, we have expanded the number of available tools to study chemical and material pattern formation and contributed towards Turing patterns with DNA strands.

A Attaching templates to agarose beads

A.1 Protocol for attaching templates to agarose beads

To attach templates T_2 to the agarose beads we followed a similar protocol as described next but we adjusted the concentration of beads and template depending on the experiment. Agarose beads were mixed at final concentration of 4% in a solution containing 100 nM of T_2 in the binding and washing (B&W) buffer (2 M NaCl, TE 10 mM and 0.2% tween). The resulting solution was constantly mixed for 30 minutes, then washed 3 times with B&W buffer to remove any unbound templates. The solution with templates attached was stored at 4°C or used in an experiment, which required pre-washing to remove the B&W buffer.

Templates did not attach uniformly to the agarose beads. They tended to concentrate more on the surface of the beads and less in the interior Fig. A.1. They formed shells of templates covering the surface of the beads.

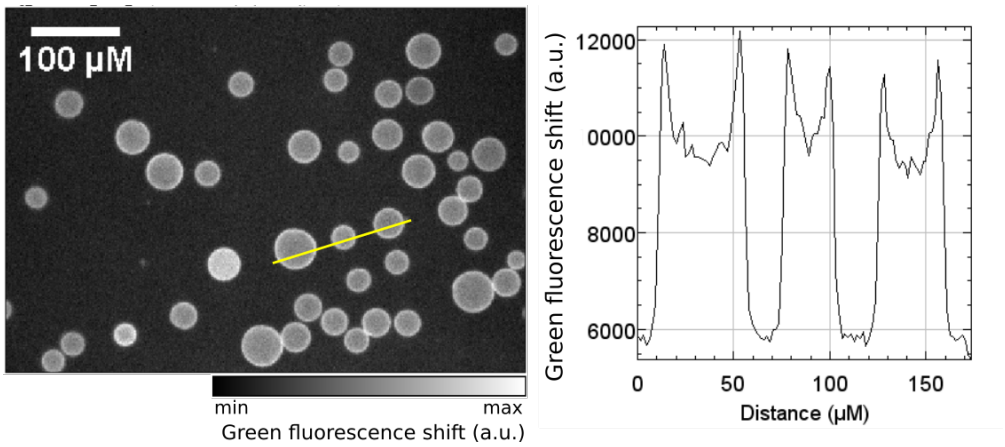

Figure A.1 – **Templates T_2 attached to agarose beads.** On the right hand side we show the images of the green fluorescence of EvaGreen in buffer PP. On the left hand side we plot the fluorescence profile at the location indicated by the yellow line. A_2 was present at a concentration of 1 µM.

A.2 Distribution of packed and diluted agarose beads in a capillary

In Section 2.5 we studied the growth kinetics and the front propagation dynamics for three cases in which the templates were attached to agarose beads that were closely packed (case 1) and diluted (case 2).

In the first case, our experimental protocol had to be adapted to generate a system of several layers of packed beads but not fully packing the entire capillary (Fig. A.2A). We point out that we have not quantified the impact of autocatalyst species diffusing freely in the upper part of the capillary where beads are not present on the front propagation. However, since there are no autocatalyst templates in this upper region of the capillary there is no growth of the autocatalyst species. We can hypothesize that the contribution to the front propagation of the autocatalyst species in the region without beads can be neglected since there is degradation of the autocatalyst species but no growth in this region. In the second case, the agarose beads were dispersed in agarose gel, thus fixing them after gelification (Fig. A.2B). We will explain in the next subsection the protocols for both cases.

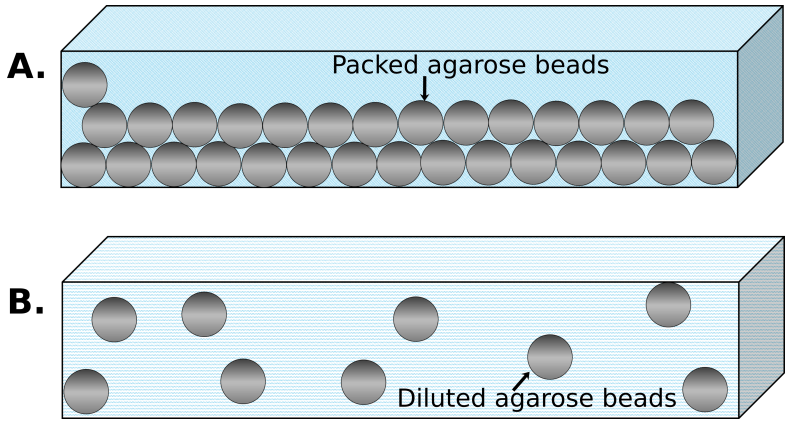

Figure A.2 – **Schematic diagrams of packed and diluted agarose beads in a capillary.(A)** Agarose beads sediment to the bottom forming layers of beads. **(B)** Diluted agarose beads are dispersed in a solidified agarose gel.

Protocol to packed agarose beads

We developed two protocols to obtained 'packed agarose beads'. One protocol allowed us to get also an entire capillary of packed beads but we did not succeed in obtaining propagating fronts with this protocol. In the second protocol we obtained packed beads in layers that do not fill the entire capillary (Fig. A.2A). We succeeded in generating propagating fronts using the second protocol.

Protocol 1

Agarose beads are packed by filling a capillary with the reaction solution containing the templates attached to the beads. The liquid is removed slowly while aiming to keep the beads inside the capillary. The capillary is refilled again with the reaction solution with the beads resulting a more concentrated in agarose beads. The liquid is removed again from the capillary, which is again refilled. These two steps are repeated until the beads are closely packed in the entire capillary.

Protocol 2

This second protocol is much simpler. We use a reaction solution that contains agarose beads at a concentration of 50% in volume. The capillary is then filled with this solution. We let the beads sediment by gravity for 15 minutes, thus resulting in several layers of packed agarose beads at the bottom of the capillary. In this protocol,

the number of layers of packed beads depends on the initial concentration of beads in the reaction solution. We can approximate the number of layers to be around seven since beads are 34 µm in diameter in a capillary of 500 µm in height. Thus at 50% beads, we get

$$\frac{500}{34} \times 50\% \approx 7.$$

B Article 1: Synthesis and materialization of a reaction-diffusion French flag pattern

Synthesis and materialization of a reaction-diffusion French flag pattern

One-sentence summary: Artificial DNA reaction networks create chemical and material patterns analogous to those observed during embryo development

Anton Zadorin[1,2], Yannick Rondelez[3,4], Guillaume Gines[3], Vadim Dilhas[1,2], Adrian Zambrano[1,2], Jean-Christophe Galas[1,2,*], André Estevez-Torres[1,2,*]

[1]Université Pierre et Marie Curie, Laboratoire Jean Perrin, 4 place Jussieu, 75005 Paris, France. [2]CNRS, UMR 8237, 75005, Paris, France. [3]LIMMS/CNRS-IIS, University of Tokyo, Komaba 4-6-2 Meguro-ku, Tokyo, Japan. [4]Ecole supérieure de physique et chimie industrielle, Laboratoire Gulliver, 10 rue Vauquelin, 75005, Paris, France. *To whom correspondence should be addressed; E-mail: jean-christophe.galas@upmc.fr, andre.estevez-torres@upmc.fr.

Abstract: During embryo development, structured regions of protein concentration appear in response to morphogen gradients. The archetypal pattern is the French flag —three chemically-distinct zones separated by sharp borders— but its synthetic analogue has remained elusive. Here we introduce an experimental model of gradient-induced pattern formation. We engineered artificial analogues of transcriptional networks based on short DNA single strands that interpret a morphogen gradient. Bistable networks created immobile, sharp and long-lasting concentration fronts. The combination of two bistable circuits generated a French flag pattern whose phenotype was reprogrammed by network mutation. As happens during morphogenesis, the patterns controlled the macroscopic organization of complex materials, namely DNA-decorated particles. This experimental framework could be used to test morphogenetic models and design programmable materials capable of morphogenesis.

Main Text

At the onset of embryonic morphogenesis, highly-ordered protein concentration profiles structure the embryo into separate regions that are 0.1 to 1 mm in size (*1*) —a process called pattern-formation. Two archetypal scenarios have shaped our view of this process: the symmetry-breaking Turing mechanism (*2–4*) and the processing of positional information (*5–7*). In the latter, a pre-existing morphogen gradient is interpreted by a molecular program producing several chemically-distinct zones with sharp borders, a situation that Lewis Wolpert named the French flag problem (*5*) (Figure 1A). Well-known examples are provided by the gradients of Bicoid in *Drosophila* (*6*) and of Sonic hedgehog in the vertebrate neural tube (*8*). Despite recent progress (*7, 9*), the generic mechanism that induces patterns determined by positional information is still under debate (*10, 11*). In a learning-by-doing approach to this question (*12–17*) we set out with the goal of synthesizing a French flag pattern outside of a living organism. To do so we used a DNA-based molecular programming language (*18*) that combines engineering simplicity with the design logic of morphogen patterning mechanisms (*11*): i) a gradient that determines the state of a reaction network, ii) a network with target nodes controlled by modular regulatory elements, and iii) a precise pattern shaped by the dynamics of the network.

The conversion of a shallow morphogen gradient into a concentration boundary that is both sharp and immobile requires a reaction network that interprets the gradient in a non-linear fashion. Diverse evidence (*19–21*) suggest that bistability is an essential property of such networks but the role of diffusion during gradient interpretation remains controversial (*10, 21, 22*). The strong historical influence of the reaction-only French flag model, which was initially opposed to the reaction-*diffusion* Turing mechanism (*23*), resulted in diffusion being neglected when considering gradient-induced patterning (*19*). Modern experiments in *Drosophila* conclude that diffusion is not needed to fit expression data (*9*) but it is necessary to explain the robustness of patterning to fluctuations (*7, 24*). Here, we show experimentally in an artificial system that combining bistability and diffusion yields a robust patterning mechanism, providing experimental evidence for recent hypotheses suggesting that a Turing-Wolpert mechanism could be at play *in vivo* (*22, 23*). We further demonstrate that these synthetic patterns are capable of shaping embedded materials in a way that is reminiscent of embryonic

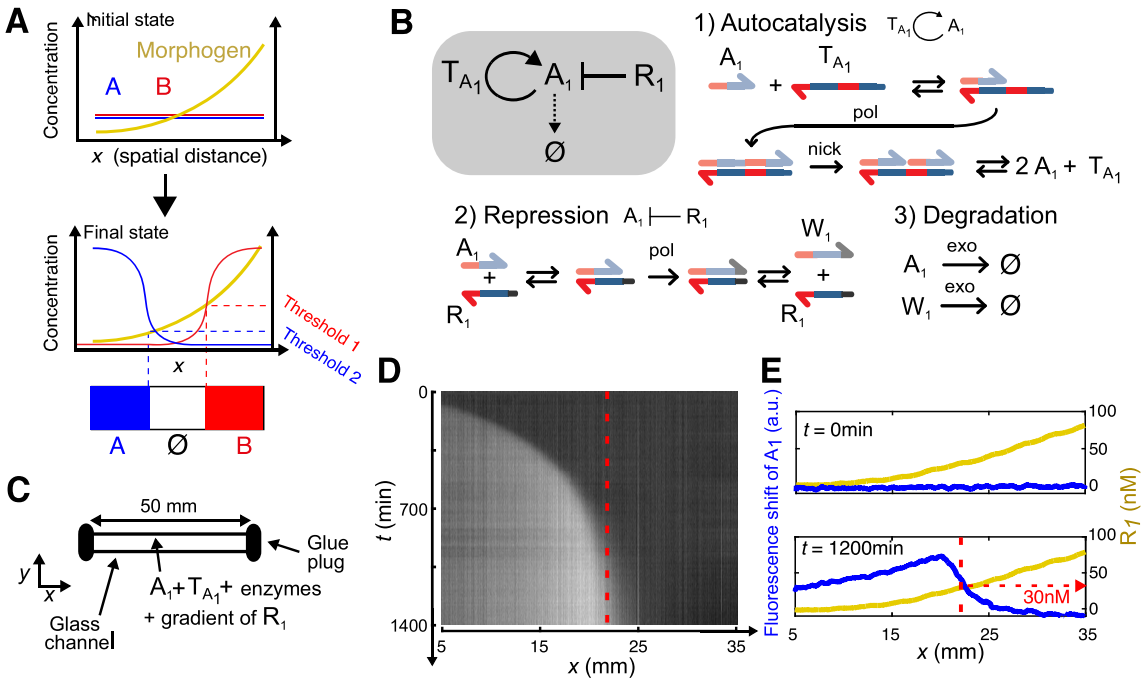

Figure 1: In a shallow gradient of morphogen, a bistable DNA network produces a Polish flag; a sharp and immobile concentration profile. (**A**) Scheme of Wolpert's French flag problem, where a gradient of morphogen yields three chemically-distinct zones: blue, white and red. (**B**) DNA-based bistable network with A_1 self-activation supported by template T_{A_1}, repressed by R_1 and continuously degraded, together with its molecular mechanism. Harpooned thick arrows are ssDNA where colors indicate sequence domains and light hue indicates complementarity. Straight black arrows denote chemical reactions. pol, nick and exo stand for polymerase, nicking enzyme and exonuclease, respectively. W_1 is a waste strand that cannot activate T_{A_1}. (**C**) Sketch of the experimental setup. (**D**) Kymograph of the fluorescence shift due to A_1 inside a capillary containing the network in (B) with initial condition $A_1(x,0) = 1$ nM and pre-patterned with the gradient $R_1(x,0)$ as in (E). The red dashed line indicates the stationary position of the profile. (**E**) Profiles of R_1 (yellow) and the fluorescence shift due to A_1 (blue) along the channel at initial time and after 1200 min.

morphogenesis.

To do so we engineered a series of bistable networks using the PEN DNA toolbox, a molecular programming language designed to construct networks analogous to transcriptional ones but using only simple biochemical reactions. This technology has recently been applied to construct out-of-equilibirum networks displaying oscillations (*18, 25*), bistability (*26*) and traveling concentration waves (*14, 27, 28*). Figure 1B depicts the simplest bistable network used here, with a first-order positive feedback loop and a non-linear repressor (Figures S6-S7). The nodes of the network, A_1 and R_1,

are respectively 11 and 15-mer single-stranded DNAs (ssDNAs), analogous to transcription factors. Self-activation is set by T_{A_1}, a 22-mer ssDNA template that plays the role of a gene. Repression is encoded by promoting the degradation of A_1 with a threshold given by R_1 (*29*) —italized species names indicate concentration throughout the text. Three enzymes —a polymerase, an exonuclease and a nicking enzyme— provide the metabolic functions homologous to the transcription-translation machinery and dissipate free energy from a reservoir of deoxynucleotides (dNTPs). As it happens in transcription networks, A_1 is continuously produced and degraded but the total template —gene— concentration is stable. In contrast to networks in vivo, molecular interactions are well-known and the mechanism (FiguresS3-S4) and kinetic rates can be precisely determined (*18*).

Our first goal was to create an immobile concentration front in the presence of a morphogen gradient, which we will call a Polish flag. We performed patterning experiments within 5 cm-long sealed glass microchannels of 4×0.2 mm^2 cross-section (Figure 1C). An exponential gradient of morphogen R_1 with a characteristic length $l = 2$ cm (Figure 1E and Figure S8-S9) was generated along the longitudinal axis of the channel by partially mixing two solutions with different R_1 by Taylor dispersion (SI Section 1.6 and Figure S5). In this geometry the gradient was stable within 10% over 10 h (Figure S10). Initially the channel contained homogeneous concentrations of the three enzymes, dNTPs, $T_{A_1} = 25$ nM, $A_1 = 1$ nM, and a gradient of R_1 in the range $0 - 200$ nM. The evolution of A_1 was measured by adding a fluorescent DNA intercalator and recording time-lapse fluorescence images in an inverted microscope. Figure 1D displays the spatio-temporal dynamics of the patterning process. A short, purely reactional, initial phase generated a sharp profile of A_1 at a location corresponding to low morphogen concentration (Figure S11). This profile later moved to the right through a reaction-diffusion (RD) mechanism, progressively decelerating until it stopped at the center of the channel at a position where $R_1^{RD} = 30 \pm 5$ nM. The characteristic width of the front was 2 mm, 10-fold sharper than the morphogen gradient, and remained immobile up to 15 h (Figure S12). When, instead of the repressor, the autocatalyst template was used as the morphogen, the complementary Polish flag pattern was obtained (Figure S13-S14). Stationary patterns were observed also when the morphogen gradient was immobilized on a surface (Figure S19).

The gap gene network, which interprets the Bicoid morphogen gradient during the development of

the *Drosophila* blastoderm (Figure 2A), is definitely more complex than the bistable network used so far. For instance, Bicoid activates Hunchback, which grows autocatalytically and strongly represses Knirps, which also grows autocatalytically and represses Hunchback (*9*). We designed a network that mimics these interactions (*26*) (Figures 2B and S15-S16) and recorded the patterning dynamics in a gradient of the Bicoid analogue, T_H (Figure 2C-E, Movie S1). At short times, a purely reactional phase created two independent and sharp fronts of the analogues of Hunchback, H, and Knirps, K. Subsequently, during an RD phase, the fronts traveled in opposite directions until they collided in the middle of the channel. At this time, the two profiles partially overlapped and a slow phase made the

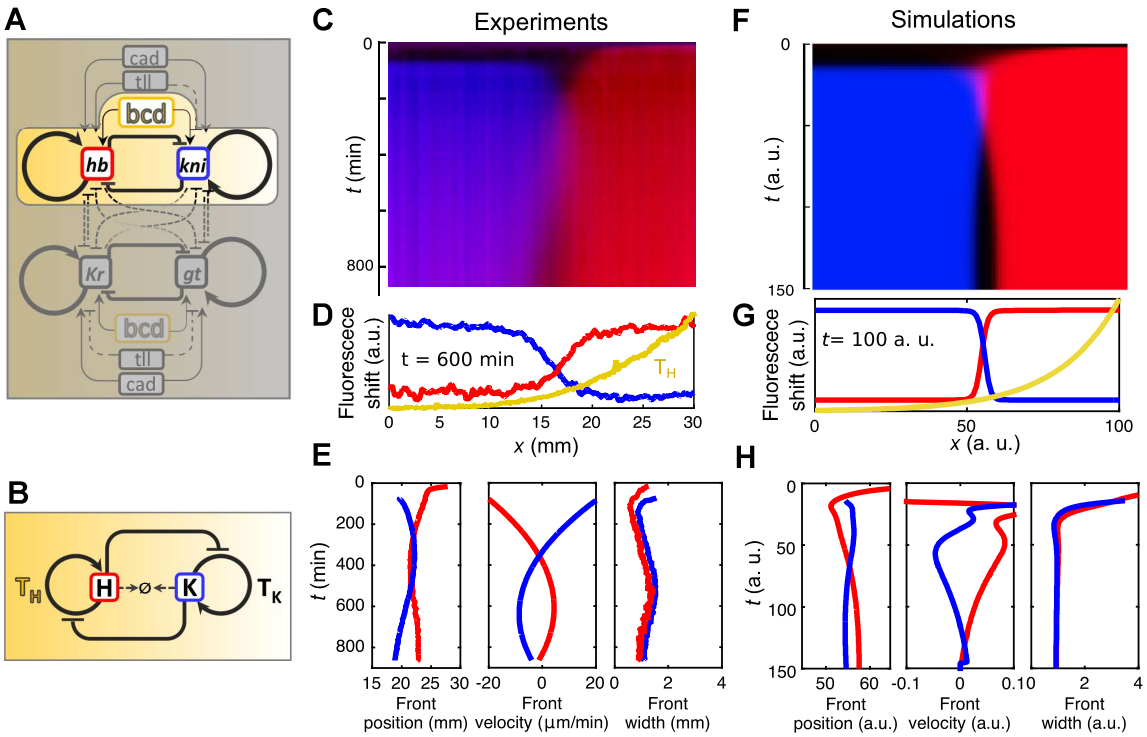

Figure 2: A DNA-based network that mimics part of the gap gene regulatory network generates two fronts that repel each other. (**A**) Topology of the gap gene network, from (*9*), the portion reproduced here is highlighted. (**B**) Analogue DNA-based network for the principal interactions between Bicoid, bcd, Hunchback, hb and Knirps, kni. Their DNA couterparts are respectively noted T_H, H and K. Experiments (**C, D, E**) and simulations (**F, G, H**) showing the kymograph of the fluorescence shift (**C, F**) for species H (red) and K (blue) inside a capillary containing the network in (B) and pre-patterned with a gradient of T_H (yellow) and fluorescence shift profiles at $t = 600$ min (**D**) and $t = 100$ a.u. (**G**). (**E, H**) Front position, velocity and width as a function of time extracted from the kymograph (colors as in D and G).

two fronts go backwards until reaching a steady-state where the overlap disappeared. 1-dimensional simulations with a 4-variable model (see SI Methods) displayed a similar behavior and suggested that this last phase was due to a slow synthesis of the repressors (Figure 2F-H). This patterning process was highly reproducible (Figure S17-S18).

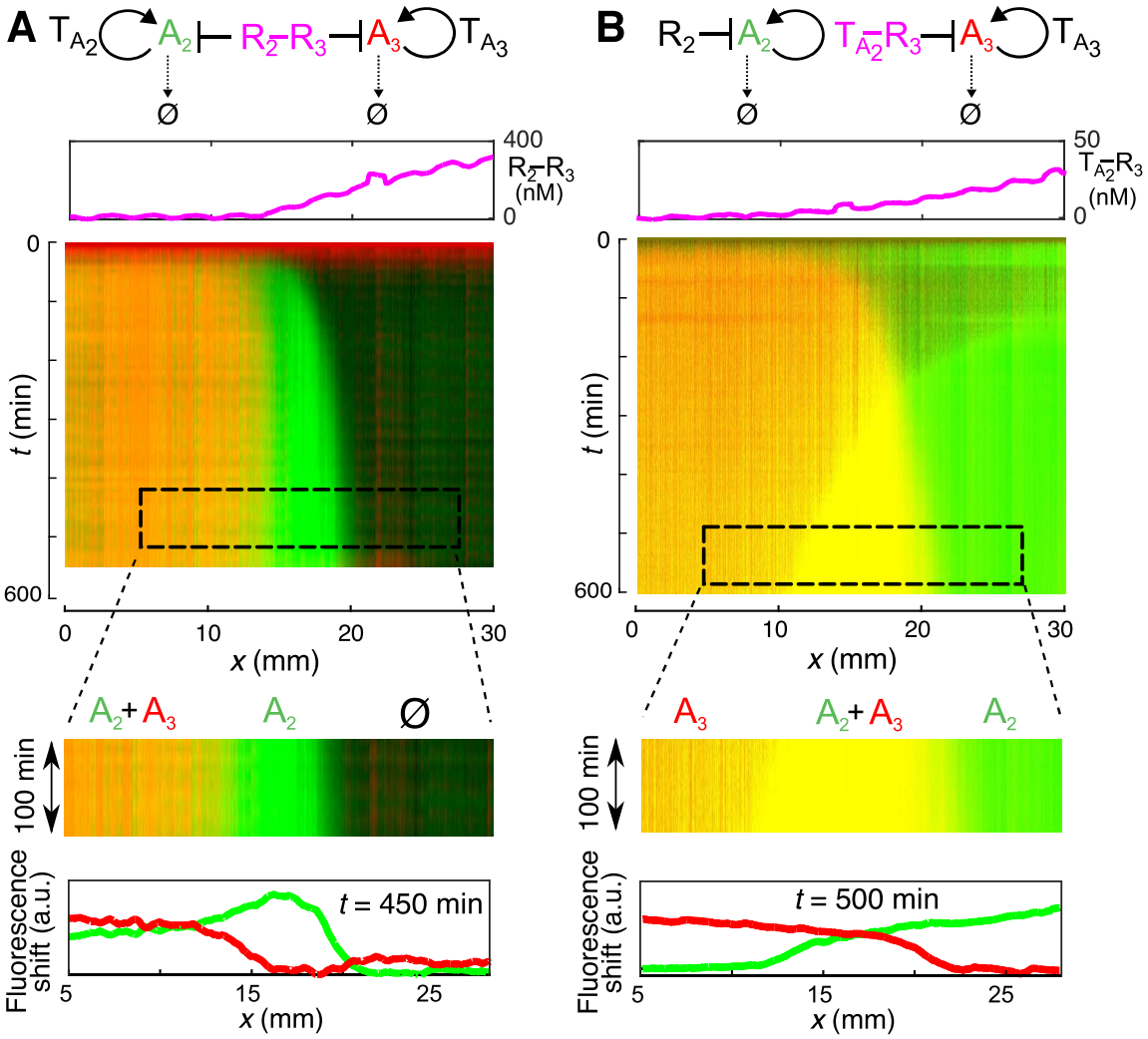

Figure 3: The combination of two orthogonal bistable networks produces a French flag pattern that can be simply reprogrammed. From top to bottom: network topology, initial morphogen gradient, kymograph and fluorescence shift profiles at steady state for two bistables coupled through either a double-repressor strand, $\mathrm{R}_2 - \mathrm{R}_3$ (**A**), or a template-repressor strand, $\mathrm{T}_{A_2} - \mathrm{R}_3$ (**B**), each used as morphogen gradient. Dashed rectangles are zooms of the kymographs where the two French flag patterns were stationary.

To implement a French flag pattern with three chemically-distinct zones (Figure 3, Figure S22 and Movie S2) we combined two orthogonal bistables, A_2 and A_3, (Figures S20-S21) into a single network using two different approaches. We used a bifunctional morphogen bearing either both repressors, $R_2 - R_3$, or one autocatalyst template and a repressor, $T_{A_2} - R_3$. In a gradient of $R_2 - R_3$, a channel containing a uniform concentration of T_{A_2} and T_{A_3} generated a French flag pattern that divided space into three regions, $A_2 + A_3$, A_2 and $\emptyset$, for 100 min (Figure 3A). By contrast, with a gradient of $T_{A_2} - R_3$ and a uniform concentration of R_2 and T_{A_3} a different pattern separated the space into A_3, $A_2 + A_3$ and A_2.

In the embryo, pattern formation induces tissue differentiation by providing localized chemical cues to pluripotent cells (*1*). Artificial materials inspired by this mechanism would bear astonishing properties, such as the capability to adapt their shape or function to different environmental conditions. As a proof of concept we coupled a Polish flag-generating network to the conditional aggregation of 1 μm diameter beads (Figure 4). Streptavidin-labeled particles were decorated with two types of biotin-labeled DNAs that had two different 11-mer ssDNA dangling ends (*30*). In the working buffer, the beads aggregated only in the presence of a linker strand L complementary to both ssDNA portions (Figure S23). A capillary containing i) a homogeneous dispersion of both types of beads, ii) a bistable network coupled to the linear production of L and iii) a gradient of R_1, produced a Polish flag of bead aggregation (Figure 4C-E). The aggregation pattern was stable for up to a month (Figure S24). Interestingly, the width of the aggregation front was 500 μm, 4-fold sharper than the front of fluorescence due to species A_1 in Figure 1. This primitive morphogenetic material thus uses two different sharpening mechanisms. The first one results from coupling the bifurcation of a bistable dynamic system to diffusion while the second is probably due to the cooperativity of bead-bead aggregation. This multi-level sharpening recalls hierarchical patterning mechanisms in vivo and could be advantageously used for microfabrication.

Our results demonstrate that DNA-based molecular programming is well suited to engineer concentration patterns reminiscent of those observed during early morphogenesis. They indicate that the combination of a bistable reaction network with diffusion is a simple engineering solution to generate immobile concentration fronts that are both sharp and long lasting. Our experimental model may help

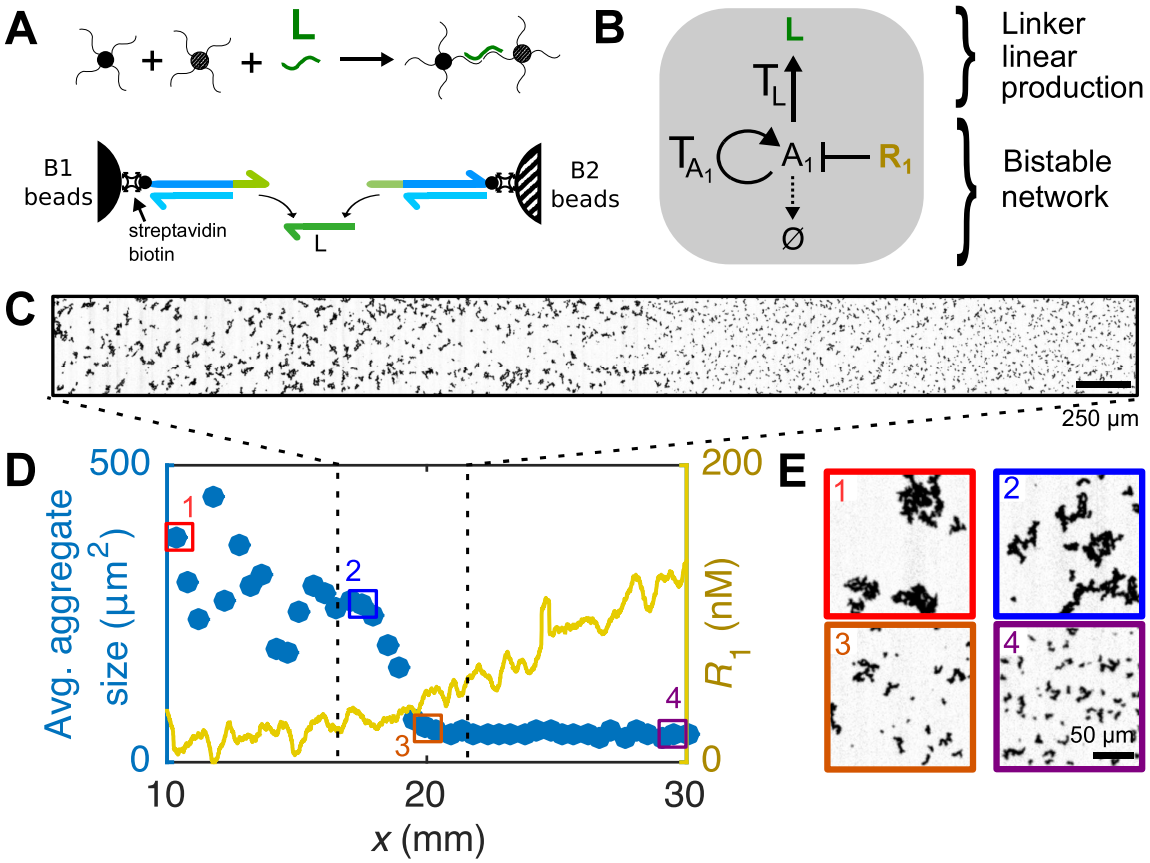

Figure 4: Materialization of a Polish flag pattern with conditional particle aggregation. (**A**) Sketch of the mechanism of particle aggregation where 1 μm particles decorated with two different DNA constructs (black and gray disks) are aggregated in the presence of linker strand L. (**B**) Scheme of the reaction network used here, where a bistable is coupled to the linear production of L with template T_L. All data were recorded after 40 h from a channel containing the particles, the network in panel (B) and an initial gradient of R_1. (**C**) Brightfield image at the center of the channel. (**D**) Average size of particle aggregates (blue disks, left axis) and initial concentration of R_1 (yellow line, right axis) along the longitudinal axis of the channel. The colored squares indicate the positions at which the brighfield images in (**E**) were recorded. The dashed lines correspond to the position where (C) was recorded.

understanding the role of regulative and diffusive processes during development and suggests that relatively simple networks may have enabled patterning at an early stage of evolution. Importantly, the simplicity of the method allowed us to record the patterning dynamics in real time, showing that a purely reactional initial phase is followed by a reaction-diffusion one. Finally, by coupling programmable patterns with matter we have engineered a morphogenetic material. This approach could

be interfaced with other DNA-compatible materials and devices (*31–33*) to create morphogenetic matter.

Acknowledgments

We thank Erwin Frey for insightful discussions, Alexis Vlandas for help with gradient generation and Ben Caller and Damien Woods for comments on the text. Supported by European commission FET-STREP under award Ribonets, by ANR jeunes chercheurs program under award Dynano, and by C'nano Ile-de-France (DNA2PROT grant).

Supplementary materials

Materials and Methods

Supplementary Text

Figures S1 to S24

Tables S1 to S3

Movies S1 and S2

References

References

1. L. Wolpert and C. Tickle. *Principles of development*. Oxford University Press, Oxford, 2011.

2. A. M. Turing. The chemical basis of morphogenesis. *Phil. Trans. Roy. Soc. B*, 237(641):37–72, 1952. 10.1098/rstb.1952.0012.

3. A. D. Economou, A. Ohazama, T. Porntaveetus, P. T. Sharpe, S. Kondo, M. A. Basson, A. Gritli-Linde, M. T. Cobourne, and J. B. A. Green. Periodic stripe formation by a Turing mechanism operating at growth zones in the mammalian palate. *Nature Genetics*, 44(3):348–351, 2012. 10.1038/ng.1090.

4. R. Sheth, L. Marcon, M. F. Bastida, M. Junco, L. Quintana, R. Dahn, M. Kmita, J. Sharpe, and M. A. Ros. Hox genes regulate digit patterning by controlling the wavelength of a Turing-type mechanism. *Science*, 338(6113):1476–1480, 2012.

5. L. Wolpert. Positional information and the spatial pattern of cellular differentiation. *J. Theo. Biol.*, 25(1):1–47, 1969.

6. D. St Johnston and C. Nüsslein-Volhard. The origin of pattern and polarity in the drosophila embryo. *Cell*, 68(2):201–219, 1992.

7. T. Gregor, D. W. Tank, E. F. Wieschaus, and W. Bialek. Probing the limits to positional information. *Cell*, 130(1):153–64, 2007.

8. E. Dessaud, A. P. McMahon, and J. Briscoe. Pattern formation in the vertebrate neural tube: a sonic hedgehog morphogen-regulated transcriptional network. *Development*, 135(15):2489–503, 2008.

9. Manu, S. Surkova, A. V. Spirov, V. V. Gursky, H. Janssens, A. Kim, O. Radulescu, C. E. Vanario-Alonso, D. H. Sharp, M Samsonova, and J. Reinitz. Canalization of gene expression and domain shifts in the drosophila blastoderm by dynamical attractors. *PLoS Comput Biol*, 5(3):e1000303, 2009.

10. J. Jaeger, Manu, and J. Reinitz. Drosophila blastoderm patterning. *Curr. Opin. Genet. Dev.*, 22(6):533–41, 2012.

11. J. Briscoe and S. Small. Morphogen rules: design principles of gradient-mediated embryo patterning. *Development*, 142(23):3996–4009, 2015.

12. M. Isalan, C. Lemerle, and L. Serrano. Engineering gene networks to emulate drosophila embryonic pattern formation. *PLoS Biol.*, 3(3):488–496, 2005.

13. M. Loose, E. Fischer-Friedrich, J. Ries, K. Kruse, and P. Schwille. Spatial regulators for bacterial cell division self-organize into surface waves in vitro. *Science*, 320(5877):789–792, 2008.

14. A. Padirac, T. Fujii, A. Estevez-Torres, and Y. Rondelez. Spatial waves in synthetic biochemical networks. *J. Am. Chem. Soc.*, 135(39):14586–14592, 2013. doi: 10.1021/ja403584p.

15. S. M. Chirieleison, P. B. Allen, Z. B. Simpson, A. D. Ellington, and Xi C. Pattern transformation with DNA circuits. *Nat Chem*, 5(12):1000–1005, 2013.

16. S. N. Semenov, A. J. Markvoort, T. F. A. deGreef, and W. T. S. Huck. Threshold sensing through a synthetic enzymatic reaction-diffusion network. *Angew. Chem. Intl. Ed.*, 53(31):8066–8069, 2014.

17. A. M. Tayar, E Karzbrun, V. Noireaux, and R. H. Bar-Ziv. Propagating gene expression fronts in a one-dimensional coupled system of artificial cells. *Nat. Phys.*, 11:1037–1041, 2015.

18. K. Montagne, R. Plasson, Y. Sakai, T. Fujii, and Y. Rondelez. Programming an in vitro DNA oscillator using a molecular networking strategy. *Mol Syst Biol*, 7:466, 2011. 10.1038/msb.2010.120.

19. P. Francois, V. Hakim, and E. D. Siggia. Deriving structure from evolution: metazoan segmentation. *Mol Syst Biol*, 3:154, 2007.

20. F. J. Lopes, F. M. Vieira, D. M. Holloway, P. M. Bisch, and A. V. Spirov. Spatial bistability generates hunchback expression sharpness in the drosophila embryo. *PLoS Comput Biol*, 4(9):e1000184, 2008.

21. S. Rulands, B. Klünder, and E. Frey. Stability of localized wave fronts in bistable systems. *Phys. Rev. Lett.*, 110(3):038102, 2013.

22. C. Quiñinao, A. Prochiantz, and J. Touboul. Local homeoprotein diffusion can stabilize boundaries generated by graded positional cues. *Development*, 142(10):1860–8, 2015.

23. J. B. Green and J. Sharpe. Positional information and reaction-diffusion: two big ideas in developmental biology combine. *Development*, 142(7):1203–11, 2015.

24. Y. Okabe-Oho, H. Murakami, S. Oho, and M. Sasai. Stable, precise, and reproducible patterning of bicoid and hunchback molecules in the early drosophila embryo. *PLoS Comput Biol*, 5(8):e1000486, 2009.

25. T. Fujii and Y. Rondelez. Predator-prey molecular ecosystems. *ACS Nano*, 7(1):27–34, 2013. doi: 10.1021/nn3043572.

26. A. Padirac, T. Fujii, and Y. Rondelez. Bottom-up construction of in vitro switchable memories. *Proc. Natl. Acad. Sci. USA*, 10.1073/pnas.1212069109, 2012. 10.1073/pnas.1212069109.

27. A. S. Zadorin, Y. Rondelez, J.-C. Galas, and A. Estevez-Torres. Synthesis of programmable reaction-diffusion fronts using DNA catalyzers. *Phys. Rev. Lett.*, 114(6):068301, 2015.

28. A. Zambrano, A. S. Zadorin, Y. Rondelez, A. Estevez-Torres, and J. C. Galas. Pursuit-and-evasion reaction-diffusion waves in microreactors with tailored geometry. *J. Phys. Chem. B*, 119(17):5349–5355, 2015.

29. K. Montagne, G. Ginés, and Y. Rondelez. Degradation-controlled nonlinearities in DNA networks. *submitted*. available to reviewers as supplementary material for review only.

30. M. E. Leunissen, R. Dreyfus, R. Sha, T. Wang, N. C. Seeman, D. J. Pine, and P. M. Chaikin. Towards self-replicating materials of DNA-functionalized colloids. *Soft Matter*, 5(12):2422, 2009.

31. P. W. K. Rothemund. Folding DNA to create nanoscale shapes and patterns. *Nature*, 440(7082):297–302, 2006.

32. E. Franco, E. Friedrichs, J. Kim, R. Jungmann, R. Murray, E. Winfree, and F. C. Simmel. Timing molecular motion and production with a synthetic transcriptional clock. *Proc. Natl. Acad. Sci. USA*, 10.1073/pnas.1100060108, 2011.

33. J. B. Lee, S. Peng, D. Yang, Young H. Roh, H. Funabashi, N. Park, E. J. Rice, L. Chen, R. Long, M. Wu, and D. Luo. A mechanical metamaterial made from a DNA hydrogel. *Nat. Nano*, 7(12):816–820, 2012. 10.1038/nnano.2012.211.

C Article 2: Pursuit-and-evasion reaction-diffusion waves in micro-reactors with tailored geometry

C.1 Main text

THE JOURNAL OF PHYSICAL CHEMISTRY B

Article

pubs.acs.org/JPCB

Pursuit-and-Evasion Reaction-Diffusion Waves in Microreactors with Tailored Geometry

A. Zambrano,[†,#] A. S. Zadorin,[†,#] Y. Rondelez,[‡] A. Estévez-Torres,*[,†,#] and J.-C. Galas[†,#]

[†]Laboratoire de Photonique et de Nanostructures, CNRS-UPR20, Marcoussis 91460, France

[‡]LIMMS/CNRS-IIS, University of Tokyo, Komaba 4-6-2 Meguro-ku, Tokyo 113-8654, Japan

Supporting Information

ABSTRACT: Out-of-equilibrium chemical systems may self-organize into structures displaying spatiotemporal order, such as traveling waves and Turing patterns. Because of its predictable chemistry, DNA has recently appeared as an interesting candidate to engineer these spatiotemporal structures. However, in addition to the intrinsic chemical parameters, initial and boundary conditions have a major impact on the final structure. Here we take advantage of microfluidics to design controlled reactors and investigate pursuit-and-evasion chemical waves generated by a DNA-based reaction network with Predator–Prey dynamics. We first propose two complementary microfabrication strategies to either control the initial condition or the two-dimensional geometry of the reactor where the waves develop. We subsequently use them to investigate the effect of curvature in wave propagation. We finally show that DNA-based waves can compute the optimal path within a maze. We thus suggest that coupling configurable microfluidics to programmable DNA-based dissipative reaction networks is a powerful route to investigate spatiotemporal order formation in chemistry.

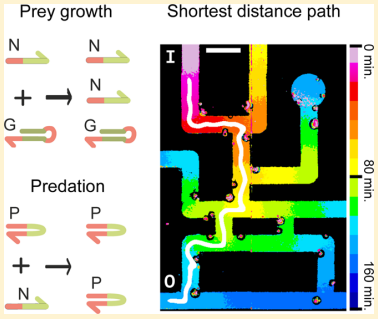

INTRODUCTION

The classic experimental approach to investigate the emergence of spatiotemporal order in chemistry relies on the Belousov–Zhabotinsky (BZ) reaction and its relatives.[1] This successful framework allowed the first proof of the existence of Turing patterns[2] and very recently the experimental verification of Turing's predictions,[3] among many other insightful observations.[4]

Spatiotemporal order in molecular systems may arise from the coupling of reaction and diffusion processes. In this case, ordered structures are steady-state solutions of the associated partial differential equations. They thus depend on the chemical mechanism, and the associated reaction rates, as well as on the diffusion coefficients of the reactants. However, of course, they are also strongly constrained by the initial and boundary conditions. BZ-related systems have highlighted the importance of initial and boundary conditions in the outcome of spatial self-organization.[5] For instance, excitable waves cannot propagate through doorways below a critical width, which has been used to implement chemical reaction-diffusion (RD) logic gates.[6] Moreover, because of their constant propagation velocity and parallel exploration of space, RD waves have been used to find optimal paths in a two-dimensional (2D) labyrinth.[7] Coupling microfabrication with BZ-related reactions has proven to be an interesting approach to investigate the influence of boundary conditions on reaction-diffusion chemical systems. For instance, Steinbock and co-workers developed polydimethylsiloxane (PDMS) microfluidic devices to characterize BZ waves,[8] while Ismagilov and collaborators were able to reproduce in a simple chemical system the complex spatiotemporal behavior of hemostasis.[9]

Despite its great importance, BZ-related reactions are difficult to engineer, and we are thus limited by a reduced set of experimentally available mechanisms. To extend this set, a recent approach, developed by Schwille and collaborators, uses purified biochemical systems: the Min system self-organizes into traveling waves *in vitro*[10] and is capable of sensing geometry over hundreds of microns.[11]

We have introduced an alternative approach that uses synthetic DNA-based dissipative systems.[12] Because of its simple synthesis and predictable reactivity toward the hybridization reaction,[13] DNA is a suitable chemical to engineer programmable chemical reaction networks (CRNs). Dissipative CRNs with various topologies and up to six nodes have been demonstrated experimentally[14] and computer-assisted design tools are now available.[15] The rate constants and diffusion coefficients of individual nodes can also be conveniently tuned.[16] However, no attempt has been made to control the initial and boundary conditions of reactions involving these versatile systems.

In this work we take advantage of microfluidics to precisely define initial and boundary conditions of a dissipative DNA-based CRN. To this end, we use a CRN with Predator–Prey (PP) dynamics that exhibits pursuit-and-evasion traveling

Received: September 18, 2014
Revised: March 31, 2015
Published: April 3, 2015

DOI: 10.1021/jp509474w
J. Phys. Chem. B 2015, 119, 5349–5355

waves. The predictable reactivity of the DNA system used here allows us to propose a model in fair agreement with the experimental data. We further investigate the effect of curvature in the dynamics of PP propagation. Finally we show that DNA-based waves can find the shortest path within a maze. These results suggest that the combination of DNA-based reaction networks with tailored microfluidic reactors is an interesting experimental framework to investigate spatiotemporal pattern formation in chemistry.

EXPERIMENTAL SECTION

Preparation of Solutions. DNA oligonucleotides were purchased from Biomers with HPLC purification. Sequences for DNA prey N, DNA predator P, and DNA template G and buffer components were described elsewhere[14b] and are given in Supporting Information (SI) Section 2 for convenience. The reaction mixture also contained two enzymes, the Bst large fragment DNA polymerase, noted pol, and 500 U/mL Nb.BsmI nicking enzyme, noted nick (both from NEB); concentrations are given as $pol_n = pol/pol_0$ with pol_0 = 16 U/mL. Unless stated otherwise, all experiments were performed at 44 °C with initial concentrations G_0 = 200 nM and P_0 = 2 nM. For kinetic experiments N_0 = 10 nM. For propagation experiments N_0 = 100 nM at the inlet of the channel.

Monitoring. The fluorescence shift of DY530 attached to the 3′ end of G was used to monitor the extent of the reaction. Kinetic experiments were performed in a real-time PCR machine (Biorad CFX96 or Qiagen Rotor-Gene Q). For propagation experiments, we used an inverted Zeiss Axio Observer Z1 microscope equipped with an HXP 120 fiber-coupled illuminator, a Brightline SpGold-B-ZHE Semrock YFP filterset (EX FF01-534/20, EM FF01-572/28, DM FF552-Di02), a 2.5× or a 10× objective EC Plan Neofluar with N.A. 0.075 and 0.3, respectively, a Marzhauser XY stage with a TokaiHit ThermoPlate, and an Andor iXon Ultra camera. During a typical experiment we recorded the fluorescence of six microfluidic channels with 1 or 2 min time lapse. Image acquisition and analysis were performed using Micro-Manager 1.4 (The Open Source Microscopy Software) and ImageJ (NIH).

Microreactor Fabrication. PDMS devices with reduced evaporation were fabricated by multilayer soft lithography.[17] To do so we superimposed two thin layers with embedded fluidic and control channels (fabricated as described elsewhere[18]) and added on top a thick PDMS layer with a punched centimetric hole filled with water to avoid evaporation. The thickness of the PDMS layer below the water tank was 250 μm. The main challenge consisted in aligning the two thin PDMS layers. The control and fluidic layers were made of spin-coated 1:20 and 1:10 PDMS, while the thick layer was 5 mm thick 1:5 PDMS. After partial curing for 30 min at 70 °C the thick and fluidic layers were assembled, cured for another 30 min and then aligned on the control layer. The device was finally sealed with a glass slide after a plasma treatment.

Microfluidic NOA81 (Norland Optical Adhesive) thiolene-based, photocurable glue devices were made as described[19] (SI Section 4). The sample was injected with a micropipette through the 1 mm access holes embedded in the NOA81 layer. The initial condition was created by injecting 0.5 μL of reaction mixture with 100 nM N. To prevent evaporation, the chip was sealed with PCR scotch tape (premium Plate sealing film, Platemax, Axigen).

RESULTS AND DISCUSSION

Predator−Prey Network without Degradation Exhibits a Single Pulse in a Well-Mixed Reactor. Throughout this work we consider a reaction network composed of two species: the prey, N, and the predator, P. In the presence of a polymerase, pol, and a nicking enzyme, nick, a 10-bases long oligonucleotide grows autocatalytically on the template G (Figure 1 and SI Figure S1). P is a palindromic oligonucleotide

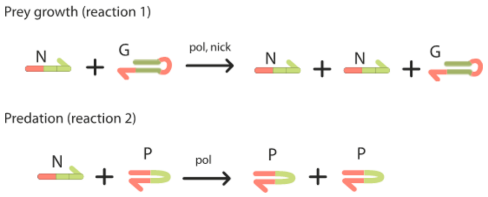

Figure 1. Mechanism of the DNA-based degradation-free Predator−Prey system consisting on the autocatalytic growth of the prey N (top) and the predation of N by P (bottom). Harpoon-ended arrows indicate single strand DNA with N, the prey, G, the template on which N grows, and P, the predator. pol and nick stand for polymerase and nicking enzyme, respectively. Colors denote DNA domains with equal or complementary sequences.

14-bases long that contains the complementary sequence of N on its 3′ end. When P and N hybridize, the polymerase extends the short strand yielding two P and thus resulting in the predation of N by P. Note that this system lacks an exonuclease providing degradation of N and P, in contrast with previous work.[12b,14b] In the following, species concentrations are noted in italics.

We first studied the kinetics of this system in a well-mixed reactor for different *pol* (Figure 2). The extent of the reaction

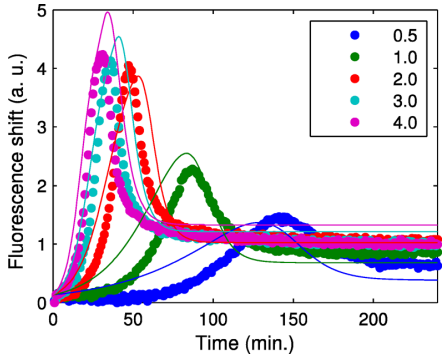

Figure 2. Predator−Prey dynamics in a well-mixed reactor. Fluorescence shift vs time for different polymerase concentrations, pol_n = 0.5−4. Disks and lines correspond, respectively, to experiments and to fits to the model in eqs 1 and 2 and eq S2 in the SI.

was followed by recording over time the fluorescence of a dye attached to the 3′ end of G (SI Figure S2). All the curves display the same qualitative behavior: the fluorescence shift grows over 20−150 min, reaches a maximum, and then decreases and eventually attains a steady state at a value higher than the initial one, 100−200 min later. This corresponds to the growth of N until a maximum value, N_{max}, reached when growth and predation rates become equal, followed by a

DOI: 10.1021/jp509474w
J. Phys. Chem. B 2015, 119, 5349−5355

decrease of N due to predation until the steady state ($N = 0$, $P = P_{max}$) is attained. A significant portion of the growth phase can be fitted by a monoexponential, with rate r_g (SI Figure S5). After the maximum of intensity is reached, the first 2/3 of the intensity drop during predation can also be fitted by a monoexponential, with rate r_p. Both r_g and r_p depend on pol_n (Figure 3A, circles). For r_g we distinguish three different regimes: for $pol_n = 0-0.5$, $r_g = (0.12\ \text{min}^{-1})pol_n$; in the range $pol_n = 0.5-4$, $r_g = (0.026\ pol_n + 0.06)\ \text{min}^{-1}$, and for $pol_n > 4$, $r_g = 0.16\ \text{min}^{-1}$. r_p coincides with r_g for $pol_n = 0.5-2$, then saturates and finally drops for $pol_n > 5$ (Figure 3A, circles). Both the maximum and final fluorescent shifts depend on pol_n (Figure 2 and SI Figure S3).

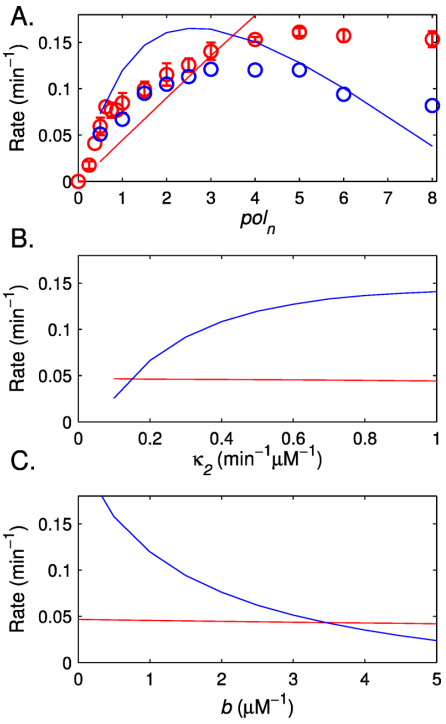

Figure 3. Dependence of the phenomenological rates, r_g (red) and r_p (blue), on the kinetic parameters pol_n (A), κ_2 (B), and b (C). Lines correspond to simulations and circles to experimental data in Figure 2. $\kappa_1 = 0.05\ \text{min}^{-1}$, $\kappa_2 = 0.5\ \text{min}^{-1}\ \mu\text{M}^{-1}$, and $b = 1\ \mu\text{M}^{-1}$ (see SI Figure S4).

Model. The aforementioned observations are compatible with the following simplified mechanism

$$N \xrightarrow{r_1} 2N \quad r_1(N) = \kappa_1 pol_n \frac{N}{1 + bN} \tag{1}$$

$$N + P \xrightarrow{r_2} 2P \quad r_2(N, P) = \kappa_2 \frac{NP}{1 + bP} \tag{2}$$

where r_i is the rate of reaction i; κ_1 and κ_2 are the rate constants for prey growth and predation, respectively (with κ_1 proportional to G_0); pol_n is the normalized concentration of pol; N and P are the concentrations of N and P at time t; and b is a saturation constant (note the addition of a saturation term for predation compared with refs 12b and 14b). Note also that predation does not explicitly depend on pol_n. However, the apparent predation rate r_p does depend on pol_n because N_{max} depends on pol_n. The different functional dependence of r_1 and r_2 on pol_n allows us to construct a phenomenological model that accounts for the fact that both the time at which the maximum fluorescence is attained and its intensity depend on pol_n (Figure 2A). To compare the experimental data to the model in eqs 1 and 2, we first measured the dependence of the fluorescence shift on N and P by titration of a solution of G (SI Figure S2 and eq S2). We then fitted the data by numerically solving eqs 1−4, together with eq S2 in the SI, with a single set of parameters and obtained $\kappa_1 = 0.05 \pm 0.02\ \text{min}^{-1}$, $\kappa_2 = 0.5 \pm 0.1\ \text{min}^{-1}\mu\text{M}^{-1}$, and $b = 1.0 \pm 0.5\ \mu\text{M}^{-1}$.

During the growth phase $N \gg P$ and $r_1 \approx \kappa_1 pol_n$ for $bN \ll 1$. We can thus identify r_1 and r_g. On the contrary, there is no simple analytical expression to link r_2 and r_p. To compare the experiments and the model we run simulations for the following parameter range: $\kappa_1 pol_n = 0.01-0.4\ \text{min}^{-1}$, $\kappa_2 = 0.1-1\ \text{min}^{-1}\ \mu\text{M}^{-1}$, and $b = 0-5\ \mu\text{M}^{-1}$. We then extracted r_g and r_p from the simulations and plotted them vs pol_n, κ_2, and b (Figure 3 and SI Figure S4). The model captures semi-quantitatively the behavior observed experimentally. Indeed r_g in the simulations depends linearly on pol_n as happens experimentally in the range $pol_n = 0.5-4$. However, as expected, our model does not capture the saturation of r_g at high pol_n. The model also captures well the bell-shaped dependence of r_p on pol_n. Further, r_g extracted from the model depends uniquely on pol_n and not on k_2 or b, as expected. r_p depends on all the parameters, and we cannot give a fundamental meaning to it. We conclude that $r_g \approx \kappa_1 pol_n$ and that this simple 2-variable model accounts for the essential dynamics of our PP system over the range $pol_n = 0.5-4$ with a single set of three parameters.

In a spatially inhomogeneous reactor, which we shall consider in the following, the evolution of N and P is given by

$$\frac{\partial N}{\partial t} = r_1(\text{N}) - r_2(\text{N, P}) + D_N \Delta N \tag{3}$$

$$\frac{\partial P}{\partial t} = r_2(\text{N, P}) + D_P \Delta P \tag{4}$$

where D_N and D_P are the diffusion coefficients of N and P, respectively, and Δ is the Laplacian operator. For a Heaviside-type initial condition for N and a homogeneous and sufficiently small one for P, one can consider that N propagates in a region where $P \approx 0$, such that $r_2 \approx 0$. Then, eq 3 is independent of eq 4, and its solution is a Fisher-KPP front of constant velocity (SI Section 1.6), given by

$$v_1^{\text{mod}} = 2\sqrt{r_1'(0)D} \tag{5}$$

where $r_1'(0) = \kappa_1 pol_n$ is the derivative of r_1 at $N = 0$ and D is the diffusion coefficient of the average species N. Indeed, N can be free or bound to G. As a result D is an average of D_N^{free} and D_N^{bound} weighted[16] by the hybridization constant of N and G, K_H. We estimated D by measuring the diffusion of fluorescently labeled 11 and 22 bases long ssDNA and found[16] $D_N^{\text{free}} = (18 \pm 3) \times 10^3\ \mu\text{m}^2\ \text{min}^{-1}$ and $D_N^{\text{bound}} = (11.8 \pm 0.8) \times 10^3\ \mu\text{m}^2\ \text{min}^{-1}$ at 44 °C. We measured $K_H = 4\ \mu\text{M}^{-1}$ (SI Figure S2), and thus, at low N and $G_0 = 200$ nM, 50% of N is bound to G yielding $D \approx 15\ \mu\text{m}^2\ \text{min}^{-1}$.

Spatial Reactors with Precise Control of the Initial Condition. A propagating pulse of prey appears when its initial concentration is inhomogeneously distributed over space. In

DOI: 10.1021/jp509474w
J. Phys. Chem. B 2015, 119, 5349−5355

our previous work, propagating wave trains arose from a homogeneous initial condition through uncontrolled phenomena that induced a symmetry break.[12b] To precisely control the position and the time where the prey pulse is triggered, we fabricated a channel reactor with embedded microvalves using soft lithography. Our device, depicted in Figure 4A, consists in

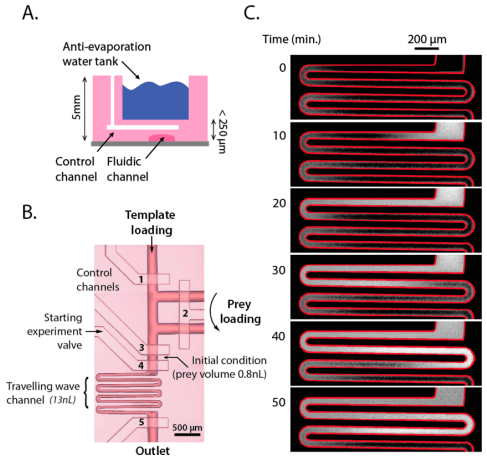

Figure 4. Control of the initial condition using a PDMS microfluidic device. (A) Side view of the device, with fluidic channel, control channelm and antievaporation tank (not to scale). (B) Photo of the main area of the device from the top. The serpentine channel is dedicated to the observation of traveling waves, while the five valves are used to prepare a precise initial condition. The fluidic channel is in deep red. (C) Time-lapse images of a traveling wave of preys in the serpentine channel. G_0 = 1 μM; pol_n = 0.5.

a long serpentine channel and a loading area with four valves dedicated to the injection of the initial condition. To minimize evaporation, the thickness of the PDMS layer above the channels was reduced to 250 μm and covered with a water reservoir.

Setting an experiment is as follows (SI Figure S5). First, the long serpentine channel is filled with a solution containing everything but species N. Once valves 4−5 are closed, a solution containing N can thus be loaded to fill the injection volume between valves 3−4. While valve 4 remains closed no change is observed in the serpentine channel, indicating that it is impermeable to N. When valve 4 is open, 80 amol of N are injected into the inlet of the serpentine channel. At this point a fluorescence pulse propagates along the channel (Figure 4C and SI Figure S6). The propagation velocity was constant and equal to 68 μm min^{-1} for G_0 = 1 μM and pol_n = 0.5. In these conditions we measured r_g = (5.2 ± 0.5) × 10^{-2} min^{-1}. From eq 5, and taking $r'_1(0) = r_g$, we found v_1^{mod} = 55 μm min^{-1}, which is 1.2-fold lower than the measured value.

PDMS microfluidic devices with embedded valves are thus compatible with DNA-based reaction networks. In particular they can be used to precisely set an initial condition to trigger a traveling pulse. Nevertheless, and despite our efforts to reduce evaporation, bubbles were observed after 2 h at 44 °C, which rendered this device impractical to operate (SI Figure S8). Several partial solutions for reducing evaporation in PDMS chips have been proposed.[20] However, it appears difficult to implement these methods with devices that include valves. We chose instead a more robust and simpler technology.

Versatile Spatial Reactors with Well-Defined Geometry and Low Evaporation. Microfluidic stickers are microfluidic devices made of the thiolene-based photocurable glue NOA81.[19] They are simple and rapid to fabricate from a PDMS mold (SI Figure S7). Moreover, they can replicate submicron features and display a low autofluorescence above 500 nm,[21] and evaporation is strongly reduced compared to PDMS (SI Figure S8).

To test the compatibility of NOA81 devices with DNA-based networks we fabricated channel reactors 1 mm wide, 120 μm high, and 15 mm long connected at both ends by 1 mm holes. Figure 5A,B shows the propagation of a pulse of preys, together

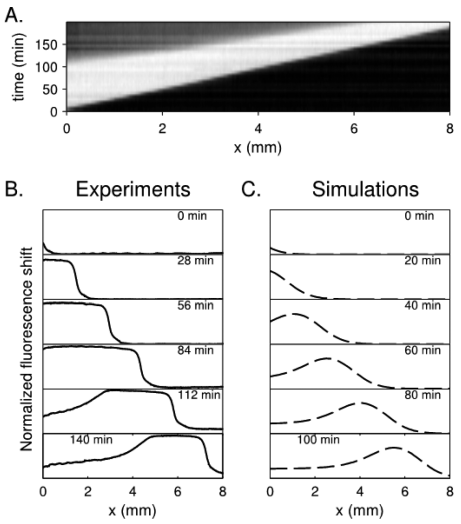

Figure 5. Pursuit-and-evasion wave propagating in a straight NOA81 channel. Kymograph (A) and corresponding fluorescence shift profiles along the channel (B) for a traveling pulse of preys. pol_n = 2. See also SI Movie 002.avi. (C) Simulated fluorescence shift profiles from eqs 1−4 and eq S2 in the SI with κ_1 = 0.05 min^{-1}, κ_2 = 0.5 min^{-1} μM^{-1}, b = 1 μM^{-1}, and $D_N = D_P = D$ = 15 × 10^3 μm^2 min^{-1}.

with the corresponding fluorescence profiles along the channel. The shape of the pulse is somewhat trapezoidal, with a sharp leading edge and a more diffuse trailing edge, 650 μm and 2 mm wide, respectively. The leading and the trailing edges correspond to propagating fronts of preys and predators, respectively. Both the leading and the trailing edges of the pulse have a stable shape over time, indicating that they correspond to traveling fronts. However, the shape of the propagating pulse is not constant but narrows over time. The velocity of the leading and trailing edges were v_1^{exp} = 51 μm min^{-1} and v_2^{exp} = 71 μm min^{-1}, respectively, at G_0 = 200 nM and pol_n = 2. At steady state we expect $v^{exp}{}_1 = v^{exp}{}_2$ indicating that the velocity of the trailing front (and thus its width) has not reached a steady state in our experimental conditions. The standard deviation of the measured velocity was as low as 5% in a series of replicate experiments with identical reaction mixtures in a single chip. It rose to 20% when comparing experiments performed in different days, which suggests variations in the state of the chip surfaces upon fabrication. From eq 5, with $r_1'(0) = r_g$ = 0.11 ± 0.01 min^{-1} (Figure 3A) we calculated v_1^{mod} = 80 ± 20 μm min^{-1}, which is 1.6-fold higher than the measured value. In the model of eqs 3 and 4 the velocity depends only on the prey

DOI: 10.1021/jp509474w
J. Phys. Chem. B 2015, 119, 5349−5355

growth rate and on the diffusion of the prey and does not depend on the predation reaction (κ_2 and b) that takes place at the trailing edge. The 1.6-fold difference between the model and the experiments could thus arise from a poor estimation of $r_1'(0)$ or D that would be at most 2.5 lower than stated. Errors on $r_1'(0)$ may appear if the intensity of our fluorescent reporter underestimates the concentration of N at low N, which cannot be excluded. Concerning the value of D, it is difficult to imagine it being lower than D_N^{bound}, which would make at most a correction factor of 1.25, although interactions with the surface may reduce D_N^{bound} further. A quantitative agreement of the modeled and experimental propagation velocities requires further investigation and is outside the scope of this work.

Subsequently, we numerically integrated eqs 1−4 in a one-dimensional space using the method of lines and the parameters extracted from Figure 2. In agreement with the experiments, the simulations predict a pulse with a leading and a trailing front that propagate at constant velocity. However, in contrast with the experiments, the velocities of these two fronts were identical in the simulations and equal to 70 μm min^{-1}. This is respectively 1.4-fold larger and identical than the measured values for the leading and trailing front. The shape of the simulated front was bell-like and its width was constant over time, in contrast with the experiments. The parameter κ_2 governed the width of the pulse (SI Figure S9) and did not influence the velocity as expected from the theory (SI Section 1.5). We thus hypothesize that the variation of the experimental pulse width over time is due to a change of κ_2. A possible mechanism for this is the saturation of the polymerase at high N, i.e., just behind the leading front. In that case pol would be sequestered by the prey growth reaction and would not be available for predation, lowering κ_2. As soon as P starts to grow and the predator front forms (at t = 84 min in the experiments), the mechanism would change and κ_2 would recover its value without saturation.

Predator−Prey Propagation in a 90°-Turn. In NOA81 it is straightforward to fabricate spatial reactors with arbitrary two-dimensional shapes. To investigate PP propagation dynamics in two-dimensions we designed channels with a 90°-turn and different curvature radii. Figure 6 shows a pulse of prey propagating in 2 mm wide channels with curvature radius, R_c, of 1.5 and 8 mm at their center. The inner and outer paths of the turn were 0.8 and 3.9 mm long, in the first case, and 11 and 14 mm in the second. In contrast with the results obtained in the straight channel the velocity of the leading edge was not constant. For R_c = 1.5, the velocity along the outer path increased up to +120 μm min^{-1}, while it decreased by up to −75 μm min^{-1} along the inner path, from 150 μm min^{-1} at the entry of the turn. For R_c = 8, the changes in velocity were less pronounced 6.2 and −18.6 μm min^{-1}, respectively, from 62 μm min^{-1} at the entry. Similar qualitative changes were obtained in simulations (SI Figure S10).

These changes in velocity can be understood considering that in a straight channel the front can be approximated by a planar wave while in the turn the front acquires a curvature, γ, that depends on space and time. The wave velocity along a coordinate normal to the front, is influenced by γ as

$$v_\perp = v_0 + \gamma D \qquad (6)$$

where v_0 is the planar wave velocity and D is the diffusion coefficient of the propagator species.[22] For R_c = 1.5 mm, we measured maximum curvatures at the outer and inner paths of γ^{out} = (3.7 ± 1.3) × 10^{-3} μm^{-1} and γ^{in} = −(9 ± 3) × 10^{-4} μm^{-1}, respectively (SI Figure S11). With D = 18000 μm^2 min^{-1} we get $\gamma^{out}D$ = 67 ± 21 μm min^{-1} and $\gamma^{in}D$ = −16 ± 5 μm min^{-1}. These figures are, respectively, 2-fold and 6-fold smaller than the experimental values for the outer and inner paths. However, the order of magnitude and the sign are correct. Moreover eq 6 was derived for excitable systems, which is not the case of the PP network studied here.

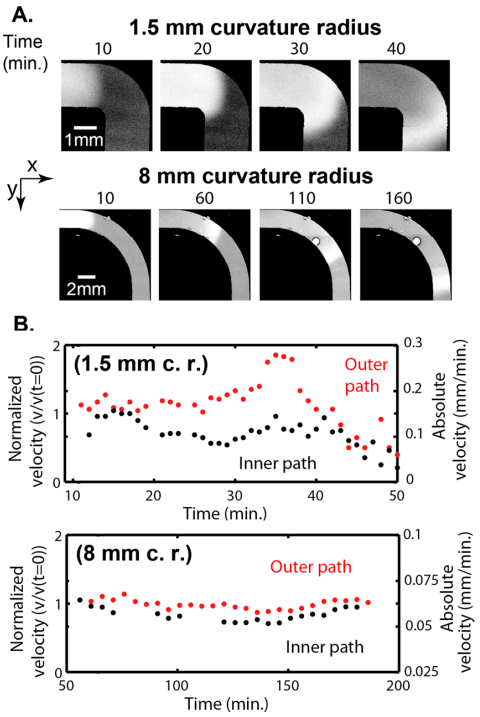

Figure 6. Effect of the front curvature in the propagation dynamics of pursuit-and-evasion waves. (A) Yellow fluorescence shift time-lapse images of a traveling pulse of N passing through a 90°-turn channel of 1.5 or 8 mm curvature radius. (B) Velocity of the leading front, v_1, along the longitudinal coordinate of the channel at different times for the inner (black) and outer (red) path of the channel. pol_n = 0.5. Channel is 2 mm wide and 500 μm deep. See also SI Movie 003.avi.

Finding the Optimal Path in a Maze. Reaction-diffusion systems are known to compute optimal paths within complex labyrinths. This approach has been undertaken using the Belousov−Zhabotinsky reaction[7] and the *Physarum* slime mold.[23] However, in none of these systems the computed output could be easily interfaced with a chemical downstream process. In contrast, DNA-based reaction-diffusion systems can be simply connected to other DNA-based networks with further information-processing capabilities or to DNA nanostructures.[24] We thus fabricated a 5.5 × 9 mm^2 maze with 500 μm wide channels and tested the capability of the PP pulse to compute optimal paths (Figure 7). A pulse was initiated at the upper-left corner of the maze. It propagated through all possible paths, splitting at each crossing and vanishing at dead ends and upon collision with a counter-propagating pulse. The pulse took 150 min to explore the whole maze. We determined the shortest path between the inlet (I) and the outlet (O) by analyzing the reverse front propagation with a homemade automated image-processing algorithm, although other algorithms have been described.[25] We first determined the position

DOI: 10.1021/jp509474w
J. Phys. Chem. B 2015, 119, 5349−5355

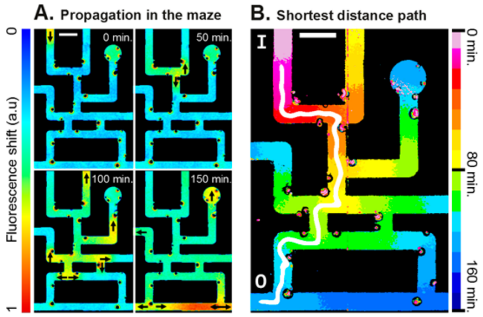

Figure 7. Pulse of prey finds the shortest path between the entrance and the exit of a maze. (A) Time-lapse fluorescence shift images, color indicates fluorescent shift. Black arrows indicate the sense of propagation of the leading edge. Black circles are air bubbles. (B) Computation of the shortest path by the reaction-diffusion pulse (white line). Color indicates the time stamp of the leading edge of the pulse. Channels are 500 μm wide and 200 μm deep. pol_n = 0.5. See also SI Movie 004.avi.

of every propagating front at all times. Then, starting from the last image, we selected the front at the exit of the maze and searched for the closest front on the previous image. By iteration, the shortest path from O to I was found (Figure 7B, white line).

In NOA devices, bubbles hindering front propagation appear after at least 25 h (SI Figure S8). With typical front speeds of 100 μm min^{-1} this makes a maximum traveled distance of about 15 cm, which is comparable to previous demonstrations of labyrinth-solving chemical systems.[7] It is to be noted that with a typical front width of 100 μm, details smaller than 100 μm will not be sensed by the propagating front. These constraints should be considered in future applications of this method.

CONCLUSION

We have recently demonstrated the capability of DNA-based reaction-networks to create traveling waves and spirals in a closed system.[12b] Such reaction-diffusion systems are moreover highly controllable: both the topology of the reaction network[12a,14a] and the reaction and diffusion rates of each node[16] can be tuned. Here we have extended the capabilities of this experimental framework to the control of the initial condition and of the geometry of the reactor where the reaction-diffusion process takes place. These controlled reactors have allowed us to investigate the intriguing dynamics of pursuit-and-evasion waves. In summary, dissipative DNA-based reactions in combination with microfluidics make an experimental framework of choice for investigating emergent spatiotemporal behaviors in synthetic systems.

ASSOCIATED CONTENT

Supporting Information

Degradation-free predator-prey mechanism and model; preparation of solutions; experimental details about PDMS devices; NOA81 device fabrication; evaporation in PDMS and NOA81 devices; influence of κ_2 on the simulated pulse width; simulation of the pulse propagation in the 90°-turn; measurement of front curvatures; supplementary movies. This material is available free of charge via the Internet at http://pubs.acs.org.

AUTHOR INFORMATION

Present Address

[#]Sorbonne Universités, Université Pierre et Marie Curie, CNRS UMR 8237, Laboratoire Jean Perrin, 75005, Paris, France.

Notes

The authors declare no competing financial interest.

ACKNOWLEDGMENTS

We are grateful to the LPN clean room staff. We thank L. Mzali and A. Kalley for performing preliminary experiments, A.-M. Haghiri-Gosnet for her kind support, and A. Vlandas for fruitful discussions. This research was partially funded by the ANR Jeunes Chercheurs Program under award Dynano. A.S.Z. was supported by a postdoctoral fellowship from NanoSciences Ile-de-France (Enginets award) and Labex Nanosaclay (Turnano award).

REFERENCES

(1) (a) Belousov, B. P. *Sb Ref Radiats Med. Medgiz Moscow* **1959**, 145−147. (b) Zaikin, A. N.; Zhabotinsky, A. M. *Nature* **1970**, *225* (5232), 535−537. (c) Epstein, I.; Pojman, J. A. *An Introduction to Nonlinear Chemical Reactions*; Oxford University Press: New York, 1998.

(2) (a) Castets, V.; Dulos, E.; Boissonade, J.; De Kepper, P. *Phys. Rev. Lett.* **1990**, *64* (24), 2953. (b) Ouyang, Q.; Swinney, H. L. *Nature* **1991**, *352* (6336), 610−612.

(3) (a) Turing, A. M. *Philos. Trans. R. Soc. London, Ser. B* **1952**, *237* (641), 37−72. (b) Tompkins, N.; Li, N.; Girabawe, C.; Heymann, M.; Ermentrout, G. B.; Epstein, I. R.; Fraden, S. *Proc. Natl. Acad. Sci. U.S.A.* **2014**, *111*, 4397−4402.

(4) Vanag, V. K.; Epstein, I. R. *Int. J. Dev. Biol.* **2009**, *53* (5−6), 673−681.

(5) (a) Vanag, V. K.; Epstein, I. R. *Chaos* **2008**, *18* (2), 026107. (b) Mikhailov, A. S.; Showalter, K. *Phys. Rep.* **2006**, *425* (2−3), 79−194.

(6) (a) Tóth, Á.; Showalter, K. *J. Chem. Phys.* **1995**, *103*, 2058−2066. (b) Á. Tóth, V. G.; Showalter, K. *J. Phys. Chem.* **1994**, *98*, 522−531. (c) Motoike, I.; Yoshikawa, K. *Phys. Rev. E* **1999**, *59* (5), 5354−5360.

(7) Steinbock, O.; Tóth, Á.; Showalter, K. *Science* **1995**, *267* (5199), 868−871.

(8) Ginn, B. T.; Steinbock, B.; Kahveci, M.; Steinbock, O. *J. Phys. Chem. A* **2004**, *108* (8), 1325−1332.

(9) Kastrup, C. J.; Runyon, M. K.; Shen, F.; Ismagilov, R. F. *Proc. Natl. Acad. Sci. U.S.A.* **2006**, *103* (43), 15747−15752.

(10) Loose, M.; Fischer-Friedrich, E.; Ries, J.; Kruse, K.; Schwille, P. *Science* **2008**, *320* (5877), 789−792.

(11) (a) Schweizer, J.; Loose, M.; Bonny, M.; Kruse, K.; Mönch, I.; Schwille, P. *Proc. Natl. Acad. Sci. U.S.A.* **2012**, *109* (38), 15283−15288. (b) Zieske, K.; Schwille, P. *Angew. Chem., Int. Ed.* **2013**, *52* (1), 459−462.

(12) (a) Montagne, K.; Plasson, R.; Sakai, Y.; Fujii, T.; Rondelez, Y. *Mol. Syst. Biol.* **2011**, *7*, 466. (b) Padirac, A.; Fujii, T.; Estévez-Torres, A.; Rondelez, Y. *J. Am. Chem. Soc.* **2013**, *135* (39), 14586−14592.

(13) Zuker, M. *Nucleic Acids Res.* **2003**, *31* (13), 3406−3415.

(14) (a) Padirac, A.; Fujii, T.; Rondelez, Y. *Proc. Natl. Acad. Sci. U.S.A.* **2012**, *109*, E3212−E3220. (b) Fujii, T.; Rondelez, Y. *ACS Nano* **2013**, *7* (1), 27−34. (c) Baccouche, A.; Montagne, K.; Padirac, A.; Fujii, T.; Rondelez, Y. *Methods* **2014**, *67*, 234−249.

(15) (a) Aubert, N. l.; Mosca, C. m.; Fujii, T.; Hagiya, M.; Rondelez, Y. *J. R. Soc. Interface* **2014**, *11*, 20131167. (b) van Roekel, H. W. H.; Meijer, L. H. H.; Masroor, S.; Felix Garza, Z. C.; Estevez-Torres, A.; Rondelez, Y.; Zagaris, A.; Peletier, M. A.; Hilbers, P. A. J.; de Greef, T. F. A. *ACS Synth. Biol.* **2014**, DOI: 10.1021/sb500300d.

(16) Zadorin, A. S.; Rondelez, Y.; Galas, J.-C.; Estevez-Torres, A. *Phys. Rev. Lett.* **2015**, *114* (6), 068301.

(17) Unger, M. A.; Chou, H.-P.; Thorsen, T.; Scherer, A.; Quake, S. R. *Science* **2000**, *288* (5463), 113−116.

(18) Galas, J.-C.; Haghiri-Gosnet, A.-M.; Estevez-Torres, A. *Lab Chip* **2013**, *13* (3), 415−423.
(19) Bartolo, D.; D, G.; Nghe, P.; Studer, V. *Lab Chip* **2008**, *8*, 274−279.
(20) (a) Polini, A.; M, E.; Sciancalepore, A. G.; Girardo, S.; Biasco, A.; Camposeo, A.; Cingolani, R.; Weitz, D. A.; Pisignano, D. *Biomicrofluidics* **2010**, *4* (3), 036502. (b) Seok Heo, Y.; M. C, L.; Song, J. W.; Futai, N.; Tung, Y.-C.; Smith, G. D.; Takayama, S. *Anal. Chem.* **2007**, *9* (3), 1126−1134. (c) Chang, W.-J.; A, D.; Sedlak, M.; Ladisch, M. R.; Bashir, R. *Biomed. Microdevices* **2003**, *5* (4), 281−290.
(21) Wägli, Ph.; Y. G, B.; Homsy, A.; de Rooij, N. F. *Proceedings of the 14th International Conference on Miniaturized Systems for Chemistry and Life Sciences* **2010**, 1937−1939.
(22) Tyson, J. J.; Keener, J. P. *Phys. D* **1988**, *32* (3), 327−361.
(23) Nakagaki, T.; Yamada, H.; Toth, A. *Nature* **2000**, *407* (6803), 470−470.
(24) (a) Rothemund, P. W. K. *Nature* **2006**, *440* (7082), 297−302. (b) Wei, B.; Dai, M.; Yin, P. *Nature* **2012**, *485* (7400), 623−626.
(25) Rambidi, N.; Yakovenchuk, D. *Phys. Rev. E* **2001**, *63* (2), 026607.

DOI: 10.1021/jp509474w
J. Phys. Chem. B 2015, 119, 5349−5355

C.2 Supplementary information

Supplementary information for

Pursuit-and-evasion reaction-diffusion waves in micro-reactors with tailored geometry

A. Zambrano[1], A.S. Zadorin[1], Y. Rondelez[2], A. Estévez-Torres[1], J.-C. Galas[1]
[1]Laboratory for Photonics and Nanostructures, CNRS UPR20, Marcoussis, France
[2]LIMMS/CNRS-IIS, University of Tokyo, Komaba 4-6-2 Meguro-ku , Tokyo, Japan

Contents

1 Degradation-free Predator-Prey mechanism and model

1.1 Mechanism of the DNA-based degradation-free Predator-Prey system

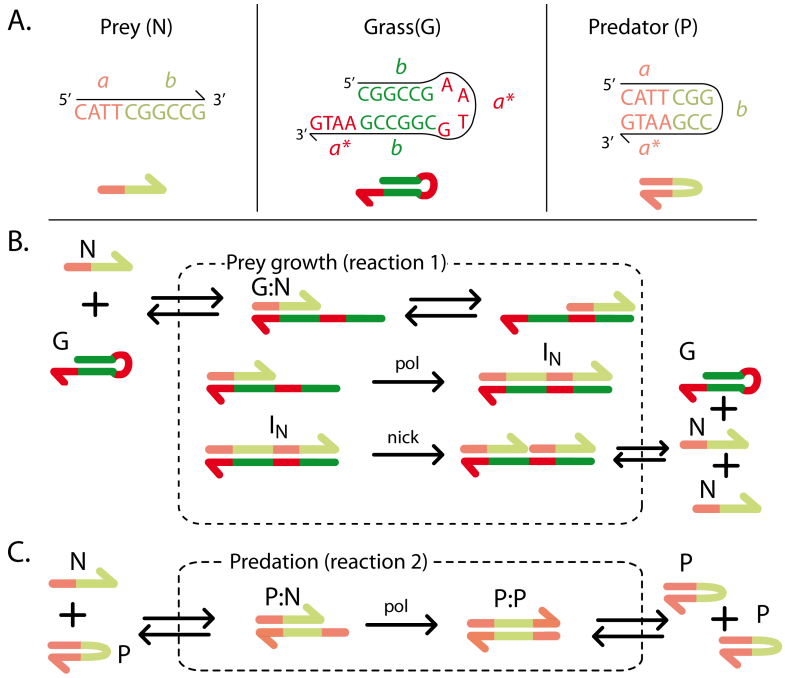

Figure S1: ***Mechanism of the DNA-based degradation-free Predator-Prey system.*** *A. The 3 DNA species involved in the reactions: prey N, predator P and grass template G. B. Reaction 1: autocatalytic prey growth of prey N in presence of the grass template G. C. Reaction 2: predation, predator P consumes prey N and reproduce, yielding two predators P. Complementary DNA sequences share the same color: pink/red for a/a* domains and green/light-green for self-complementary b domain. And pol stands for polymerase while nick stands for nicking enzyme*

1.2 Dependence of the fluorescence shift on *N* and *P*

We followed the extent of the reaction by recording the fluorescence from DY530 attached to the 3' end of G. Because P contains the sequence of N, both can hybridize on the 3' end of G, and both contribute to the quenching of fluorescence. To determine this dependence we titrated a solution of 200 nM G with N or P.

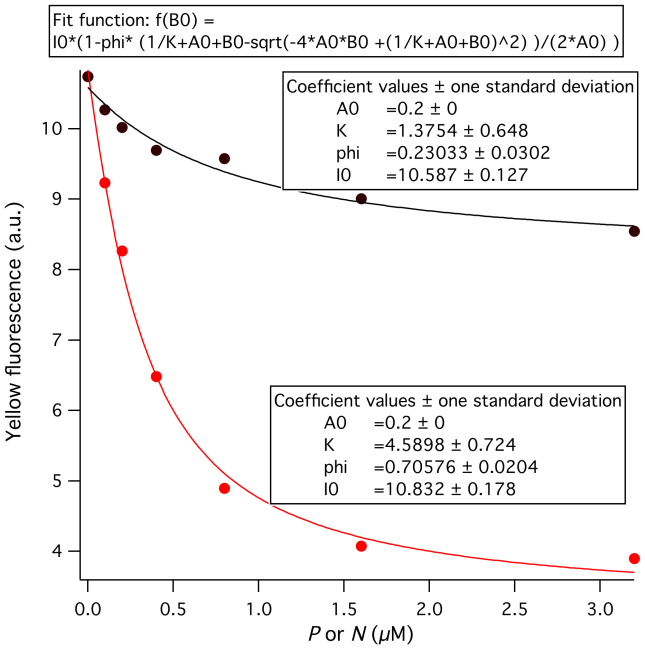

Figure S2: Fluorescence of a 200 nM solution of G as a function of P (black) or N (red) concentration in the working buffer without enzymes at 44 ºC. Note that the fluorescence shift used in the main text corresponds to an arbitrary constant minus the yellow luorescence.

From the data in Figure S2 we can relate the normalized yellow fluorescence shift to the actual concentrations of P and N as

$$I_{shift}^{norm} = \phi_N N_G + \phi_P P_G \tag{1}$$

where N_G and P_G are the concentrations of N bound to G and P bound to G, respectively and φ_N and φ_P are their respective fluorescence quantum yields. Writing the equilibriums N + G = N_G and P + G = P_G with equilibrium constants K_N and K_P, respectively, we find:

$$I_{shift}^{norm} = \frac{\phi_N}{2G_0}\left(1/K_N + G_0 + N - \sqrt{-4G_0N + (1/K_N + G_0 + N)^2}\right) + \frac{\phi_P}{2G_0}\left(1/K_P + G_0 + P - \sqrt{-4G_0P + (1/K_P + G_0 + P)^2}\right) \tag{2}$$

From Figure S2 and Eq. 2 we find $\varphi_N = 0.7$ and $\varphi_P = 0.23$, $K_N = 1.4\ \mu M^{-1}$ and $K_P = 4.6\ \mu M^{-1}$. In the simulations in Figs. 2A and 4C of the Main Text we use Eq. 2 to calculate the fluorescence shift from the simulated values of *N* and *P*.

1.3 Dependence of the maximum and final fluorescence shift on pol_n

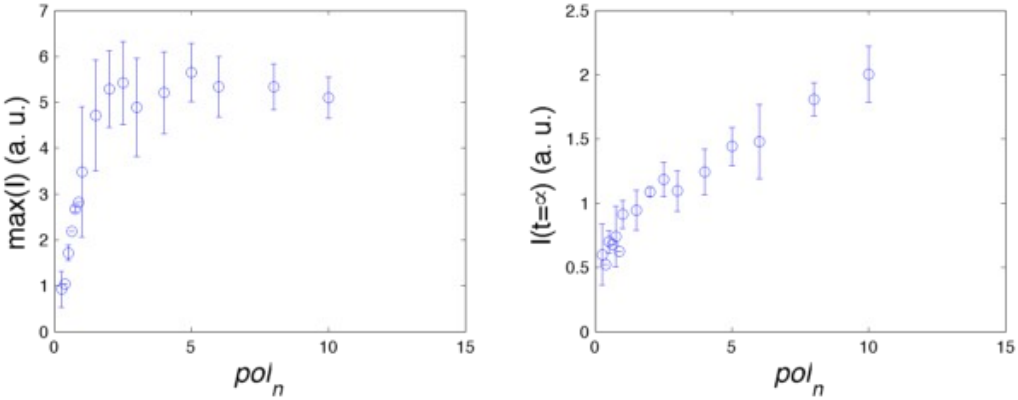

Figure S3: Maximum (left) and final (right) fluorescence shift vs pol_n for the data in Figure 2A of the Main Text.

1.4 Fitting of the growth rate

At the beginning of an experiment in Figure 2A of the Main Text, we can consider the concentration of both preys and predators to be low - solutions are prepared with 10 nM prey and 2 nM predator respectively and thus

$$r_1 \ll r_2 \tag{3}$$

which leads to

$$\frac{dN}{dt} \approx \kappa_1 pol_n \frac{N}{1+bN} \tag{4}$$

Otherwise, at low concentration of prey, $bN \ll 1$, we have

$\frac{dN}{dt} \approx \kappa_1 pol_n N$ for which a solution is $N(t) = N_0 e^{\kappa_1 pol_n t} = N_0 e^{r_g t}$

Fitting the exponential growth of preys using a nonlinear least square fitting algorithm – red curve in Figure S4 - we extracted the corresponding rate constant r_g as a function of the polymerase concentration as summarized in Figure 2 B in the main text.

Note that although the exponential growth is only fitted for the initial prey growth, the exponential growth is nicely maintained further along prey growth for higher concentrations of prey. The computation of the rate constant r_g is not exactly straightforward as we must fit only the initial prey growth up to a valid growth time that holds true to the assumptions from equations. Therefore the criteria for selecting the upper growth time came from the exponential fitting: we selected k when the values were not changing much from iteration to iteration and for the lowest values of the square root of residuals as depicted in Figure S4 B.

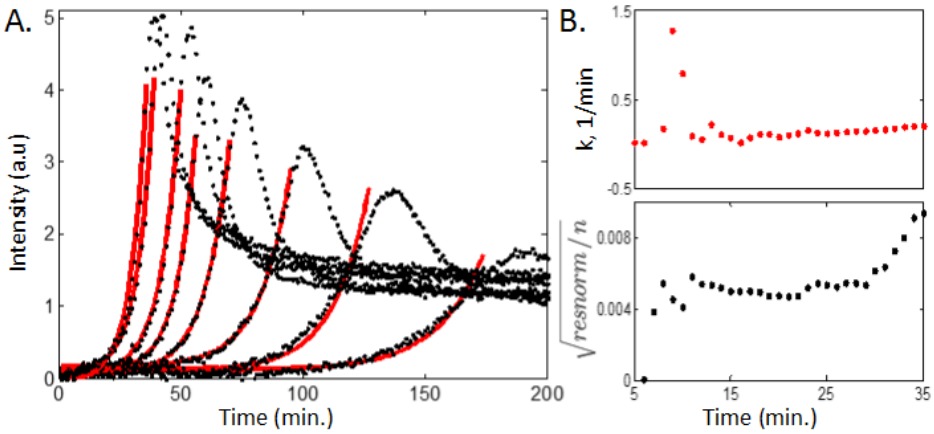

Figure S4: ***Prey growth exponential fitting of predator-prey system in the absence of degradation in a 0D reactor.*** *A. Prey concentration is monitored over time for different normalized polymerase concentrations, pol_n, (right to left polymerase concentration: 0.5, 0.75, 1, 1.5, 2, 2.5, 4, 5). Initial prey N, predator P and template G concentrations were 10 nM, 2 nM and 200 nM. B. Computed rate constant (red, top graph) and square root of residues (black, bottom graph) for prey growth (k) for pol_n=5 exponential fitted curve (far left red line in A.) as a function of time.*

1.5 1D model and derivation of the front velocity

For simplicity we will assume that effective diffusion coefficients of both prey and predator are fixed parameters and are equal. Indeed, N and P are 10- and 14-mere DNA strands, and their diffusion coefficients are very close by value. With this assumption, the reaction-diffusion equations governing the system become

$$\begin{aligned} \frac{\partial N}{\partial t} &= \frac{\kappa_1 \cdot pol_n \cdot N}{1 + b\,N} - \frac{\kappa_2 N\,P}{1 + b\,P} + D\frac{\partial^2 N}{\partial x^2}, \\ \frac{\partial P}{\partial t} &= \frac{\kappa_2 N\,P}{1 + bP} + D\frac{\partial^2 P}{\partial x^2}. \end{aligned} \tag{5}$$

To facilitate the following analysis we introduce new, adimensionalized dependent variables, independent variables and a parameter

$$\begin{gathered} \tau = \kappa_1 \cdot pol_n \cdot t, \quad \xi = x\sqrt{\frac{\kappa_1 \cdot pol_n}{D}}, \quad n = \frac{\kappa_2}{\kappa_1 \cdot pol_n} N, \\ p = \frac{\kappa_2}{\kappa_1 \cdot pol_n} P, \quad \mu = \frac{\kappa_1 \cdot pol_n \cdot b}{\kappa_2}. \end{gathered} \tag{6}$$

Substitution of this into (5) results in the following system:

$$\begin{aligned} \frac{\partial n}{\partial \tau} &= \frac{n}{1 + \mu\,n} - \frac{n\,p}{1 + \mu\,p} + \frac{\partial^2 n}{\partial \xi^2}, \\ \frac{\partial p}{\partial \tau} &= \frac{n\,p}{1 + \mu\,p} + \frac{\partial^2 p}{\partial \xi^2}. \end{aligned} \tag{7}$$

To find a traveling wave solution of this system we search for a solution of the form $n(\xi,\tau) = n(\xi - \upsilon\tau) = n(\eta), \quad p(\xi,\tau) = p(\xi - \upsilon\tau) = p(\eta),$ where $\eta = \xi - \upsilon\tau$ is the automodel variable. Here υ has a meaning of an adimensional speed of propagation of the solution. We will find later how it is linked with the speed of propagation in laboratory units. Such substitution results in the following system of second order ODEs:

$$\begin{aligned} -\upsilon\dot{n} &= \frac{n}{1 + \mu\,n} - \frac{n\,p}{1 + \mu\,p} + \ddot{n}, \\ -\upsilon\,\dot{p} &= \frac{n\,p}{1 + \mu\,p} + \ddot{p}, \end{aligned} \tag{8}$$

where a dot means derivative with respect to η.

It is convenient to consider a system of first order ODEs equivalent ot (8) by introduction of new dependent variables $m = \dot{n}$ and $q = \dot{p}$. The resulting system is

$$
\begin{aligned}
&\dot{n} = m,\\
&\dot{p} = q,\\
&\dot{m} = -\upsilon m - \frac{n}{1+\mu n} + \frac{n\,p}{1+\mu\,p},\\
&\dot{q} = -\upsilon q - \frac{n\,p}{1+\mu\,p}.
\end{aligned}
\tag{9}
$$

The steady states of this system in $\mathbb{R}^4$ are points $(0,p,0,0)$, and they continuously fill the p-axis. A traveling wave, that has in front of it $n=0,\ p=p_0$, and behind it $n=0,\ p=p_1>p_0$, corresponds to a solution of (5) that begins in a point $(0,p_1,0,0)$ and ends in a point $(0,p_0,0,0)$ (note the sign in front of time in $\eta=\xi-\upsilon\tau$). It is important, that experimental initial conditions define the point $(0,p_0,0,0)$, and in our experiments $p_0<(1-\mu)^{-1}$. The point $(0,p_1,0,0)$ is defined by the corresponding trajectory. To find possible propagation velocities we will perform a simple local stability analysis near the steady states. To do so, we find eigenvalues of (9) in steady states by solving the secular equation:

$$
\begin{vmatrix}
-\lambda & 0 & 1 & 0\\
0 & -\lambda & 0 & 1\\
\dfrac{(1-\mu)p-1}{1+\mu\,p} & 0 & -\upsilon-\lambda & 0\\
-\dfrac{p}{1+\mu\,p} & 0 & 0 & -\upsilon-\lambda
\end{vmatrix} = 0.
$$

Its solutions are

$$
\lambda_1=0,\ \ \lambda_2=-\upsilon,\ \ \lambda_{3,4}=\frac{1}{2}\left(-\upsilon\pm\sqrt{\upsilon^2+4\frac{(1-\mu)p-1}{1+\mu\,p}}\right).
$$

As was expected from the fact that the steady states form a continuous line, all of them are degenerate at least once. One particular steady state $(0,(1-\mu)^{-1},0,0)$ is double degenerate.

When $p>(1-\mu)^{-1}$, the steady state is a saddle with hyperbolic eigenvalues, and its local center manifold conforms to the p-axis. In this case $\lambda_{3,4}$ are real, and $\lambda_3\lambda_4<0$. λ_2 corresponds to an eigenvector $l_2=(0,1,0,-\upsilon)^T$, while $\lambda_{3,4}$ correspond to eigenvectors $l_{3,4}=\left(1,-\dfrac{p}{(1-\mu)p-1},\lambda_{3,4},-\dfrac{p\lambda_{3,4}}{(1-\mu)p-1}\right)^T$ respectively.

When $p<(1-\mu)^{-1}$, the local center manifold is again 1-dimensional and corresponds to the p-axis, but the stable manifold is now 3-dimensional, and the eigenvectors have the same expressions as in the previous case. This case further splits into two subcases: $\upsilon\geqslant 2\sqrt{1-\dfrac{p}{1+\mu\,p}}$, and $\upsilon<2\sqrt{1-\dfrac{p}{1+\mu\,p}}$. In the first subcase, all the eigenvalues are

real, and the stable manifold has a (may be degenerate) node. In the second subcase, $\lambda_{3,4}$ become complex conjugate, and there is a focus-node in the stable manifold.

The steady states with $p < (1-\mu)^{-1}$ can only be stocks, and the ones with $p > (1-\mu)^{-1}$ are the only ones that can be sources. Therefore, the only physically meaningful possibility is to have a trajectory that starts at a steady state with $p > (1-\mu)^{-1}$ and ends at a steady state with $p < (1-\mu)^{-1}$. For a given $p_0 < (1-\mu)^{-1}$, there exists the smallest velocity $\upsilon_c = 2\sqrt{1-\frac{p_0}{1+\mu\, p_0}}$. Indeed, there is only two trajectories that enter this point in direction of l_2, as $\lambda_2 < \mathrm{Re}\,\lambda_4 \leqslant \mathrm{Re}\,\lambda_3 < 0$. Because all such trajectories, as seen from (9), evolve strictly in the *pq*-plane, they cannot begin at some other point with $p > (1-\mu)^{-1}$. If $\upsilon < 2\sqrt{1-\frac{p_0}{1+\mu\, p_0}}$, then entering trajectories, that originate at some steady state with $p > (1-\mu)^{-1}$, form spirals in a plane spanned by $l_3 + l_4$ and $i(l_3 - l_4)$, and this plane is transversal to the *pmq*-hyperplane. It means, that approaching trajectories will have $n < 0$ at any neighborhood of the steady state in question. Assuming that this smallest velocity corresponds to the only stable front, like in the Fisher-KPP case, we can expect the velocity of the traveling solution of (7) to be equal to $2\sqrt{1-\frac{p_0}{1+\mu\, p_0}}$.

The corresponding velocity in laboratory units, *i.e.* the parameter v in the solution $N(x,t) = N(x - vt)$, $P(x,t) = P(x - vt)$, as readily seen from (5), equals to $v = \upsilon\sqrt{D\kappa_1 \cdot pol_n} = 2\sqrt{D\left(\kappa_1 \cdot pol_n - \frac{\kappa_2 P_0}{1 + bP_0}\right)}$. Assuming $P_0 \ll 1/b$, and $\kappa_2 P_0 \ll \kappa_1 \cdot pol_n$, as it is in current experiments, we have $v = 2\sqrt{D\kappa_1 \cdot pol_n}$.

If $D_N \neq D_P$, using the same adimentionalized variables except $\xi = x\sqrt{\kappa_1 \cdot pol_n / D_N}$, we obtain instead of (9) the following system

$$\begin{aligned}
&\dot{n} = m,\\
&\dot{p} = q,\\
&\dot{m} = -\upsilon m - \frac{n}{1+\mu n} + \frac{n\,p}{1+\mu\, p},\\
&\dot{q} = -\frac{1}{\delta}\upsilon q - \frac{n\,p}{\delta(1+\mu\, p)},
\end{aligned}$$

where $\delta = D_P / D_N$.

The eigenvalues in this case are

$$\lambda_1 = 0,\ \ \lambda_2 = -\frac{\upsilon}{\delta},\ \ \lambda_{3,4} = \frac{1}{2}\left(-\upsilon \pm \sqrt{\upsilon^2 + 4\frac{(1-\mu)\,p - 1}{1+\mu\, p}}\right).$$

The expression for the eigenvectors becomes more complicated, but it does not change the reasoning outlined above. The final expression for the minimal velocity becomes $v = \upsilon\sqrt{D_N \kappa_1 \cdot pol_n} = 2\sqrt{D_N\left(\kappa_1 \cdot pol_n - \frac{\kappa_2 P_0}{1 + bP_0}\right)}$.

At small initial predator concentration we have $v = 2\sqrt{D_N \kappa_1 \cdot pol_n}$.

2 Preparation of solutions

The DNA oligonucleotides were purchased from Biomers with HPLC purification. As depicted in figure S1, sequences for DNA prey N, DNA predator P and DNA template G, are respectively

DNA	Sequence (5'> 3')	3'-modifications
N (prey)	CATTCGGCCG	
P (predator)	CATTCGG-CCGAATG	
G (template)	CGGCC**GAATG-C**GGCCGAATG	Dy530 (yellow fluorescence) *Area in bold is the recognition sequence of the nicking enzyme*

Table S1: DNA oligonucleotides sequences and modifications

Reaction buffer contains salts (20 mM Tris-HCl, 10 mM (NH4)2SO4, 10 mM KCl, 50 mM NaCl, 8 mM MgSO4), dNTP (400 µM of each, New England Biolabs), BSA and surfactant for enzyme stability (500µg/mL BSA, New England Biolabs, 0.1% Synperonic F108, Aldrich), single-stranded binding protein to prevent premature annealing of DNA (5 ng/µL extremely thermostable single-stranded binding protein (ETSSB), New England Biolabs), a double stranded DNA stabilizer (2 µM Netropsin, Sigma-Aldrich), and a reducing agent (4 mM dithiothreitol, Sigma-Aldrich).

3 PDMS devices

3.1 Setting an experiment

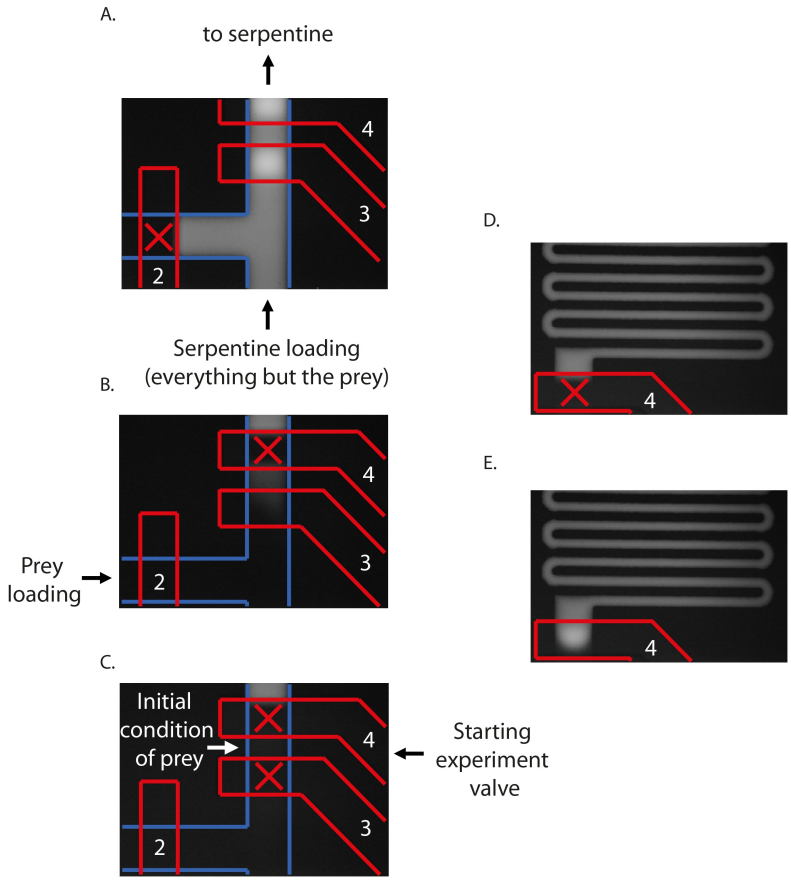

Figure S5: ***Setting an experiment in the PDMS device.*** *A. The long serpentine channel is filled with a solution containing everything but the prey. B. The serpentine channel is then isolated closing valves #4 and opening valve #2 a solution containing prey can thus be loaded in order to fill the "initial condition prey volume". C. Once done, valve #3 is closed. D. and E. Opening the valve #4 ("Starting experiment valve") will thus add some prey into the serpentine channel. Growth will start from this point and propagates, then followed by predator.*

3.2 Prey propagation and corresponding profile

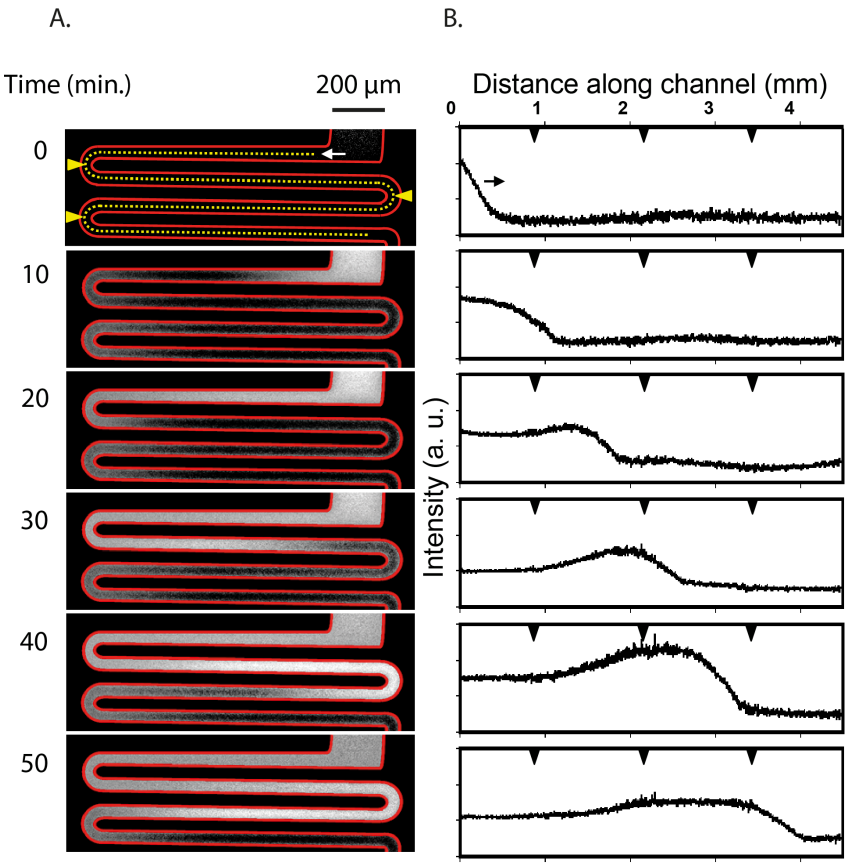

Figure S6: ***Propagation in the PDMS microfluidic device.*** *A. Traveling wave of preys in the serpentine channel. Wave of preys propagates at constant velocity, 68 µm.min-1. B. Corresponding profiles along the channel. Initial predator P and template G concentrations were 2 nM and 1 µM. To start the front, we had a solution of prey at 100 nM on top of the channel. Pol=8 U/mL.*

4 NOA81 device fabrication

Microfluidic NOA81 (Norland Optical Adhesive) thiolene-based, photocurable glue devices were made as described{D. Bartolo, 2008 #2279}. First, a PMMA negative mold was prepared using a CNC micromilling machine (MiniTech). PDMS was poured onto this mold and baked for 2 hours at 70°C to obtain a positive PDMS mold. Then, a drop of NOA81 was pressed in between the PDMS mold and a flat PDMS layer and cured by UV exposure at 20 mW cm^{-2} for 20 s. The structured PDMS was then carefully removed in order to keep the NOA81 layer bound to the flat PDMS. This flat PDMS was then pressed over a glass slide and a second UV exposure was carried out to finally seal the device (20 mW cm^{-2} for 60 s). Finally the flat PDMS layer was removed. Note that the PDMS mold, prepared from a micro-milled PMMA sheet, is easy to obtain and widely reusable. The whole fabrication process takes less than 4 hours to obtain several copies of a NOA81 device. Sample was injected with a micropipette through the 1 mm access holes embedded in the NOA layer. The initial condition was created by injecting 0.5 µL of reaction mixture with 100 nM N. To prevent evaporation, the chip was sealed with PCR scotch tape (premium Plate sealing film, Platemax, Axigen).

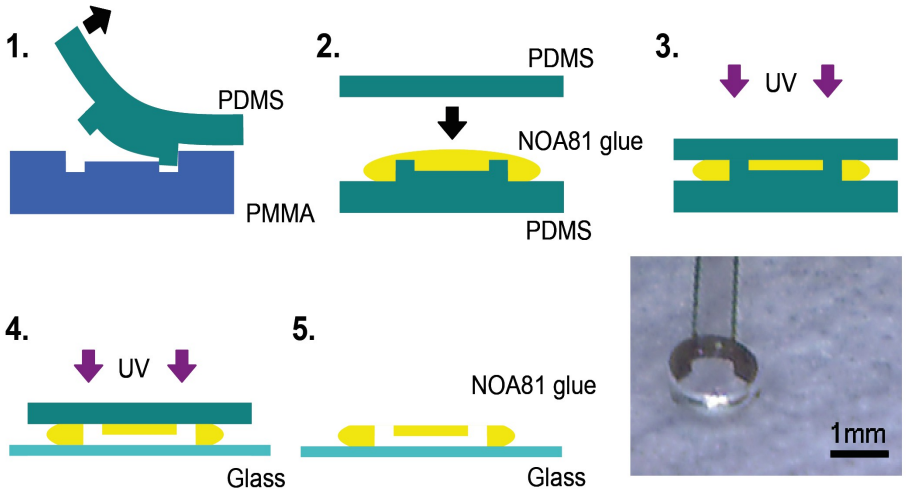

Figure S7: ***Step by step fabrication process of a NOA device.*** *1. A PDMS mold is first obtained by replica-molding of a micro-milled PMMA sheet (Minitech Machinery Corporation). 2. and 3. A drop of NOA is pressed in between the structured PDMS and a flat layer, and then UV insulate. 4. The structured PDMS is removed revealing a thin layer of non-cross-linked glue which is used to seal the device to a glass slide. 5. Removing the flat PDMS is the final step. Photography is a closed view of a 1mm in diameter inlet. Channel size is 300 µm width 120 µm high. Total thickness of the glue is 300 µm.*

5 Evaporation in PDMS and NOA81 devices

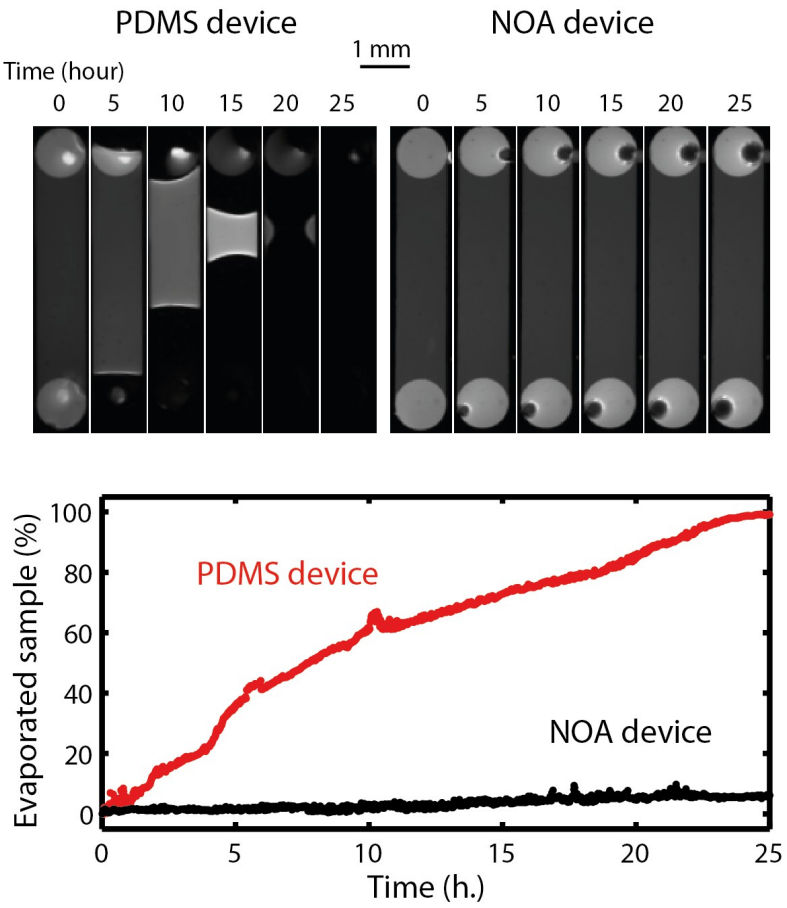

Figure S8: ***Comparison of the evaporation in PDMS and NOA81 devices.*** *120 µm high, 1mm width channels are filled with 100 µM fluorescein and sealed with PCR dedicated scotch tape. Experiment takes place on a microscope heating stage (Tokai Hit thermoplate) at 44°C for 25 hours. Percentage of evaporated sample represents the thickness-corrected area for which there is no more fluorescence signal.*

6 Influence of κ_2 on the simulated pulse width

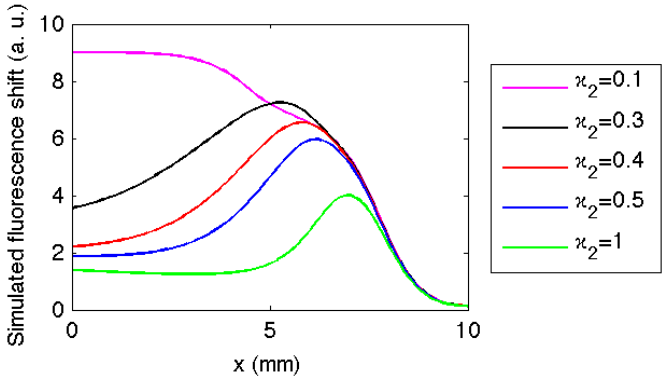

Figure S9: ***The width of the simulated pulse depends on κ_2.*** *Fluorescence shift profiles simulated with Eq. 1-4 in the Main Text and Eq. 2 in the SI with different values of κ_2 (in μM^{-1} min^{-1}) for $\kappa_1 = 0.05$ min^{-1}, $b = 1$ μM^{-1} and $D_N = D_P = 18 \times 10^3$ μm^2 min^{-1}.*

7 Simulation of the pulse propagation in the 90º turn

7.1 Parameters

We simulated the front propagation in the 90º turn using COMSOL MultiPhysics, Transport of Diluted Species interface. We solved the following equation

$$\frac{\partial N}{\partial t} = \frac{k_1 \cdot N}{1 + bN} - \frac{\kappa_2 \cdot N P}{1 + b P} + D_N \frac{\partial^2 N}{\partial x^2},$$
$$\frac{\partial P}{\partial t} = \frac{\kappa_2 \cdot N P}{1 + b P} + D_P \frac{\partial^2 P}{\partial x^2}.$$

using the parameter values given in the Table S2 below.

D_N	0.018 mm^2/min	Diffusion coefficient of prey
D_P	0.018 mm^2/min	Diffusion coefficient of predator
k_1	0.025 min^{-1}	Rate constant for prey growth
κ_2	0.0005 $nM^{-1}min^{-1}$	Rate constant for predation
N_0	100 nM	Initial concentration of prey
P_0	2nM	Initial concentration of predator
b	10^{-3} nM^{-1}	saturation of the growth reaction by N

Table S2: Meaning of the parameters present in the equations and their values used in the simulation.

We defined the following conditions:

- boundary condition: no flux,
- initial condition in the reactor, outside the triggering front area, N=0, P= P_0
- initial condition in the reactor, triggering front area, N=N_0, P= P_0

Mesh was automatically generated (Physics-controlled mesh, extremely fine). A control simulation was performed by increasing the mesh 2-fold, without change.

7.2 Results

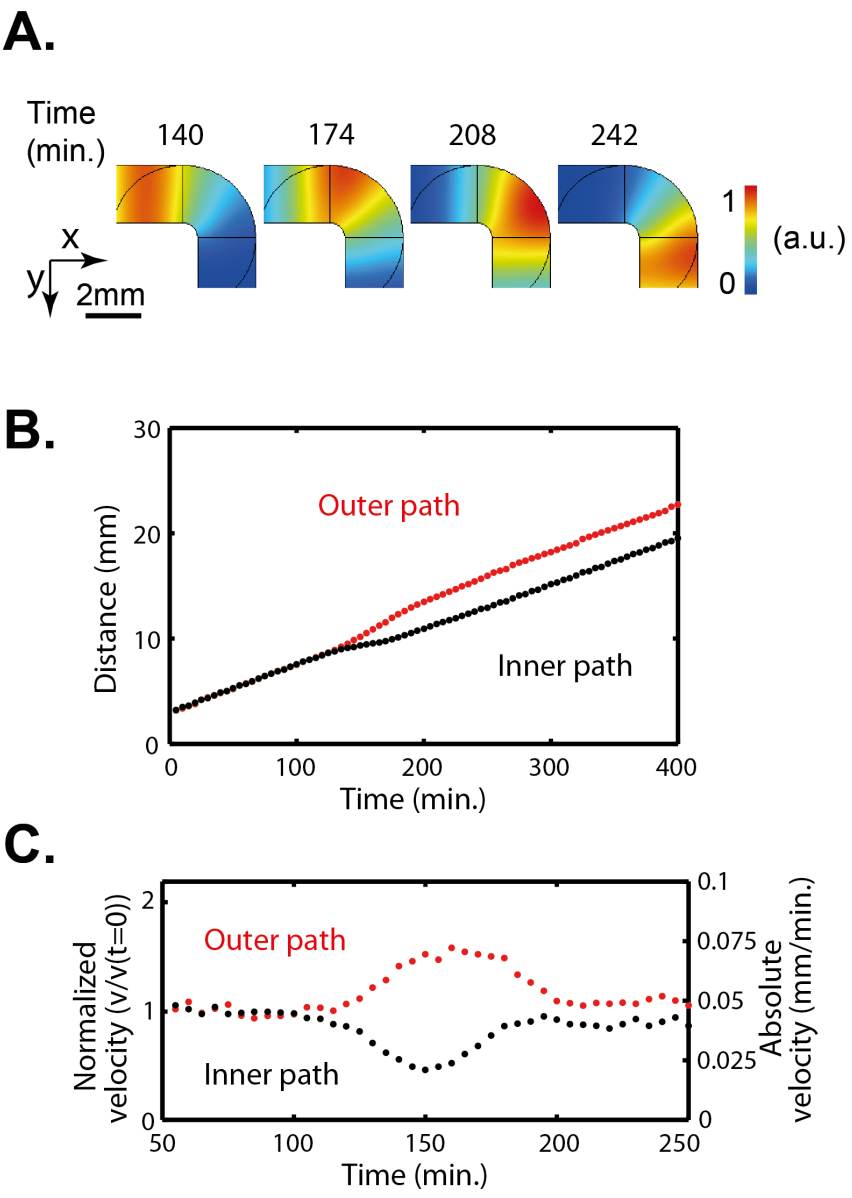

Figure S10: ***Simulation of the front propagating in a 90° turn, 1.5 mm curvature radius****. A. Time-lapse pictures of the front. B. Front position as a function of time for both inner path (black) and outer path (red). C. Corresponding velocity of the front for both inner path (black) and outer path (red).*

8 Measurement of front curvatures

Front curvatures, γ, in the experiments described in Figure 5 in the Main Text where measured manually after binarization of the corresponding fluorescence image.

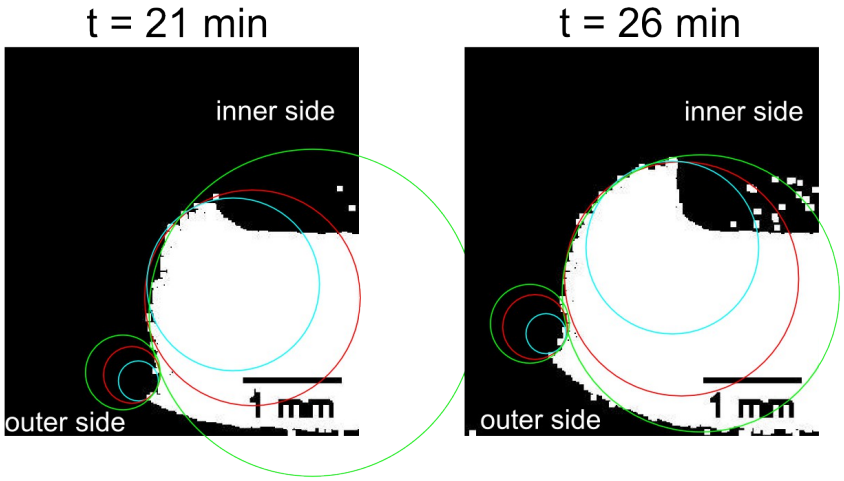

Figure S11: ***Measurement and precision of front curvatures.*** *Binarized fluorescent shift images for prey front propagating in a turn channel with inner curvature radius 1.5 mm at 21 and 26 min. Front curvatures for the inner and outer sides of the front were measured by manually adapting a circle to the front shape. To estimate the precision of these measurements three circles were used with largest (green), optimal (red) and lowest (light blue) radius.*

The data extracted from Figure S11 are summarized in the table below

	t = 21 min		t = 26 min	
	inner	**outer**	**inner**	**outer**
$\langle R \rangle$ (10^3 μm)	1.2	0.3	1.2	0.3
σ_R (10^3 μm)	0.4	0.1	0.3	0.1
$\langle \gamma \rangle$ (10^{-3} μm^{-1})	0.9	3.7	0.9	3.5
σ_γ (10^{-3} μm^{-1})	0.3	1.2	0.2	1.3

9 Supplementary movies

9.1 Movie S1: straight channel

Associated to figure 4 in the main text: traveling wave passing through a straight channel. Time-lapse (1 image every minute), yellow fluorescence shift imaging (corresponding to prey concentration). Channel is 1 mm width. Experimental conditions as in figure 4 in the main text.

Figure S12: Movie S1, straight channel

9.2 Movie S2: 90° turn, 1.5 mm curvature radius

Associated to figure 5 in the main text: traveling wave passing through a 90° turn. Time-lapse (1 image every minute), yellow fluorescence shift imaging (corresponding to prey concentration). Channel is 2 mm width. Experimental conditions as in figure 5 in the main text.

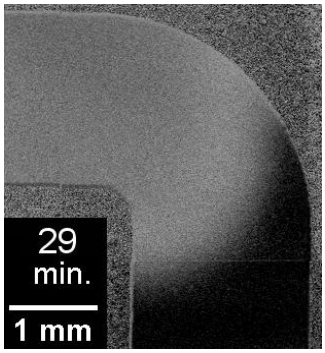

Figure S13: Movie S2, 90° turn, 1.5 mm curvature radius

9.3 Movie S3: maze

Associated to figure 6 in the main text: traveling wave passing through an arbitrary maze. Time-lapse (1 image every minute), yellow fluorescence shift imaging (corresponding to prey concentration). Channels are 500 µm width. Experimental conditions as in figure 6 in the main text.

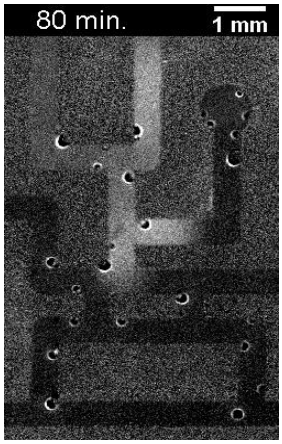

Figure S14: Movie S3, maze

Bibliography

[1] James Dickson Murray. *Spatial Pattern Formation with Reaction Diffusion Systems*, volume II. Springer, New York, 3rd edition, 2004.

[2] Lewis Wolpert. *Principles of Development*. Oxford University Press, USA, 2011.

[3] Takehiko Ichikawa, Kenichi Nakazato, Philipp J. Keller, Hiroko Kajiura-Kobayashi, Ernst H K Stelzer, Atsushi Mochizuki, and Shigenori Nonaka. Live Imaging of Whole Mouse Embryos during Gastrulation: Migration Analyses of Epiblast and Mesodermal Cells. *PLoS One*, 8(7):4–12, 2013.

[4] Lewis Wolpert. Positional information and the spatial pattern of cellular differentiation. *J. Theor. Biol.*, 25(1):1–47, 1969.

[5] Daniel St Johnston and Christiane Nüsslein-Volhard. The origin of pattern and polarity in the Drosophila embryo. *Cell*, 68(2):201–219, jan 1992.

[6] Thomas Gregor, David W. Tank, Eric F. Wieschaus, and William Bialek. Probing the Limits to Positional Information. *Cell*, 130(1):153–164, 2007.

[7] Rushikesh Sheth, Luciano Marcon, M Félix Bastida, Marisa Junco, Laura Quintana, Randall Dahn, Marie Kmita, James Sharpe, and Maria A Ros. Hox genes regulate digit patterning by controlling the wavelength of a Turing-type mechanism. *Science*, 338(6113):1476–80, dec 2012.

[8] Alan Mathison Turing. The Chemical Basis of Morphogenesis. *Philos. Trans. R. Soc. B Biol. Sci.*, 237(641):37–72, aug 1952.

[9] Andrew D Economou, Atsushi Ohazama, Thantrira Porntaveetus, Paul T Sharpe, Shigeru Kondo, M Albert Basson, Amel Gritli-Linde, Martyn T Cobourne, and Jeremy B A Green. Periodic stripe formation by a Turing mechanism operating at growth zones in the mammalian palate. *Nat. Genet.*, 44(3):348–51, 2012.

[10] Jeremy B. A. Green and James Sharpe. Positional information and reaction-diffusion: two big ideas in developmental biology combine. *Development*, 142 (7):1203–1211, apr 2015.

[11] Donald E. Ingber. Mechanical control of tissue morphogenesis during embryological development. *Int. J. Dev. Biol.*, 50(2-3):255–66, 2006.

[12] Shigeru Kondo and Takashi Miura. Reaction-diffusion model as a framework for understanding biological pattern formation. *Science*, 329(5999):1616–1620, sep 2010.

[13] Kenneth Showalter and Irving R. Epstein. From chemical systems to systems chemistry: Patterns in space and time. *Chaos*, 25(9), 2015.

[14] Alfred Gierer and Hans Meinhardt. A theory of biological pattern formation. *Kybernetik*, 12(1):30–39, dec 1972.

[15] A N Zaikin and Anatol Markovich Zhabotinsky. Concentration wave propagation in two-dimensional liquid-phase self-oscillating system. *Nature*, 225(5232):535–7, feb 1970.

[16] Klara Kovacs, Rachel E. McIlwaine, Stephen K. Scott, and Annette F. Taylor. An Organic-Based pH Oscillator. *J. Phys. Chem. A*, 111(4):549–551, feb 2007.

[17] Irving Epstein. Making Waves with DNA. *Physics (College. Park. Md).*, 8:12, 2015.

[18] Vincent Castets, Etiennette Dulos, Jacques Boissonade, and Patrick De Kepper. Experimental evidence of a sustained standing Turing-type nonequilibrium chemical pattern. *Phys. Rev. Lett.*, 64(24):2953–2956, 1990.

[19] Qi Ouyang and Harry L. Swinney. Transition from a uniform state to hexagonal and striped Turing patterns. *Nature*, 352(6336):610–612, aug 1991.

[20] Nathan Tompkins, Ning Li, Camille Girabawe, M. Heymann, G. Bard Ermentrout, Irving R. Epstein, and Seth Fraden. Testing Turing's theory of morphogenesis in chemical cells. *Proc. Natl. Acad. Sci.*, 111(12):4397–4402, mar 2014.

[21] D Ewen Cameron, Caleb J Bashor, and James J Collins. A brief history of synthetic biology. *Nat. Rev. Microbiol.*, 12(5):381–90, 2014.

[22] Michael B Elowitz and Stanislas Leibler. A synthetic oscillatory network of transcriptional regulators. *Nature*, 403(6767):335–338, jan 2000.

[23] J H Chen and Nadrian C Seeman. Synthesis from DNA of a molecule with the connectivity of a cube. *Nature*, 350(6319):631–3, apr 1991.

[24] Paul W K Rothemund. Folding DNA to create nanoscale shapes and patterns. *Nature*, 440(7082):297–302, mar 2006.

[25] Milan N. Stojanovic, Tiffany Elizabeth Mitchell, and Darko Stefanovic. Deoxyribozyme-based logic gates. *J. Am. Chem. Soc.*, 124(14):3555–3561, 2002.

[26] Kevin Montagne, Raphael Plasson, Yasuyuki Sakai, Teruo Fujii, and Yannick Rondelez. Programming an in vitro DNA oscillator using a molecular networking strategy. *Mol. Syst. Biol.*, 7(466):466, feb 2011.

[27] Jongmin Kim and Erik Winfree. Synthetic in vitro transcriptional oscillators. *Mol. Syst. Biol.*, 7(1):465, 2011.

[28] Adrien Padirac, Teruo Fujii, André Estévez-Torres, and Yannick Rondelez. Spatial Waves in Synthetic Biochemical Networks. *J. Am. Chem. Soc.*, jun 2013.

[29] Anton S. Zadorin, Yannick Rondelez, Jean-Christophe Galas, and André Estevez-Torres. Synthesis of Programmable Reaction-Diffusion Fronts Using DNA Catalyzers. *Phys. Rev. Lett.*, 114(6):068301, 2015.

[30] Atsushi Yamagata, Ryoji Masui, Yoshimitsu Kakuta, Seiki Kuramitsu, and Keiichi Fukuyama. Overexpression, purification and characterization of RecJ protein from Thermus thermophilus HB8 and its core domain. *Nucleic Acids Res.*, 29(22): 4617–24, nov 2001.

[31] Adrien Padirac, Teruo Fujii, and Yannick Rondelez. Bottom-up construction of in vitro switchable memories. *Proc. Natl. Acad. Sci. U. S. A.*, 109(47):E3212–20, nov 2012.

[32] Teruo Fujii and Yannick Rondelez. Predator-prey molecular ecosystems. *ACS Nano*, 7(1):27–34, jan 2013.

[33] Nathanaël Aubert, Clément Mosca, Teruo Fujii, Masami Hagiya, and Yannick Rondelez. Computer-assisted design for scaling up systems based on DNA reaction networks. *J. R. Soc. Interface*, 11(93):20131167, 2014.

[34] Eugene S Han, Deani L Cooper, Nicole S Persky, Vincent A Sutera, Richard D Whitaker, Melissa L Montello, and Susan T Lovett. RecJ exonuclease: substrates, products and interaction with SSB. *Nucleic Acids Res.*, 34(4):1084–91, feb 2006.

[35] Alexandre Baccouche, Kevin Montagne, Adrien Padirac, Teruo Fujii, and Yannick Rondelez. Dynamic DNA-toolbox reaction circuits: A walkthrough. *Methods*, 67 (2):234–249, feb 2014.

[36] Hendrik W. H. van Roekel, Lenny H. H. Meijer, Saeed Masroor, Zandra C. Félix Garza, André Estévez-Torres, Yannick Rondelez, Antonios Zagaris, Mark A. Peletier, Peter A. J. Hilbers, and Tom F. A. de Greef. Automated Design of Programmable Enzyme-Driven DNA Circuits. *ACS Synth. Biol.*, 4(6):735–745, jun 2015.

[37] Adrien Padirac, Teruo Fujii, and Yannick Rondelez. Quencher-free multiplexed monitoring of DNA reaction circuits. *Nucleic Acids Res.*, 40(15):e118, aug 2012.

[38] Anthony J. Genot, A. Baccouche, R. Sieskind, Nathanael Aubert-Kato, N. Bredeche, J. F. Bartolo, V. Taly, Teruo Fujii, and Yannick Rondelez. High-resolution mapping of bifurcations in nonlinear biochemical circuits. *Nat. Chem.*, 8(8):760–767, jun 2016.

[39] Irving R. Epstein and John A. Pojman. *Introduction to Nonlinear Chemical Dynamics. Oscillations, Waves, Patterns and Chaos.* Oxford University Press, USA, New York, NY, 1998.

[40] Istvan Lengyel and Irving R. Epstein. A chemical approach to designing Turing patterns in reaction-diffusion systems. *Proc. Natl. Acad. Sci.*, 89(9):3977–3979, may 1992.

[41] John E. Pearson. Pattern formation in a (2 + 1)-species activator-inhibitor-immobilizer system. *Phys. A Stat. Mech. its Appl.*, 188(1-3):178–189, sep 1992.

[42] K. Korvasová, E.A. Gaffney, P.K. Maini, M.A. Ferreira, and V. Klika. Investigating the Turing conditions for diffusion-driven instability in the presence of a binding immobile substrate. *J. Theor. Biol.*, 367:286–295, feb 2015.

[43] Kouichi Asakura, Ryo Konishi, Tomomi Nakatani, Takaya Nakano, and Masazumi Kamata. Turing pattern formation by the CIMA reaction in a chemical system consisting of quaternary alkyl ammonium cationic groups. *J. Phys. Chem. B*, 115 (14):3959–3963, 2011.

[44] Istvan Lengyel and Irving R. Epstein. Modeling of turing structures in the chlorite–iodide–malonic Acid–starch reaction system., 1991.

[45] Zoltan Noszticzius, Ouyang Qi, William D. McCormick, and Harry L Swinney. Effect of Turing pattern indicators on CIMA oscillators. *J. Phys. Chem.*, 96(15): 6302–6307, jul 1992.

[46] István Szalai and Patrick De Kepper. Pattern formation in the ferrocyanide-iodate-sulfite reaction: The control of space scale separation. *Chaos*, 18(2), 2008.

[47] Vladimir K. Vanag and Irving R. Epstein. Pattern formation in a tunable medium: the Belousov-Zhabotinsky reaction in an aerosol OT microemulsion. *Phys. Rev. Lett.*, 87(22):228301, 2001.

[48] Arthur T. Winfree. Spiral waves of chemical activity. *Science (80-.).*, 175(4022): 634–636, 1972.

[49] Irving R. Vanag, Vladimir K. and Epstein. Inwardly Rotating Spiral Waves in a Reaction-Diffusion System. *Science (80-.).*, 294(5543):835–837, oct 2001.

[50] Peter B. Allen, Xi Chen, and Andrew D. Ellington. Spatial control of DNA reaction networks by DNA sequence. *Molecules*, 17(11):13390–402, jan 2012.

[51] Lang Feng, Lea-Laetitia Pontani, Rémi Dreyfus, Paul Chaikin, and Jasna Brujic. Specificity, flexibility and valence of DNA bonds guide emulsion architecture. *Soft Matter*, 9(41):9816, 2013.

[52] K. van Ommering. Magnetic properties of sub-micrometer superparamagnetic beads used for biosensors. Technical report, Technische Universiteit Eindhoven (TUE), 2006.

[53] John Crank. *The mathematics of diffusion*, volume 50. Clarendon Press, Oxford, 2nd editio edition, jun 1975.

[54] A.N. Stokes. On two types of moving front in quasilinear diffusion. *Math. Biosci.*, 31(3-4):307–315, jan 1976.

[55] Joseph N. Zadeh, Conrad D. Steenberg, Justin S. Bois, Brian R. Wolfe, Marshall B. Pierce, Asif R. Khan, Robert M. Dirks, and Niles A. Pierce. NUPACK: Analysis and design of nucleic acid systems. *J. Comput. Chem.*, 32(1):170–173, jan 2011.

[56] Nicholas R. Markham and Michael Zuker. DINAMelt web server for nucleic acid melting prediction. *Nucleic Acids Res.*, 33(SUPPL. 2):577–581, 2005.

[57] Kristin A Marshall and Andrew D Ellington. Molecular Parasites That Evolve Longer Genomes. *J. Mol. Evol.*, 49(5):656–663, nov 1999.

[58] Bruce J. MacLennan. The Morphogenetic Path to Programmable Matter. *Proc. IEEE*, 103(7):1226–1232, jul 2015.

[59] Chad A. Mirkin, Robert L. Letsinger, Robert C. Mucic, and James J. Storhoff. A DNA-based method for rationally assembling nanoparticles into macroscopic materials. *Nature*, 382(6592):607–609, aug 1996.

[60] Mirjam E. Leunissen, Rémi Dreyfus, Roujie Sha, Tong Wang, Nadrian C. Seeman, David J. Pine, and Paul M. Chaikin. Towards self-replicating materials of DNA-functionalized colloids. *Soft Matter*, 5(12):2422, 2009.

[61] James D. Lechleiter, Linu M. John, and Patricia Camacho. Ca2+ wave dispersion and spiral wave entrainment in Xenopus laevis oocytes overexpressing Ca2+ ATPases. *Biophys. Chem.*, 72(1-2):123–129, may 1998.

[62] James Lechleiter, Steven Girard, David Clapham, and Ernest Peralta. Subcellular patterns of calcium release determined by G protein-specific residues of muscarinic receptors. *Nature*, 350(June):505–508, 1991.

[63] Hans Meinhardt and Piet A. J. De Boer. Pattern formation in Escherichia coli: A model for the pole-to-pole oscillations of Min proteins and the localization of the division site. *Proc. Natl. Acad. Sci.*, 98(25):14202–14207, dec 2001.

[64] John J. Tyson, Kevin A. Alexander, V. S. Manoranjan, and J. D. Murray. Spiral waves of cyclic amp in a model of slime mold aggregation. *Phys. D Nonlinear Phenom.*, 34(1-2):193–207, 1989.

[65] Tm Konijn and Jg Van De Meene. The acrasin activity of adenosine-3', 5'-cyclic phosphate. *Proc. Natl. Acad. Sci. U. S. A.*, 4:1152–1154, 1967.

[66] Petra Foerster, Stefan C. Muller, and Benno Hess. Curvature and Propagation Velocity of Chemical Waves. *Science (80-.).*, 241(4866):685–687, aug 1988.

[67] John J Tyson and James P Keener. Singular perturbation theory of traveling waves in excitable media (a review). *Phys. D Nonlinear Phenom.*, 32(3):327–361, dec 1988.

[68] Richard J Field and Richard M Noyes. Oscillations in chemical systems. V. Quantitative explanation of band migration in the Belousov-Zhabotinskii reaction. *J. Am. Chem. Soc.*, 96(7):2001–2006, apr 1974.

[69] Ágota Tóth and Kenneth Showalter. Logic gates in excitable media. *J. Chem. Phys.*, 103(6):2058–2066, 1995.

[70] Oliver Steinbock, Petteri Kettunen, and Kenneth Showalter. Chemical Wave Logic Gates. *J. Phys. Chem.*, 100(49):18970–18975, 1996.

[71] Oliver Steinbock, A. Toth, and Kenneth Showalter. Navigating Complex Labyrinths: Optimal Paths from Chemical Waves. *Science (80-.).*, 267(5199): 868–871, feb 1995.

[72] Jakob Schweizer, Martin Loose, Mike Bonny, Karsten Kruse, Ingolf Mönch, and Petra Schwille. Geometry sensing by self-organized protein patterns. *Proc. Natl. Acad. Sci. U. S. A.*, 109(38):15283–8, sep 2012.

[73] Joe Lutkenhaus. Assembly dynamics of the bacterial MinCDE system and spatial regulation of the Z ring. *Annu. Rev. Biochem.*, 76:539–62, jan 2007.

[74] Brent T. Ginn, Bettina Steinbock, Murat Kahveci, and Oliver Steinbock. Microfluidic Systems for the Belousov-Zhabotinsky Reaction. *J. Phys. Chem. A*, 108(8): 1325–1332, 2004.

[75] Masahiro Toiya, Vladimir K. Vanag, and Irving R. Epstein. Diffusively coupled chemical oscillators in a microfluidic assembly. *Angew. Chemie - Int. Ed.*, 47(40): 7753–7755, 2008.

[76] Emmanuel Delamarche, André Bernard, Heinz Schmid, Bruno Michel, and Hans Biebuyck. Patterned Delivery of Immunoglobulins to Surfaces Using Microfluidic Networks. *Science (80-.).*, 276(5313):779–781, may 1997.

[77] Stephen R Unger, Marc A and Chou, Hou-Pu and Thorsen, Todd and Scherer, Axel and Quake. Monolithic Microfabricated Valves and Pumps by Multilayer Soft Lithography. *Science (80-.).*, 288(5463):113–116, apr 2000.

[78] Guilhem Velve-Casquillas, Maël Le Berre, Matthieu Piel, and Phong T. Tran. Microfluidic tools for cell biological research. *Nano Today*, 5(1):28–47, 2010.

[79] George M Whitesides. The origins and the future of microfluidics. *Nature*, 442 (7101):368–73, 2006.

[80] Jing Dai, Sung Ho Yoon, Hye Young Sim, Yoon Sun Yang, Tae Kwang Oh, Jihyun F. Kim, and Jong Wook Hong. Charting microbial phenotypes in multiplex nanoliter batch bioreactors. *Anal. Chem.*, 85(12):5892–5899, 2013.

[81] Mingzhe Gan, Yunfang Tang, Yiwei Shu, Hongkai Wu, and Liwei Chen. Massively parallel bacterial and yeast suspension culture on a chip. *Small*, 8(6):863–867, 2012.

[82] Ji Y. Cheng, Cheng W. Wei, Kai Hsiung Hsu, and Tai Horng Young. Direct-write laser micromachining and universal surface modification of PMMA for device development. *Sensors Actuators, B Chem.*, 99(1):186–196, 2004.

[83] Denis Bartolo, Guillaume Degré, Philippe Nghe, and Vincent Studer. Microfluidic stickers. *Lab Chip*, 8(2):274–9, feb 2008.

[84] John S. McCaskill and G. J. Bauer. Images of evolution: origin of spontaneous RNA replication waves. *Proc. Natl. Acad. Sci.*, 90(9):4191–4195, may 1993.

Université Paris-Saclay
Espace Technologique / Immeuble Discovery
Route de l'Orme aux Merisiers RD 128 / 91190 Saint-Aubin, France

université PARIS-SACLAY
ÉCOLE DOCTORALE
Physique et ingénierie : électrons, photons, sciences du vivant (EOBE)

Titre : Synthèse de structure de réaction-diffusion à base d'ADN : vers la génération de structure de Turing.

Mots clés : Réaction-diffusion, les réseaux de réaction à base d'ADN, la formation de motif, la microfluidique.

Résumé : Un exemple fascinant illustrant la pertinence des structures spatio-temporels en biologie est le développement de l'embryon à partir d'un œuf fertilisé quasi-homogène. Les structures chimiques qui apparaissent ensuite le long de l'embryon, orchestrées selon des programmes moléculaires, sont utilisées comme patrons par les processus en aval impliqués dans la génération d'un organisme entièrement développé.

L'article d'Alan Turing sur les mécanismes de réaction-diffusion capables de produire des brisures de symétrie a inspiré de nombreuses études théoriques et expérimentales. Depuis, la capacité des systèmes chimiques hors-équilibre à s'auto-organiser en motifs spatio-temporels a été démontré. Pour autant, l'application des théories de Turing aux structures biologiques reste controversée en raison de preuves expérimentales limitées. Malgré de nombreux succès dans la formation de structures à partir de la célèbre réaction de Belousov-Zhabotinsky (BZ) et ses dérivées, ces motifs spatio-temporels sont difficiles à réaliser, limitant ainsi la mise en œuvre expérimentale à quelques mécanismes disponibles.

Les systèmes basés sur l'ADN permettent de rationaliser la mise en place d'un ordre spatio-temporel grâce à leur chimie prévisible. Cette thèse porte sur la conception et le développement de modèles spatio-temporels impliquant des oligonucléotides ADN qui réagissent entre eux tout en diffusant dans la solution. La contribution de ce travail de doctorat dans la maîtrise de modèles de réaction-diffusion a consisté en : (1) Tester un réseau de réaction à base d'ADN dans une topologie d'inhibiteur-activateur, (2) Développer une stratégie pour modifier le coefficient de diffusion des brins d'ADN activateurs, (3) Explorer comment des motifs chimiques déterminent la forme d'un matériau et (4) Contrôler la géométrie de l'environnement d'un système de réaction-diffusion à base d'ADN. Globalement nous avons étendu le nombre d'outils disponibles pour étudier la formation de motifs chimiques et leurs couplages aux matériaux, et réalisé une avancée vers la production de motifs de Turing à partir d'ADN.

A l'issue de ce travail, nous pensons que la programmabilité et la biocompatibilité de systèmes à base d'ADN ouvrent de nouvelles perspectives pour l'ingénierie de systèmes chimiques de type réaction-diffusion, en particulier dans deux directions. Premièrement, pour étudier les mécanismes bio-inspirés de formation de motifs dans des conditions expérimentales simplifiées mais pertinentes. Deuxièmement pour construire de nouveaux matériaux qui pourraient s'auto-assembler par un processus s'inspirant de l'embryogenèse.

Université Paris-Saclay
Espace Technologique / Immeuble Discovery
Route de l'Orme aux Merisiers RD 128 / 91190 Saint-Aubin, France

université PARIS-SACLAY
ÉCOLE DOCTORALE
Physique et ingénierie : électrons, photons, sciences du vivant (EOBE)

Title: Synthesis of reaction-diffusion patterns with DNA: towards Turing patterns.

Keywords: Reaction-diffusion, DNA-based synthetic reaction networks, pattern formation, microfluidics.

Abstract: One fascinating example that highlights the biological relevance of spatio-temporal patterns in biology is the development of an embryo starting with a nearly homogenous fertilized egg. Subsequently, chemical patterns across the length of the embryo, orchestrated by molecular programs, are used as blue prints for downstream processes involved in the generation of a fully developed organism.

Alan Turing's paper about reaction-diffusion mechanisms capable of symmetry breaking inspired numerous theoretical and experimental studies. Since then, the potential of out-of-equilibrium chemical systems to self-organize into spatiotemporal patterns has been demonstrated. Yet, the relevance of Turing's idea in biological patterning remains controversial due to the limited experimental proofs. And despite of the exceptional achievements in pattern formation using the well-known Belousov-Zhabotinsky (BZ) reaction and its relatives, these are difficult to engineer, thus limiting their experimental implementation to few available mechanisms.

Potentially, DNA-based systems may allow the rational engineering of spatio-temporal order due to the predictable chemistry of DNA. This thesis focuses on the design and development of spatio-temporal patterns involving DNA oligonucleotides that react and diffuse. The contribution of this PhD work to controlling reaction-diffusion patterns consisted in: (1) testing a DNA-based reaction network with an activator-inhibitor topology, (2) developing a strategy to tune the diffusion coefficient of activator DNA strands, (3) exploring how chemical patterns determine the shape of a material, and (4) controlling the geometry over a DNA-based reaction-diffusion system. Overall, we have expanded the number of available tools to study chemical and material pattern formation and advance towards Turing patterns with DNA.

This work suggests that the programmability and biocompatibility of DNA-based systems open new perspectives for the engineering of the reaction-diffusion chemical synthesis, in particular in two directions. Firstly, to study biologically-inspired pattern-forming mechanisms in simplified, yet relevant, experimental conditions. Secondly to build new materials that would self-build by a process inspired from embryo morphogenesis.

Université Paris-Saclay
Espace Technologique / Immeuble Discovery
Route de l'Orme aux Merisiers RD 128 / 91190 Saint-Aubin, France